

## REPORT DOCUMENTATION PAGE

1a. REPORT SECURITY CLASSIFICATION <b>UNCLASSIFIED</b>			1b. RESTRICTIVE MARKINGS <b>UNCLASSIFIED</b>		
2a. SECURITY CLASSIFICATION AUTHORITY			3. DISTRIBUTION / AVAILABILITY OF REPORT  Approved for public release; distribution unlimited.		
2b. DECLASSIFICATION / DOWNGRADING SCHEDULE			5. MONITORING ORGANIZATION REPORT NUMBER(S)		
4. PERFORMING ORGANIZATION REPORT NUMBER(S)  SIO REFERENCE 87-15 [MPL-U-26/86]					
6a. NAME OF PERFORMING ORGANIZATION  Marine Physical Laboratory		6b. OFFICE SYMBOL (If applicable) MPL		7a. NAME OF MONITORING ORGANIZATION  Office of Naval Research	
6c. ADDRESS (City, State, and ZIP Code) University of California, San Diego Scripps Institution of Oceanography San Diego, CA 92152			7b. ADDRESS (City, State, and ZIP Code) Department of the Navy 800 North Quincy Street Arlington, VA 22217-5000		
8a. NAME OF FUNDING / SPONSORING ORGANIZATION Office of Naval Research		8b. OFFICE SYMBOL (If applicable) ONR		9. PROCUREMENT INSTRUMENT IDENTIFICATION NUMBER  N00014-79-C-0472	
8c. ADDRESS (City, State, and ZIP Code) Department of the Navy 800 North Quincy Street Arlington, VA 22217-5000			10. SOURCE OF FUNDING NUMBERS		
			PROGRAM ELEMENT NO.	PROJECT NO.	TASK NO.
			WORK UNIT ACCESSION NO.		
11. TITLE (Include Security Classification)  OBSERVATIONS OF THE UPPER OCEAN USING A MULTI-BEAM DOPPLER SONAR					
12. PERSONAL AUTHOR(S) Albert James Plueddemann					
13a. TYPE OF REPORT summary/thesis		13b. TIME COVERED FROM _____ TO _____		14. DATE OF REPORT (Year, Month, Day) May 1987	
15. PAGE COUNT 145					
16. SUPPLEMENTARY NOTATION					
17. COSATI CODES			18. SUBJECT TERMS (Continue on reverse if necessary and identify by block number)		
FIELD	GROUP	SUB-GROUP	Doppler sonar, internal waves, diurnal migration		
19. ABSTRACT (Continue on reverse if necessary and identify by block number)					
<p>This dissertation presents several different, but related topics which involve both the analysis techniques for, and applications of, Doppler sonar measurements. Data were collected from four downward-slanting sonars operated on the Research Platform FLIP during a field experiment conducted off of the California coast. The sonars provide profiles of backscattered intensity and slant velocity from approximately 100 m to 1000 m in depth with 20 m depth resolution.</p> <p>A technique to measure the vertically-acting Reynolds stresses, <math>\overline{u'w'}</math> and <math>\overline{v'w'}</math>, in the oceanic internal wave field using a multi-beam Doppler sonar is presented. The stress measurement technique is applied to the Doppler velocity data collected during the experiment. The principal result is a lack of observed Reynolds stresses in the high-vertical wavenumber, high-frequency internal wave band which can be considered significantly different from zero, despite the use of a scale separation which is more restrictive than that of previous investigators, and the consideration of stresses on several different time scales. The results are consistent with a high-frequency internal wave field which tends to be dominated by mode-like rather than ray-like waves, and which, on average, exhibits a high degree of vertical symmetry. No evidence is found of a correlation between internal wave stresses and mean-flow shear. There is weak evidence of a correlation between stress divergence and mean-flow acceleration.</p> <p>A characterization of the diurnal migration patterns of acoustic scattering layers based on the Doppler sonar measurements is presented. The effects of the diurnal migration of scatterers are evident in both backscattered intensity and Doppler velocity, and the two measurements provide complementary methods of analysis. The principal result is the observation of three distinct scattering layers whose patterns of vertical migration show a high degree of persistence in both space and time.</p> <p>It is found that the covariance-based estimator of mean Doppler shift exhibits a bias in the presence of band-limited noise. Pulse-to-pulse incoherent Doppler sonars are often operated under conditions where the biasing effect is important. Methods of correcting for noise-biasing are presented.</p>					
20. DISTRIBUTION / AVAILABILITY OF ABSTRACT <input type="checkbox"/> UNCLASSIFIED/UNLIMITED <input checked="" type="checkbox"/> SAME AS RPT. <input type="checkbox"/> DTIC USERS			21. ABSTRACT SECURITY CLASSIFICATION <b>UNCLASSIFIED</b>		
22a. NAME OF RESPONSIBLE INDIVIDUAL A.J. Plueddemann (now at WHOI, MA 02543)			22b. TELEPHONE (Include Area Code) (617) 548-1400 (x2780)		22c. OFFICE SYMBOL



# MARINE PHYSICAL LABORATORY

LIBRARY  
RESEARCH REPORTS DIVISION  
NAVAL POSTGRADUATE SCHOOL  
MONTEREY, CALIFORNIA 93946

*de* SCRIPPS INSTITUTION OF OCEANOGRAPHY .

San Diego, California 92152

---

## OBSERVATIONS OF THE UPPER OCEAN USING A MULTI-BEAM DOPPLER SONAR .

Albert James Plueddemann

*copy of*  
*de* SIO REFERENCE 87-15 .

MPL-U-26/86 .  
May 1987

*Approved for public release; distribution unlimited.*

---

**OBSERVATIONS OF THE UPPER OCEAN  
USING A MULTI-BEAM DOPPLER SONAR**

*A dissertation submitted in partial satisfaction of the  
requirements for the degree Doctor of Philosophy  
in Oceanography*

Albert James Plueddemann

**SIO REFERENCE 87-15**

Sponsored by the  
Office of Naval Research  
Contract N00014-79-C-0472

MPL-U-26/86  
May 1987

# Table of Contents

	Page
List of Figures .....	v
List of Tables .....	vii
Acknowledgements .....	ix
Abstract .....	x
 Introduction .....	 1
 <b>I Data collection and processing</b> .....	 3
1.1 Introduction .....	3
1.2 The Mixed Layer Dynamics Experiment .....	3
1.3 Doppler sonar operation .....	10
1.3.1 Background .....	10
1.3.2 Doppler sonar fundamentals .....	11
1.3.3 The MPL Doppler sonar system .....	14
1.4 Velocity estimation .....	18
1.4.1 The velocity estimates .....	18
1.4.2 Velocity estimation errors .....	21
1.5 Chapter summary .....	27
 <b>II The measurement of Reynolds stresses associated with       internal waves in the ocean</b> .....	 28
2.1 Introduction .....	28
2.2 Background .....	30
2.2.1 Internal waves in a slowly-varying mean flow .....	30
2.2.2 Estimates and observations of wave-induced stresses .....	32
2.3 Methods .....	35
2.3.1 Stress measurement using multi-beam Doppler sonar .....	35
2.3.2 Data analysis procedure .....	38
2.3.3 Evaluation of errors .....	43
2.4 Results and discussion .....	47
2.4.1 Stress measurements .....	47
2.4.2 Relationship of stress to the mean flow .....	54
2.5 Chapter summary .....	57

<b>III</b>	<b>Characterization of the patterns of diurnal migration using a Doppler sonar .....</b>	<b>62</b>
3.1	Introduction .....	62
3.2	Methods .....	63
3.2.1	Intensity data .....	66
3.2.2	Velocity data .....	69
3.3	Results .....	70
3.4	Discussion .....	79
3.5	Chapter summary .....	83
 <b>IV</b>	 <b>Biasing of the covariance-based mean frequency estimator in the presence of band-limited noise .....</b>	 <b>84</b>
4.1	Introduction .....	84
4.2	Covariance processing .....	85
4.3	CP in the presence of band-limited noise .....	87
4.4	Bias correction trials for the MPL Doppler sonar .....	98
4.5	Chapter summary .....	101
 <b>Appendices</b>		
A.	Correction for platform motion .....	A-1
B.	The covariance processing technique .....	B-1
 <b>References</b> .....		<b>R-1</b>

## List of Figures

Figure		Page
Chapter I		
1.1	The MILDEX site .....	4
1.2	MILDEX cruise tracks .....	5
1.3	Schematic of FLIP instrumentation .....	7
1.4	MILDEX 1983: SIO-FLIP operational summary .....	8
1.5	Heading, wind speed, and tilt time series .....	9
1.6	Schematic of acoustic Doppler velocity measurement .....	12
1.7	Photo of MPL Doppler sonar array .....	16
1.8	Slant velocity as a projection .....	20
1.9	Slant velocity precision .....	24
Chapter II		
2.1	Slant velocity time series .....	40
2.2	Janus Velocity time series .....	41
2.3	Velocity and shear spectra .....	42
2.4	Cross-spectra of Janus velocities .....	46
2.5	Phase distribution for the North direction .....	49
2.6	Root-mean-square stress vs. averaging time .....	51
2.7	Stress estimate components .....	53
2.8	Cross-spectra of stress vs. mean flow shear .....	55
2.9	Cross-spectra of stress divergence vs. mean flow acceleration .....	56
2.10	Phase distribution for stress divergence vs. mean flow acceleration .....	58
2.11	Coherence for stress divergence vs. mean flow acceleration .....	59
Chapter III		
3.1	Intensity profiles: Day vs. night .....	65
3.2	Twenty four hour intensity sequence .....	68
3.3	Composite log intensity anomaly sequence .....	72
3.4	Composite log intensity anomaly contours .....	74
3.5	Composite vertical velocity contours .....	75
3.6	Intensity vs. vertical velocity comparison .....	77
3.7	Log intensity standard deviation contours .....	78
3.8	Vertical velocity standard deviation contours .....	82



Figure		Page
Chapter IV		
4.1	Effect of band-limiting .....	89
4.2	Fractional bias vs. covariance amplitude ratio .....	89
4.3	Fractional bias vs. Doppler shift .....	92
4.4	Normalized bias vs. Doppler shift .....	192
4.5	Normalized spectra for the MPL Doppler sonar .....	97
4.6	Fractional bias vs. Doppler shift for the MPL Doppler sonar .....	97
4.7	Covariance slopes: Model vs. data comparison .....	100
4.8	Bias corrected velocity profiles .....	102
Appendix A		
A.1	Plan view of FLIP coordinate system .....	A-2
A.2	Heading of the North beam .....	A-2
A.3	Rotation of coordinates .....	A-6
A.4	Uncorrected vertical velocity: East axis .....	A-6
A.5	Uncorrected vertical velocity: North axis .....	A-15
A.6	Corrected vertical velocity .....	A-15
Appendix B		
B.1	Schematic representation of Doppler sonar transmission .....	B-4

## List of Tables

Table	Page
Chapter I	
1.1 Characteristics of the MPL Doppler sonar .....	15
Chapter II	
2.1 Estimates and observations of wave-induced stresses .....	35
Chapter IV	
4.1 Covariance amplitude ratios for the MPL Doppler sonar .....	93
Appendix A	
A.1 Heading correction table .....	A-3
A.2 Tilt correction results .....	A-14



## ACKNOWLEDGMENTS

I am indebted to Dr. Robert Pinkel for guidance and assistance throughout the course of this work. Dr. Pinkel's ideas and encouragement stimulated much of the analysis presented in this dissertation.

I would like to thank all of the members of my committee. Each has provided useful comments and suggestions which have contributed to the improvement of the dissertation.

The informal seminars sponsored by Drs. Spiess and Anderson and Dr. Cox have provided a forum for exchanging and enriching many interesting ideas.

The Doppler sonar system used as a measurement tool for this work was constructed and operated successfully due to the continued efforts of the Upper Ocean Physics Group of the Marine Physical Lab: Steve Beck, Mike Goldin, Lloyd Green, Larry Occhiello, Eric Slater, and Lee Tomooka. The sonar equipment was safely and professionally accommodated on the R/P FLIP under the direction of Dewitt Efrid.

Many hours of useful discussion and criticism were afforded by D. Alexandrou, C. deMoustier, and R. Williams. Additional thanks go to D. Bryan, S. Elgar, A. Miller, J. Napp, J. Sherman, B. Sotorin, and many other friends and colleagues in the Scripps community for assistance in various aspects of my thesis work, and for providing companionship during my years as a graduate student.

Assistance in typing the manuscript was provided by E. Ford and L. Stockinger. Illustrations were expertly prepared by Jo Griffith.

This work was supported by the Office of Naval Research in the form of a research assistantship under contract N00014-79-C-0472.

## ABSTRACT OF THE DISSERTATION

Observations of the Upper Ocean Using a Multi-Beam Doppler Sonar

by

Albert James Plueddemann

Doctor of Philosophy in Oceanography  
University of California, San Diego, 1987  
Professor Robert Pinkel, Chairman

This dissertation presents several different, but related topics which involve both the analysis techniques for, and applications of, Doppler sonar measurements. Data were collected from four downward-slanting sonars operated on the Research Platform FLIP during a field experiment conducted off of the California coast. The sonars provide profiles of backscattered intensity and slant velocity from approximately 100 m to 1000 m in depth with 20 m depth resolution.

A technique to measure the vertically-acting Reynolds stresses,  $\overline{u'w'}$  and  $\overline{v'w'}$ , in the oceanic internal wave field using a multi-beam Doppler sonar is presented. The stress measurement technique is applied to the Doppler velocity data collected during the experiment. The principal result is a lack of observed Reynolds stresses in the high-vertical wavenumber, high-frequency internal wave band which can be considered significantly different from zero, despite the use of a scale separation which is more restrictive than that of previous investigators, and the consideration of stresses on several different time scales. The results are consistent with a high-frequency internal wave field which tends to be dominated by mode-like rather than ray-like waves, and which, on average, exhibits a high degree of vertical symmetry. No evidence is found of a correlation between internal wave stresses and mean-flow shear. There is weak evidence of a correlation between stress divergence and mean-flow acceleration.

A characterization of the diurnal migration patterns of acoustic scattering layers based on the Doppler sonar measurements is presented. The effects of the diurnal migration of scatterers are evident in both backscattered intensity and Doppler velocity, and the two measurements provide complementary methods of analysis. The principal result is the observation of three distinct scattering layers whose patterns of vertical migration show a high degree of persistence in both space and time.

It is found that the covariance-based estimator of mean Doppler shift exhibits a bias in the presence of band-limited noise. Pulse-to-pulse incoherent Doppler sonars are often operated under conditions where the biasing effect is important. Methods of correcting for noise-biasing are presented.

## INTRODUCTION

The title chosen for this dissertation is a general one, reflecting the broad and interdisciplinary nature of the topics discussed herein. The unifying element for these topics is a multi-beam Doppler sonar used for observation of the backscattered intensity field and the velocity field in the upper ocean. Techniques for the use of acoustic Doppler current measuring devices in the ocean are in the early stages of development. Similarly, the application of Doppler sonar measurements to important oceanographic problems is just beginning. This dissertation presents several different, but related topics which involve both the analysis techniques for, and potential applications of, Doppler sonar measurements.

The dissertation is organized into four chapters. The first chapter provides introductory and background information, while the second through fourth chapters describe the results of three distinct investigations which involve the use of Doppler sonar measurements. Each chapter is largely self-contained. No overall summary is given, but the outline below includes a summary of the principal results for each chapter.

The first chapter is an introduction to the data collection and processing techniques used for Doppler sonar measurements. Data were collected from four downward-slanting sonars operated on the Research Platform FLIP during a field experiment conducted off of the California coast in October and November of 1983. FLIP drifted over a distance of about 200 km during the experiment from a starting position near  $34^{\circ}$  N,  $127^{\circ}$  W. The sonars were operated over a 17 day period, providing profiles of backscattered intensity and slant velocity from  $\sim 100$  m to  $\sim 1000$  m in depth with 20 m depth resolution. The azimuthal orientation of FLIP was controlled by a hull-mounted thruster which maintained the ships heading to within about  $1^{\circ}$  of a desired value during the majority of the experiment. The tilt of the platform was measured by accelerometers, and these measurements were used to correct for tilt-induced errors in the Doppler velocity estimates (see Appendix A).

In the second chapter, the measurement of Reynolds stresses associated with high-vertical wavenumber, high-frequency internal waves in the ocean is described. Internal waves are viewed as a potentially important mechanism for the vertical mixing of momentum in the ocean, but the nature of internal wave momentum transfer processes is not well established. Understanding the role of internal waves in vertical momentum transfer ultimately rests with the measurement of the Reynolds stresses associated with fluctuating velocity components in the internal wave field, and determining their relationship to the large-scale flow. A technique to measure the vertically-acting Reynolds stresses,  $\overline{u'w'}$  and  $\overline{v'w'}$ , in a fluctuating oceanic velocity field using a multi-beam Doppler sonar is presented. The principal result of the chapter is a lack of observed Reynolds stresses in the high-vertical wavenumber, high-frequency internal wave band which can be considered significantly different from zero, despite the use of a scale separation which is more restrictive than that of previous investigators, and the consideration of stresses on several different time scales. The results are consistent with an internal wave field which tends to be dominated by mode-like

rather than ray-like waves, and which, on average, exhibits a high degree of vertical symmetry. No evidence is found of a correlation between internal wave stresses and mean-flow shear. There is weak evidence of a correlation between stress divergence and mean-flow acceleration.

The third chapter presents a characterization of the diurnal migration patterns of acoustic scattering layers based on the backscattered intensity and Doppler velocity measurements made by the sonar. The effects of the diurnal migration of scatterers are evident in both intensity and velocity, and the two measurements provide complementary methods of characterizing migration patterns. Previous investigators have typically examined the diurnal migrations of scattering layers by comparing scattering strength profiles for day and night, or by presenting echograms of backscattered intensity over a 12 to 24 hr period, but most results have not been analyzed in such a way that the persistence and variability of migration patterns can be quantified. In this work, measurements of backscattered intensity and scatterer velocity are available at 6 min intervals over a period of 13 days, allowing estimation of simple statistics (mean and variance) of the daily migration cycle. The principal result of the chapter is the observation of three distinct acoustical scattering layers whose patterns of vertical migration show a high degree of persistence over a time period of 13 days, and horizontal scales of order 50 km.

In the fourth chapter, the covariance processing (CP) technique of estimating the mean Doppler shift in the spectrum of backscattered energy from a pulsed sonar transmission is discussed. It is found that the CP mean frequency estimator exhibits a bias in the presence of band-limited noise. Pulse-to-pulse incoherent Doppler sonars are often operated under conditions where the biasing effect is important. Methods of correcting for noise-biasing are presented with emphasis on situations where the noise covariance is not known explicitly. It is shown that bias correction in the absence of noise covariance measurements can be accomplished using simple models of the signal and noise covariance functions. Covariance models provide a generalized method of bias correction, and allow prediction of potential biasing effects for the class of Doppler systems to which they apply. The covariance modelling technique of bias correction is applied to oceanic velocity measurements made with a pulse-to-pulse incoherent Doppler sonar. Biasing is found to be important in regions of low SNR which may be as much as  $1/3$  of the total depth of the profile.



## CHAPTER I DATA COLLECTION AND PROCESSING

### 1.1 Introduction

The results presented in this dissertation are based on measurements made with a multi-beam Doppler sonar deployed on the Research Platform FLIP during a field experiment conducted off of the California coast. In order to provide the proper background for interpretation of these measurements, it is useful to describe the data collection procedures and processing techniques, as well as provide a brief review of Doppler sonar operation.

This chapter begins with an overview of the experimental plan and a detailed description of the FLIP Doppler sonar measurements. The instruments deployed on FLIP during the experiment are described. Next the principles of Doppler sonar operation are reviewed, with emphasis on the characteristics of the sonar system used during the experiment. Finally, the techniques of velocity estimation from a multi-beam sonar system are described, and velocity estimation errors are summarized.

### 1.2 The Mixed Layer Dynamics Experiment

The data analyzed in this dissertation were collected as a part of the Mixed Layer Dynamics Experiment (MILDEX) conducted off of the California coast during October and November of 1983. MILDEX was intended to extend the results of previous mixed layer studies (e.g. Davis, et al., 1981) to include the effects of horizontal variability and the influence of the deeper ocean on the mixed layer. The central elements of MILDEX were two drifting platforms; the R/P FLIP of the Scripps Institution of Oceanography (SIO), and a "current meter drifter" deployed by Oregon State University. The drifter consisted of a surface buoy attached to a sub-surface line instrumented with current meters and thermistor chains. The experimental site was a region of relatively flat topography near  $34^{\circ}$  N,  $126^{\circ}$  W, about 500 km west of Point Conception (Fig. 1.1). Two ships followed both FLIP and the current meter drifter as they slowly diverged and drifted over an area roughly one degree square (Fig. 1.2). The R/V Wecoma of Oregon State University provided large scale ( $\sim 50$  km square) box surveys of the area using a towed thermistor chain and a Doppler current profiler, as well as making other measurements en route. The R/V Acania of the Naval Postgraduate School executed a sequence of small ( $\sim 5$  km square) boxes around FLIP collecting density and velocity profiles to about 200 m depth. Further description of the overall operational plan and data collection efforts during MILDEX can be found in Pinkel (1983b).

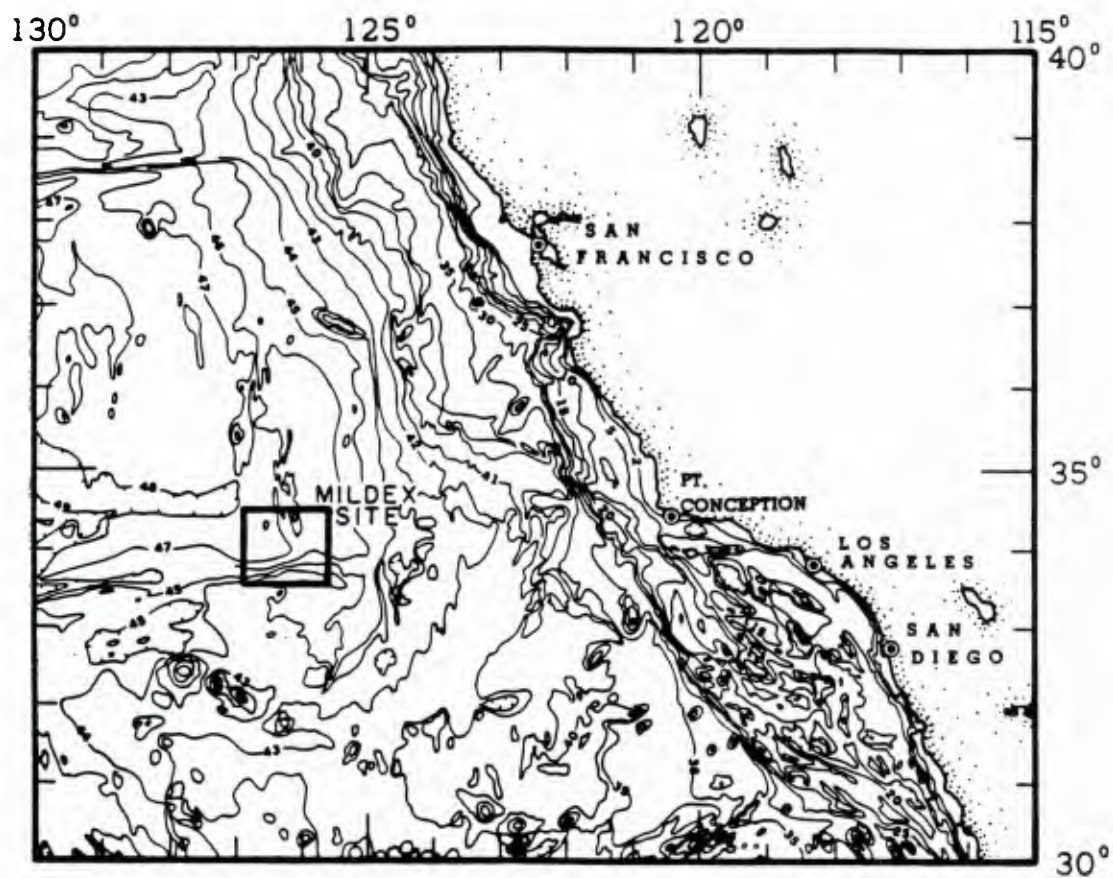


**Figure 1.1.** *The MILDEX site.* The Mixed Layer Dynamics Experiment (MILDEX) was conducted within a 1° square area off of the California coast approximately 500 km West of Point Conception. Depth contours are in hundreds of meters.

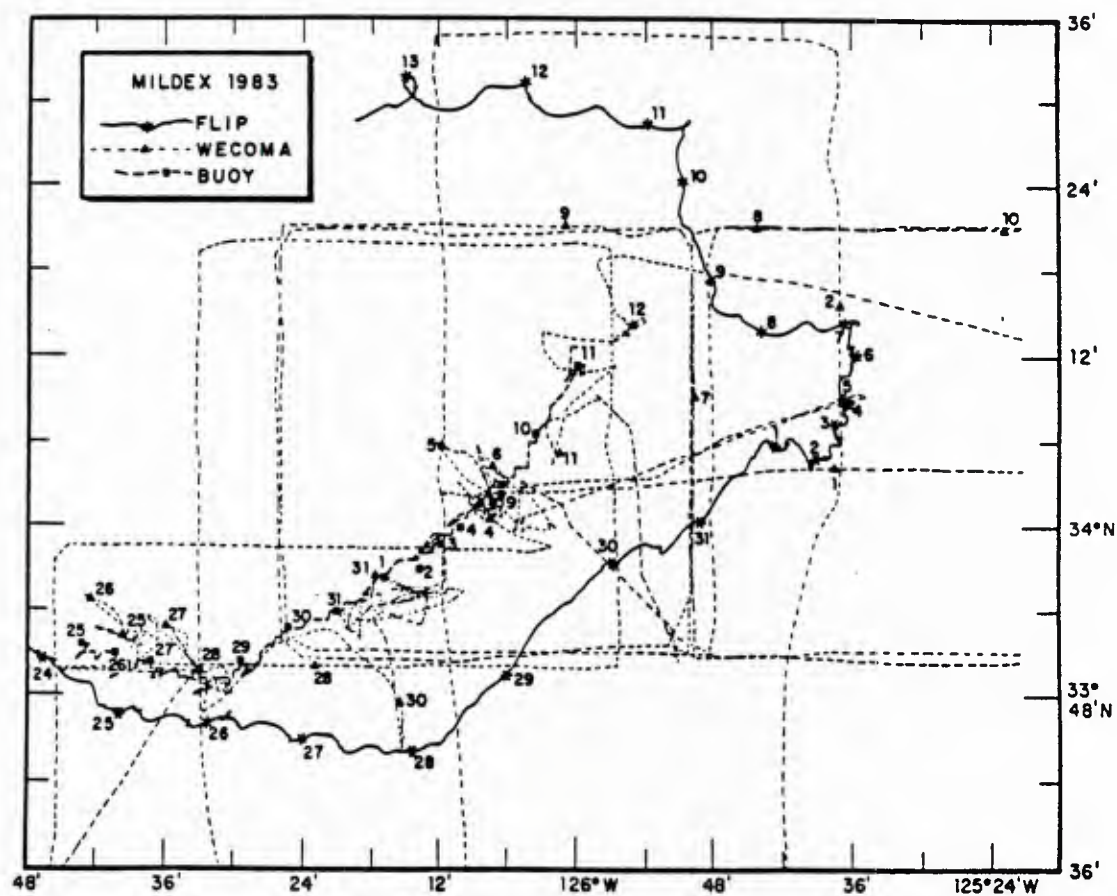


**Figure 1.2.** *MILDEX* cruise tracks. The tracks of the R/P FLIP, R/V WECOMA, and the current meter drifter during MILDEX. The R/P ACANIA (not shown) executed 5 km box surveys around FLIP from 2 November to 9 November. This plot is adapted from the original supplied by R. Weller of WHOI.



The R/P FLIP arrived on station on 24 October, 1983 and collected data throughout the next 24 days. During this time FLIP drifted along a roughly circular path covering approximately 200 km at an average rate of 10 km/day (Fig. 1.2). A schematic diagram indicating the instruments deployed on FLIP during MILDEX is shown in Fig. 1.3. The suite of instruments operated on FLIP included four downward-slanting sonars, two horizontally-pointed sonars, and a profiling CTD deployed by SIO, several current meters deployed by the Woods Hole Oceanographic Institution, and a combined set of environmental sensors used to measure wind speed and direction, incident and backscattered solar radiation, barometric pressure, wet and dry bulb air temperature, sea surface temperature, and wave height. Ships heading was recorded directly from the gyrocompass controller, and position was recorded from LORAN-C navigational fixes at one minute intervals. A summary of instruments operated by SIO during the experiment is given in Fig. 1.4.

The data selected for analysis were collected from the four downward-slanting Doppler sonars during a 17 day period from Julian day 300 through 316 of 1983 (henceforth, Julian days will be used as the time base, the correspondence between Julian days and dates in Oct.-Nov. can be found in Fig. 1.4). The four downward slanting sonars were operated in the so-called "Janus configuration", each beam separated by  $90^\circ$  in azimuth from neighboring beams and pointed downward at an angle of  $52.5^\circ$  from the horizontal. This configuration can be considered as two pairs of sonars; the transducers making up each pair form a "two-faced" array with beams separated by  $180^\circ$  in azimuth, and the two pairs operate in orthogonal planes. Each individual sonar provides profiles of backscattered intensity and radial or "slant" velocity over a depth interval of order 1 km with vertical resolution of about 20 m. The coplanar beam pairs can be used to estimate horizontal and vertical velocity components (Sec. 1.4). All four sonars operated nearly continuously throughout the period selected for analysis (Fig. 1.4).

It was desired to maintain the orientation of the two beam pairs along the East and North axes so that the slant velocities measured by the sonars could be interpreted directly in terms of  $u$  (East) and  $v$  (North) components without the necessity of a coordinate rotation. This was accomplished by means of a servo controlled, bi-directional thruster mounted beneath the waterline on FLIP's hull. The thruster was connected to the ship's gyrocompass through an adjustable azimuth control device and used to maintain a desired heading with very high accuracy in winds up to  $15 \text{ m s}^{-1}$ . As wind speed and direction changed in such a way that the desired heading could not be maintained, the ship was rotated in increments of  $90^\circ$  in azimuth and locked on to a new, more easily maintained heading (Fig. 1.5). This technique was used to accommodate significant changes in the wind field while always keeping a sonar beam pointed in the direction of each of the four compass points. Further information about correction for the azimuthal motion of the ship is given in Appendix A.

In addition to influencing FLIP's azimuthal orientation, the wind is the principal contributor to the tilt of the hull from a vertical position over periods longer than the periods of surface waves. Current shears in the upper 100 m of the sea, and ballasting of fuel and equipment on the ship also contribute to long-term tilts. The tilt of FLIP is small in comparison to that of conventional ships, but even small tilts can cause significant errors in estimates of vertical velocity if the ratio of horizontal to vertical velocity is large. In order to compensate for platform motion during velocity estimation, accelerometers mounted

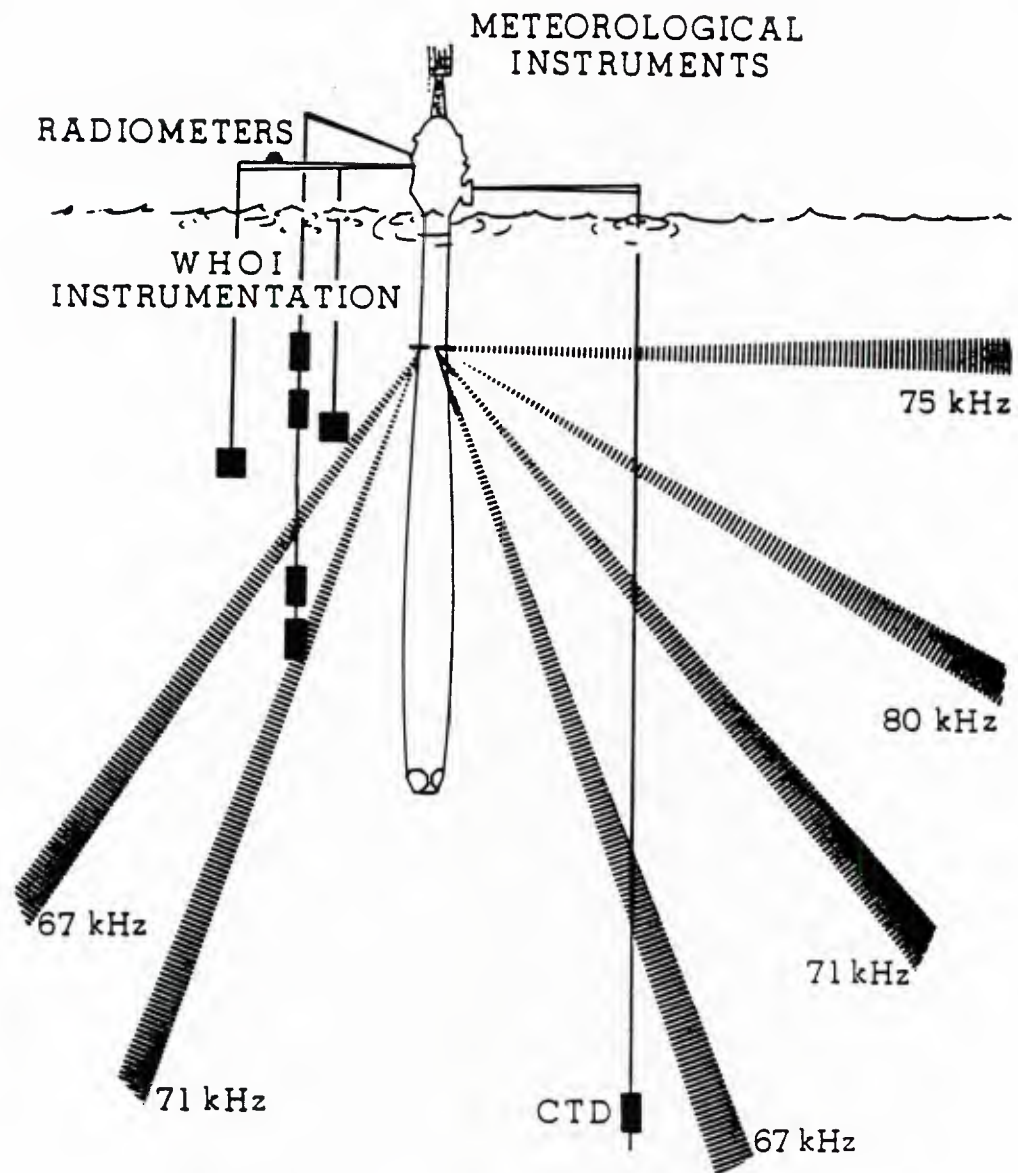


**Figure 1.3.** *Schematic of FLIP instrumentation.* The R/P FLIP instrumentation during MILDEX consisted of four downward-slanting sonars operating at 67 and 71 kHz, two horizontally-pointed sonars operating at 75 and 80 kHz, a profiling CTD, several current meters deployed by WHOI, and various environmental sensors.

## MILDEX 1983

## SIO - FLIP Operational Summary

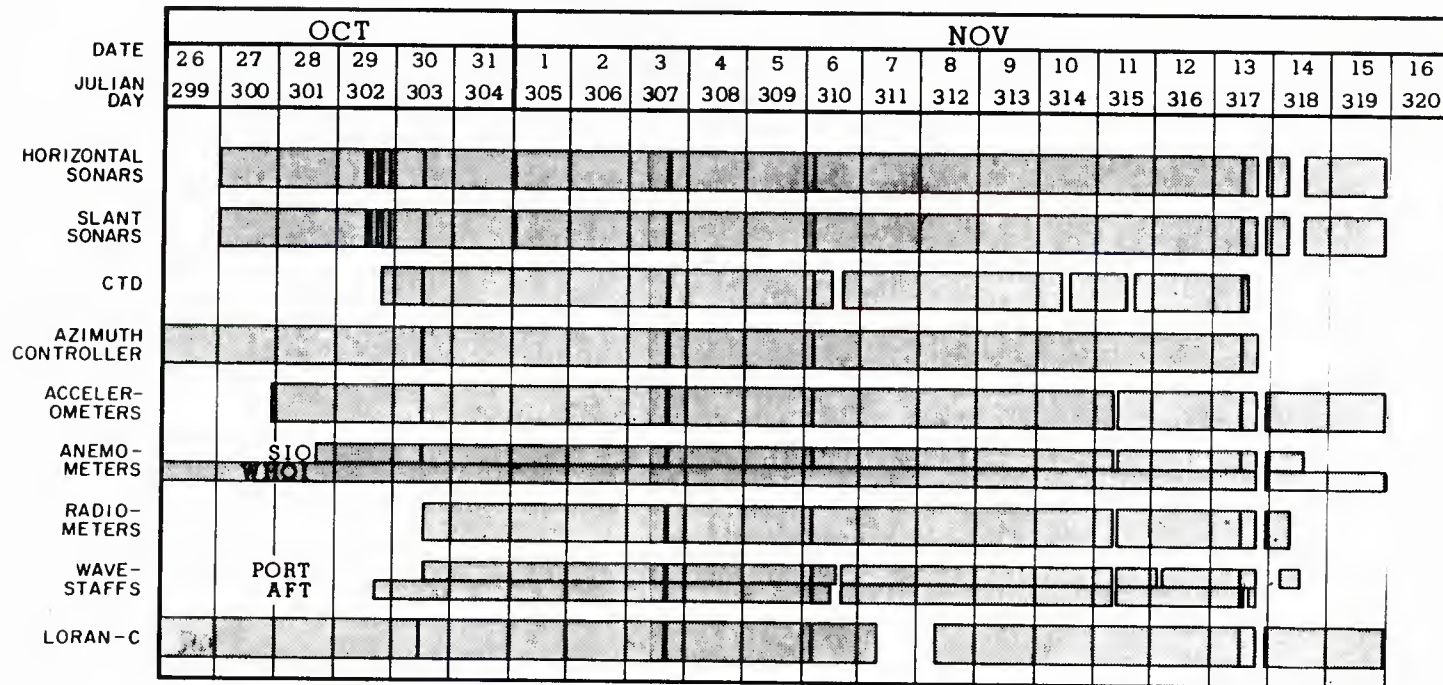


**Figure 1.4. MILDEX 1983: SIO-FLIP Operational summary.** Shaded areas represent times of operation for each instrument or group of instruments. Heavy vertical lines indicate non-operational periods from 15 min to 45 min. A gap is shown for non-operational periods of greater than 1 hr. During the LORAN-C malfunction on 7 and 8 November, navigational data was provided by satellite fixes.



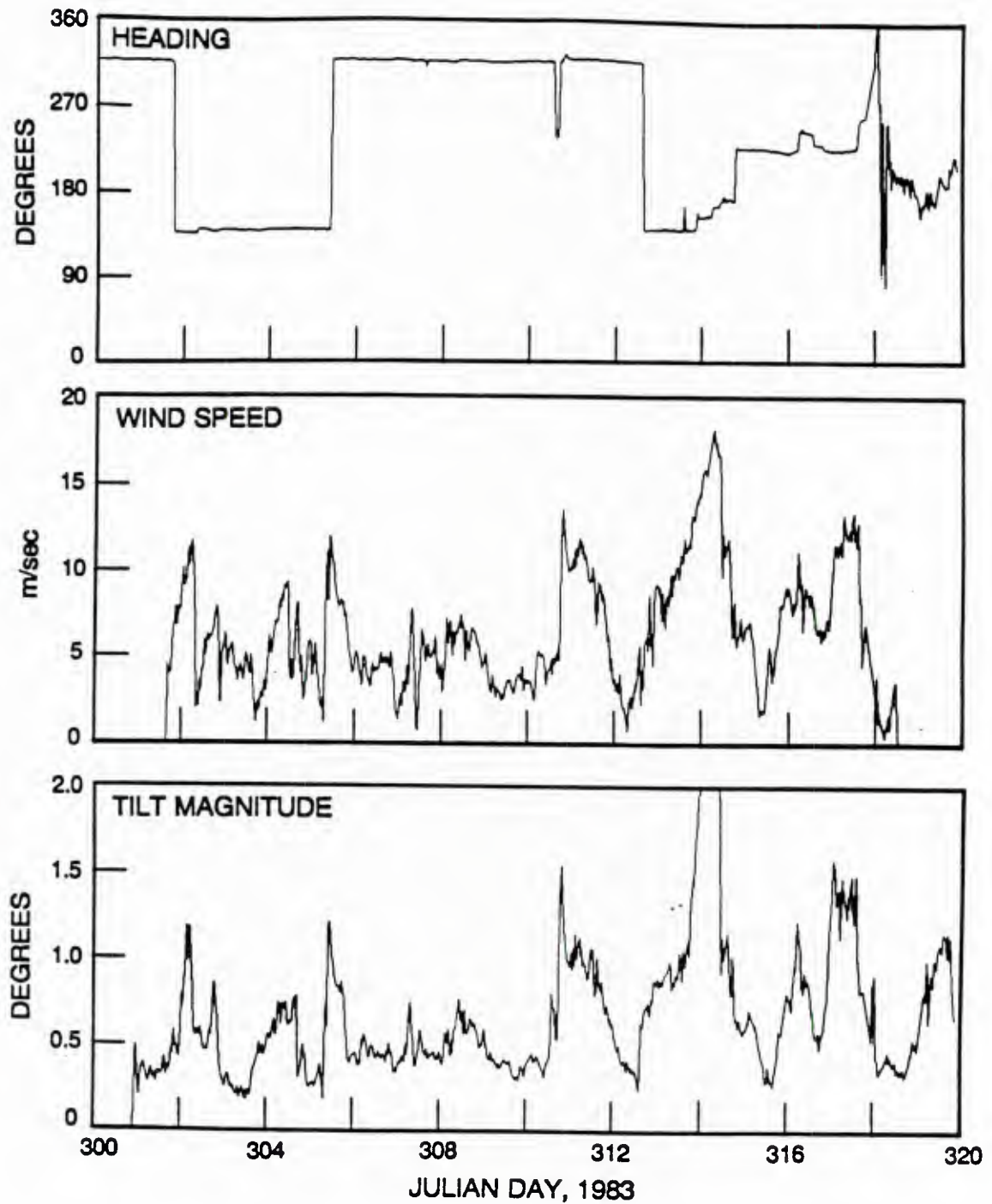


**Figure 1.5.** *Heading, wind speed, and tilt time series.* Ships heading (top) was maintained by a servo-controlled thruster, with major heading changes being in 90° increments. Wind speed (middle) was recorded by anemometers on FLIP's port boom and tilt (bottom) by accelerometers mounted to the hull. Note the high degree of visual correlation between wind speed and tilt magnitude.

to the ship's hull were used as "inclinometers" to measure tilt in two axes, parallel to the planes of the sonar beams. The measured values of platform tilt were used to correct the Doppler velocity estimates (Appendix A).

The time series of tilt magnitude observed during the experiment is shown in Fig. 1.5. Typical tilts during the calm period of the cruise range from  $0.5^\circ$  to  $1.0^\circ$ . During the maximum wind on day 314 tilts of greater than  $2^\circ$  are observed. The high degree of visual correlation between wind speed and tilt magnitude supports the hypothesis that the primary cause of tilt over periods greater than 30 minutes is due to windage on the portion of FLIP's hull above the waterline.

### 1.3 Doppler sonar operation

#### 1.3.1 Background

The Doppler effect is a change in the perceived frequency of electromagnetic or acoustic radiation due to relative motion between the source and receiver. This effect was first described in 1842 by the Austrian mathematician Christian Doppler, and has since been applied to research in many fields including astronomy, physics, geophysics, navigation, meteorology, and oceanography (Gill, 1965; Toman, 1984).

The application of Doppler principles in meteorology preceded that in oceanography by about 20 years, and many oceanographic Doppler techniques grew directly from those used in the atmospheric sciences. Hence, the meteorological literature can provide a background for understanding oceanic Doppler sonar. Doviak and Zrnic (1984) give a broad-based introduction to pulsed Doppler radar principles, many of which are directly applicable to Doppler sonars. Lhermitte (1973) and Serafin (1975) provide readable accounts of Doppler processing techniques, and Sirmans and Bumgarner (1975a) compare several Doppler frequency estimation schemes.

Acoustic Doppler techniques for measuring water flow were introduced by Vlasak (1968) with further developments by Squier (1968) and Wiseman, et al. (1972). These early Doppler flowmeters used a bi-static configuration (separate transmitter and receiver), and CW transmissions to measure one or more components of fluid velocity in a small averaging volume. Current profiles could be provided only by lowering the instrument through the water column (Squier, 1968).

Acoustic Doppler Current Profilers (ADCP's) useful for oceanographic measurements were pioneered by Pinkel (1979; 1980; 1981) and Regier (1979; 1982). Pinkel used large ( $\sim 1$  m diameter), low-frequency (60 to 90 kHz) transducers mounted on the R/P FLIP to obtain velocity profiles from 100 to 1000 m in depth. Regier used a higher frequency (300 kHz) system, adapted from an existing Doppler speed log by Amatek-Straza (Rowe and Young, 1979), to measure upper ocean shears from a moving ship. Distinguishing characteristics of the systems of Pinkel and Regier were their monostatic configuration (combined transmitter and receiver), use of pulsed transmissions, and Doppler processing by pulse-to-pulse incoherent techniques (the distinction between coherent and

incoherent processing is discussed in Appendix B).

The use of Doppler profilers has grown steadily since the introduction of the first systems, and several types of ADCP's are now available commercially. Many ships are now equipped with ADCP's to make velocity profiles while underway (Joyce, Bitterman and Prada, 1982; Bitterman and Wilson, 1983; Kosro, 1985; Trump, et al., 1985). Self contained ADCP's suitable for bottom mounted or moored applications have been developed and tested (Mero, Appell, and Porter, 1983; Pettigrew and Irish, 1983; Appell, et al., 1985) and several new instruments using varied Doppler techniques and applications are under development (Lhermitte, 1983; Sanford, et al., 1985, Rowe, et al., 1986).

### 1.3.2 Doppler sonar fundamentals

An oceanic Doppler sonar estimates fluid velocity by measuring the Doppler frequency shift of the acoustic reverberation generated by sound scattering bodies in the water column. For a sonar operating in the 50 to 500 kHz frequency range, the primary scatterers are biological, with various species of zooplankton (euphausiids, copepods, siphonophores, and pteropods) and occasional nekton (fishes and squid) contributing the majority of backscattered energy (Ch. 3). To the extent that these scatterers are drifting passively with the surrounding water, the Doppler shift from the volume insonified by the sonar beam is representative of the component of volume-averaged velocity in the direction of the beam axis. The basic principles of velocity estimation for backscatter Doppler sonars are introduced below, and further developed in Section 1.4.1. Discussion of velocity measurement errors is deferred to Section 1.4.2.

The nature of oceanic velocity measurement using Doppler sonar is illustrated using the simple example of scattering from an isolated target. Consider a transducer at a position T below the water surface, moving with velocity  $\vec{v}_t$  (Fig. 1.6). The transducer emits a pulse of acoustic energy at frequency  $f_c$  in a narrow beam directed along  $\vec{d}$  which reflects (scatters) from a target or "receiver" at position R moving with velocity  $\vec{v}_r$ . The expression for the perceived frequency at the receiver in a medium with soundspeed  $c$  is (Halliday and Resnick, 1970)

$$f_r = f_c \frac{c - v_r}{c - v_t} \quad (1.1)$$

where  $v_t$  and  $v_r$  are the components of the transducer and receiver velocities, respectively, which are in the direction of  $\vec{d}$ . Upon reflection of the incident acoustic wave, the receiver acts as a "transmitter", and the backscattered energy observed at the transducer has a perceived frequency

$$f_t = f_r \frac{c + v_t}{c + v_r} = f_c \frac{(c - v_r)(c + v_t)}{(c + v_r)(c - v_t)} \quad (1.2)$$

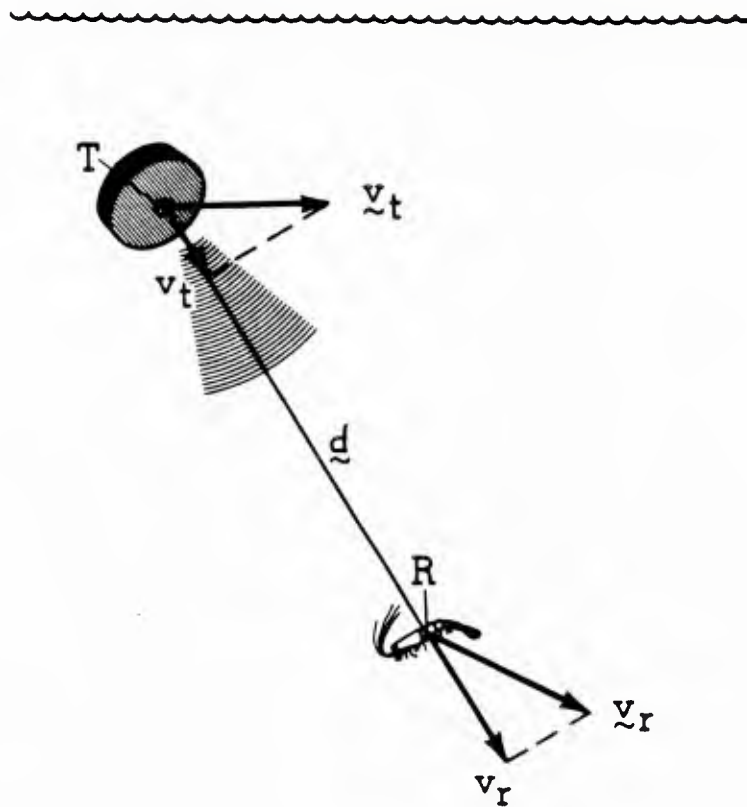


**Figure 1.6.** *Schematic of acoustic Doppler velocity measurement (not to scale).* Acoustic energy emitted by the transducer (T) at frequency  $f_c$  is backscattered, primarily by biota in the water column, resulting in a net Doppler shift of the received signal at the transducer of  $f_t = f_c [ 1 + 2 (v_t - v_r) / c ]$ .



Typical velocities of ocean currents are small enough ( $0.1$  to  $1.0 \text{ m s}^{-1}$ ) compared to the speed of sound ( $1500 \text{ m s}^{-1}$ ) that the expression (1.2) can be written in terms of a small parameter  $\epsilon = v/c$  and simplified to first order in  $\epsilon$  as

$$f_t = f_c \left[ 1 + \frac{2}{c} (v_t - v_r) \right] \quad (1.3)$$

Defining the Doppler shift at the transducer as  $f_d = f_t - f_c$  gives

$$V = cf_d / 2f_c = v_t - v_r \quad (1.4)$$

where  $V$  is the so-called slant velocity measured by the instrument. In order to recover the velocity of the fluid ( $v_r$ ) the velocity of the instrument through the water ( $v_t$ ) must be known or considered negligible.

In actual operation the sonar does not measure the acoustic return from a single scatterer, but rather receives energy from a sample volume composed of many scatterers. A simple Doppler system interrogates a sample volume in the medium with a pulsed transmission of the form

$$X_o(t) = a \cos(2\pi f_c t) G(t) \quad (1.5)$$

where

$$G(t) = \begin{cases} 1 & t_o \leq t \leq t_o + T_p \\ 0 & \text{otherwise,} \end{cases}$$

$f_c$  is the carrier frequency, and  $T_p$  is the pulse duration. The received signal is the sum over the sample volume of contributions to amplitude and phase from many individual scatterers. It is convenient to refer to the region of space interrogated by the transmitted pulse using the along-beam dimension of the sample volume, commonly called a range gate or range bin. The signal received at time  $t$  after the start of transmission comes from a range gate of extent  $\Delta r = cT_p/2$  centered at range  $r = ct/2 - cT_p/4$  and can be expressed as (Serafin, 1975)

$$X(t) = \text{Re} \left\{ Z(t) \exp[i2\pi f_c t] \right\} \quad (1.6)$$

where  $Z(t) = S(t) \exp[i\phi(t)]$  is the complex envelope and  $S(t)$  and  $\phi(t)$  are the resultant amplitude and phase, respectively, of the backscattered signal. Since only the complex envelope is of interest, a base-banding and filtering operation is often used to remove the carrier frequency.

The mean Doppler shift introduced by an aggregate of moving scatterers is related to the average velocity within the sample volume. The scatterers within the volume may have varying acoustic cross sections and be moving at slightly different speeds. As a result, the received signal does not contain a single Doppler shift, but rather a distribution of received power with frequency forming a Doppler spectrum  $P(f)$  with a power-weighted mean frequency

$$\bar{f} = \int_{-\infty}^{\infty} f P(f) df / \int_{-\infty}^{\infty} P(f) df \quad (1.7)$$

Neglecting the motion of the instrument, the component of fluid velocity along the transmitter beam axis is given by

$$V = c\bar{f} / 2f_c = \underline{v} \cdot \underline{d} \quad (1.8)$$

where  $\underline{v}$  is the average velocity measured in the sample volume, and  $\underline{d}$  is the unit vector in the direction of the beam. The volume-averaged slant velocity (1.8) is a fundamental measurement for all Doppler systems. Knowledge of  $\bar{f}$  is sufficient to determine  $V$  since  $c$  and  $f_c$  are known constants for a particular system operating in a given medium.

Classical methods for determining the mean Doppler frequency involve computing the power spectrum  $P(f)$  of the complex receive signal  $Z(t)$  and estimating the power-weighted mean frequency from (1.7). Recently, the computationally efficient, covariance-based mean frequency estimator (Rummler, 1968) has gained popularity. The covariance processing technique is described in Appendix B where it is shown that the power-weighted mean frequency can be well approximated by

$$\hat{\bar{f}} = (2\pi\tau)^{-1} \text{Arg} [ C(\tau) ] \quad (1.9)$$

The function  $C(\tau)$  is the complex covariance function, computed from the complex envelope  $Z(t)$  using

$$C(\tau) = \langle Z(t)Z^*(t+\tau) \rangle \quad (1.10)$$

where the brackets imply ensemble averaging and  $*$  denotes conjugation. For a noise-free, symmetric Doppler spectrum  $\hat{\bar{f}}$  is an unbiased estimator for  $\bar{f}$  as  $\tau$  approaches zero. In practice, the estimator performs well for covariance lags  $\tau \ll \sigma_s^{-1}$ , where  $\sigma_s$  is the bandwidth of the Doppler spectrum. The value of  $\hat{\bar{f}}$  computed from (1.9) can be used in place of  $\bar{f}$  in (1.8) to estimate the volume-averaged slant velocity.

### 1.3.3 The MPL Doppler sonar system

The ADCP used in this study was developed at the Marine Physical Lab (MPL) of SIO and will be referred to as the MPL Doppler sonar system. In a typical deployment, this narrow-beam, high-power, pulse-to-pulse incoherent Doppler sonar uses multiple downward-slanting beams to provide profiles of intensity and velocity from  $\sim 100$  m to  $\sim 1000$  m in depth with  $\sim 20$  m depth resolution and precision of order  $0.01 \text{ m s}^{-1}$ . Details of the development and application of this system can be found in Slater and Pinkel (1979), Ochiello and Pinkel (1979), and Pinkel (1981; 1983a). The characteristics of the system as configured for MILDEX are summarized in Table 1.1 and described in detail below.

**Table 1.1. Characteristics of the MPL Doppler sonar.** A summary of the operating characteristics of the MPL Doppler sonar system as configured for MILDEX is shown. Values are for a sonar composed of a single transducer panel. For MILDEX, twenty transducer panels were combined to form six sonars with beams pointing in different directions.

<b>CHARACTERISTICS OF THE MPL DOPPLER SONAR</b>	
wavelength (cm)	2
peak electrical power (KW)	1
pulse repetition time (s)	2
pulse length (ms)	30
sampling frequency (Hz)	400 or 500
receiver bandwidth (Hz)	195
half-power beam width (deg)	2
range resolution (m)	22.5
maximum range (m)	1500

For the MILDEX deployment, twenty separate transducer "panels" were configured to form six sonars operating in four, 1 kHz wide frequency bands. Each transducer panel is composed of 210 ceramic transducer elements arranged in the shape of a half-hexagon, and has dimensions of approximately 0.36 m by 0.61 m. The half-power beam width of a sonar composed of a single panel is about 2°. The six sonar array, composed of two horizontally-pointed sonars and four downward-slanting sonars, is shown in Fig. 1.7 and depicted schematically in Fig. 1.3. The two horizontally-pointed sonars, made up of six panels each, have beams separated by 90° in azimuth and are operated in frequency bands centered at 75 and 80 kHz. The four downward-slanting sonars, composed of two panels each, have beams separated by 90° in azimuth and pointed downward at an angle of 52.5° from the horizontal. The four beams form two, co-planar "Janus" pairs with one pair having a frequency band centered at 67 kHz and the other at 71 kHz. The sonars are mounted to FLIP's hull by attachment to a deck located at 36 m below the water line (Fig. 1.7). The horizontal sonars are mounted on the center of the deck at 36 m depth,

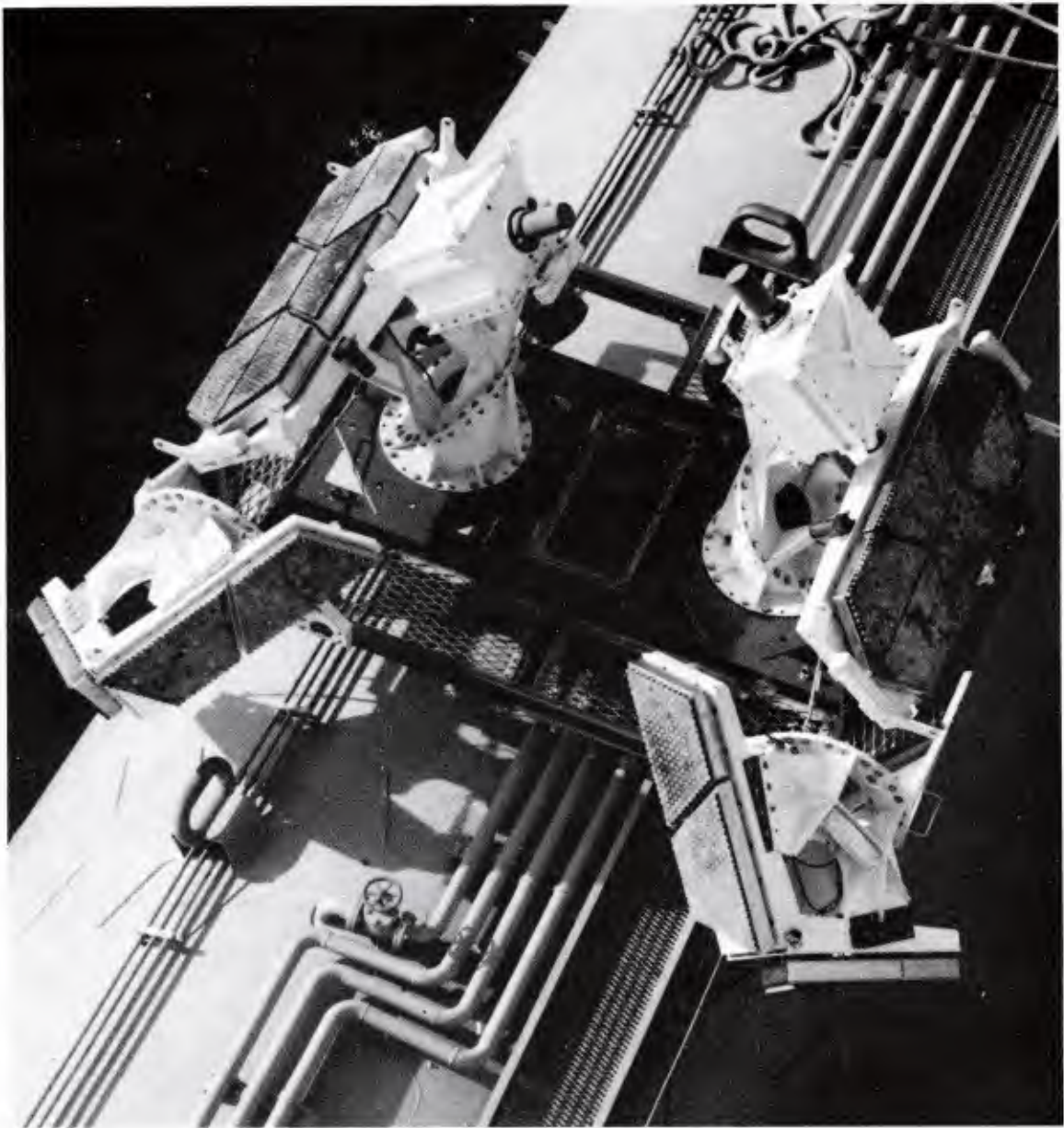


**Figure 1.7.** *Photo of MPL Doppler sonar array.* The MPL Doppler sonar array as configured for MILDEX is shown in a view from above and to the right of FLIP's stern while in the horizontal position at the dock. The twenty, half-hexagonal transducer panels making up the six sonars can be seen, as well as the hardware used to attach them to the mounting deck. The accelerometers are mounted beneath the rectangular grating in the center of the deck.



**Table 1.1. Characteristics of the MPL Doppler sonar.** A summary of the operating characteristics of the MPL Doppler sonar system as configured for MILDEX is shown. Values are for a sonar composed of a single transducer panel. For MILDEX, twenty transducer panels were combined to form six sonars with beams pointing in different directions.

CHARACTERISTICS OF THE MPL DOPPLER SONAR	
wavelength (cm)	2
peak electrical power (KW)	1
pulse repetition time (s)	2
pulse length (ms)	30
sampling frequency (Hz)	400 or 500
receiver bandwidth (Hz)	195
half-power beam width (deg)	2
range resolution (m)	22.5
maximum range (m)	1500

For the MILDEX deployment, twenty separate transducer "panels" were configured to form six sonars operating in four, 1 kHz wide frequency bands. Each transducer panel is composed of 210 ceramic transducer elements arranged in the shape of a half-hexagon, and has dimensions of approximately 0.36 m by 0.61 m. The half-power beam width of a sonar composed of a single panel is about 2°. The six sonar array, composed of two horizontally-pointed sonars and four downward-slanting sonars, is shown in Fig. 1.7 and depicted schematically in Fig. 1.3. The two horizontally-pointed sonars, made up of six panels each, have beams separated by 90° in azimuth and are operated in frequency bands centered at 75 and 80 kHz. The four downward-slanting sonars, composed of two panels each, have beams separated by 90° in azimuth and pointed downward at an angle of 52.5° from the horizontal. The four beams form two, co-planar "Janus" pairs with one pair having a frequency band centered at 67 kHz and the other at 71 kHz. The sonars are mounted to FLIP's hull by attachment to a deck located at 36 m below the water line (Fig. 1.7). The horizontal sonars are mounted on the center of the deck at 36 m depth,

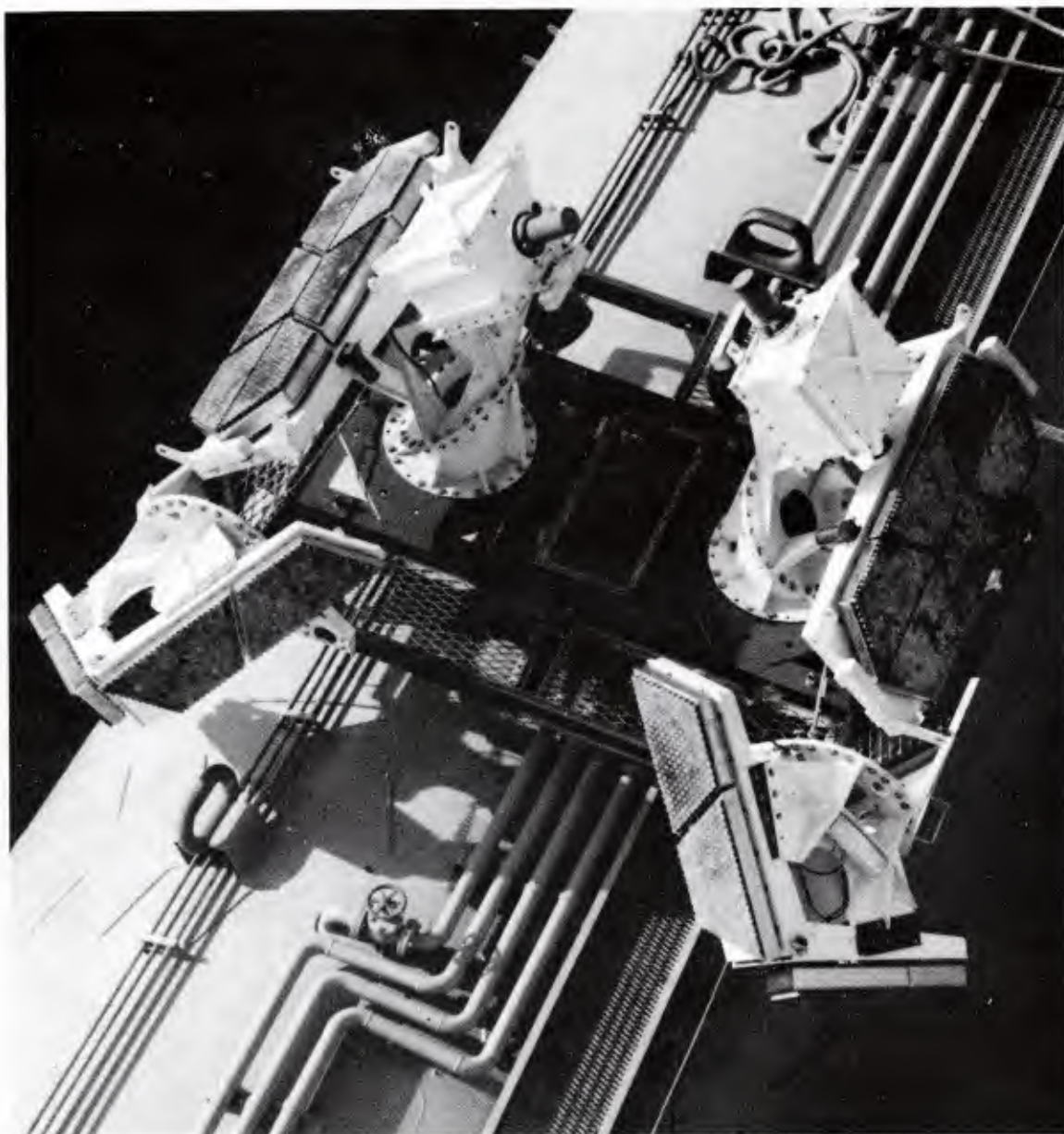


**Figure 1.7.** *Photo of MPL Doppler sonar array.* The MPL Doppler sonar array as configured for MILDEX is shown in a view from above and to the right of FLIP's stern while in the horizontal position at the dock. The twenty, half-hexagonal transducer panels making up the six sonars can be seen, as well as the hardware used to attach them to the mounting deck. The accelerometers are mounted beneath the rectangular grating in the center of the deck.

while the slant sonars are on the lower end of the deck at a depth of about 38 m.

During operation each sonar sends out a sequence of four pulsed transmissions of the form (1.5). The center frequency for each pulse is a pure tone separated by 300 Hz from neighboring tones, and the four tone group is centered within the 1 kHz bandwidth of the sonar (e.g. for the 80 kHz sonar the center frequencies of the four tones are 79.55, 79.85, 80.15, and 80.45 kHz). As configured for MILDEX, each pulse was of duration 30 ms and the four-tone transmission sequence was repeated every 2 s.

For each transmission sequence, the complex envelope of the backscattered signal for each tone is sampled by the data acquisition system at an interval  $\tau_o = 2.0$  or  $2.5$  ms. In incoherent Doppler operation, the sampling interval  $\tau_o$  is much less than the pulse duration  $T_p = 30$  ms. Taking  $j = 1, 2, 3, \dots$  as the discrete sample index, it can be seen that the returns from times  $j \tau_o$  and  $(j+1) \tau_o$  come from a region of space which is highly overlapped for  $\tau_o \ll T_p$ . The two successive samples have the effect of being time-delayed versions of the return from a common-volume range gate centered at  $r_j = c [ j \tau_o / 2 - (T_p - \tau_o) / 4 ]$ . The discretely sampled complex envelope for a given pulse at time  $j \tau_o$  after transmission can be written as  $Z_m(j \tau_o)$  where  $m = 1, 2, 3, \dots$  indicates the sequence number, and  $j$  is interpreted as the range index. The covariance function for a given common-volume range gate is computed as a function of range from successive samples of  $Z$  by

$$\hat{C}(k \tau_o, r_j) = \frac{1}{M} \sum_{m=1}^M Z_m(j \tau_o) Z_m^*((j+k) \tau_o) \quad (1.11)$$

where  $k$  is the covariance lag index. In MILDEX covariance estimates were recorded for the three discrete lags given by  $k = 0, 1$ , and  $2$ . The covariance for lag zero ( $k = 0$ ) is simply the squared amplitude of the complex envelope, and measures the relative acoustic intensity of the backscattered signal. The covariance for lag one ( $k = 1$ ) is used in the computation of the slant velocity as described below. Further discussion of covariance processing for incoherent sonar systems can be found in Appendix B.

The covariance estimate (1.11) is the discrete analog of (1.10). The ensemble averaging indicated by the brackets in (1.10) is approximated by averaging over  $M$  sequences for one tone, as shown in (1.11), and then averaging over the four tones in each sequence. In MILDEX, covariance data were averaged over 4 tones and 15 sequences (30 seconds) by an array processor before being written to 9 track tape. Post-processing of the covariance data included removal of bad data using an intensity-based deglitching routine, further averaging to 3 minute intervals, and correction for velocity biasing at low signal-to-noise ratio using the method described in Chapter 4. The covariance-based mean Doppler shift  $\bar{f}$  is estimated as a function of range using the 3 min average, lag 1 covariance estimate in place of  $C(\tau)$  in the expression (1.9). The discretely sampled, volume-averaged slant velocity profile is computed using  $\bar{f}$  in place of  $\bar{f}$  in (1.8) and can be written as

$$V(r_j) = \frac{c}{4\pi f_c \tau_o} \text{Arg} [ \hat{C}(\tau_o, r_j) ] \quad (1.12)$$



The two second pulse-repetition time gives a maximum range (based on the round-trip travel time of the pulse) of 1500 m. Due to the attenuation and spreading of the transmitted signal, the backscattered energy level decays with range  $r$  as approximately  $r^{-2}$ , and the maximum range is not always attainable before the signal is lost in the background noise of the system. Useful ranges of about 1300 m were obtained during MILDEX, corresponding to a depth interval of about 1000 m for the downward-slanting sonars at an elevation angle of  $\theta_o = -52.5^\circ$ . The range resolution for the velocity profiles is determined by the pulse duration. For  $T_p = 30$  ms, the range resolution is  $\Delta r = cT_p/2 = 22.5$  m corresponding to a depth resolution of 18 m for  $\theta_o = -52.5^\circ$ .

The slant velocity observed by the instrument includes contributions from both the actual fluid velocity, and the relative velocity of the instrument through the fluid [c.f. (1.4)]. The instrument velocity can be removed by adding the slant component of the drift velocity of the platform, computed from LORAN-C navigation, to each slant velocity profile. Drift velocities derived from LORAN-C navigation are accurate indicators of long-term drift, but may have noise variance on short time scales which is large compared to that of the Doppler velocities. Thus, drift correction using LORAN-C may successfully account for the relative velocity of the instrument, but add unwanted noise to the Doppler velocity estimates. An alternate method of drift correction involves subtracting the vertical average of the slant velocity profile from the observed velocity at each depth for each time step. This method is effective if the true, depth-averaged velocity in the water column over which the slant velocities are averaged is small compared to the velocity of the platform through the water. Comparison of FLIP's drift track computed from LORAN-C navigation and from progressive vectors of depth-averaged Doppler velocity (Pinkel, 1983a, and unpublished results from this work) show that the depth-averaged Doppler velocity is an good indicator of short-term drift. The difference between velocities corrected by adding the LORAN-C drift velocity and those corrected by subtracting the depth-averaged Doppler velocity is small compared to the magnitude of the corrected velocity (Pinkel, et al., 1987). The data presented in this work have been corrected for platform drift by subtracting the depth-average Doppler velocities from the observed velocities.

## 1.4 Velocity estimation

### 1.4.1 The velocity estimates

Assuming that a slant velocity estimate of the form (1.12) is available, it remains to interpret the slant velocity in terms of component velocities in the geographic reference frame. The FLIP velocity data are analyzed in a standard geographic tangent plane coordinate system with positive  $x$  and  $y$  axes being to the East and North, respectively, and the  $z$  axis being positive upwards (Fig. A.1). After correction for platform motion (Appendix A), the sonar beams for the two pairs of downward slanting sonars are considered to be in the  $x$ - $z$  and  $y$ - $z$  planes, with one beam pointing in the direction of each of the four compass points. The relationship of the slant velocities to the component velocities in geographic coordinates is found by defining the unit vectors for each beam.

With the beams separated by  $90^\circ$  in azimuth and at an elevation angle of  $\theta_o = -52.5^\circ$ , the unit vectors in the direction of positive slant velocity (positive Doppler shift) are

$$\underline{\hat{E}} = -\cos\theta_o \underline{\hat{i}} + \sin\theta_o \underline{\hat{k}} , \quad \underline{\hat{W}} = \cos\theta_o \underline{\hat{i}} + \sin\theta_o \underline{\hat{k}} \quad (1.13a)$$

$$\underline{\hat{N}} = -\cos\theta_o \underline{\hat{j}} + \sin\theta_o \underline{\hat{k}} , \quad \underline{\hat{S}} = \cos\theta_o \underline{\hat{j}} + \sin\theta_o \underline{\hat{k}} \quad (1.13b)$$

where  $\underline{\hat{i}}$ ,  $\underline{\hat{j}}$ , and  $\underline{\hat{k}}$  are the unit vectors in the East, North, and up directions, respectively. The slant velocity estimate for each sonar is simply the projection of the volume-averaged component velocities onto the beam axis. The slant velocities at a given range expressed in terms of the component velocities are

$$\begin{aligned} V_E &= \underline{v}_E \cdot \underline{\hat{E}} = -u_E \cos\theta_o + w_E \sin\theta_o \\ V_W &= \underline{v}_W \cdot \underline{\hat{W}} = +u_W \cos\theta_o + w_W \sin\theta_o \\ V_N &= \underline{v}_N \cdot \underline{\hat{N}} = -v_N \cos\theta_o + w_N \sin\theta_o \\ V_S &= \underline{v}_S \cdot \underline{\hat{S}} = +v_S \cos\theta_o + w_S \sin\theta_o \end{aligned} \quad (1.14)$$

where the subscripts E, W, N, and S refer to quantities measured by the East, West, North, and South beams, respectively. The relationship of slant velocities to component velocities for the East-West beam pair is depicted in Fig. 1.8.

The set (1.14) provides four equations and eight unknowns. Component velocities in the same geographic direction for different beams (e.g.  $u_E$  and  $u_W$ ) cannot be considered equal in general because they come from measurements separated in space by the distance between the beams. However, the component velocities can be estimated with some assumptions about the parameters of the fluid process being measured. For oceanic motions, the parameter of importance is the aspect ratio  $\delta = D/L$ , where  $D$  is a characteristic vertical scale, and  $L$  a characteristic horizontal scale for the motion. The ratio of vertical to horizontal velocity is proportional to the aspect ratio. For motions with frequencies less than the local inertial frequency, the aspect ratio is much less than one and the horizontal scale  $L$  is large compared to the separation between the beams. In this case, the contribution of the vertical velocity in (1.14) can be neglected, and horizontal velocity profiles can be approximated from the slant velocity using

$$u \approx (-V_E, +V_W) / \cos\theta_o , \quad v \approx (-V_N, +V_S) / \cos\theta_o \quad (1.15)$$

For motions in the internal wave band, the aspect ratio can be estimated from (Gill, 1982)

$$\delta = \left[ \frac{N^2 - \omega^2}{\omega^2 - f^2} \right]^{-1/2} \quad (1.16)$$

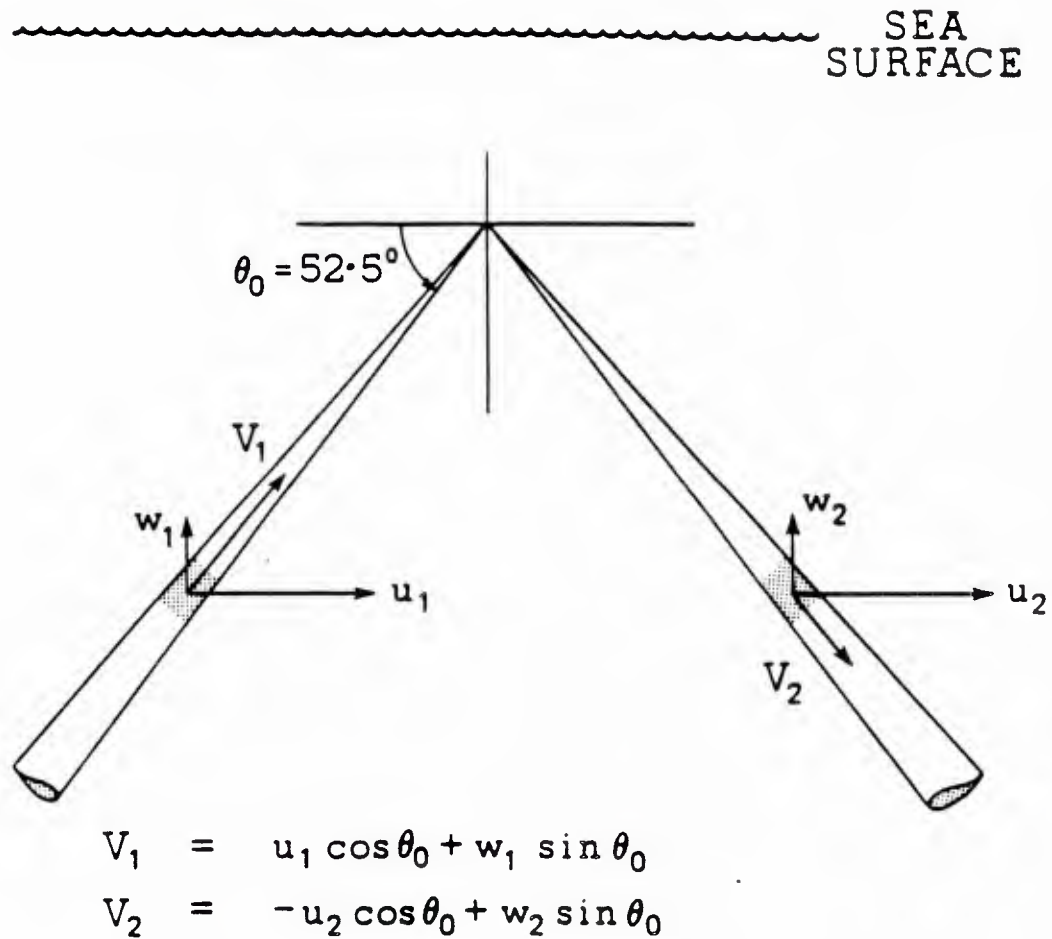


**Figure 1.8.** *Slant velocity as a projection.* The slant velocity measured by a given sonar is the projection of horizontal and vertical component velocities onto the beam axis. The figure depicts the x-z plane, containing two downward-slanting sonar beams at  $180^\circ$  in azimuth. The sonar transducers are at a depth of 38 m below the sea surface with the centerline of FLIP's hull forming the bisector of the angle between the beams. Doppler velocities are taken as positive in the direction of positive Doppler shift (towards the transducer).

where  $\omega$  is the wave frequency,  $f$  is the inertial frequency, and  $N^2 = -g\rho^{-1} d\rho/dz$  is the buoyancy frequency. For a sonar beam pointed downward with an elevation angle of  $\theta_0 \leq 45^\circ$ , the approximation (1.15) is quite good for frequencies up to  $\omega = N/\sqrt{2}$ . This effect is illustrated by Pinkel (1981) and exploited in processing of single beam Doppler sonar data by Pinkel (1983a). As frequencies increase beyond  $\omega = N/\sqrt{2}$  the interpretation of data from a single slanting beam in terms of a vertical profile of horizontal velocity is inappropriate.

For a multi-beam Doppler sonar in the Janus configuration, information from co-planar beam pairs can be used to estimate velocity components averaged over the horizontal extent of the array (e.g. Joyce, Bitterman, and Prada, 1982). This technique will properly resolve horizontal and vertical velocity components as a function of depth for arbitrarily high aspect ratio as long as the horizontal scale  $L$  is greater than the separation between the sonar beams. The Janus velocity components are estimated from the sum and difference of the slant velocities according to

$$\begin{aligned} u_J &= \frac{V_W - V_E}{2 \cos \theta_0} , & v_J &= \frac{V_S - V_N}{2 \cos \theta_0} \\ w_{JE} &= \frac{V_W + V_E}{2 \sin \theta_0} , & w_{JN} &= \frac{V_S + V_N}{2 \sin \theta_0} \end{aligned} \quad (1.17)$$

The quantities  $u_J$  and  $v_J$  are the Janus horizontal velocities in the East and North directions, respectively, and  $w_{JE}$  and  $w_{JN}$  are the Janus vertical velocities. The subscripts JE and JN denote the vertical velocities computed from the East-West and North-South beam pairs, respectively. Substitution of the expressions (1.14) for the slant velocities in (1.17) shows that the Janus horizontal (vertical) velocities are equal to the average of the horizontal (vertical) component velocities plus an error term proportional to the difference in vertical (horizontal) velocity between the beams.

#### 1.4.2 Velocity estimation errors

Velocity estimation errors are separated into three categories based on their effect on the velocity measurement: a) errors effecting measurement accuracy (bias), b) errors effecting measurement precision (variance), and c) secondary errors. Errors in the first two categories are considered primary errors in the sense that they are inherent in the measurement system for a given configuration. These errors are generally treated by changing the system parameters. Secondary errors may effect both the accuracy and precision of the measurement, but are due to factors unique to the operating environment of the system during a particular deployment. These errors are generally treated in the processing of the data after collection. Velocity estimation errors for the



MPL Doppler sonar are described below for each of the three categories.

**a. Accuracy.** In order to accurately measure Doppler shift, the transmitted frequency of the Doppler sonar system must be precisely controlled, and the system electronics must be calibrated to eliminate errors due to amplitude and phase imbalances in the in-phase (I) and quadrature (Q) components of the complex envelope (Doviak and Zrnic, 1984). Laboratory calibrations of the MPL system, performed both before and after the MILDEX deployment, indicate a measurement accuracy of order  $0.1 \text{ cm s}^{-1}$ . This value represents the expected calibration bias for a pure tone input signal in a noise-free environment. Another type of noise-independent bias which may be important is due to the "clipping" of the signal spectrum by the bandpass filters used in the homodyning system. This effect is discussed by Hansen (1985b). Using Hansen's results with the system parameters appropriate for the MPL Doppler sonar indicates an expected bias of about 5%, or  $1.0 \text{ cm s}^{-1}$  for a true velocity of  $20 \text{ cm s}^{-1}$ .

Noise dependent biases may be caused by DC offsets in the data channels recording the I and Q signals, and by the effect of band-limited (i.e. autocorrelated) noise in the covariance estimate. During operation of the MPL Doppler sonar, correction for biasing due to DC offsets was made by computing the DC levels for each data channel and subtracting this value from the I and Q components of the complex envelope before computation of the covariance. The correction scheme is equivalent to that described by Underwood (1981) and is described briefly in Section 4.3b. Bias errors from band-limited noise can be important at low signal-to-noise ratio if the receiver filter bandwidth is not large compared to the signal bandwidth. This effect is discussed in detail in Chapter 4, where it is shown that the covariance-based mean frequency estimate (1.9) in the presence of band-limited noise has the expected value

$$\hat{\bar{f}} = (2\pi\tau)^{-1} \arctan \left[ \frac{\sin(2\pi\bar{f}\tau)}{\cos(2\pi\bar{f}\tau) + \alpha(\tau) / \text{SNR}} \right] \quad (1.18)$$

where  $\tau$  is the autocovariance lag,  $\bar{f}$  is the true mean Doppler shift, SNR is the signal-to-noise power ratio, and  $\alpha(\tau)$  is the normalized, noise-to-signal covariance amplitude ratio. Values of fractional bias  $(\hat{\bar{f}} - \bar{f}) / \bar{f}$  for the MPL Doppler sonar can be as large as 10% to 40% for values of SNR between 10 dB and 0 dB (Fig. 4.5). Velocity profiles in low SNR regions were corrected for this type of noise biasing using the method described in Section 4.4.

Other errors effecting measurement accuracy come from nonlinearities in the receiver electronics, and "coloring" of the magnitude transfer function of the overall receive system. Experience with the MPL Doppler sonar system has shown that transient nonlinearities may be important for data collected within  $6 \sigma_n^{-1}$  after pulse transmission, where  $\sigma_n$  is the -3 dB receiver bandwidth (Sec. 4.3a). For the MPL system the -3 dB receiver bandwidth is 195 Hz, giving  $6 \sigma_n^{-1} \approx 30 \text{ ms}$ , a value equal to the pulse duration. In order to avoid possible contamination from transient nonlinearities covariance data were not computed within the first range gate. A receive system with a magnitude transfer function which is not flat or "white" with frequency causes an uneven weighting of the true Doppler spectrum, and may result in biasing of the estimate of the power weighted mean Doppler shift at low signal-to-noise ratios (Hansen, 1985b). This

"coloring" effect is considered small for the MPL system in comparison to other bias errors.

The ability of backscatter Doppler sonars to accurately measure water flow has been demonstrated under a variety of conditions. Volume-averaged velocity estimates from particular range gates of bottom-mounted ADCP's have been compared to nearby mechanical (rotor-and-vane or VMCM) current meters by several investigators (e.g. Mero, Appell and Porter, 1983; Pettigrew and Irish, 1983; Appell, et al., 1985). These studies show minimum rms differences between acoustic and mechanical velocity estimates of about  $2 \text{ cm s}^{-1}$ . This disagreement is typically of the same order as that between two mechanical sensors. A profile-by-profile comparison of velocity measurements made by the MPL Doppler sonar system to those made by an Electro-Magnetic Velocity Profiler (EMVP; Sanford, et al., 1985) showed rms differences of about  $2 \text{ cm s}^{-1}$  (Pinkel, 1982). These differences are of the same order as the differences between the EMVP and other velocity profiling devices (Sanford, 1982). In sum, the estimates of bias magnitudes and the results of field experiments indicate that the MPL Doppler sonar system can measure oceanic velocity profiles with an accuracy of about  $1\text{-}2 \text{ cm s}^{-1}$ , which is within the ability to define "sea-truth" for these profiles.

**b. Precision.** The precision of velocity estimates from pulse-to-pulse incoherent Doppler sonars has been investigated theoretically by Theriault (1981; 1986). Theriault uses a simplified model of the scatterer field and the velocity field to derive an expression for the lower bound on velocity estimate variance. The model employed by Theriault (1986) involves two major assumptions: First, it is assumed that within the insonified volume corresponding to a range gate, the medium is composed of a large number of individual scatterers with a net reflection response (complex envelope) which can be characterized as a Gaussian random variable. Second, the scatterers within each range gate are considered to be moving with the same radial velocity, so that the resulting velocity profile is piecewise-constant. The model ignores effects such as receiver noise (Sec. 4.3) and platform motion (Appendix A) which may increase velocity estimate variance.

With the above assumptions, it is possible to derive an expression for the Cramer-Rao lower bound; a theoretical lower bound on the variance of any unbiased estimator (Van Trees, 1968). For high signal-to-noise ratio ( $\text{SNR} > 20 \text{ dB}$ ) the form of the velocity estimate variance derived by Theriault is

$$\sigma_v^2 = c^2 (4N \omega_c^2 T_p^2)^{-1} \quad (1.19)$$

where  $\omega_c = 2\pi f_c$ ,  $f_c$  is the center frequency of the sonar,  $T_p$  is the pulse duration,  $c$  is the speed of sound, and  $N$  is the number of independent estimates of velocity. The MPL Doppler sonar system as configured for MILDEX (Sec. 1.3.3) operates with center frequencies near 75 kHz and transmits pulses of duration 30 ms. Each sonar transmits four tones every 2 s giving  $N = 120$  independent samples per minute. The lower-bound slant velocity precision for a 3 min average velocity estimate computed from (1.19) with  $f_c = 75 \text{ kHz}$ ,  $T_p = 30 \text{ ms}$ ,  $c = 1500 \text{ m s}^{-1}$ , and  $N = 360$  is  $\sigma_v = 0.28 \text{ cm s}^{-1}$ . Curves of lower-bound slant velocity precision  $\sigma_v$  as a function of  $\omega_c$  and  $T_p$  for an averaging interval of 6 min are shown in Fig. 1.9.

## SLANT VELOCITY PRECISION

N = 720 (6 min)

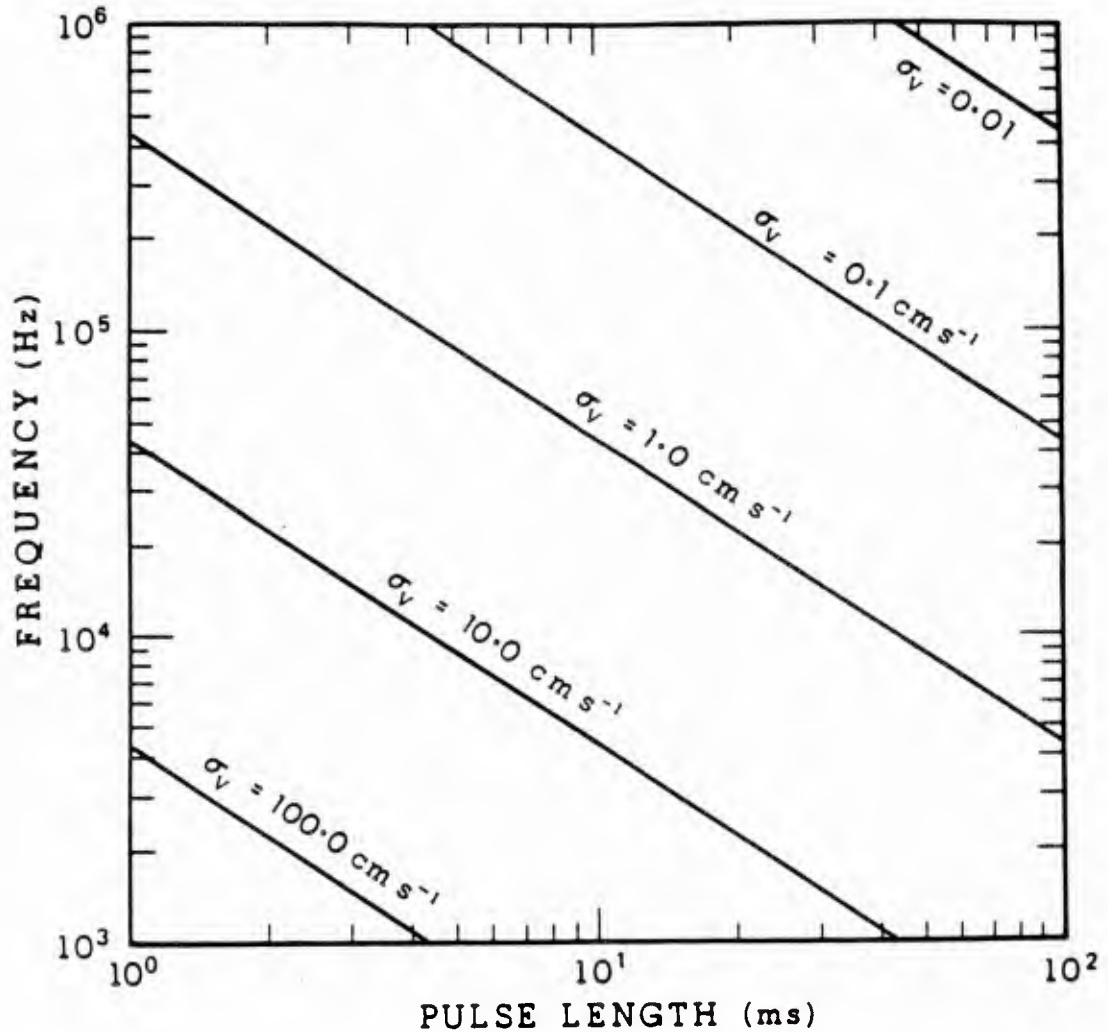


**Figure 1.9.** *Slant velocity precision.* Lower-bound slant velocity precision for a slant velocity estimate is shown as a family of curves vs. frequency and pulse length. Values of  $\sigma_v$  are computed according to (1.19). For the MPL Doppler sonar, with an operating frequency near 75 kHz and pulse length of 30 ms, the standard deviation of the slant velocity estimate for an averaging interval of 6 min ( $N = 720$ ) is  $\sigma_v = 0.20 \text{ cm s}^{-1}$ .



The expression (1.19) for estimator variance can be recast in terms of a normalized standard deviation constant (Miller and Rochwarger, 1972; Hansen, 1985a)

$$\Phi = c (2 \omega_c)^{-1} = \alpha^{-1} N^{1/2} T_p \sigma_v \quad (1.20)$$

The parameter  $\alpha$  has been included to accommodate differences between the theoretical lower bound ( $\alpha = 1$ ) and observed values of  $\Phi$  ( $\alpha > 1$ ) which are relevant in predicting  $\sigma_v^2$  for a particular Doppler system. For the MPL system as configured during MILDEX, the lower-bound normalized standard deviation is  $\Phi = 160$  cm. It remains to determine an appropriate value of  $\alpha$  to translate the theoretically predicted variance of (1.19) into a representative precision for an operational instrument.

The precision of velocity estimates for pulse-to-pulse incoherent Doppler sonars has been investigated experimentally by Pinkel (1982) and Hansen (1985a). Pinkel (1982) compares observed velocity estimate variance for the MPL Doppler sonar to the theoretical lower bound derived by Theriault using two parallel beams with an elevation angle of  $-45^\circ$ . The resulting slant velocity precision, computed for several different values of  $T_p$ , was consistent with a value of  $\alpha = 3.0$ . A similar analysis performed by Hansen (1985a) resulted in values of  $\alpha$  between 1.25 and 2.0. Data collected during MILDEX is consistent with a value of  $\alpha = 2.0$ . Based on this information, the slant velocity precision is estimated from (1.20) with  $\alpha = 2.0$  giving

$$\sigma_v = 2 \Phi N^{-1/2} T_p^{-1} \quad (1.21)$$

Values of estimate variance for the Janus velocity components are derived in terms of  $\sigma_v$  following Theriault (1986). Using (1.21) for the slant velocity precision, the Janus horizontal and vertical velocity precision are found from

$$\begin{aligned} \sigma_{u_J, v_J} &= [\sqrt{2} \cos \theta_0]^{-1} \sigma_v \\ \sigma_{w_J} &= [\sqrt{2} \sin \theta_0]^{-1} \sigma_v \end{aligned} \quad (1.22)$$

where  $\theta_0 = -52.5^\circ$  is the elevation angle of the beams. For the 3 min average data used as a basis for much of the work in this dissertation, the slant velocity precision estimated from (1.21) is  $\sigma_v = 0.56 \text{ cm s}^{-1}$ , and the corresponding Janus velocity precision from (1.22) is  $\sigma_{u_J, v_J} = 0.65 \text{ cm s}^{-1}$  and  $\sigma_{w_J} = 0.51 \text{ cm s}^{-1}$ .

**c. Secondary errors.** The important secondary measurement errors for the MPL Doppler sonar during MILDEX come from mechanical alignment errors, which primarily effect measurement accuracy, platform motion, which primarily effects measurement precision, and the deterministic movement of biological scatterers, which may effect both accuracy and precision.

Mechanical alignment errors arise from differences between the reference planes used to measure platform motion and the actual planes in which the sonars operate. The correction for velocity biases due to alignment errors is conveniently accomplished as a part of the correction for platform motion, and is described in Appendix A (Sec. A.7). Initial bias errors in slant velocity as large as  $0.6 \text{ cm s}^{-1}$  are reduced to values less than  $0.1 \text{ cm s}^{-1}$  after correction.

Velocity measurement errors due to platform motion are discussed in detail in Appendix A. Errors from both translation and rotation of the observational coordinate system from a geographic reference frame are considered. It is shown in Section A.5 that translation errors can be easily corrected under the assumption that vertical derivatives of velocity are much larger than horizontal derivatives in the geographic coordinate system. The translation correction insures that velocity estimates from a given range gate of any of the four downward-slanting sonars come from the same interval of actual ocean depth. Errors due to rotation (Sec. A.6) are most important for the Janus vertical velocity estimate. Correction for rotation errors in vertical velocity is accomplished using the Janus horizontal velocities to estimate the horizontal velocity components for each beam. The rotation correction, after accounting for angle measurement errors due to imperfect mechanical alignment (Sec. A.9), yields a reduction of nearly an order of magnitude in vertical velocity variance (Table A.2).

The deterministic (non-random) movement of biological scatterers can cause errors in the measurement of velocity at isolated depths and times. The use of Doppler sonar for velocity measurement relies on the assumption that the acoustic scatterers are, on average, passively drifting with the surrounding fluid. Obvious exceptions to this assumption come from actively swimming nekton and from zooplankton executing diurnal vertical migrations.

The acoustic returns from the 75 kHz MPL Doppler sonar come primarily from zooplankton, but occasional nekton or groups of nekton may dominate the return from a given range gate (c.f. Greenblatt, 1981). The nekton cannot be considered passively drifting, and may contribute a Doppler shift which is not representative of the fluid velocity. Range gates dominated by nekton can be identified by a large, transient increase in backscattered intensity. Velocity estimates at depths and times associated with these intensity "spikes" are considered to be contaminated by a false (non-fluid) Doppler shift. A velocity correction scheme based on the elimination of velocity estimates associated with intensity "spikes" was implemented on the data collected during MILDEX. This intensity-based "deglitching" scheme was associated with a reduction of slant velocity variance of about 2% from a rejection of approximately 1% of the available velocity estimates. This correction is also presumed to increase measurement accuracy.

The existence of vertically migrating acoustic scattering layers in the ocean has been recognized for some time (e.g. Hersey and Backus, 1962). These layers are known to be associated with the movements of marine organisms whose diurnal migrations are related to changes in ambient light levels. The extensive (100-500 m) and rapid ( $1-10 \text{ cm s}^{-1}$ ) vertical movement of scatterers can result in a false (non-fluid) vertical velocity measurement from a Doppler sonar. This effect can be clearly seen when the Janus vertical velocity estimates from many 24 hr periods are averaged together to emphasize the diurnal migration cycle (Fig. 3.5). The Janus horizontal velocity, in contrast, shows no indication of the migration signal, suggesting that the horizontal scale of the scattering layers is large compared to the separation between the beams. The vertical velocity of the scatterers is considered the signal of interest for the analysis in Chapter 3, and is shown to provide a useful characterization of migration patterns. For the analysis in Chapter 2, the vertical migration velocity is considered a source of noise and is removed by filtering in wavenumber-frequency space (Sec. 2.3.2).

## 1.5 Chapter summary

This chapter has provided an overview of data collection and processing during the MILDEX experiment. A description of MILDEX data collection was given in Section 1.2, with emphasis on the velocity measurements made with a multi-beam Doppler sonar deployed on the R/P FLIP. The data of interest for this dissertation were collected from four downward-slanting sonars operated during a 17 day period while FLIP drifted over some 200 km from a starting position near  $34^{\circ}$  N,  $127^{\circ}$  W. The azimuthal orientation of the platform was controlled by a hull-mounted thruster which maintained the ships heading to within about  $1^{\circ}$  of a desired value during the majority of the experiment. The tilt of the platform was measured by accelerometers. The accelerometer measurements were used to correct for tilt-induced errors in the Doppler velocity estimates.

A brief historical review of Doppler sonar applications, and an introduction to Doppler sonar operation was provided in the third section. Specialized Doppler sonars useful for oceanographic current measurements were introduced in the late 1970's. Several types of acoustic Doppler instruments have recently become available for use by the general oceanographic community. A summary of Doppler sonar fundamentals provided the background for discussion of the MPL Doppler sonar and its configuration during MILDEX. The MPL Doppler sonar is a narrow-beam, high-power system operated in a pulse-to-pulse incoherent mode, and provides profiles of backscattered intensity and slant velocity from  $\sim 100$  m to  $\sim 1000$  m in depth with  $\sim 20$  m depth resolution.

The nature of slant velocity and component velocity estimation from a multi-beam Doppler sonar was discussed in the last section. The velocity data from each beam may be used separately or in combination depending on the desired application. The benefits and disadvantages of several velocity estimation techniques, including the popular "Janus" technique, were briefly reviewed. Velocity estimation errors come from several sources. These errors were discussed in terms of primary errors, inherent in the instrument for a given system configuration, and secondary errors, unique to the operating environment during a particular deployment. As configured for MILDEX, the MPL Doppler sonar can be expected to measure the oceanic velocity field with accuracy of  $1\text{-}2\text{ cm s}^{-1}$  and precision of about  $0.6\text{ cm s}^{-1}$  after 3 min of averaging. Secondary errors, which may reduce the accuracy and increase the variance of the velocity estimates, are treated in the post-processing of the data.



## CHAPTER II

### THE MEASUREMENT OF REYNOLDS STRESSES ASSOCIATED WITH INTERNAL WAVES IN THE OCEAN

#### 2.1 Introduction

Internal waves are viewed as a potentially important mechanism for the vertical mixing of momentum in the ocean (Garrett, 1979; Munk, 1981), but the nature of internal wave momentum transfer processes is not well established. Understanding the transfer of momentum by internal waves is important in determining the dynamic balance leading to the observed oceanic internal wave spectrum (Olbers, 1983; Müller, et al., 1986), and is necessary for the proper parameterization of internal wave processes in terms of large-scale flow characteristics (e.g. vertical eddy viscosity, Müller, 1976). In fact, it has been suggested that "determining how to parameterize the effects of internal waves on low-frequency flows remains the central oceanographic problem associated with internal waves" (Garrett, 1984).

Understanding the role of internal waves in vertical momentum transfer ultimately rests with the measurement of the covariance between fluctuating velocity components (Reynolds stresses) in the internal wave field, and determining their relationship to the large-scale flow. The Reynolds stress tensor for a fluctuating velocity field is formally written  $\tau_{ij} = \rho_o \overline{u'_i u'_j}$  where  $\rho_o$  is the reference density and the primes denote fluctuating quantities. In this study, attention is focused on the tangential stresses ( $i \neq j$ ) which contain the vertical component of velocity (i.e.  $\rho_o \overline{u'w'}$  and  $\rho_o \overline{v'w'}$ ). These stresses are associated with a vertical transport of horizontal momentum and are termed the vertically-acting stresses. Direct measurements of vertically-acting Reynolds stresses associated with internal waves are few, with those of Ruddick and Joyce (1979) and Frankignoul and Joyce (1979) comprising the only well documented examples. These investigators report stresses which are of marginal significance relative to statistical error, and find no evidence of a relationship between internal wave stresses and large-scale shears which would be indicative of a wave-induced vertical eddy viscosity.

In this chapter, estimates of the vertical flux of horizontal momentum due to internal waves are made by the direct measurement of Reynolds stresses in the oceanic velocity field. The stress measurement technique used in this study exploits the ability of Doppler sonar (Pinkel, 1980; 1981) to simultaneously measure the contributions from horizontal and vertical velocity components within a small averaging volume. Multiple downward-slanting sonar beams are used to separate the contribution of the velocity component cross-covariances  $\overline{u'w'}$  and  $\overline{v'w'}$  from a product of slant velocities which also includes the auto-covariances  $\overline{(u')^2}$ ,  $\overline{(v')^2}$  and  $\overline{(w')^2}$ . This technique, described in Section 2.3.1, improves on previous stress measurements by eliminating errors inherent in



estimating  $w$  from an approximate heat equation (Ruddick and Joyce, 1979). The Doppler sonar provides profiles of slant velocity over depths of order 1 km with depth resolution of about 20 m, allowing estimation of the mean-flow shears  $\partial/\partial_z \bar{u}$  and  $\partial/\partial_z \bar{v}$ , as well as the stress divergences  $\partial/\partial z (\overline{u'w'})$  and  $\partial/\partial z (\overline{v'w'})$ . Estimates of mean-flow shear from vertical profiles of horizontal velocity represent an improvement over estimates made from a small number of vertically separated velocity measurements. The stress divergence is a fundamental term in the equations describing wave vs. mean flow interaction (Sec. 2.2.1), but has not been measurable using previous techniques.

A key aspect of this study which is different than that of previous investigations is the separation of the fluctuating part of the velocity field from the mean part. In this study, the fluctuations are separated in both vertical wavenumber and frequency using a filter which passes wavenumbers greater than 7 cpm and frequencies greater than 0.2 cph. In previous work, the fluctuations have been separated only in frequency. The ability to make this more restrictive separation of the fluctuating part of the velocity field comes from the additional information provided by the Doppler sonar measurements as compared to the traditional current meter measurements used by Ruddick and Joyce (1979) and Frankignoul and Joyce (1979). The latter measurements provide velocity information only for isolated depths as a function of time, and the separation of mean and fluctuating parts can only be done in frequency. For the Doppler sonar measurements, time series of velocity are obtained for a continuous set of depth bins, and the fluctuating part can be separated in both vertical wavenumber and frequency. Thus, the Reynolds stresses investigated here are those associated with high-vertical wavenumber, high-frequency internal waves.

Emphasis in this study is placed on estimating the magnitude of wave-induced stresses and determining their relationship to the low-frequency, "mean" flow. Assuming that the high-frequency portion of the internal wave field is responsible for the majority of momentum transfer (Ruddick and Joyce, 1979), the "mean" flow can be interpreted as including both the mesoscale (Müller, 1976) and the low-frequency portion of the internal wave field (Broutman, 1982). The duration of the experiment (17 days) is not sufficient to explore the relationship of internal wave stresses to the mesoscale flow. Instead, the relationship of stresses associated with high-frequency (0.3 to 1.0 cph) internal waves to the velocity field in the sub-inertial and near-inertial bands (0.01 to 0.10 cph) is considered. Correlations between stress and mean-flow shear which could arise from a wave-induced vertical eddy viscosity, like that proposed by Müller (1976), are investigated, as well as correlations between stress divergence and mean-flow acceleration which could arise from critical layer (Booker and Bretherton, 1967) or refractive convergence (Broutman, 1982) processes.

A brief discussion of internal waves in a slowly-varying mean flow is given in Section 2. Equations for the mean flow and the internal wave fluctuations are presented. Simplified examples are used to demonstrate the form of the wave-induced stress and the effect of the stress divergence on the mean flow. The results of previous studies of internal wave stresses, both theoretical and observational, are reviewed. In Section 3 the method of stress measurement is described, along with an explanation of data analysis procedures and an

evaluation of error sources. The results of stress measurements made during a 17 day experiment in the eastern North Pacific (  $34^\circ$  N,  $126^\circ$  W ) are presented and discussed in Section 4. Stress values are reported in units of  $\text{cm}^2 \text{s}^{-2}$ , equivalent to units of  $\text{dyn cm}^{-2}$  for a reference density of  $\rho_0 = 1.0 \text{ gm cm}^{-3}$ . It is shown that observed values of vertically-acting stress are of marginal significance relative to statistical error, indicating a high degree of vertical symmetry in the high frequency internal wave field during the experiment. No evidence is found of a correlation between internal wave stresses and mean-flow shear. There is weak evidence of a correlation between stress divergence and mean-flow acceleration. The chapter is summarized in Section 5.

## 2.2 Background

### 2.2.1 Internal waves in a slowly-varying mean flow

The starting point for discussion of wave vs. mean flow interaction is the equations of motion for an incompressible, inviscid, rotating, stratified fluid subject to the Boussinesq approximation. The flow is described in terms of the vector velocity field  $\mathbf{u} = (u, v, w)$ , the pressure  $p$ , representing the departure from the (hydrostatic) reference pressure, and the buoyancy  $b = -g\rho/\rho_0$ , where  $g$  is the acceleration of gravity,  $\rho_0$  is the reference density, and  $\rho$  is the departure from the reference density. Each of the parameters for the total flow is separated into a slowly-varying mean part [e.g.  $\bar{\mathbf{u}} = (\bar{u}, \bar{v}, \bar{w})$ ] and a fluctuating part [ $\mathbf{u}' = (u', v', w')$ ] by choosing a space-time averaging scale which is intermediate between the scale of the mean flow and that of the fluctuations. For purposes of simplification, the mean-flow amplitude is taken to be  $O(a^2)$  compared to the fluctuations which are  $O(a)$ , where  $a \ll 1$ . This small amplitude assumption results in the  $O(a^2)$  mean-flow equations

$$\partial_t \bar{u} - f \bar{v} + \rho_0^{-1} \partial_x \bar{p} = -\partial_x(\bar{u}^2) - \partial_y(\bar{u}'v') - \partial_z(\bar{u}'w') \quad (2.1a)$$

$$\partial_t \bar{v} + f \bar{u} + \rho_0^{-1} \partial_y \bar{p} = -\partial_x(\bar{u}'v') - \partial_y(\bar{v}^2) - \partial_z(\bar{v}'w') \quad (2.1b)$$

$$\partial_t \bar{w} - \bar{b} + \rho_0^{-1} \partial_z \bar{p} = -\partial_x(\bar{u}'w') - \partial_y(\bar{v}'w') - \partial_z(\bar{w}^2) \quad (2.1c)$$

$$\partial_t \bar{b} + N^2 \bar{w} = -\partial_x(\bar{u}'b') - \partial_y(\bar{v}'b') - \partial_z(\bar{w}'b') \quad (2.1d)$$

$$\partial_x \bar{u} + \partial_y \bar{v} + \partial_z \bar{w} = 0 \quad (2.1e)$$

where  $f$  is the coriolis parameter,  $N^2 = -g/\rho_0 \partial_z \rho = \partial_z b$  is the buoyancy

frequency, and the notation  $\partial_s$  represents partial differentiation with respect to the subscripted variable (e.g.  $\partial_z b = \partial b / \partial z$ ). These equations are similar to those of Müller (1976, eq. 2.10 and 2.11), but here the advective terms ( $\bar{\mathbf{u}} \cdot \nabla \bar{\mathbf{u}}$ ) are  $O(a^4)$  and can be neglected, and the "wave-induced pressure" has not been separated from the total pressure field.

The fluctuating part of the velocity field is restricted to be a linear ( $a \ll 1$ ) wave field of high frequency ( $\omega > f$ ) and high vertical wavenumber ( $k_z > H^{-1}$ , where  $H$  is the vertical scale of the mean flow). In this case, the mean flow can be considered slowly varying compared to the fluctuations, and the  $O(a)$  equations for the fluctuations, obtained by subtracting the mean-flow equations from the total flow, are simply the internal wave equations

$$\partial_t u' - f v' + \rho_o^{-1} \partial_x p' = 0 \quad (2.2a)$$

$$\partial_t v' + f u' + \rho_o^{-1} \partial_y p' = 0 \quad (2.2b)$$

$$\partial_t w' - b' + \rho_o^{-1} \partial_z p' = 0 \quad (2.2c)$$

$$\partial_t b' + N^2 w' = 0 \quad (2.2d)$$

$$\partial_x u' + \partial_y v' + \partial_z w' = 0 \quad (2.2e)$$

The slowly-varying approximation for the mean flow allows the wave field to be defined locally by solutions to (2.2), but to have amplitude, wavenumber, and frequency which evolve slowly over the scales of the mean flow. This is the standard WKB approximation (Gill, 1982) and is essential to most wave vs. mean flow interaction theories including those of Booker and Bretherton (1967), Bell (1975), Müller (1976), and Broutman (1982).

The terms on the right hand side of the mean-flow equations (2.1) represent the  $O(a^2)$  forcing by the fluctuations which are internal wave solutions to (2.2). For a quasi-geostrophic mean flow, the wave vs. mean flow interaction can be succinctly described by forming the potential vorticity equation (Müller, 1976). The forcing terms in the quasi-geostrophic potential vorticity equation appear as the curl of the divergence of an "interaction stress tensor" which includes a wave-induced momentum flux *and* a wave-induced buoyancy flux. The relative contributions of the momentum flux terms (Reynolds stresses) and buoyancy flux terms have been examined in detail by Ruddick (1977). The principal results are given here in the context of a different, and simpler problem described by McIntyre (1980). McIntyre considers a special case of the wave vs. mean flow interaction problem given by (2.1) and (2.2) wherein it is assumed that the mean flow is x-invariant ( $\partial_x[\ ] = 0$ ) and that only a single internal wave group is present with horizontal wavenumber vector aligned with the x-axis ( $\bar{u}'v' = \bar{v}'w' = \bar{w}'b' = 0$ ). The interesting dynamics are

now contained in the x-momentum equation, the mass conservation equation and the continuity equation which are (McIntyre, 1980)

$$\partial_t \bar{u} - f \bar{v} = -\partial_z (\overline{u'w'}) \quad (2.3a)$$

$$N^2 \bar{w} = -\partial_y (\overline{v'b'}) \quad (2.3b)$$

$$\partial_y \bar{v} + \partial_z \bar{w} = 0 \quad (2.3c)$$

The wave-induced buoyancy flux in (2.3b) drives an  $O(a^2)$  vertical velocity  $\bar{w} = -N^{-2} \partial_y (\overline{v'b'})$  which is coupled to (2.3a) through the "degenerate" continuity equation (2.3c) and results in an x-momentum equation of the form

$$\partial_t \bar{u} = -\partial_z (\overline{u'w'} - f N^{-2} \overline{v'b'}) \quad (2.4)$$

This somewhat restrictive example is used by McIntyre to emphasize that the stress whose divergence is in balance with the mean-flow acceleration is composed of two parts, a Reynolds stress  $\overline{u'w'}$  and a buoyancy flux  $\overline{v'b'}$ .

Ruddick (1977) derives the relationship between Reynolds stress and buoyancy flux for linear internal waves as  $\overline{v'b'} = f N^2 \omega^{-2} \overline{u'w'}$  so that (2.4) can be rewritten

$$\partial_t \bar{u} = -\partial_z [ (1 - f^2 \omega^{-2}) \overline{u'w'} ] \quad (2.5)$$

The ratio of Reynolds stress to buoyancy flux terms goes like  $f^2/\omega^2$ , where  $\omega$  is the frequency of the waves generating the stress. In general the Reynolds stress is insufficient to describe the internal wave forcing of the mean flow. For the analysis presented in this chapter, however, stresses generated by internal waves with frequencies  $\omega > 5f$  are considered. In this case, the contribution of the buoyancy flux terms will be less than 4% of the Reynolds stress terms and the wave-induced stresses can be considered to be fully described by the Reynolds stresses.

### 2.2.2 Estimates and observations of wave-induced stresses

There is little precedent for estimating the magnitude of the vertically-acting Reynolds stresses associated with internal waves in the ocean. Some idea of stress magnitude can be obtained by considering the relationship between stress and shear in a gradient transport equation

$$\overline{u'w'} = A_v \partial_z \bar{u} \quad (2.6)$$

where  $\overline{u'w'}$  is the wave-induced stress,  $A_v$  is the vertical eddy viscosity, and  $\partial_z \bar{u}$



is the mean-flow shear. For an ocean with  $A_v = 1.0 \text{ cm}^2 \text{ s}^{-1}$  and mean-flow shears of  $10^{-4}$  to  $10^{-3} \text{ s}^{-1}$ , the balance (2.6) would give stresses of order  $10^{-4}$  to  $10^{-3} \text{ cm}^2 \text{ s}^{-2}$ . This estimate is fraught with conceptual difficulties regarding the validity of (2.6), the appropriateness of  $A_v = 1 \text{ cm}^2 \text{ s}^{-1}$ , and the tacit assumption that the internal wave field supports the majority of oceanic momentum flux. Despite these problems, this rough estimate is sufficient to show that vertically-acting internal wave stresses on the *global* scale (averaged over climatological time scales and spatial scales on the order of ocean basins) are probably so small that they are unmeasurable using present techniques.

Rather than concentrate on the global scale, it is of interest to consider internal wave stresses on the *local* scale (space and time scales comparable to the scales of the internal wave field) where isolated generation and dissipation processes have not been averaged out. On the local scale, stress magnitudes may be substantially larger than the  $10^{-4}$  to  $10^{-3} \text{ cm}^2 \text{ s}^{-2}$  estimated for the global scale, and may be measurable. One of the earliest estimates of the magnitude of internal wave stresses on the local scale comes from Bell (1975). Following the development of Bretherton (1969), Bell considers stresses due to internal waves generated by a steady flow over the topography of the ocean bottom. For a steady flow of  $4 \text{ cm s}^{-1}$  over abyssal hills with a prescribed (from measurement) horizontal wave number spectrum, Bell computes a wave-induced stress of  $0.5 \text{ cm}^2 \text{ s}^{-2}$ .

Ruddick (1980) estimates the maximum stress which could be supported by an internal wave field with a spectrum like that of Garrett and Munk (1972; 1975) which encounters critical layers (Booker and Bretherton, 1967). Using the Garrett and Munk model to specify the energy density spectrum of the wave field, Ruddick allows vertical asymmetry (not considered in the Garrett and Munk model) while always maintaining the same spectral shape. As an extreme example, it is assumed that all of the waves in the spectrum are propagating in one direction, and the change in the momentum of the mean flow which would arise if the waves encountered a critical layer is computed. The fraction of the waves which "go critical" is a function of the mean-flow speed and hence the stress estimates vary with the mean horizontal velocity  $\bar{u}$  from a value of about  $0.02 \text{ cm}^2 \text{ s}^{-2}$  for  $\bar{u} = 5 \text{ cm s}^{-1}$  to  $0.20 \text{ cm}^2 \text{ s}^{-2}$  for  $\bar{u} = 50 \text{ cm s}^{-1}$ .

Theoretical work on the interaction of a weakly nonlinear internal wave field with a quasi-geostrophic mean flow has been done by Müller (1976). The effect of the mean flow on the wave field is treated as a small perturbation to an otherwise vertically symmetric and horizontally isotropic equilibrium internal wave spectrum. The analysis assumes that nonlinear wave-wave interactions act to rapidly "relax" the perturbed spectrum back to its equilibrium state. If relaxation processes are rapid compared to the typical propagation times of internal wave groups, Müller's theory predicts a linear relationship between the internal wave stress and mean-flow shear of the form (2.6) and allows evaluation of  $A_v$ . The most important result of Müller's work is the prediction of a wave-induced vertical eddy viscosity which is quite large ( $A_v \sim 4 \times 10^3 \text{ cm}^2 \text{ s}^{-2}$ ), indicating that for typical mean-flow shears of  $10^{-4}$  to  $10^{-3} \text{ s}^{-1}$  the internal wave stresses would be of order  $0.4$  to  $4.0 \text{ cm}^2 \text{ s}^{-2}$ . It is now believed (McComas and Bretherton, 1977; Müller, et al., 1986) that Müller's

original estimate of  $A_v$  is too large by one to two orders of magnitude. The resulting estimates of internal wave stresses are correspondingly reduced to order  $0.04$  to  $0.4 \text{ cm}^2 \text{ s}^{-2}$ .

The original estimate of vertical eddy viscosity by Müller (1976) was surprisingly large, and motivated several experiments which attempted to measure vertically-acting internal wave stresses, mean shears, and the correlation coefficient between them which would represent  $A_v$ . The principal measurements are those of Ruddick and Joyce (1979) and Frankignoul and Joyce (1979), the former using data collected during POLYMODE and the latter using data from IWEX (Briscoe, 1975). Both investigations use the same technique to estimate internal wave stresses: Horizontal velocity components are measured directly from current meter data, and vertical velocities are estimated from the time rate of change of temperature and the vertical temperature gradient using an approximate heat equation

$$w \approx \partial_t T (\partial_z \bar{T})^{-1} \quad (2.7)$$

The cospectrum of horizontal and vertical velocities is then computed and summed over the high-frequency internal wave band, giving an estimate of wave-induced stress. Ruddick and Joyce (1979) give a critical assessment of errors in stress which arise from the estimate (2.7) of vertical velocity and find errors due to finestructure contamination which are of the same order as the statistical uncertainty. For a 75 hr average stress estimate, the combination of finestructure contamination, statistical uncertainty, and other errors gives an expected error standard deviation of  $0.08 \text{ cm}^2 \text{ s}^{-2}$ . Considering the variability of the observed stresses [ mean  $\sim 0.003 \text{ cm}^2 \text{ s}^{-2}$ , std. dev.  $\sim 0.04 \text{ cm}^2 \text{ s}^{-2}$ , (Ruddick, 1977) ] compared to the expected errors shows that few of the observed stresses are significantly different from zero. Despite a smaller contribution from finestructure contamination, due to better measurements of the temperature gradient, Frankignoul and Joyce (1979) also find that observed 75 hr average stresses in the high-frequency internal wave band cannot be distinguished from zero.

The estimates and observations of wave-induced, vertically-acting Reynolds stresses described in this section are summarized in Table 2.1. Due to the rather extreme examples used for the theoretical estimates, and the statistical uncertainty of the observations, these values should be considered representative of the maximum stress likely to be supported by the internal wave field. The available evidence (excluding Müller's original overestimate) is consistent with vertically-acting internal wave stresses of order  $0.02$  to  $0.5 \text{ cm}^2 \text{ s}^{-2}$  on the local scale where internal wave generation and dissipation processes are active. One of the goals of this paper is to evaluate the feasibility of using multi-beam Doppler sonar to make direct measurements of internal wave stresses on the local scale.

**Table 2.1.** *Estimates and observations of wave-induced stresses.* Estimates of the magnitude of vertically-acting Reynolds stresses  $S = \overline{u'w'}$  from several theoretical investigations, and observations of the standard deviation  $\sigma_s$  of 75 hr average stresses from two experiments are summarized. All values come from published work except those of Müller, where mean shears of  $10^{-4}$  to  $10^{-3}$   $s^{-1}$  are used to translate eddy viscosities to stress values, and Frankignoul and Joyce, where values are estimated by the author from published plots of observed stress vs. time.

<b>Estimates and Observations of Wave Induced Stresses</b>	
<b>Estimates</b>	<b><math>S, cm^2 s^{-2}</math></b>
Bell, 1975	0.5
Ruddick, 1980	0.02 to 0.2
Müller, 1976	0.4 to 4.0
Müller, 1977	0.04 to 0.4
(see McComas and Bretherton, 1977)	
<b>Observations (75 hr avg)</b>	<b><math>\sigma_s, cm^2 s^{-2}</math></b>
Ruddick and Joyce, 1979	0.04
Frankignoul and Joyce, 1979	0.02

## 2.3 Methods

### 2.3.1 Stress measurement using multi-beam Doppler sonar

The technique used to estimate the vertically-acting Reynolds stresses is based on the fact that the "slant" (radial) velocity variance from a single sonar beam contains contributions from the component cross-variance  $\overline{u'w'}$  as well as the auto-covariances  $\overline{(u')^2}$  and  $\overline{(w')^2}$ . The cross-covariance can be evaluated by combining the velocity information from two, co-planar beams under the assumption of either horizontal homogeneity or horizontal coherence

of velocity components. The technique is similar to that described by Lhermitte (1983) and Lhermitte and Poor (1983), with the primary difference being one of scale. While Lhermitte considers slant velocity variance measured over time scales of seconds and spatial scales of centimeters, the method used in this study considers slant velocity variance measured over time scales of hours and spatial scales of tens of meters. The latter method is described below.

The first step in generating a stress estimate is to separate time series of volume-averaged slant velocity into mean and fluctuating parts  $V = \bar{V} + V'$ , where  $V$  is as in (1.8) and the overbar represents the same conceptual averaging time as in (2.1). In this study, the scale separation is done by wavenumber-frequency filtering of the velocity field, described in the next section. The fluctuating part of the slant velocity can be interpreted as the projection of the fluctuating velocity components into the beam axis (c.f. (1.14) and Fig. 1.8). For a pair of beams in the  $x$ - $z$  plane, at an elevation angle  $\theta_0$  from the horizontal, this gives

$$V'_E = -u'_E \cos\theta_0 + w'_E \sin\theta_0 \quad (2.8a)$$

$$V'_W = +u'_W \cos\theta_0 + w'_W \sin\theta_0 \quad (2.8b)$$

where subscripts E and W denote quantities measured by the East- and West-pointing beams, respectively. The variance of the slant velocities (2.8) is

$$\sigma_E^2 = \overline{(u'_E)^2} \cos^2\theta_0 + \overline{(w'_E)^2} \sin^2\theta_0 - 2 \overline{u'_E w'_E} \sin\theta_0 \cos\theta_0 \quad (2.9a)$$

$$\sigma_W^2 = \overline{(u'_W)^2} \cos^2\theta_0 + \overline{(w'_W)^2} \sin^2\theta_0 + 2 \overline{u'_W w'_W} \sin\theta_0 \cos\theta_0 \quad (2.9b)$$

Since the variances  $\sigma_E^2$  and  $\sigma_W^2$  are computed from a *time series* composed of many samples of volume-averaged velocity, they represent fluctuations with spatial scales greater than the insonified volume of the sonar and time scales greater than the time required to make a single estimate of  $V'$ . In contrast, the variance  $\sigma_d^2$  discussed by Lhermitte (1983) is computed from the width of the Doppler spectrum associated with a *single measurement* of volume-averaged velocity, and represents fluctuations with spatial scales less than the insonified volume of the sonar and time scales less than the measurement interval of  $V'$ .

The velocity components contributing to the variances in (2.9) cannot be considered equal in general because they come from measurements separated in space by the distance between the beams (hence the subscripts E and W). However, if the wave field is horizontally homogeneous, then the statistics of the velocity components will be identical for each beam. Dropping the subscripts on averaged quantities on the right-hand side of (2.9) under the assumption of horizontal homogeneity, the component cross-covariance in the  $x$ - $z$  plane can be evaluated from

$$\sigma_W^2 - \sigma_E^2 = 4 \sin\theta_0 \cos\theta_0 \overline{u'w'} \quad (2.10)$$



Using an analogous argument for the slant velocities measured by the North and South beams gives the cross-covariance in the  $y$ - $z$  plane from

$$\sigma_S^2 - \sigma_N^2 = 4 \sin\theta_0 \cos\theta_0 \overline{v'w'} \quad (2.11)$$

If the fluctuating velocity field is of large enough spatial scale to be coherent over the horizontal distance separating the beams, then the cross-covariances can be estimated from (2.10) and (2.11) without the assumption of horizontal homogeneity.

Doppler sonar measurements of the vertically-acting Reynolds stresses are given in (2.10) and (2.11) in terms of the difference between the slant velocity variance from two beams. This is consistent with previous work (e.g., Lhermitte, 1983) and is sufficient to understand the results presented in this chapter, but it has been found that a completely equivalent description of Doppler sonar stress measurements in terms of the Janus velocities (Sec. 1.4.1) can also be useful. Consider the Janus horizontal and vertical fluctuating velocities for the East-West beam pair given by [c.f. (1.17)]

$$u'_J = \frac{V'_W - V'_E}{2 \cos\theta_0} \quad , \quad w'_{JE} = \frac{V'_W + V'_E}{2 \sin\theta_0} \quad (2.12)$$

The subscript JE denotes the Janus velocity computed from the East-West beam pair, and is used to distinguish the vertical velocity in (2.12) from the corresponding quantity computed from the North-South beam pair. By substituting the expressions (2.8) into (2.12) it can be shown that the average product of the Janus components is equal to the difference between the slant velocity variances (2.9b) and (2.9a), except for a multiplicative constant. Thus, under the assumption of horizontal homogeneity (or horizontal coherence) for velocity components, the cross-covariances in (2.10) and (2.11) can be evaluated from the Janus velocities using

$$\overline{u'_J w'_{JE}} = (4 \sin\theta_0 \cos\theta_0)^{-1} [\sigma_W^2 - \sigma_E^2] = \overline{u'w'} \quad (2.13)$$

$$\overline{v'_J w'_{JN}} = (4 \sin\theta_0 \cos\theta_0)^{-1} [\sigma_S^2 - \sigma_N^2] = \overline{v'w'} \quad (2.14)$$

The description of Doppler sonar stress estimation in terms of the cross-covariance of Janus velocities is adopted in the remainder of the chapter.

### 2.3.2 Data analysis procedure

The velocity data of interest for this study were collected during the Mixed Layer Dynamics Experiment (MILDEX) using a multi-beam Doppler sonar deployed on the R.P. FLIP of the Scripps Institution of Oceanography. Data were collected over a 17-day period from Julian day 300 through 316 of 1983 while FLIP drifted over an approximately  $1^\circ$  square area in the eastern North Pacific, centered at  $34^\circ$  N,  $126^\circ$  W (Fig. 1.2). The Doppler sonar stress measurements were made using four sonars mounted at a depth of 38 m on FLIP's hull with beams pointing downward at an angle of  $\theta_0 = -52.5^\circ$  from the horizontal (Fig. 1.3). The four downward-slanting sonars were composed of transducer panels with dimensions of approximately 0.36 m by 0.61 m and a -3 dB beam width of about  $2^\circ$ . The sonars were mounted with each beam separated by  $90^\circ$  in azimuth from neighboring beams. An azimuth control system was used to maintain the beam orientations so that the four beams formed two Janus pairs aligned along the North-South and East-West axes of a standard geographic coordinate system (Appendix A). One Janus pair was operated at a center frequency of 67 kHz, the other at 71 kHz.

The sonars provide estimates of water velocity from measurement of the Doppler shift in the backscattered energy from targets (primarily zooplankton; see Ch. 3) in the water column. During operation, each sonar sends out a sequence of pulsed transmissions of duration 30 ms at intervals of 2 s. The 2 s repetition time gives a maximum range (based on the round-trip travel time for the pulse) of 1500 m, but due to the decrease in signal-to-noise ratio with increasing range, the useful range was reduced to about 1300 m (1000 m depth). The depth resolution of the sonar velocity measurements is set by the duration of the transmitted pulse and is equal to 18 m for the 30 ms pulses used during MILDEX. The precision of the sonar velocity estimates can be computed from (1.21) and (1.22). After taking into account the reduction of variance due to wavenumber-frequency filtering (see below), the precision of 12 min average horizontal and vertical Janus velocity estimates is  $0.28 \text{ cm s}^{-1}$  and  $0.21 \text{ cm s}^{-1}$ , respectively.

The autocovariance of the complex envelope of the backscattered signal was computed as a function of range according to (1.11) for 30 s averaging intervals and recorded on tape during the experiment. Post-processing of the covariance included the removal of bad data using an intensity-based deglitching routine (Sec 1.4.2), further averaging to three-minute intervals, and correction for biasing at low signal-to-noise ratio (Sec. 4.4), before computation of the volume-averaged velocity using (1.12). The three-minute average slant velocity profiles were then corrected for platform motion using the method described in Appendix A. The effect of FLIP's drift was removed by subtracting the vertical average of the slant velocity profiles from the observed velocity at each depth for each time step. To the extent that the true, depth-averaged velocity in the water column over which the slant velocities are averaged is small compared to the velocity of FLIP through the water, this method has the same effect as adding the drift velocity of the platform to each profile (see discussion in Sec. 1.3.3). The temporal mean velocity for the 17-day measurement interval was

also removed at each depth.

A segment of the depth-time array of slant velocity for the North beam computed using the steps outlined above is shown in Figure 2.1. Velocity fluctuations with periods from tens of hours to several minutes can be seen. Two of the primary error sources in the stress measurements can also be identified; velocity "spikes" due to the vertical migration of biological scatterers, and high frequency noise generated by the orientation system during high wind conditions. Errors in vertical velocity due to vertical migration (see Fig. 2.2), and occasional noise bursts at the deepest depths combine to make the upper and lower limits of the depth interval unsuitable for stress measurements. Thus, only the subset of depths indicated in Fig. 2.1 were ultimately used in the analysis.

For application to the measurement of high-frequency internal wave stresses, the slant velocity data for beam pairs aligned with the North-South and East-West axes are combined to form the Janus velocities (1.17). The Janus velocities are subsampled at half-depth bin intervals (8.9 m), averaged to 12 min in time, and set up as a  $128 \times 2048$ -point depth-time array covering depths from roughly 60 m to 1160 m and a time interval of 17 days. A segment of the depth-time array of Janus horizontal and vertical velocity for the North-South axis is shown in Fig. 2.2. The depth-time array for each of the four Janus velocities (1.17) is then Fourier-transformed into wavenumber-frequency space and subjected to a high-pass filter which passes frequencies  $\omega > 0.2$  cph (period  $< 5$  hr) and vertical wavenumbers  $k_z > 7$  cpkm (wavelength  $< 140$  m). This filtering operation serves as the scale separation for the velocity field and also provides very effective rejection of the vertical migration signal which would otherwise be found in the Janus vertical velocity.

The fluctuating part of the velocity field is defined as the high-wavenumber, high-frequency portion of the original data which is passed by the filter, and the mean part is the original data minus the fluctuating part. Due to this definition of mean and fluctuations, the mean flow contains not only low-wavenumber, low-frequency energy, but also some high-wavenumber energy (at low frequency), and some high-frequency energy (at low wavenumber). In all subsequent analysis, except that involving relationships between fluctuating Janus components, the data for both mean and fluctuating fields are in the low-frequency band ( $\omega < 0.2$  cph), so that the high-frequency portion of the mean field is eliminated. No depth averaging of the mean or fluctuating fields is done, however, so the high-wavenumber portion of the mean field remains. This makes little difference in analyses involving the mean velocity, which is dominated by low-wavenumber energy at low frequency (Fig 2.3a), but allows for the presence of mean-flow shear at low frequency which may be concentrated at mid to high wavenumbers in the internal wave band (Fig. 2.3b).

In the first part of the data analysis, the nature of vertically-acting internal wave stresses is explored using the fluctuating part of the data, both in the depth-frequency domain and in the depth-time domain. In the frequency domain, the cross-spectra of Janus horizontal and vertical velocity components is computed in the frequency band from 0.3 to 1.0 cph. Significant coherence in the high-frequency band indicates a degree of relatedness between velocity



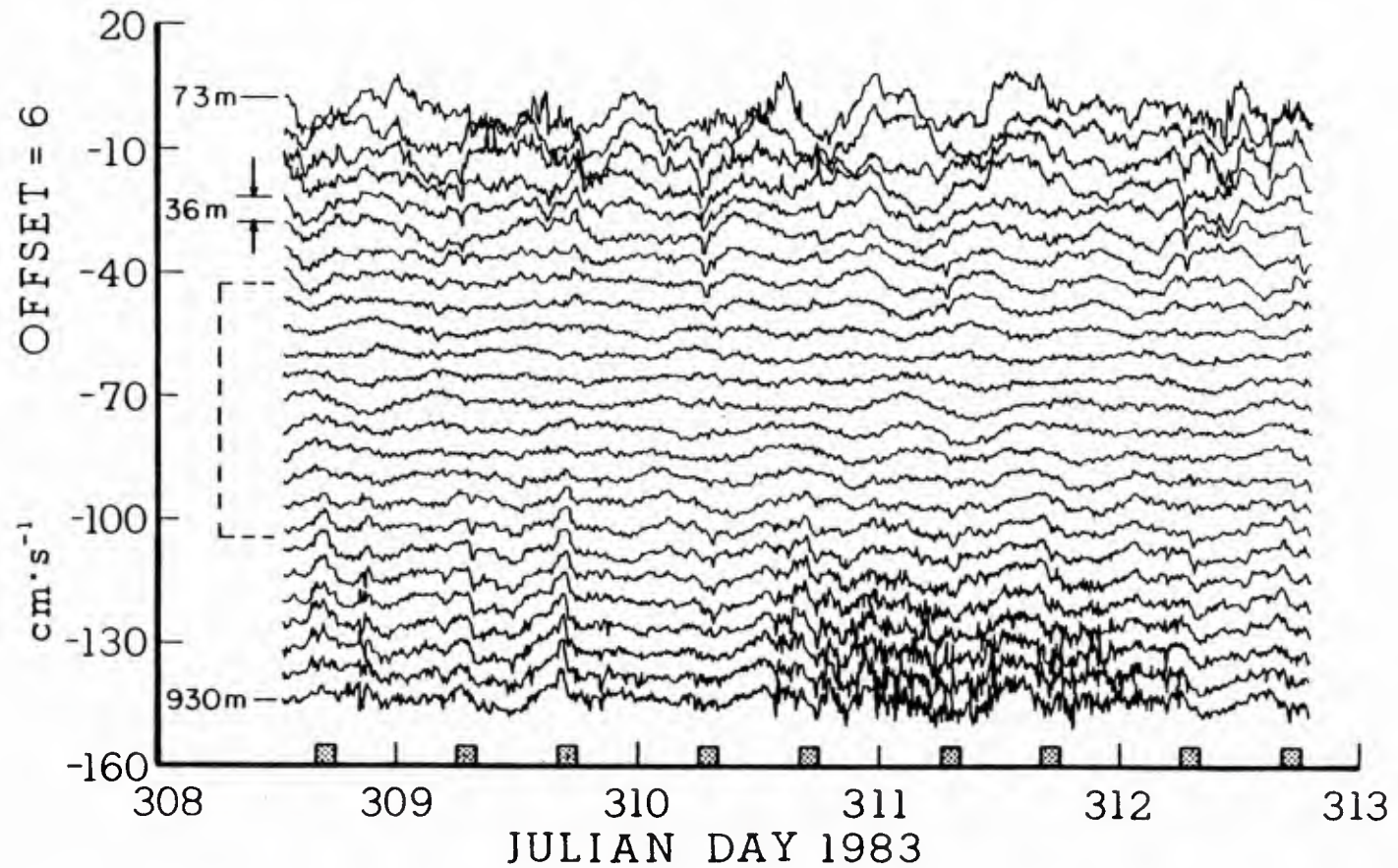


**Figure 2.1.** *Slant velocity time series.* Slant velocity measured by the North beam is shown as a function of depth and time for a 4.3 day segment near the middle of the 17 day data analysis period. The velocity scale is correct for the first time series, with successive lines offset by  $-6 \text{ cm s}^{-1}$ . Dashed lines on the depth axis enclose the interval from 332 m to 689 m where stress estimates were computed. Shaded boxes on the time axis represent intervals near dawn and dusk where the slant velocity is influenced by the vertical migration of biological scatterers. High frequency variability below 700 m on day 311 is due to noise from the orientation system.



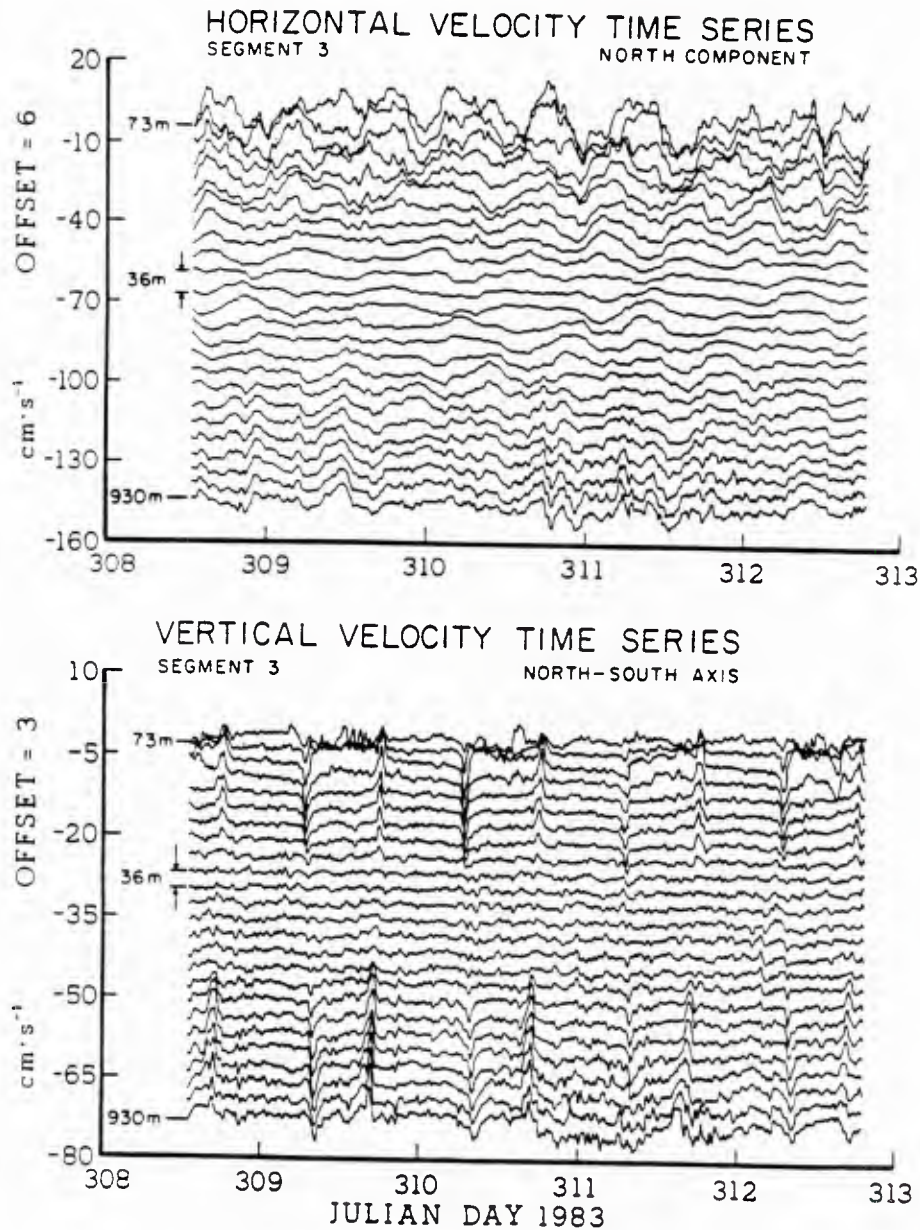


**Figure 2.2.** *Janus velocity time series.* Depth-time arrays of horizontal (top) and vertical (bottom) Janus velocity components computed from the North and South sonar beams are shown for the same segment as in Fig. 2.1. These velocities represent the Janus components *before* the separation into mean and fluctuating parts. Velocity 'spikes' from the vertical migration of scatterers, seen faintly in Fig. 2.1, are obvious in the Janus vertical velocity and notably absent in the Janus horizontal velocity. The data in this figure have been smoothed over 30 min in time and averaged over 2 depth bins (36 m).

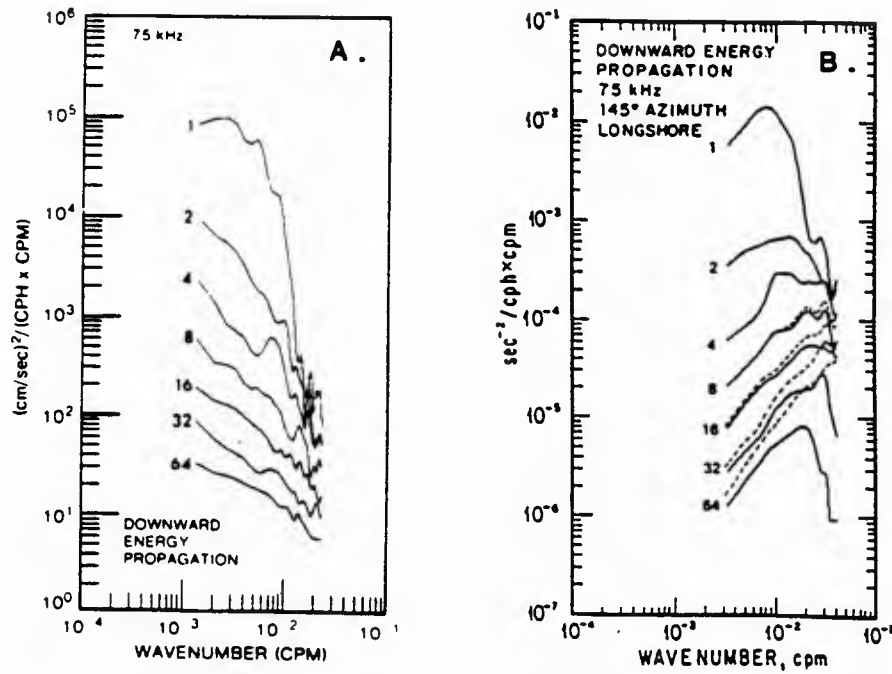


**Figure 2.3.** *Velocity and shear spectra.* Cross-sections of vertical wavenumber-frequency spectra at 1, 2, 4, 8, 16, 32, and 64 cpd for horizontal velocity (a, from Pinkel, 1984) and horizontal velocity shear (b, from Pinkel, 1985) are presented. The spectra show the downward-propagating part of the wave field (positive  $k_z$ ) for a single velocity component, and represent the energetic portion of the spectra observed by Pinkel (1984; 1985). Dashed lines on the shear spectra are for the observed spectra before correction for measurement noise.

components. Phase near  $0^\circ$  or  $180^\circ$  where coherence is significant implies dominance of the cospectrum over the quadrature spectrum, to be expected in the presence of ray-like internal waves which contribute to a net stress. Phase near plus or minus  $90^\circ$  where coherence is significant implies dominance of the quadrature spectrum, expected in the presence of mode-like waves with no net stress. The frequency domain analysis is most sensitive to stresses which are persistent throughout the observation interval, although they may be small in magnitude. In the time domain, the covariance of the fluctuating Janus velocities is formed according to (2.13) and (2.14) for averaging intervals between 5 hr and 76 hr. The zero-lag covariance corresponds to the frequency-integrated cospectrum, and values of covariance which are large relative to statistical error imply significant stresses. The time domain analysis is most sensitive to stresses which are large in magnitude, but may be of limited duration.

The relationship between internal wave stresses and the mean flow is investigated in the depth-frequency domain. First, the cross-spectra of stress and mean-flow shear is computed in the low frequency band (0.01 to 0.1 cph). Significant coherence between stress and mean-flow shear with phases near  $0^\circ$  would indicate a linear relationship of the form (2.6), suggestive of an internal wave-induced vertical eddy viscosity. Next, the stress divergence is formed from the time series of averaged Janus velocity products (2.13) and (2.14), and the cross-spectra of stress divergence and mean-flow acceleration is computed in the low-frequency band. Significant in-phase coherences would arise from a wave vs. mean flow relationship of the form

$$\partial_t \bar{u} - f \bar{v} = \partial_z (\overline{u'w'}) \quad (2.15)$$

$$\partial_t \bar{v} + f \bar{u} = \partial_z (\overline{v'w'}) \quad (2.16)$$

which could be expected in the region of a critical layer, refractive convergence, or other process in which momentum is exchanged between internal waves and the mean flow. The relationships (2.15) and (2.16) contain all of the information about the wave vs. mean flow momentum balance available from the analysis, but represent only part of the balance described by (2.1). For example, no information about the horizontal gradients of pressure is available. Thus, it is recognized that the correlation between stress divergence and mean flow acceleration considered here address only a portion of the potential wave vs. mean flow momentum balance.

### 2.3.3 Evaluation of errors

The largest source of error in measuring stresses is statistical uncertainty. In the time domain, the stresses are estimated from the covariance of horizontal and vertical Janus components according to (2.13) and (2.14). Using the East-West axis as an example, the covariance estimate is

$$\hat{C} = \frac{1}{N} \sum_{i=1}^N (u'_J)_i (w'_{JE})_i = \overline{u'_J w'_{JE}} \quad (2.17)$$

If the number of independent samples is sufficiently large ( $N > 10$ ) the estimate (2.17) can be considered unbiased, with an expected value equal to the true covariance. The variance of the covariance estimate can be derived under the assumption that  $u'_J$  and  $w'_{JE}$  are realizations of stationary random processes with Gaussian probability density functions. Noting that  $C$  is computed at zero lag, the variance is (Jenkins and Watts, 1968)

$$\sigma_{\hat{C}}^2 = \frac{1}{N} \sum_{r=-\infty}^{\infty} [C_{uu}(r) C_{ww}(r) + C_{uw}(r) C_{uw}(-r)] \quad (2.18)$$

where  $C_{ab}(r)$  is the true covariance of  $a$  and  $b$  at lag  $r$ , and the subscripts and primes on  $u$  and  $w$  have been dropped for simplicity. If successive samples of  $u$  and  $w$  are independent [ $C_{aa}(r) = 0$  for  $r \neq 0$ ;  $C_{aa}(0) = \sigma_a^2$ ] and have a true cross-covariance of zero [ $C_{ab}(r) = 0$  for all  $r$ ], then (2.18) simplifies to

$$\sigma_{\hat{C}}^2 = \frac{1}{N} \sigma_{u'_J}^2 \sigma_{w'_{JE}}^2 \quad (2.19)$$

In practice, the observed variances of  $u'_J$  and  $w'_{JE}$  are substituted for the true variances in (2.19).

The simplified expression (2.19) may be used to determine the significance of stress estimates by computing the expected statistical error in the covariance estimate when the true covariance is zero. It is recognized, however, that the assumption of independence does not strictly hold for the actual data. For example, it is known that  $u'_J$  has a "red" spectrum, implying a degree of dependence between successive samples. The effect of dependent samples is to increase the contribution from the auto-covariance terms in (2.18), thus increasing the variance of  $C$  relative to that given by (2.19). In order to investigate the effect of dependent samples in the actual data, an artificial data set is created which is known to have a true cross-covariance of zero between horizontal and vertical velocity components, but which has a degree of auto-covariance similar to that of the actual data.

The artificial data is created by generating sequences of independent, Gaussian, pseudo-random numbers to represent the real and imaginary parts of complex Fourier series. The random numbers come from a distribution with mean of zero and variance of one. These sequences are then "colored" using depth and frequency averaged versions of the observed Fourier coefficients for the four Janus components ( $u'_J$ ,  $v'_J$ ,  $w'_{JE}$ , and  $w'_{JN}$ ). The "coloring" process consists of multiplication of the random sequences by the standard deviation of the observed data, followed by addition of the observed mean, for each frequency band. The result is a set of artificial Fourier series (equivalently time series) which, on average, reproduce the power spectra of the observed fluctuating Janus components, but have random phases between horizontal and vertical velocities in each frequency band.



It is expected that the dependence of successive samples of velocity, simulated in the artificial data, will increase the variance of the covariance estimate from that predicted for the case of independent samples. Covariance estimate variability computed from the artificial data is compared to that for the independent case in the following manner: The covariance of the artificial Janus components is computed according to (2.17) for averaging intervals between 5 and 76 hr. The root-mean-square (rms) value of covariance for each averaging interval is then computed along with the standard deviation from (2.19), which represents the independent case (rms values can be compared to standard deviations because the mean covariances for the artificial data are small enough to be insignificant). The results are shown in Fig. 2.6.

Values of rms covariance computed from the artificial data are roughly 10 % larger than those computed from (2.19) for averaging intervals up to 12 hr, decreasing to within 5 % for intervals greater than 12 hr. This shows that the degree of auto-correlation of velocity components in this study has only a moderate effect on the covariance estimate, and indicates that simplified expressions like (2.19) provide an adequate measure of statistical error. Nevertheless, the artificial data set provides a convenient method of assessing the significance of observed cross-spectra: Both observed and artificial data are processed in parallel and the resulting distributions of coherence and phase are compared. This technique is used in evaluation of the Janus component cross-spectra in the high frequency band (Fig. 2.4), and the cross-spectra of stress and mean-flow shear (Fig. 2.8) and of stress divergence and mean-flow acceleration (Fig. 2.9) in the low frequency band.

Errors other than statistical error come from two main sources; the motion of the platform on which the sonars are mounted, and the deterministic vertical movement (diurnal migration) of the biological scatterers that provide the acoustic reverberation signal from which Doppler shift is estimated. Errors due to platform motion can be separated into a part due to the translation of the nominal velocity measurement point to a new point in space, and a part due to the rotation of the nominal velocity measurement vector to a new angle. The vertical component of translation causes errors in the stress estimate which are related to the local shear field. Rotation effects the stress estimate through errors in vertical velocity measurement. A detailed discussion of errors due to platform motion, and their correction, is provided in Appendix A. The residual errors in Janus velocity components due to inaccuracies in the tilt correction could result in a false stress of as large as  $0.006 \text{ cm}^2 \text{ s}^{-2}$ . This value is small compared to other errors for all but the largest averaging intervals.

Vertically migrating scattering layers have been observed since the earliest application of oceanic echosounders (Hersey and Backus, 1962), and it is not surprising that the movement of biological scatterers, so evident in the back-scattered intensity field of an active sonar, would also be observed in the vertical component of the Doppler velocity field. Treating the velocities of migrating scatterers as the signal of interest from Doppler sonar measurements results in a useful characterization of migration patterns (Ch. 3). However, for the purpose of stress measurement, vertical migration is a source of noise and must be eliminated. In the present study, correction for the false (non-fluid) vertical velocity

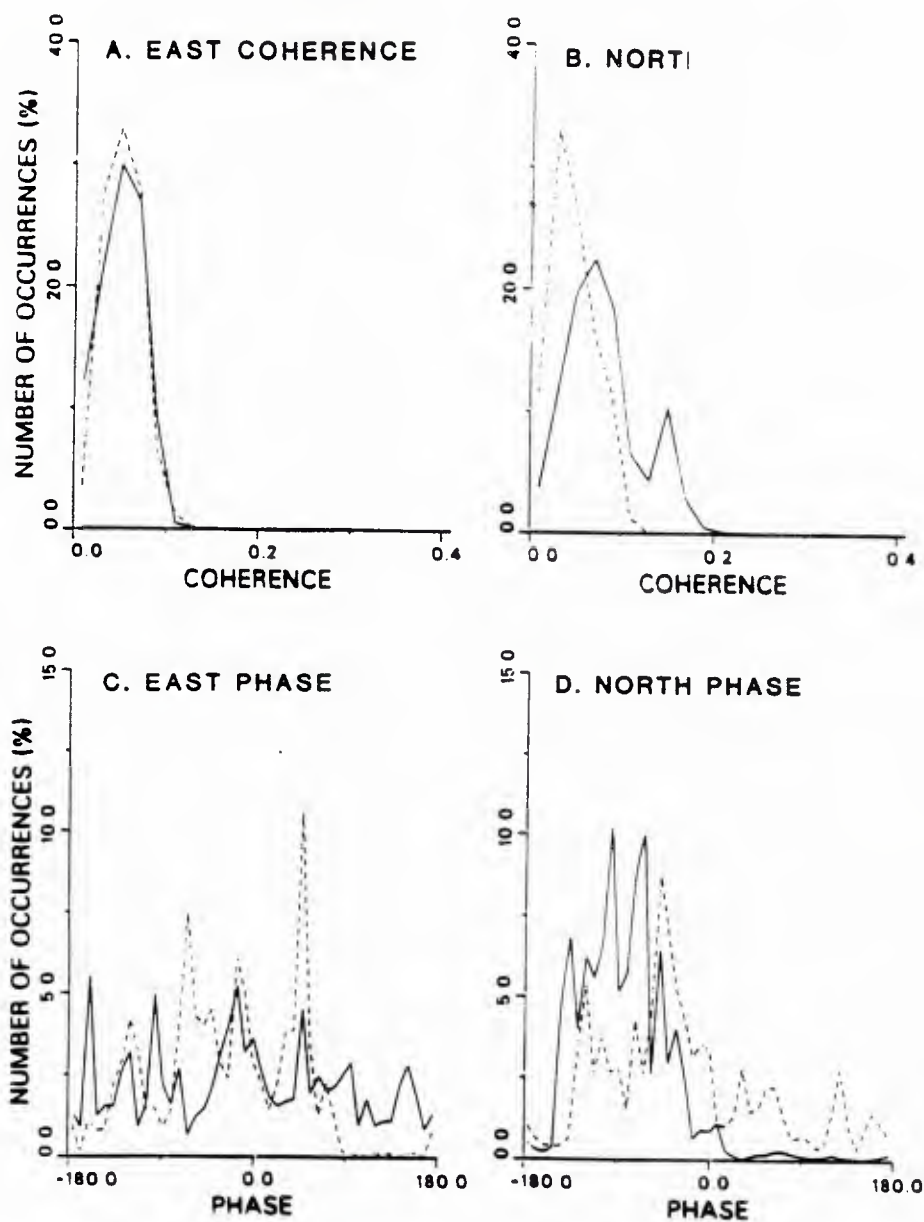


**Figure 2.4.** *Cross-spectra of Janus velocities.* Cross-spectra of horizontal and vertical components of the fluctuating Janus velocities are presented as histograms of coherence (top) and phase (bottom) for the East (right) and North (left) directions. Results for both observed data (solid lines) and artificial data (dashed lines) are shown. Cross-spectra are computed in the frequency band from 0.3 to 1.0 cph for 20 depth bins between 332 and 689 m. Cross-spectral estimates are smoothed in frequency and depth prior to computing coherence and phase, and the resulting coherence and phase values for all frequencies and depths within the ranges given above are included in the histograms.

due to scatterer migration is accomplished as a part of the wavenumber-frequency filtering used to separate the mean and fluctuating velocity fields. The migration signal appears in the vertical velocity as alternating upward- and downward-propagating disturbances which travel over  $\sim 300$  m vertically in roughly 2 hr, giving a "phase speed" of  $0.15 \text{ km hr}^{-1}$ . The high-pass, wavenumber-frequency filter used to separate the fluctuating velocities has a vertical wavenumber cutoff of 7 cpkm. Up to a maximum frequency of 1.0 cph (the limit of the high frequency band) this filter effectively rejects disturbances with phase speeds greater than  $\omega / k_z = 1.0 \text{ cph} / 7 \text{ cpkm} = 0.14 \text{ km hr}^{-1}$ . Residual errors in the Janus vertical velocity field due to migration are estimated to contribute less than  $0.01 \text{ cm}^2 \text{ s}^{-2}$  to a 12 hr average stress estimate, and decrease with increasing averaging time.

## 2.4 Results and discussion

### 2.4.1 Stress measurements

It is of interest to determine whether there is evidence of a depth-time average, vertically-acting stress in the high-frequency internal wave band during the experiment. To this end, cross-spectra from the full 17 day time series of fluctuating horizontal and vertical Janus velocity components are computed for each direction (East and North axes). Cross-spectra are computed in the high-frequency band (0.3 to 1.0 cph) for 20 depth bins between 332 and 689 m, averaged in frequency and depth, and recorded as coherence and phase values vs. frequency and depth for each direction. The cross-spectra of the artificial Janus components, representing a psuedo-velocity field with the same energy spectra as the actual data, but with true coherence known to be zero, are computed in a manner identical to that used for the actual data. The resulting coherence and phase values for all frequencies and depths of each direction are presented as histograms in Fig. 2.4.

The observed coherence distribution for the East direction (Fig. 2.4a) is virtually identical to that for the artificial data, indicating that none of the coherence values differ from those expected from statistical error in a velocity field where there is no true coherence. In other words, if the observed coherences were presented versus frequency for each depth and confidence limits were chosen based on the cumulative distribution of the artificial data, the number of observed coherence values above the confidence limit would be no more than that expected from random chance. For distributions of observed and artificial coherence as similar as those in Fig. 2.4a, the above argument would remain true no matter what confidence level is chosen. This, of course, implies that the net stress over the 17 day averaging interval cannot be distinguished from zero. The phases for the East direction (Fig. 2.4c) show a roughly uniform distribution between plus and minus  $180^\circ$ , to be expected when the coherence is not significant.



The observed coherence distribution for the North direction (Fig. 2.4b) shows a clear peak at a coherence of about 0.15. Coherence values within this peak are significant at the 99 % confidence level based on the distribution of the artificial data. This indicates a relationship between the Janus horizontal and vertical velocity components for the North direction, but the interpretation of this relationship in terms of stress depends on the values of phase. The phase distribution (Fig. 2.4d) of the actual data is strongly skewed towards negative values. To determine which part of the phase distribution is associated with the significant coherences, coherence-phase pairs were selected for only those values of coherence contributing to the peak in Fig. 2.4b. The resulting phase distribution is shown in Fig. 2.5. The approximate 95 % confidence interval for phase, based on the Fisher F distribution with 2 and 400 degrees of freedom and an estimated coherence of 0.15 [ Jenkins and Watts (1968), eq. (10.3.21) ], is indicated in the figure. Evaluation of the significance of the observed phases using this confidence interval shows that only the phases for the 653 m depth interval can be considered different from  $-90^\circ$  at the 95 % level of confidence.

Coherence-phase pairs which come from different depth bins within the 350 m depth interval are shown in Fig. 2.5 with different symbols. The phases appear strongly discretized; remaining stable over a range of coherence values for a given depth, then jumping to a new value for a different depth, forming horizontal "stripes" in the plot. The changes in phase are not progressive (i.e. monotonic) with changing depth, and in some cases, multiple stable values are seen for a single depth. The "stripiness" in Fig. 2.5 is somewhat misleading since the coherence-phase pairs in the plot are not independent. This is the result of smoothing (averaging without decimation) of the cross-spectra in frequency prior to computation of coherence and phase. Plotting only the independent points would collapse the observations to roughly two coherence-phase pairs for each depth bin. However, the fact that the dependent points are "smeared" in coherence, but not in phase, remains of interest. It is found that the coherence-phase pairs which make up the stripes in Fig. 2.5 come from coherence peaks in a variety of frequency bands at different depths which have no clear relationship to one another. Multiple coherence peaks are found for certain depths, resulting in multiple-valued phases for a given coherence at that depth. The stripiness in the figure results from a high degree of stability in the phase values for each coherence peak.

The small, but significantly non-zero coherence in Fig. 2.4b with phases near  $-90^\circ$ , as shown in Fig. 2.4d and Fig. 2.5, indicates a tendency for an out-of-phase relationship between horizontal and vertical velocity. This result suggests that the coherence peak in Fig. 2.4b is due to the presence of mode-like internal waves with very little net momentum transfer and very small net stress. Thus, despite the significant coherences between the horizontal and vertical Janus velocities, the net stress over the 17 day data record for the North direction is small. More careful consideration of the distribution of coherence vs. frequency, and the distribution of phase vs. depth, gives no indication that the "modes" are the result of wave groups of a particular wavenumber and frequency which may have reflected off of the sea surface, for example, to form a standing wave. Instead, it must be assumed that the observed coherences come from the complex superposition of mode-like waves spread throughout the high



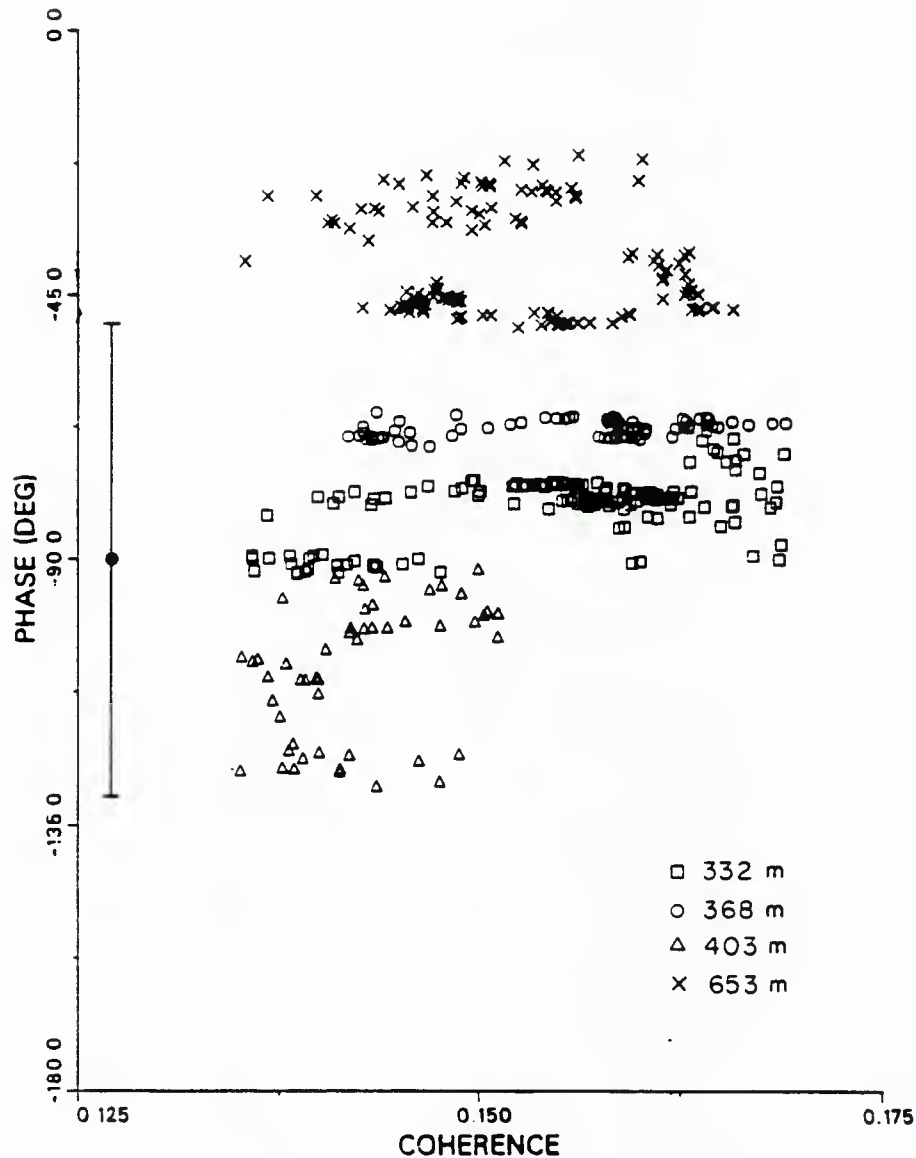


**Figure 2.5.** *Phase distribution for the North direction.* Coherence-phase pairs computed from the cross-spectra of observed horizontal and vertical components of the fluctuating Janus velocities for the North direction are shown. Data pairs are plotted only for coherences between 0.13 and 0.17 which define the peak of significant coherence in Fig. 2.4b. Each symbol represents a different depth interval according to the key given above. Only a subset of the available depth intervals is represented since not all depth intervals contain significant coherences. The coherence and phase values are computed from cross-spectra which are averaged in depth and smoothed (averaged but not decimated) in frequency, resulting in coherence-phase pairs which are not independent, and accounting for some of the "smearing" seen in the plot. The approximate 95 % confidence interval for phase is indicated in the figure.

wavenumber, high frequency band.

The results of the cross-spectral analysis show that the net stresses for the duration of the experiment are small. Not surprisingly, the 17 day mean values of stress computed in the time domain using (2.13) and (2.14) are not significantly different from zero using 95 % confidence limits based on the statistical error (2.19). However, these small mean values could be made up of a succession of stress "events" on shorter time scales which are large enough to be significant individually, but tend to cancel in the mean. To investigate the nature of stress variability on short time scales, stresses were averaged over intervals from several hours to many tens of hours, and the resulting stress variability compared to that expected from statistical error for each averaging interval.

Stresses for the North and East directions are estimated according to (2.13) and (2.14) for each of the 20 depth bins between 332 and 689 m using temporal averaging intervals of 5.6, 12, 20, 40, and 76 hr. The variability of the stress for the different averaging intervals is characterized by computing the mean-square value of the averaged stress for each depth bin. The depth-averaged, root-mean-square (rms) stress for each averaging interval, computed from the square root of the 20 depth bin average of the mean-square stress, is shown in Fig. 2.6. Also plotted in Fig. 2.6 is a curve representing the statistical error for the covariance, computed from (2.19) for values of  $N$  representing averaging times from 1 to 100 hr. The statistical error  $\sigma_{\hat{c}}$  represents the variability expected in the covariance estimate (2.17) when each observation  $\hat{C}$  is a realization of a random process where the true value of the covariance is equal to zero, and is the most probable value of the observed rms stress if the true stress is zero. The depth-averaged values of rms stress for all temporal averaging intervals fall close enough to the  $\sigma_{\hat{c}}$  curve that the observed stress variability, in the depth-averaged sense, is not significantly different than that expected from statistical error when the true stress is zero. This is taken to mean that most stress values are not large enough to be considered significantly different from zero at any reasonable level of confidence, regardless of the averaging interval.

Realizing that the rms value may not fully characterize the observed stress distribution, some care is needed in interpreting these results. The observed stress may contain occasional bursts of relatively large magnitude which result in "tails" on the depth-time average stress distribution. Thus, it is possible that there are isolated periods in depth and time where the observed stresses are large enough to be considered significantly different from zero. This issue could be explored, for example, by comparing the distribution of the observed stresses for selected depth and/or time intervals to the distribution computed from the artificial stresses. This technique would represent the time-domain equivalent of the comparison of actual and artificial coherence and phase distributions described above. A similar, though perhaps less sensitive, assessment of the significance of observed stresses can be made by comparing the observed stresses as a function of depth and time to the expected statistical error for a given level of confidence. Only the latter technique is employed in this study.

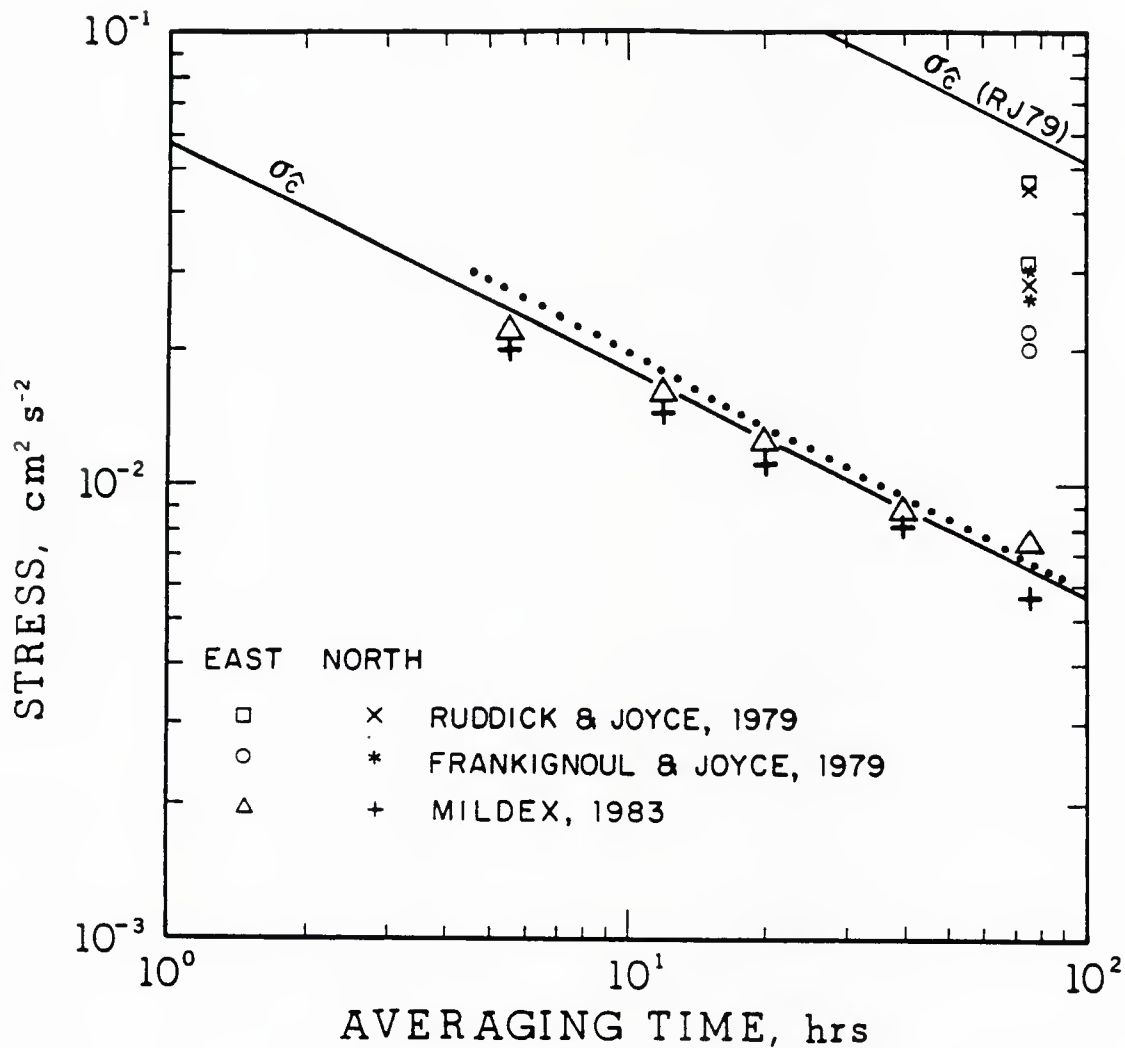


**Figure 2.6.** *Root-mean-square stress vs. averaging time.* Expected statistical error in stress estimates for a true stress of zero (lines) is compared to observed values of rms stress for several experiments (symbols). The upper solid line gives the statistical error reported by Ruddick and Joyce (1979). The lower solid line gives the statistical error  $\sigma_e$  for this study (MILDEX) computed from (2.19) for averaging intervals from 1 to 100 hr. The dotted line gives the statistical error for MILDEX computed from artificial data, which accounts for a degree of sample-to-sample dependence similar to that in the actual data. Values of depth-averaged rms stress observed during MILDEX for temporal averaging intervals of 5.6, 12, 20, 40, and 76 hr are shown for the East and North directions. Rms values of 75 hr average stresses reported by Ruddick and Joyce (1979) and Frankignoul and Joyce (1979) are also shown.

Observed 12 hr average stresses for the East and North directions are presented as a function of depth and time in Fig. 2.7 for the full 17 day data analysis period. The plot shows depth intervals where stress variability is relatively large for long periods of time (e.g. 332 to 385 m), times when variability is large over many depths (e.g. day 315 to 317 for the East component), and depth-time intervals where relatively large stresses are seen in both components (e.g. 475 to 546 m near the beginning of day 304). A typical "large" value of 12 hr average stress has magnitude of about  $0.025 \text{ cm}^2 \text{ s}^{-2}$ , which can be considered significantly different from zero at the 85 % level of confidence based on (2.19). Although these stresses are not significant at a high level of confidence, if they are strongly related to mean-flow parameters it is possible that stress vs. mean flow correlations can still be detected. Potential relationships between stress and mean-flow shear, and between stress divergence and mean-flow acceleration are investigated in the next section.

The lack of observed stresses which are significant relative to statistical error in this study (MILDEX) is a result similar to that of previous studies, but here the values of statistical error for the measurements are substantially less. For equal averaging intervals, the statistical error for MILDEX is about an order of magnitude less than that reported by Ruddick and Joyce (1979). A curve giving the value of statistical error reported by Ruddick and Joyce (1979) is shown in Fig. 2.6 along with their observed rms stresses for a 75 hr averaging interval, computed from the data presented by Ruddick (1977). Observed rms stresses for the study of Frankignoul and Joyce (1979), which has statistical errors similar to that of Ruddick and Joyce (1979), are also shown.

The primary reason for the improved statistical precision in MILDEX is that the fluctuating part of the velocity field has been separated from the mean part in both vertical wavenumber and frequency. In previous studies, this separation has only been done in frequency. Formally, the result of including vertical wavenumber filtering in separating the fluctuating part of the velocity field is that the variance of the horizontal and vertical velocities contributing to the statistical error in (2.19) is reduced, and the statistical precision of the covariance estimate (2.17) is increased. Conceptually, the *desired* separation for the fluctuating part of the velocity field is not straightforward. If the high-vertical wavenumber, high-frequency portion of the wave field is responsible for the majority of the vertically-acting internal wave stresses, then the technique used here more clearly separates the stress-carrying waves from the "background", where the background includes not only the mean flow, but also other portions of the internal wave field which may contribute very little to the stress. In other words, the proper scale separation for the fluctuations will decrease the total variance of the stress estimate by discarding the portion of the wave field which supports no stress, but the stress "signal" will not be reduced if all of the stress carrying waves are included. Thus, the signal-to-noise ratio is increased and the sensitivity of the measurement is enhanced. An improper scale separation, however, may result in discarding the signal of interest entirely. It is possible that a scale separation different than that used in this study would increase the sensitivity of the measurements, but there is little information available to determine what the "proper" scale separation would be.



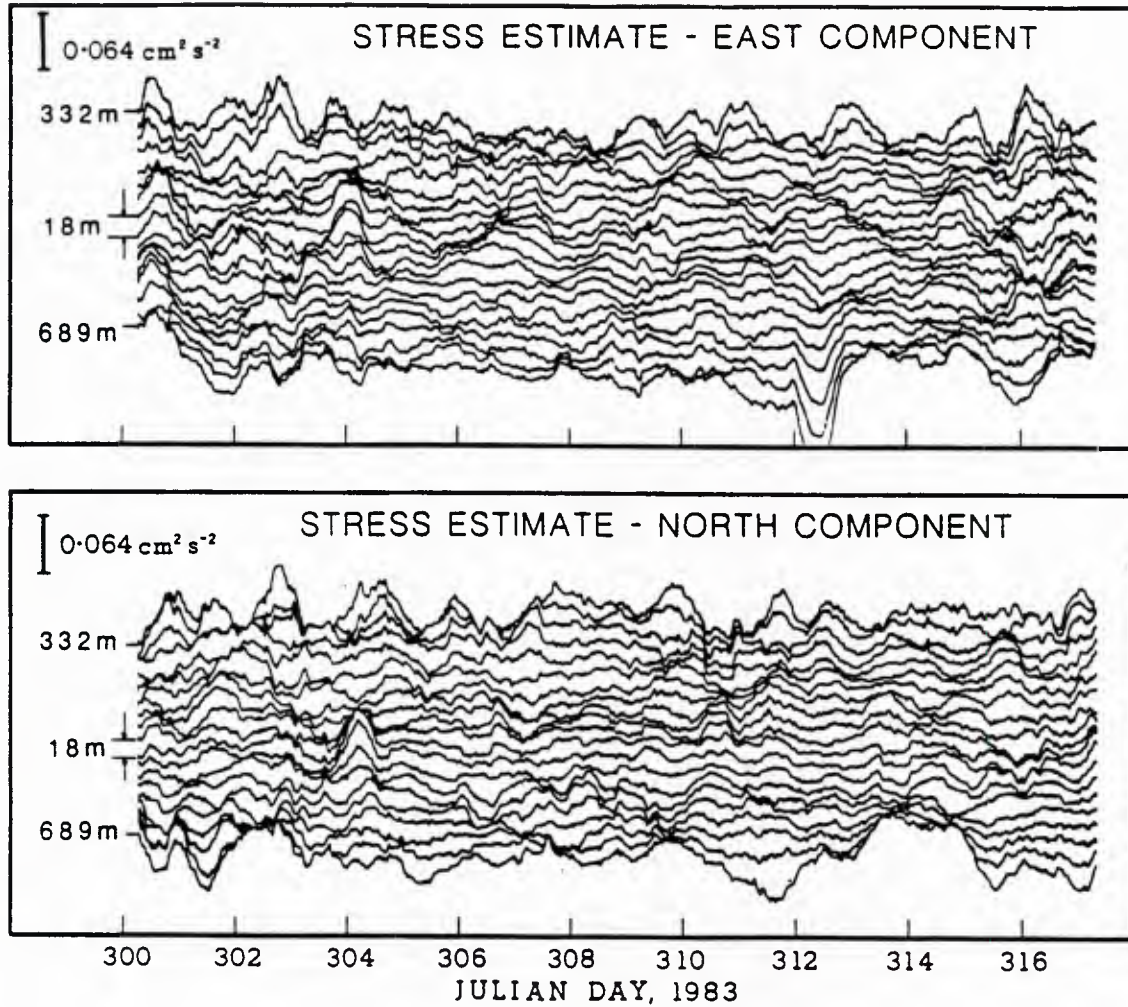


**Figure 2.7.** *Stress estimate components.* Stress estimates for East and North directions are shown vs. depth and time for the full 17 day analysis period. Stresses are computed according to (2.13) and (2.14) for each depth bin using a 48 min averaging interval, and then smoothed (averaged but not decimated) over 54 m and 12 hr prior to plotting. The scale bar has magnitude  $0.064 \text{ cm}^2 \text{ s}^{-2}$  and represents plus and minus two standard deviations of the statistical error computed from (2.19) for a 12 hr average. Large excursions of the stress estimates at the deepest depths from day 311 to 316 are due to noise.

### 2.4.2 Relationship of stress to the mean flow

A potential relationship between internal wave stress and mean-flow shear suggested by (2.6) is explored by computing the cross-spectra of the two fields in the low frequency band (0.01 to 0.10 cph) over the subset of depths for which stress estimates are available (332 to 689 m). A depth-time array of "artificial" stress, formed from the time series of artificial Janus velocity described in Sec. 2.3.3, is utilized in assessing the significance of the observed coherence between stress and shear in the same manner that the artificial Janus velocities were used to assess the significance of observed component coherences. Coherence and phase values computed from both observed stress vs. observed mean shear, and artificial stress vs. observed mean shear over the range of frequencies and depths given above are presented as histograms in Fig. 2.8. The similarity of the coherence distributions for observed and artificial data in both directions, and the corresponding uniformity of the phase distributions, indicates that there is no detectable coherence between internal wave stresses and mean-flow shear.

It has been suggested by Jacobs and Cox (1987) that negative results for stress vs. shear coherence could be due to an improper choice of reference frames. Using data from numerical models of high-frequency, high-wavenumber internal waves propagating through a background shear field, they show that the net stress may be largest in a reference frame rotating with the low-frequency (near-inertial) shear. This stress effectively cancels out when averaged in a geographic reference frame over many cycles of the shear. The issue of a rotating "stress vector" related to rotating near-inertial shears in MILDEX was addressed qualitatively by computing the angle of the stress vector formed by the two components of observed stress (c.f. Fig. 2.7) to the mean-flow shear vector for an averaging time of 5.6 hr, roughly  $1/4$  of an inertial period. No apparent relationship was seen between the two angles. It is possible that a careful quantitative analysis would reveal a more subtle relationship, but the existence of stress vs. shear coherence during MILDEX, even in a rotating reference frame, appears unlikely. It should be noted, however, that the energy at near inertial frequency during MILDEX was substantially lower than that seen in other open ocean experiments (Pinkel, et al., 1987). Thus the inertial shears may be too weak to produce a detectable stress vs. shear relationship of the type proposed by Jacobs and Cox (1987).

The possibility of a stress vs. mean flow interaction of a different type, where stresses are not parameterized as an eddy viscosity, is investigated by computing the cross-spectra of stress divergence and mean-flow "geocentric" acceleration (e.g.  $\partial_t \bar{u} - f \bar{v}$ ). A relationship between these two fields would arise from a momentum balance such as (2.15) and (2.16). Although it is not anticipated that this is a primary momentum balance in the ocean, there are indications from numerical and laboratory studies (e.g. Thorpe 1981) that such a balance could exist in a region of large stress divergence. Cross-spectra of stress divergence and mean-flow acceleration are shown in Fig. 2.9 using a computation and presentation scheme analogous to that used for the cross-spectra of stress and shear described above. Peaks in the coherence distribution for the

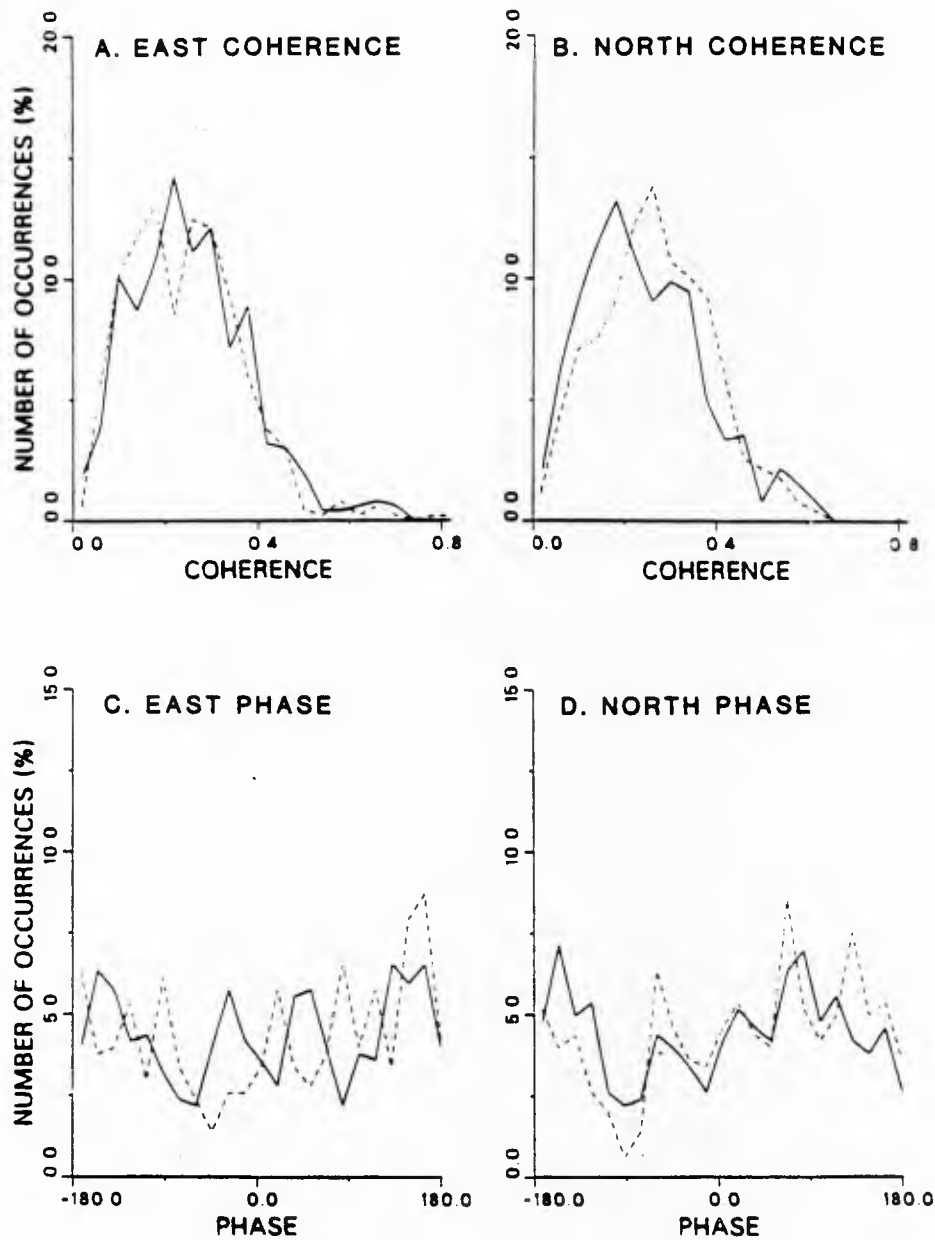


**Figure 2.8.** *Cross-spectra of stress vs. mean-flow shear.* Cross-spectra of vertically-acting internal wave stress and mean-flow shear are presented as histograms of coherence (top) and phase (bottom) for the East (right) and North (left) directions. Results for both observed data (solid lines) and artificial data (dashed lines) are shown. Cross-spectra are computed in the frequency band from 0.01 to 0.1 cph for 20 depth bins between 332 and 689 m. Cross-spectral estimates are smoothed in frequency and depth prior to computing coherence and phase, and the resulting coherence and phase values for all frequencies and depths within the ranges given above are included in the histograms.



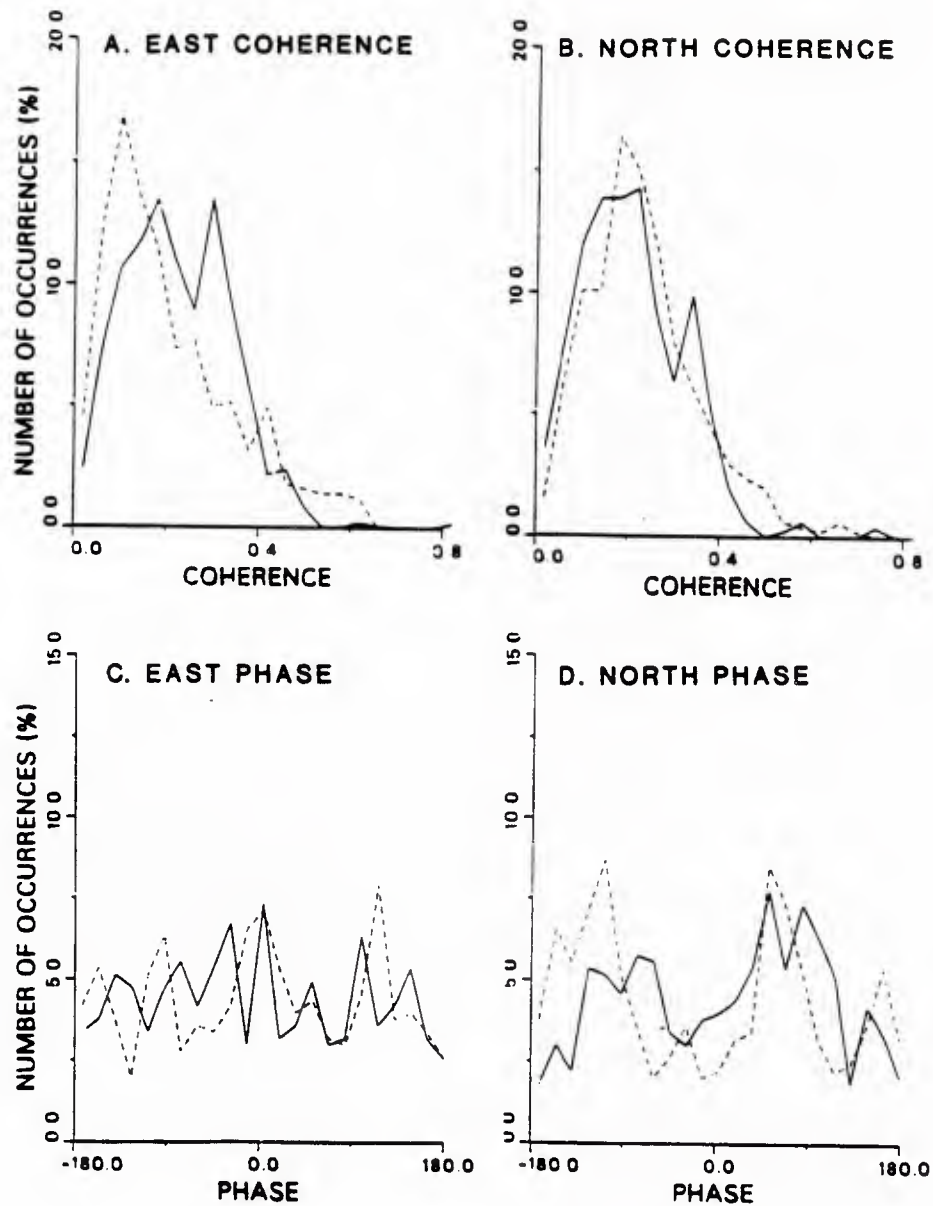


**Figure 2.9.** *Cross-spectra of stress divergence vs. mean-flow acceleration.* Cross-spectra of stress divergence and mean-flow acceleration are presented as histograms of coherence and phase for the East and North directions. Description is the same as that for Fig. 2.8.



observed data in both East and North directions (Fig. 2.9a,b) are seen at a coherence value of about 0.35. Based on the distributions of the artificial data, these coherences can be considered significant at the 75 % level of confidence. The phase distributions (Fig. 2.9c,d) are relatively uniform, and considerable scatter in phase remains even after restricting coherence-phase pairs to the regions of significant coherence (Fig. 2.10).

The coherences which make up the distributions observed in Fig. 2.9 are separated into individual depth intervals and plotted as a function of frequency in Fig. 2.11. Several depth- and frequency-isolated coherence "bumps" are seen for both the East and North components. There is some tendency for the bumps to align in frequency, appearing and disappearing with changing depth. The data in Fig. 2.11 have been smoothed in such a way that the resulting points are equally spaced in log frequency, but the actual number of independent data points is very small for the bumps at the lowest frequencies compared to those at higher frequencies. Hence, the primary contribution to the peaks in the coherence distributions shown in Fig. 2.9 comes from the bumps in Fig. 2.11 which fall roughly between 0.04 and 0.07 cph. This suggests the possibility that the observed coherences are due to an interaction of the near-inertial portion of the mean flow with internal waves in the high-frequency band.

It is found that the typical values of mean-flow geocentric acceleration in the near-inertial band are of order  $1 \times 10^{-4} \text{ cm s}^{-2}$  compared to typical magnitudes for stress divergence of only  $1 \times 10^{-5} \text{ cm s}^{-2}$ . Thus, although no information about cause and effect is contained in the coherence measurements, it is implausible that the stresses are "driving" the mean flow since the stress could account for at most a tenth of the mean-flow acceleration. It is more likely that the mean flow is modulating the high frequency wave field, causing local convergence and divergence of stresses.

## 2.5 Chapter summary

Theoretical investigations of internal gravity waves have shown that a propagating wave group exerts a stress on the surrounding fluid which can be interpreted as a vertical flux of horizontal momentum. The generation, propagation, and dissipation of internal wave groups may be an important factor in the distribution of momentum in the ocean. A technique to measure the vertically-acting Reynolds stresses,  $\overline{u'w'}$  and  $\overline{v'w'}$ , in a fluctuating oceanic velocity field using a multi-beam Doppler sonar has been presented. The Doppler sonar technique improves on previous stress measurements by simultaneously measuring contributions from horizontal (u,v) and vertical (w) velocities, thereby eliminating errors inherent in estimating w from temperature measurements using an approximate heat equation. Thus, the results in this experiment are associated with smaller measurement errors than those of previous studies.

The Doppler sonar used in this study provides continuous profiles of velocity over a substantial depth range ( $\sim 1000 \text{ m}$ ) which have several advantages over single-depth velocity measurements. First, the mean-flow shear field

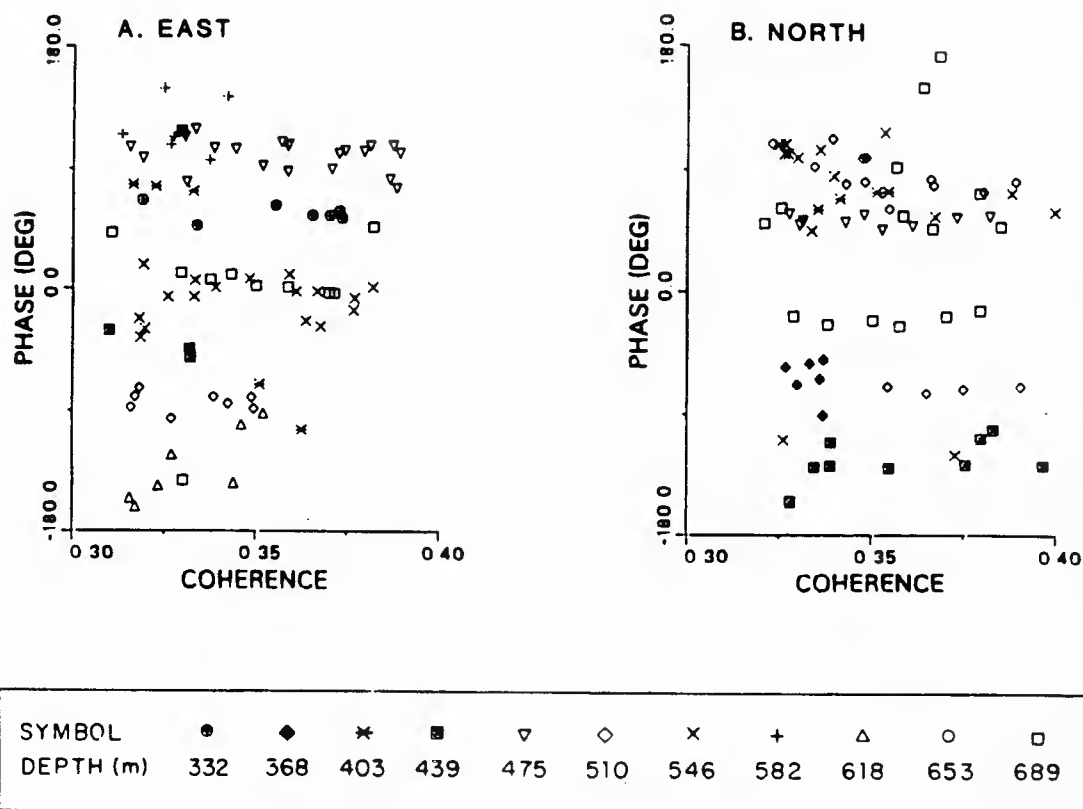


**Figure 2.10.** *Phase distribution for stress divergence vs. mean-flow acceleration.* Coherence-phase pairs computed from the cross-spectra of stress divergence and mean-flow acceleration for the East (left) and North (right) directions are shown. Data pairs are plotted only for coherences which define the peaks in the coherence distributions in Fig. 2.9. Each symbol represents a different depth according to the key above. Only a subset of depth intervals is represented in the plots since not all depths contain significant coherences.

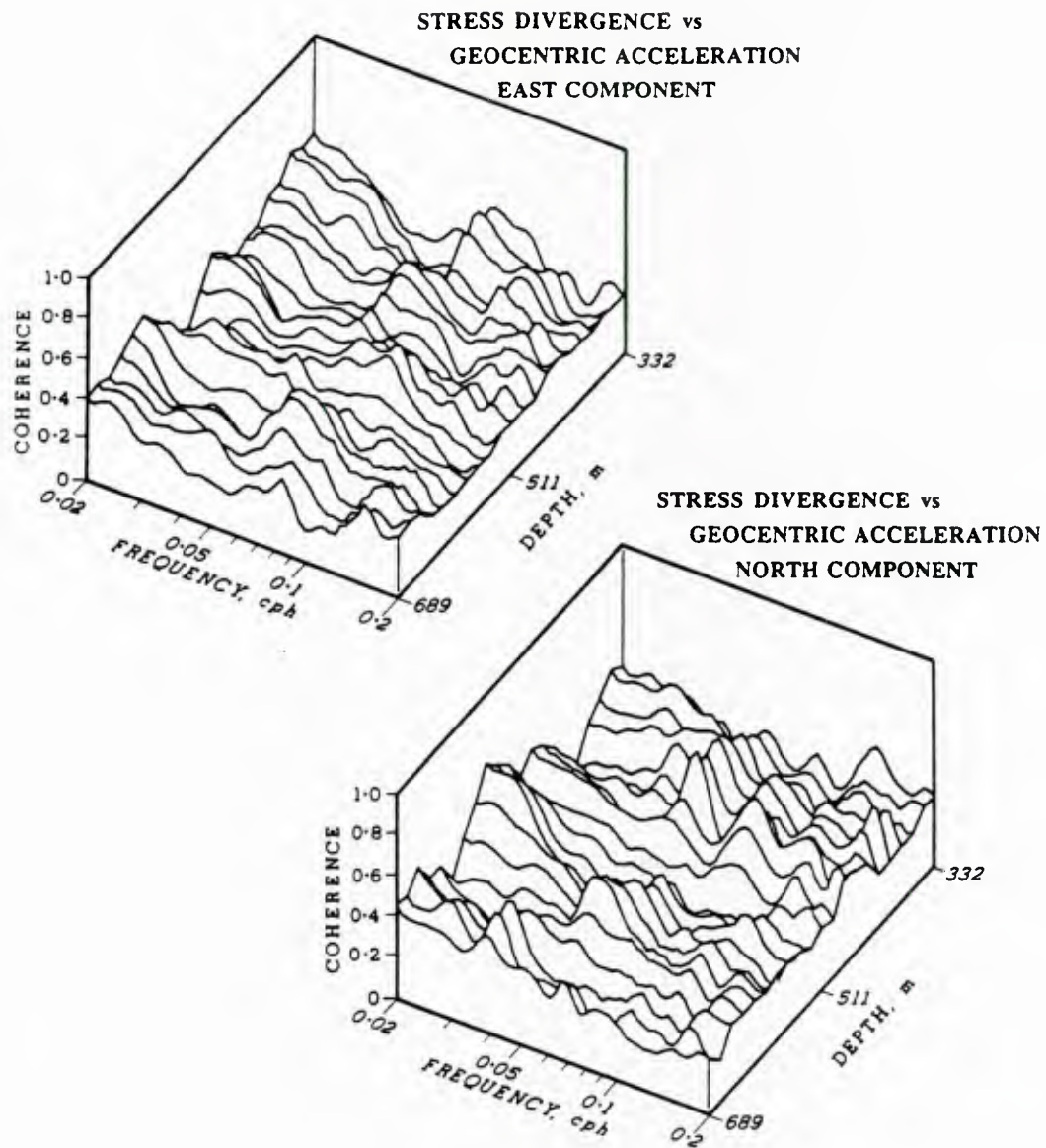


**Figure 2.11.** *Coherence for stress divergence vs. mean flow acceleration.* The coherences which make up the observed data distributions in Fig. 2.9 are shown vs. depth and frequency for the East and North directions. Coherences have been averaged over logarithmic intervals in frequency to improve the appearance of the display.

is better resolved in depth from the Doppler profiles than from vertically-separated current meter measurements. Second, the stress divergence can be computed and compared directly to the mean-flow acceleration. Third, the mean and fluctuating parts of the velocity field can be separated in both vertical wavenumber and frequency. The ability to make a more restrictive separation of the fluctuating part of the velocity field results in a reduction of the statistical error associated with the stress measurements. If the high-vertical wavenumber, high-frequency part of the wave field is responsible for the majority of internal wave stresses, then this technique can be considered to improve the sensitivity of the measurements.

The stress measurement technique is applied to a 17 day time series of Doppler sonar data collected from the R. P. FLIP during October and November of 1983. Results show that the net stresses over the full 17 day data analysis interval are small compared to statistical error and cannot be distinguished from zero. The lack of significant long-term average stresses is similar to the results of previous investigations, but the more restrictive scale separation for the fluctuating part of the velocity field in this study results in improved statistical precision, and allows more restrictive upper bounds to be put on the stress values. For a 75 hr averaging interval, the upper bound on vertically-acting internal wave stresses found during MILDEX is approximately  $0.006 \text{ cm}^2 \text{ s}^{-2}$ . This value is roughly an order of magnitude less than the upper bounds found from previous measurements.

Although no significant long-term stresses are found in this study, a small, but significant coherence between horizontal and vertical velocity is observed with associated phase values near  $-90^\circ$ . The results are consistent with a high-frequency internal wave field which tends to be dominated by mode-like rather than ray-like waves, and which, on average, exhibits a high degree of vertical symmetry. The existence of a high degree of vertical symmetry in the high frequency internal wave field for relatively long averaging intervals (weeks to months) has been demonstrated by other open ocean measurements of the internal wave field (e.g. Müller, et al., 1978) and sheds no new light on the problem of internal wave momentum transfer.

In an effort to detect more localized stresses which may occur on short space and time scales, the variability of the observed stresses was computed for 18 m depth intervals and time intervals between 5 and 76 hr. It is found that the observed stresses, in a depth-averaged sense, cannot be considered significantly different from zero, regardless of the temporal averaging interval. A careful examination of the depth-time array of 12 hr average stress values shows several isolated depth-time intervals where stresses are of marginal significance (significant at low levels of confidence). These marginally significant stresses are of interest to the extent that they are related to the mean flow.

The investigation of a potential relationship between stress and mean-flow shear resulting from a wave-induced vertical eddy viscosity was undertaken in a manner which included the contribution of near inertial motion as a part of the mean flow. This involves a definition of the mean flow considerably different than that used in previous observational investigations, but is consistent with more recent theoretical studies. The results of coherence computations for



stress vs. mean-flow shear in the frequency band from 0.01 to 0.10 cph indicate no relationship between stress and shear during this study. There are several possible explanations for this result, one of which is the relative lack of near-inertial shear during the experiment. Another stress vs. mean flow relationship was considered by computing the coherence between stress divergence and mean-flow acceleration. The results indicate low, but significant coherences with phases which show a large degree of scatter. No clear indication of the physical mechanism which may be responsible for this result is found, but the possibility of internal wave stresses driving the mean flow is unlikely based on the relative magnitudes of the stress divergence and the mean-flow acceleration.

The principal result of this study is the lack of observed Reynolds stresses in the high-vertical wavenumber, high-frequency internal wave band which can be considered significantly different from zero, despite the use of a more restrictive scale separation for the internal wave fluctuations, and the investigation of stresses on several different time scales. It is possible that a different approach to the separation of wave and mean-flow velocities would improve the sensitivity of the measurements to small stresses, but the guidelines to be followed in developing a successful approach are not clear. The proper choice of location for an experiment designed to observe internal wave stresses may be as important as the choice of separation scales for the wave field. The few observations to date have been from the open ocean, where internal wave generation and dissipation mechanisms may be too weak, or too intermittent, to result in detectable stresses.

## CHAPTER III

### CHARACTERIZATION OF THE PATTERNS OF DIURNAL MIGRATION USING A DOPPLER SONAR

#### 3.1 Introduction

Sound scattering layers have been observed in many areas of the world ocean since the 1940's. Many of these deep scattering layers (DSL's) are observed to execute diurnal migrations, presumably regulated by changes in light intensity (Clarke, 1971; Kampa, 1971). A migrating DSL moves to shallower water as the sub-surface light level decreases (sunset) and returns to deeper water as light levels increase (sunrise). Typical DSL's have daytime depths of 200 to 600 m, and migrate vertically to depths above 100 m at rates as high as 1 to 10 cm s<sup>-1</sup>. Extensive research on the nature of the DSL (e.g. Farquhar, 1971; Anderson and Zahuranec, 1977) has revealed that the acoustic signature of the layer is due to marine organisms which swim vertically through the water column. The earliest observations of DSL's were made with echosounders operating in the 1 to 20 kHz frequency range, where the acoustic return is likely to be caused by resonant scattering from the swim bladders of mesopelagic fishes (Hersey and Backus, 1962), or from other gas-bearing organisms such as siphonophores (Barham, 1963; 1966). Later observations using echosounders in the 50 to 500 kHz frequency range suggested that scattering at high frequencies was non-resonant, and caused primarily by various zooplankton such as euphausiids (Bary and Pieper, 1971), pteropods (Hansen and Dunbar, 1971), and copepods (Castile, 1975).

Previous investigators using low-frequency echosounders have typically characterized the patterns of DSL migration by comparing scattering strength profiles for day and night, or by presenting echograms of backscattered intensity over a 12 to 24 hr period. Isolated day vs. night scattering strength comparisons (Chapman, Bluy, and Adlington, 1971; Friedl, Pickwell, and Vent, 1977) show the depth dependence of scattering strength, and may indicate regions of high day vs. night variability. However, unless several day vs. night comparisons are made in the same location, the significance of the observed differences in scattering strength is unclear. Continuous echograms of backscattered intensity (Dunlap, 1971; Bradbury *et al.*, 1971) can provide an intriguing look at DSL migration patterns, but typically only qualitative information for a single 24 hr period is presented. Repeated observations over several diurnal cycles have been made (Percy and Mesecar, 1971; Kinzer, 1971; Greenlaw and Percy, 1985) but most results have not been analyzed in such a way that the persistence and variability of DSL migration patterns can be quantified.

This chapter presents a characterization of DSL migration based on high-frequency (67 kHz) acoustic backscatter measurements. Three unique elements combine to provide a description of the DSL which has previously been

unavailable. First, the sonar used in this study operates over a depth interval from approximately 60 to 1200 m, whereas most previous high-frequency acoustic backscatter measurements have been limited to the upper 300 m (e.g. Bary and Pieper, 1971; Hansen and Dunbar, 1971; Castile, 1975; Holliday and Pieper, 1980; Greenlaw, 1979). Second, the sonar is designed as an acoustic Doppler current profiler, rapidly sampling both magnitude and phase of the returned echo, so that the Doppler shift, and hence the velocity, of the scatterers can be directly estimated. Vertical migration rates estimated from intensity data are compared to scatterer vertical velocities measured using the Doppler technique. Third, measurements of backscattered intensity and scatterer velocity are available at 6 min intervals over a period of 13 days, allowing estimation of simple statistics (mean and variance) of the daily migration cycle. The mean values emphasize the persistent patterns of the diurnal cycle over many days, while the variance identifies portions of the cycle which show large relative variability from one day to the next.

### 3.2 Methods

Measurements of backscattered intensity and Doppler velocity were made using a multi-beam Doppler sonar mounted on the Research Platform FLIP of the Scripps Institution of Oceanography (SIO). Sonar data were collected continuously over a 17 day period from 27 October through 12 November, 1983, while FLIP drifted within a  $1^\circ$  square area centered on  $34^\circ$  N,  $126^\circ$  W (Fig. 1.2). A 13 day period from 28 October to 9 November was selected for the analysis presented in this chapter. This segment represented the longest continuous period where far-range noise levels were low enough that intensity features at the maximum ranges could be consistently identified.

The instrument used in this study is a high-power, narrow-beam Doppler sonar developed at the Marine Physical Lab (MPL) of SIO. The MPL Doppler sonar system is designed to provide measurements of the upper ocean velocity field by transmitting a short pulse of acoustic energy which insonifies a small volume of the ocean interior, and estimating the Doppler shift of the back-scattered signal. The insonified volume can be expressed as a function of beam width, pulse duration  $T_p$ , and range  $r$  along the beam axis as (Urlick, 1983)  $\Delta V = \frac{1}{2} (c T_p \Psi r^2)$  where  $c$  is the speed of sound and  $\Psi = 0.001$  steradian is the equivalent solid angle beam width for the MPL Doppler sonar. The insonified volume varies from  $360 \text{ m}^3$  at 100 m depth to  $36000 \text{ m}^3$  at 1000 m depth. The system has been described extensively by Pinkel (1981; 1983a). The configuration of the system for the present experiment is discussed in Sec. 1.3.3 and summarized in Table 1.1. Only a brief review is given here.

The Doppler sonar system consists of 20 transducer "panels", each approximately 0.36 m by 0.61 m in size, arranged to form 6 separate sonars with beams which point in different directions (Fig. 1.7). The half power beam width of a beam composed of a single panel is about  $2^\circ$ . During operation each sonar

sends out a pulsed transmission of duration 30 ms every 2 s. The returned echo is sampled at a rate of 400 Hz. The system gain is stepped-up by 20 dB at 750 ms after transmission to accommodate the large dynamic range of the signal (see Fig. 3.1a). For each transmission, the complex covariance of the backscattered signal is computed as a function of range. The covariance data provides the basis for the estimation of both the intensity and the mean Doppler shift of the signal (Sec. 1.3.3). Intensity and velocity data are averaged to 6 min time intervals during the post-processing phase.

Two of the six sonars point horizontally into the mixed layer from a depth of 36 m, and are not of interest for this study. The remaining four sonars point downward from a depth of 38 m at an elevation angle of  $\theta_o = -52.5^\circ$ , and provide profiles of intensity and velocity from approximately 60 m to 1200 m depth. The four downward-slanting sonars operate as two pairs, with one pair having a center frequency of 67 kHz, and the other 71 kHz. Only data from the 67 kHz pair is presented in this chapter.

No biological samples were taken during the experiment. Thus, the sources of backscattered energy can only be inferred from the results of previous studies. Several investigations (e.g. Greenlaw, 1977; 1979; Holliday and Pieper, 1980) have used fluid sphere models (Anderson, 1950; Johnson, 1977) to predict the acoustical scattering properties of marine organisms. Greenblatt (1981) reviews these techniques, and provides an expression for the percent of backscattered energy which comes from organisms of size  $a_o \leq a \leq a_1$ , where  $a$  is the equivalent spherical radius. Using this expression (Greenblatt, 1981, Eq. 6) it is estimated that in the present study the majority of scattering comes from organisms with equivalent spherical radius  $0.1 \text{ cm} \leq a \leq 0.4 \text{ cm}$ , corresponding to approximate organism lengths of  $0.6 \text{ cm} \leq L \leq 2.4 \text{ cm}$  using  $L = 6a$  (Greenblatt, 1981). Organisms in this size class which may be the sources of backscattered energy include large zooplankton such as euphausiids, amphipods, pteropods, and copepods, and small nekton such as myctophid fishes and squid.



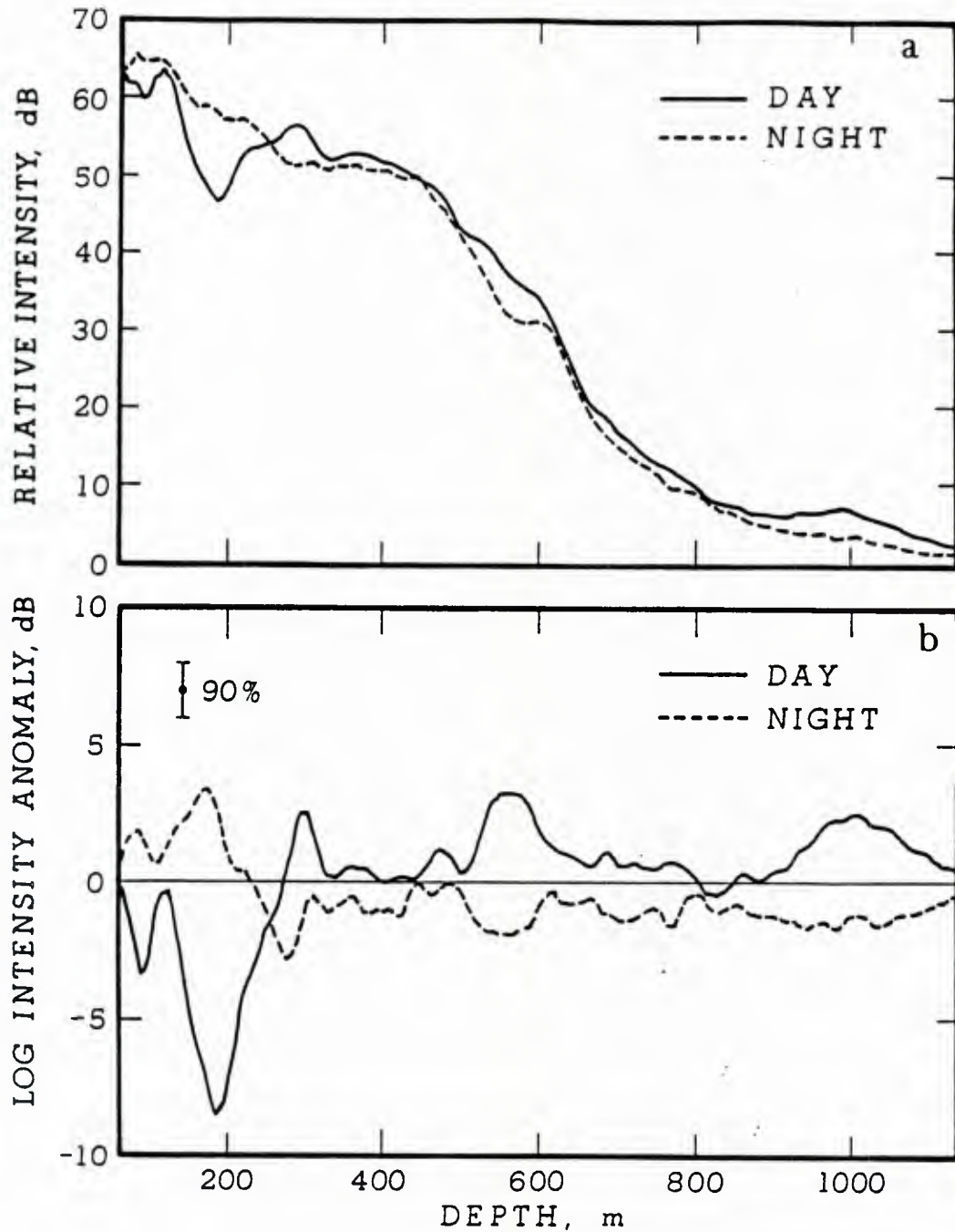


**Figure 3.1.** *Intensity profiles: Day vs. night.* Profiles of intensity (a) and log intensity anomaly (b) are shown. Data represent 13 day average of profiles selected within 6 min of noon (solid line, day) and midnight (dashed line, night) of each day. The log intensity anomaly is formed from the difference between the average of the log intensity profile at a given time (noon or midnight) of each day and the 13 day mean log intensity profile. The error bar in the lower panel represents the 90% confidence interval for the log intensity anomaly.

### 3.2.1 Intensity data

Intensity data are presented for one of the downward-slanting sonars, which has an operation frequency of 67 kHz. Results for all four downward slanting sonars are qualitatively similar. The returns from a pulsed sonar can be separated into "range time" and "pulse time" (Appendix B). The range-time increment  $\tau_r$  is the interval between samples of the echo from a particular pulse, and for the purposes of this discussion can be considered equal to the pulse duration. The downward-slanting sonars effectively form a vertical profile of intensity averaged over intervals  $\Delta z = (cT_p/2) \sin\theta_0$ , where  $c$  is the speed of sound,  $T_p$  is the pulse duration, and  $\theta_0$  is the elevation angle of the beam. The pulse-time increment  $\tau_p$  is the interval from one transmission to the next; successive samples at fixed range (or depth) are separated by  $\tau_p$ . After enough pulses have been transmitted to provide intensity profiles for a period of 24 hours, the data can be considered to fill a one day depth-time intensity array expressed as

$$A_n(z,t) ; \quad z = z_0 + i \Delta z , \quad t = t_0 + j \Delta t \quad (3.1)$$

where  $A_n$  is the intensity of the backscattered signal, proportional to the square of the voltage measured at the transducer,  $n$  is the day index, and  $i$  and  $j$  are the indices for the discretely sampled depth and time, respectively. For the MPL Doppler sonar, with a pulse duration of  $T_p = 30$  ms and pulse repetition time of  $\tau_p = 2$  s, the values of the depth and time averaging intervals for the post-processed data are  $\Delta z = 17.85$  m and  $\Delta t = 180 \tau_p = 6$  min. The initial depth  $z_0 = 64$  m is the center of the first depth bin. The initial time  $t_0 = 0.1$  hr is the first time step after midnight of a given day, and the maximum time  $t_{\max} = 240 \Delta t = 24$  hr is the following midnight. Data collection, as described above, is over a period of  $N = 13$  days.

Measurements of the intensity of sound scattered from the ocean volume are generally reported in terms of the volume scattering strength (Urick, 1983)

$$S_v = 10 \log_{10} [ I_{\text{scat}} / I_{\text{inc}} ] \quad (3.2)$$

where  $I_{\text{scat}}$  is the intensity of sound scattered by a volume of  $1 \text{ m}^3$  referred to a distance of 1 m, and  $I_{\text{inc}}$  is the incident plane wave intensity. Use of the volume scattering strength serves as a normalization of the received intensity level, accounting for attenuation and spreading losses, as well as the increase in the insonified volume with increasing range. A profile of  $S_v$  is sensitive to changes in the abundance and acoustic cross section of scatterers as a function of depth. If the ocean volume contained a uniform distribution of scatterers of constant cross section, and if transmission loss, attenuation, and changes in the volume insonified by the beam were correctly modelled by the sonar equation (Urick, 1983), then the expected  $S_v$  profile would be constant with depth.

In this study, the depth dependence of the scattering field is not of primary importance. Instead, emphasis is placed on the temporal changes in the

intensity at a given depth relative to a long-term mean value. For this purpose a normalized measure of intensity similar to the scattering strength is formed. The *log intensity anomaly* is defined as the difference between the log intensity at a given depth and time and the long-term mean log intensity profile

$$I_n'(z,t) = I_n(z,t) - \bar{I}(z) \quad (3.3)$$

where

$$I_n(z,t) = 10 \log_{10} [ A_n(z,t) ]$$

is the total log intensity field, and

$$\bar{I}(z) = \frac{1}{J} \sum_{j=1}^J \frac{1}{N} \sum_{n=1}^N I_n(z, j\Delta t)$$

is the 13 day mean log intensity profile. The interpretation of depth ( $z$ ) and time ( $t$ ) is the same as in (3.1). The log intensity anomaly  $I_n'(z,t)$  represents the difference between the log intensity on day  $n$  at depth  $z$  and time  $t$ , and the 13 day mean profile. The long-term mean log intensity profile  $\bar{I}(z)$  is formed from the average of the depth-time log intensity array over all times of day for all days. The units of  $I_n'$  are dB, and are relative to an arbitrary reference; the values have meaning only as a comparative measure of deviation from the long-term mean.

The log intensity anomaly emphasizes the temporal variability of scatterer abundance and cross section at each depth, rather than their depth dependence at a given time. The effects of attenuation, spreading, and insonified volume, even if included in (3.1), would not change the nature of the intensity anomaly (3.3) since these effects are functions of range only, and would be absorbed in the long-term mean profile  $\bar{I}(z)$ . In addition to providing an effective normalization for the intensity data, use of the log intensity anomaly serves as a noise suppressing "filter". Intensity profiles are occasionally contaminated by high values of background noise which mask the true intensity variability at far range (see Fig. 3.2). Taking the log before averaging minimizes the effect of these noise "spikes" in the intensity time series.

The patterns of diurnal migration are characterized by computing the *composite log intensity anomaly* and the *log intensity variance* over the 13 day period. The composite log intensity anomaly is formed from the 13 day average of the single-day, depth-time arrays

$$I'(z,t) = \frac{1}{N} \sum_{n=1}^N I_n'(z,t) \quad (3.4)$$

Whereas the single-day log intensity anomaly (3.3) represents deviations of log intensity from the long-term mean profile for a given day, the composite log intensity anomaly (3.4) represents deviations for a "composite" day, formed from the average of the 13 single-day arrays. In other words, the individual values of  $I'$  represent the "typical" log intensity anomaly at a given depth and time of day for the 13 day interval.



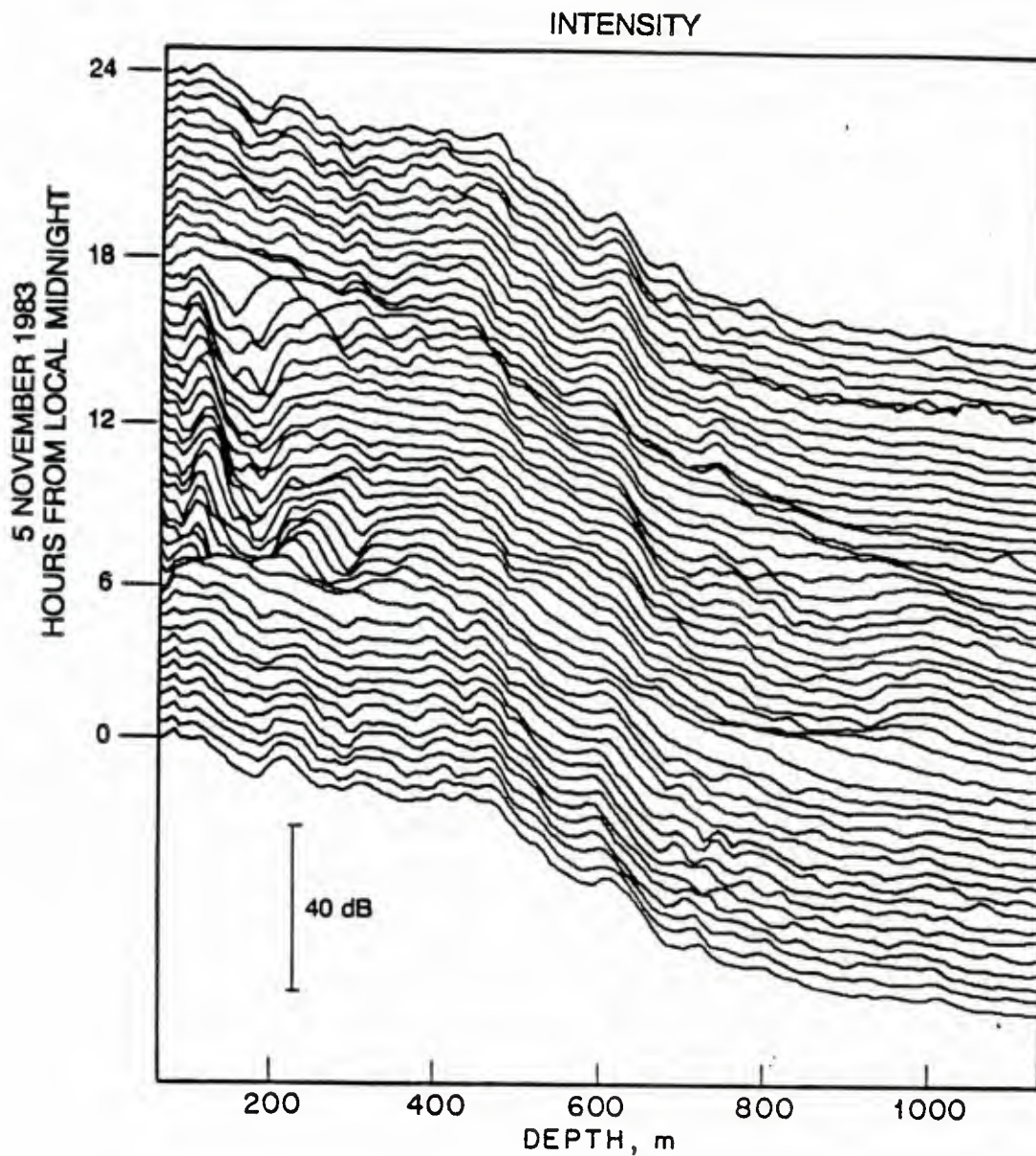


**Figure 3.2.** *Twenty-four hour intensity sequence.* Intensity data averaged over 30 min in time are shown as a cascaded sequence of profiles for a 24 hour period starting at midnight on 5 November, 1983. These profiles come from a single-day, "raw" intensity array [c.f. (3.1)], before normalization by the long-term mean profile. A day-time intensity trough at a depth of about 180 m can be seen, as well as intensity ridges defining the upper and lower scattering layers.



The log intensity variance can be computed directly from the anomaly field and is given by

$$\sigma_I^2(z,t) = \frac{1}{N} \sum_{n=1}^N [I_n'(z,t) - I'(z,t)]^2 \quad (3.5)$$

Values of  $\sigma_I^2$  represent the day-to-day variability of the 13 samples of log intensity anomaly at a given depth and time of day. It can be shown that the log intensity standard deviation is related to the coefficient of variation of the "raw" intensity computed from

$$cv = \sigma_A(z,t) / A(z,t) \quad (3.6)$$

where

$$A(z,t) = \frac{1}{N} \sum_{n=1}^N A_n(z,t)$$

$$\sigma_A^2 = \frac{1}{N} \sum_{n=1}^N [A_n(z,t) - A(z,t)]^2$$

and  $A_n(z,t)$  is as in (3.1). The depth-time array computed from (3.6) is virtually indistinguishable, in a qualitative sense, from that computed from (3.5). The log intensity standard deviation (3.5) is used to represent day-to-day variability in this study. Corresponding numerical values of coefficient of variation are quoted when pertinent.

### 3.2.2 Velocity data

The four downward-slanting sonars operated during the experiment have beams which are separated by  $90^\circ$  in azimuth and pointed downward at an angle of  $52.5^\circ$  from the horizontal. The four beams make up two, co-planar "Janus" pairs, with one pair operating in frequency band centered at 67 kHz, and the other at 71 kHz. Velocity data are presented only for the 67 kHz beam pair. An individual sonar provides an estimate of the radial component of scatterer velocity (the component of velocity in the direction of the beam) as a function of distance along the beam. A co-planar beam pair can be used to compute horizontal and vertical velocity profiles from the difference and sum, respectively, of the radial velocities of each beam (Sec. 1.4.1)

$$v = \frac{V_S - V_N}{2 \cos \theta_0}, \quad w = \frac{V_S + V_N}{2 \sin \theta_0} \quad (3.7)$$

The quantities  $v$  and  $w$  are the Janus horizontal and vertical velocities, respectively, in the  $y$ - $z$  plane of the coordinate system defined in Sec. 1.4.1. The slant velocities  $V_S$  and  $V_N$  are computed from the Doppler shift measured by the South and North beams according to

$$V = c\hat{f} / 2f_c \quad (3.8)$$

where  $f_c$  is the carrier frequency of the sonar, and  $\hat{f}$  is the covariance-based mean Doppler shift estimate (Appendix B). The vertical velocities used in this study are corrected for platform motion using the method developed in Appendix A. The precision (error standard deviation) of the vertical velocity estimate in (3.7) is computed from (1.22) and has a value of  $0.36 \text{ cm s}^{-1}$  after 6 min of averaging.

The vertical velocity is processed in a manner completely parallel to that of the log intensity, since the intent is to compare the patterns of DSL migration observed by the two measurement techniques. The *vertical velocity anomaly* is defined as

$$w_n'(z,t) = w_n(z,t) - \bar{w}(z) \quad (3.9)$$

where  $n$ ,  $z$ , and  $t$  are interpreted as in (3.1). The *composite vertical velocity anomaly* and *vertical velocity variance* are given by

$$w'(z,t) = \frac{1}{N} \sum_{n=1}^N w_n'(z,t) \quad (3.10)$$

$$\sigma_w^2(z,t) = \frac{1}{N} \sum_{n=1}^N [w_n'(z,t) - w'(z,t)]^2 \quad (3.11)$$

The interpretation of the velocity quantities defined by (3.9), (3.10), and (3.11) is analogous to that for the intensity quantities defined in (3.3), (3.4), and (3.5).

### 3.3 Results

The fundamental measurements for the Doppler sonar system are back-scattered intensity and scatterer velocity as a function of depth and time. Profiles of intensity from a single sonar beam operating at 67 kHz are shown in Fig. 3.1. Profiles measured within 6 minutes of noon and midnight are selected for each day, and averaged over the 13 day period from 28 October to 9 November, 1983. The intensity data is in arbitrary units, and only the relative values are meaningful. The "raw" intensity profiles (Fig. 3.1a) show a general decrease in intensity level with depth, to be expected from attenuation and spreading of the transmitted signal. The intensity levels extend over a dynamic

range of almost 70 dB. Clear differences between the day and night profiles can be seen at certain depth intervals, corresponding to changes in the distribution of scatterers. The log intensity anomaly (Fig. 3.1b) shows particularly well the changes in the depth distribution of scatterers between day and night. The average noon profile shows intensity peaks centered at 300 m, 560 m, and 1000 m depth, as well as a trough at 190 m. The successively deeper peaks are associated with what will be referred to as the upper, intermediate, and lower scattering layers. The largest difference between day and night intensity levels occurs at a depth of 180 m and has a magnitude of 12 dB.

In Fig. 3.1a the lower scattering layer is seen in the day profile as an intensity peak centered at 1000 m, compared to a night profile which is relatively flat. In Fig. 3.1b the night profile in the region of the lower layer is not flat, but shows a trough at the same depth as the peak in the day profile. Similarly, the night profile in Fig. 3.1a appears relatively flat near 190 m depth, where the day profile shows a deep trough, but there is a distinct peak near 190 m in the night profile in Fig. 3.1b associated with the trough of the day profile. These effects are due to the nature of the anomaly field, which, by definition, has zero mean if averaged in time over the 13 day period. The relative values of peaks and troughs are retained in the anomaly presentation, but the existence of a peak at one time of day must be associated with a trough at another time (and visa-versa) in order for the time-mean anomaly value to be zero. The existence of true peaks and troughs in the intensity field, rather than regions greater or less than the mean value, can be inferred only from the "raw" intensity (e.g. Fig. 3.1a and Fig. 3.2).

Based on a standard estimate of the significance of the difference between two sample means (Mack, 1966), it can be shown that the differences between the day and night profiles in the regions of the upper, intermediate, and lower scattering layers, as well as in the trough region centered at 190 m, are significant at the 90% confidence level. This implies that the difference between noon and midnight intensity profiles for a given day is larger than the expected variability of the noon profile and the midnight profile from one day to the next. This comparison of day and night profiles demonstrates that there is a significant day vs. night variation in scattering strength at certain depths, and highlights the depths of maximum variability. However, a presentation of this type does not show the space-time patterns of the daily migration cycle. These patterns can be identified in the 24 hour sequences of intensity and log intensity anomaly presented in Figs. 3.2 through 3.4.

A single-day sequence of "raw" intensity profiles is shown in Fig. 3.2. The trough seen at 190 m in the day profile of Fig. 3.1 is perhaps the most prominent feature of Fig. 3.2, and is found to extend from about 0800 to 1600 hrs. Intensity ridges outlining the upper and lower scattering layers can also be seen. Downward movement of both layers begins near 0600 hrs, with stabilization at depth from about 0900 to 1500 hrs, and upward movement ending near 1800 hrs. The intermediate layer is not easily seen in this presentation, but can be identified in the log intensity anomaly (Fig. 3.3). The distinct line which extends throughout the 24 hr record at a depth of 480 m is due to the system gain change (Sec. 3.2). Since this feature is very stable over the 13 day period,



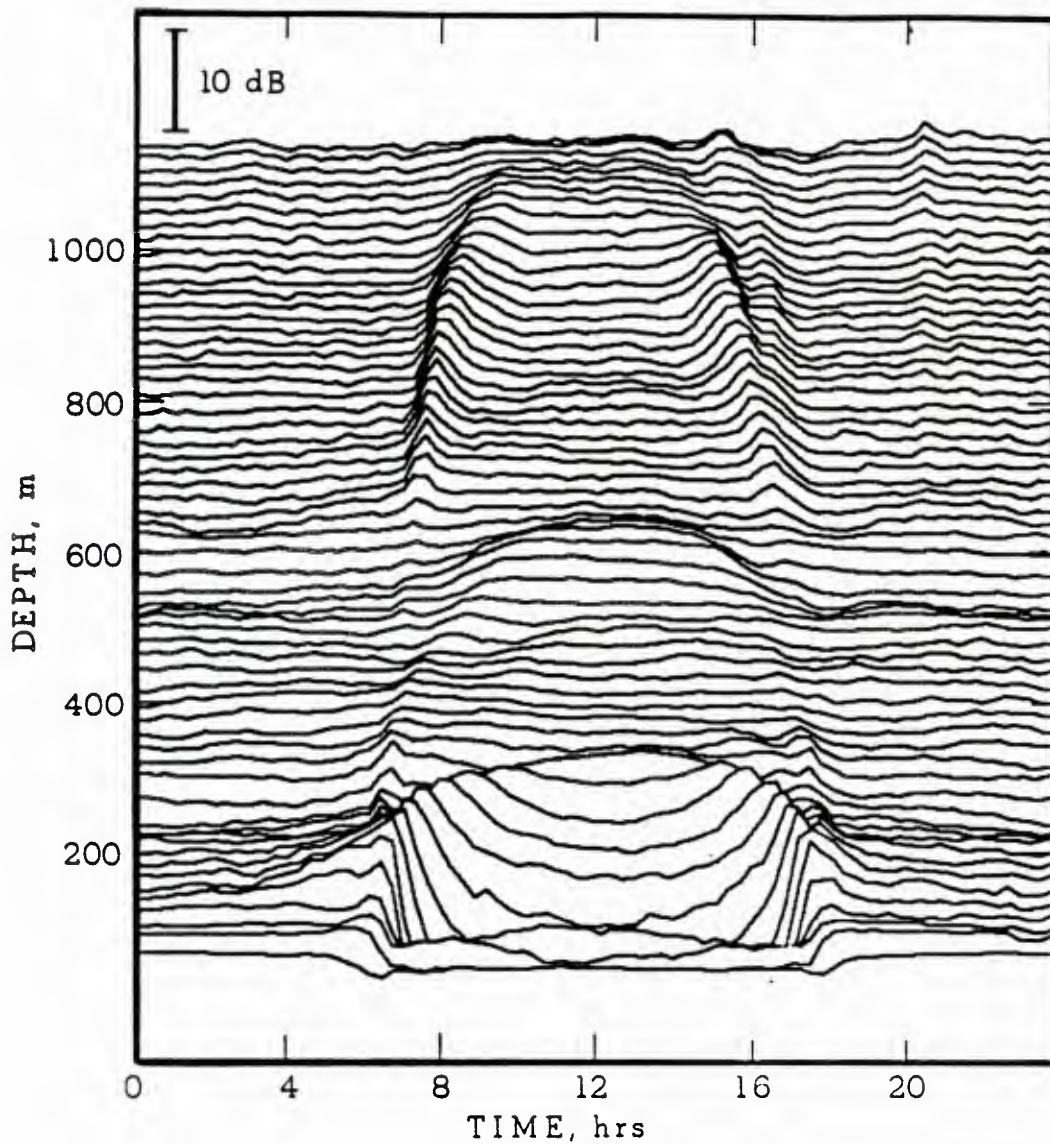


**Figure 3.3.** *Composite log intensity anomaly sequence.* Composite log intensity anomaly is presented as a cascaded sequence of time series for depths between 60 and 1200 m. The log intensity anomaly [c.f. (3.3)] is the difference between the log intensity at a given depth and time, and the long-term mean log intensity profile. The composite log intensity anomaly is formed by averaging the single-day arrays of log intensity anomaly over 13 consecutive days [c.f. (3.4)]. Data in this plot are averaged over 18 min in time, and the depth interval between lines is 18.75 m. Note that the depth axis is "reversed" in this figure.



it is not emphasized in the anomaly field.

The ridge of high intensity in Fig. 3.2 which extends from roughly 700 m to 1100 m at about 2100 hrs is due to system noise. Similar ridges can be seen in many of the single day intensity sequences, and some evidence of noise ridges remains in the 13 day composite intensity. These noise ridges tend to obscure the underlying patterns in the scattering field, and to increase the variance of the composite profiles. The relative infrequency of occurrence of noise ridges, and the use of log intensity serve to minimize these effects, but some care must be exercised in interpreting features in the intensity (and velocity) anomaly fields which extend over many depths, but are localized in time.

The composite log intensity anomaly field is presented as a cascaded sequence of time series vs. depth in Fig. 3.3, and as a contour plot in Fig. 3.4. Relative to the "raw" intensity in Fig. 3.2, the intensity anomaly in Fig. 3.3 shows suppression of those parts of the field which are steady with time, and the enhancement of temporal variability. This presentation gives a clear indication of the extent to which the peaks and troughs due to the DSL migration stand out from the background variability of the intensity field over a 24 hour period. The cascaded sequence (Fig. 3.3) emphasizes the continuity of the scattering layer "ridges" over depth and time, and is the only presentation which effectively shows the continuity of the intermediate layer. This layer is seen as an intensity ridge near 300 m depth at 0700 hr, moving downward to roughly 600 m by 1200 hr, and back up to 300 m at 1700 hr. The contour plot (Fig. 3.4) is presented in such a way that the scattering layers are isolated from the background field, and the depth and thickness of the layers can be estimated. Note that the day and night profiles in Fig. 3.1b represent cross-sections through the contours of Fig. 3.4, parallel to the depth axis, at times of noon and midnight, respectively. Three layers with daytime depths of 300 m, 560 m, and 1000 m, as suggested by Fig. 3.1, can be clearly seen in Fig. 3.4. Typical thickness for all three layers is well characterized by a scale of about 100 m, although the upper layer thickness is reduced to approximately 50 m during the day.

Migration rates for the scattering layers can be estimated from the slope  $\Delta z/\Delta t$  of the intensity anomaly ridges in Fig. 3.3 and 3.4. The upper scattering layer appears to migrate from a day-time depth of about 300 m to roughly 160 m or less in a period of about 3.4 hr, giving an average migration rate of  $1.1 \text{ cm s}^{-1}$ . The intermediate layer moves from day-time depth of 560 m to 220 m or less in about 2.6 hr, giving a migration rate of  $3.7 \text{ cm s}^{-1}$ , while the lower layer moves from 1000 m to about 650 m in only about 2.3 hr, giving a rate of  $4.2 \text{ cm s}^{-1}$ .

The migration rates based on the slope of the ridges in the composite intensity anomaly field can be compared to scatterer velocities estimated by the Doppler technique. A contour plot of the composite vertical velocity anomaly is shown in Fig. 3.5. Regions of large positive and negative vertical velocity are seen which correspond to the times of upward and downward scatterer migration, respectively. The majority of the composite velocity field has magnitude less than  $0.5 \text{ cm s}^{-1}$ , while velocities in the regions of migration may be as large as  $4.0 \text{ cm s}^{-1}$ . The increase in variability below about 800 m is not due to true variability in the velocity of the scatterers, but rather to the decrease in signal-

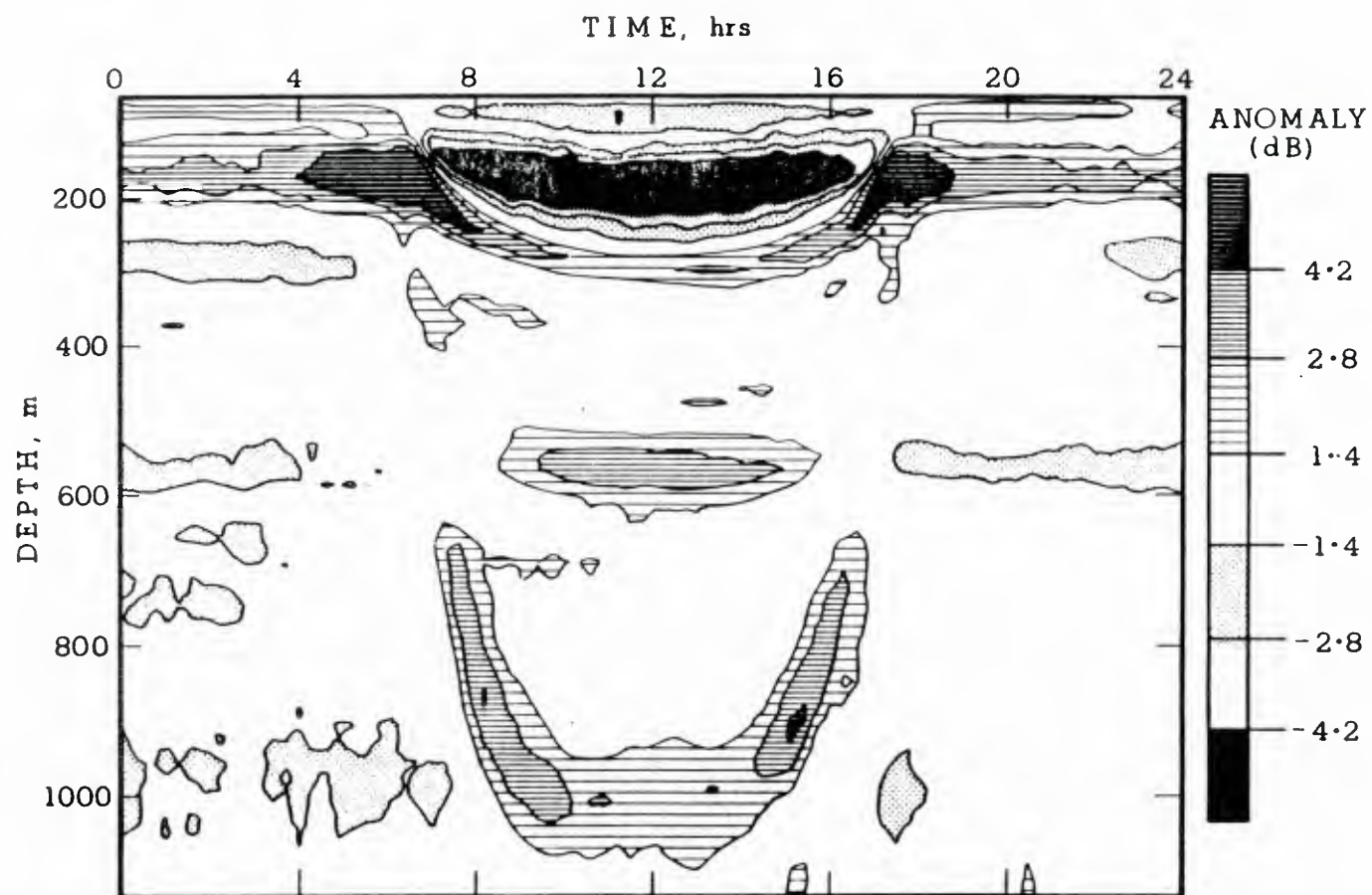


**Figure 3.4.** *Composite log intensity anomaly contours.* Composite log intensity anomaly data from Fig. 3.3 are presented in a contour plot. The contour interval is 1.4 dB, and the contour levels are shown in the key above. Data in this plot, and in all successive contour plots, are averaged over 18 min in time and 18.75 m in depth.

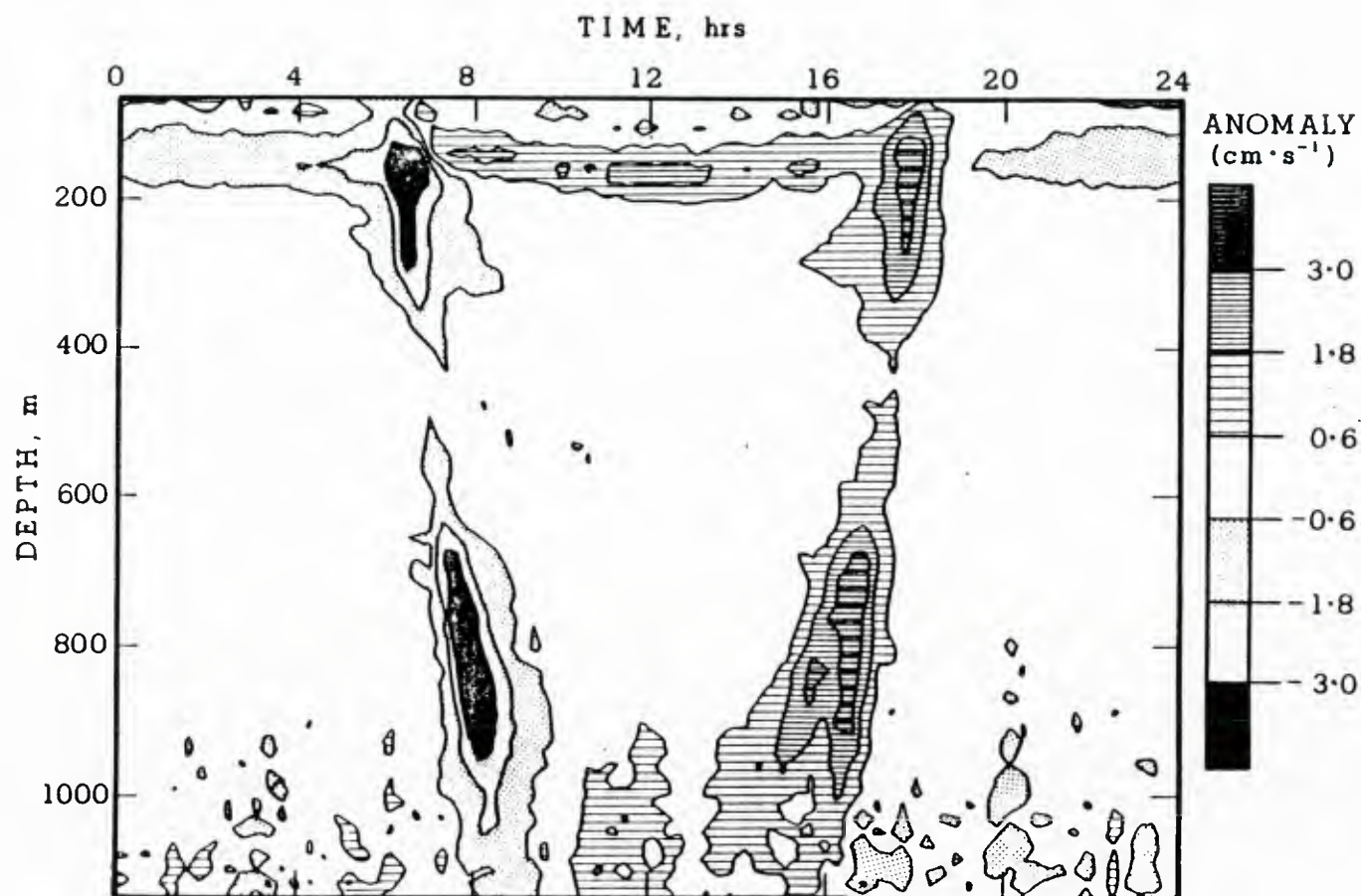


**Figure 3.5.** *Composite vertical velocity contours.* Thirteen day composite of vertical velocity anomaly is presented in a contour plot. The depth-time array of vertical velocity for each day is computed from two beams of the four-beam Doppler sonar array. Composite vertical velocity anomaly is formed from the single-day arrays in the same manner as the composite log intensity anomaly. The contour interval is  $1.2 \text{ cm s}^{-1}$  and the contour levels are shown in the key above.



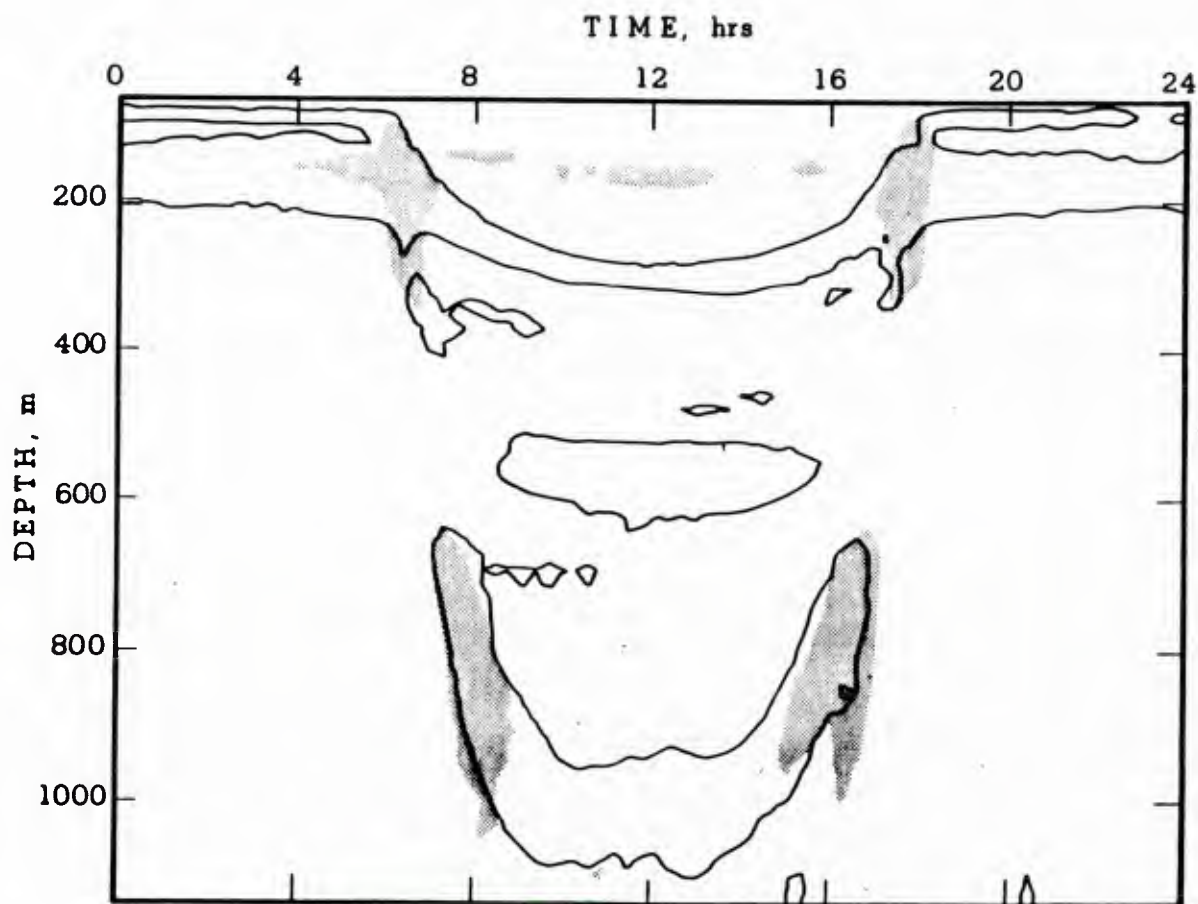
to-noise ratio with depth which causes an increase in the variance of the vertical velocity estimate (see discussion of Figs. 3.7 and 3.8 below).

Figure 3.6 shows contours which enclose regions of positive log intensity anomaly (from Fig. 3.4) compared with contours enclosing regions of vertical velocity anomaly with magnitude greater than  $1.8 \text{ cm s}^{-1}$  (from Fig 3.5). For the lower layer, the correspondence between the region of largest scattering layer slope based on the intensity data, and the region of largest vertical velocity from the Doppler data is striking. The maximum Doppler velocities in the "core" of the lower layer are from  $3\text{-}4 \text{ cm s}^{-1}$ , somewhat less than the rate of  $4.2 \text{ cm s}^{-1}$  computed from the intensity data. For the upper layer, the regions of large Doppler velocity appear to "cut through" the intensity field in a section where the scattering layer slope is small. Layer migration speeds based on the intensity data in this region are about  $1.0 \text{ cm s}^{-1}$ , while the Doppler velocities have magnitudes from  $1.8$  to  $3.6 \text{ cm s}^{-1}$ . The comparison of intensity-based and Doppler velocities is explored further in the discussion section.

The variability of the intensity and velocity fields from one day to the next is presented in terms of the log intensity standard deviation (Fig. 3.7) and the vertical velocity standard deviation (Fig. 3.8). The two fields show a very similar structure, with two distinct features; an isolated region of high variability from about 0600 hr to 1800 hr extending over depths from 100-250 m, and a gradual increase in variability with depth at all times of day, starting at about 800 m. The latter effect is the most easily explained. Due to attenuation and spreading of the transmitted signal, the backscattered energy level decays with range  $r$  as approximately  $r^{-2}$ . For the downward-slanting sonars used in this study, this amounts to a decreasing signal-to-noise ratio (SNR) with increasing depth. Values of SNR drop to order 10 dB at a depth of about 800 m. Below this depth, estimates of intensity and velocity become less stable because of the increasing influence of noise. Thus, the variability below 800 m in Figs. 3.7 and 3.8 is due to noise, not to an actual increase in the variability of the scattering field. Note that the existence of the lower scattering layer, centered at about 1000 m during the day, causes an increase in SNR, and an associated decrease in variance of the intensity and velocity estimates.

The isolated region of large daytime variability from 100-250 m depth seen in Fig. 3.7 and Fig. 3.8 is closely associated with the intensity trough seen in Figs. 3.2 and 3.4. This trough represents a decrease in SNR, but the values of SNR in this region remain above those responsible for the increased estimate variance at depths below 800 m. It is likely that the high values of intensity and velocity variance in the region of the intensity trough are due to an actual increase in the variability of the scattering field.





**Figure 3.6.** *Intensity vs. vertical velocity comparison.* Contours representing large values of composite vertical velocity anomaly are plotted over contours of composite log intensity anomaly which represent the 'cores' of the three main scattering layers. Shaded areas contain vertical velocity anomalies with magnitude greater than  $1.8 \text{ cm s}^{-1}$ . Areas enclosed by solid contours contain values of positive log intensity anomaly greater than 1.4 dB.

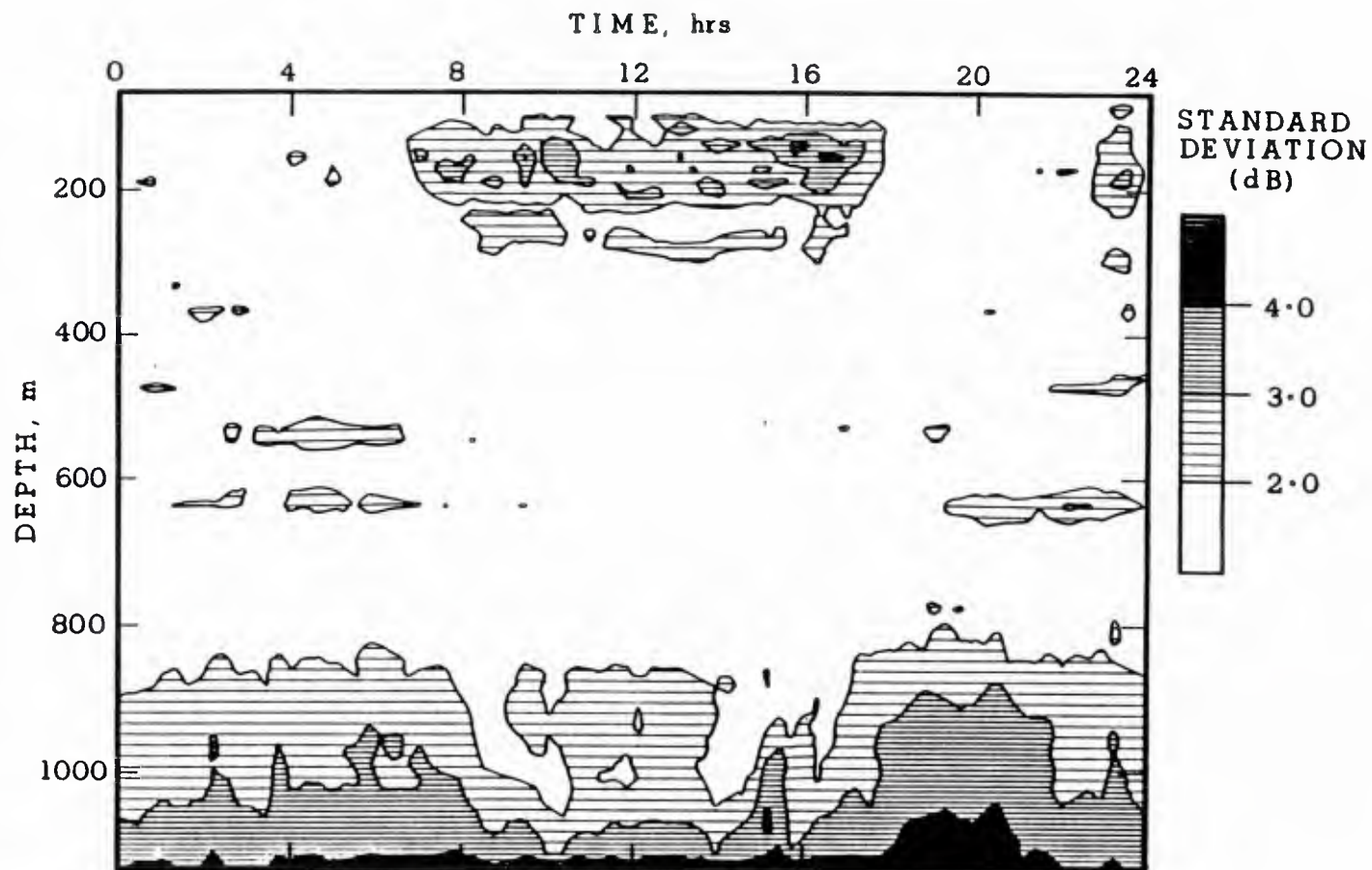


**Figure 3.7.** *Log intensity standard deviation contours.* Standard deviation of the 13 log intensity arrays is shown. The value of standard deviation at a given depth-time "grid point" represents the relative variability of the 13 samples at that depth and time over the 13 day period. The contour interval is 1.0 dB, and the contour levels are given in the key above.

### 3.4 Discussion

The distinguishing feature of the DSL migration pattern observed in this study is its persistence in both depth and time. The relative variability from day-to-day is small throughout the region where intensity ridges corresponding to the three scattering layers are seen (compare Figs. 3.4 and 3.7), implying a high degree of persistence in the migration patterns of the three layers over the 13 day observation period. The coefficient of variation in this region (not shown) has values less than 0.5. The temporal persistence scale of order 10 days indicated by these results is in contrast to that found by other investigators. Percy and Mesecar (1971) observed patterns of diurnal migration using a 12 kHz echosounder in a region about 200 km west of Newport, Oregon. They found that the depth-time distribution of backscattered intensity showed "pronounced" variability between two 24 hour cycles separated by 3 days. A more recent study by Greenlaw and Percy (1985), using a 20 kHz echosounder in the same general area as Percy and Mesecar (1971), found persistence in the spatial structure of the scattering layer between two successive 24 hour periods, but "little similarity" in the structure of the scattering layer for observations separated by 1 day.

The observing platform (R. P. FLIP) was not stationary with respect to the scatterers during the present experiment, implying some degree of spatial persistence in the DSL migration pattern. Over the 13 day measurement period, FLIP was pushed by prevailing winds and currents over a path of length  $\sim 115$  km, giving an average drift rate of  $\sim 9$  km per day. A high degree of similarity has been observed between FLIP's drift track and progressive vectors of depth-averaged velocity computed from Doppler sonar data (Pinkel, 1983a, and unpublished data from this study). The results indicate that for depths greater than about 300 m, the ocean can be considered nearly stationary relative to the earth, when compared to the drift speed of FLIP. The scatterers making up the DSL migrate vertically, spending part of each day in the relatively fast moving surface water, and part in the slower moving deep water. For the scatterers in the intermediate layer, it might be assumed that residence time is split evenly between water moving with the same velocity as FLIP, and water stationary with respect to FLIP. In this case the displacement of the observing platform relative to the scatterers in the intermediate layer would be 4-5 km per day, or  $\sim 50$  km over the 13 day observation period. The overall displacement relative to scatterers in the intermediate layer would be somewhat less, and that relative to the lower layer somewhat more than 50 km. Based on the arguments above, spatial persistence over scales of order 50 km is implied by the results of the present study. This is in agreement with the results of Greenlaw and Percy (1985), who found patches of high scattering strength with horizontal extent of 40-60 km within a scattering layer with a daytime depth of about 300 m. The apparent low degree of temporal persistence reported in the studies quoted above may be due to spatial variability if relative displacements between the observing platform and the underlying scatterers are greater than those encountered here.

It should be noted that persistence scales based on low day-to-day intensity variability are not representative of scales of "patchiness" in the usual sense. Patches of migrating organisms aggregating on scales of order 50 km in the horizontal, and remaining aggregated for times of order 10 days would not be inconsistent with the results of this study. The low levels of variability in the scattering field from day-to-day tend to support this hypothesis. However, it is possible that the observed persistence is the result of several different patches, encountered at different times and horizontal locations during the observation period, all of which show similar patterns of migration. The low values of day-to-day variability would then be interpreted to mean that differences in scattering strength between patches are small compared to the magnitude of the scattering strength anomalies which define the layers. In other words, the low values of relative variability in regions where distinct ridges are seen in the 13 day composite intensity field indicate that well defined scattering layers are consistently present, and that the migration patterns of these layers are very similar from one day to the next. However, the variability of scattering strength *within* a layer could be as large as 50% of the mean value and still be consistent with the observations.

The only pronounced day-to-day variability, other than that expected due to decreasing SNR below 800 m depth, is found in a region where a well defined scattering layer is not present. This high variability is seen in both the intensity and Doppler velocity fields over depths from 100-250 m during daylight hours (Figs. 3.7 and 3.8), matching the location of the daytime intensity trough (Fig. 3.4). Values of the coefficient of variation in this region are from 0.5 to 1.25. The increase in day-to-day variability may be due to the occasional occurrence of relatively large and mobile scatterers within insonified volumes which are composed mostly of small scatterers during these depths and times. Greenblatt (1981; 1982) reports the results of simultaneous biological and high-frequency acoustic sampling at a depth of 87 m off of the coast of Southern California. He argues that the acoustic measurements are dominated by larger scatterers at night than during the day, and that the occasional occurrence of large scatterers during the day accounts for an increase in daytime scattering strength fluctuations. Similarly, the intensity anomalies defining the upper and intermediate scattering layers in the present study may be caused by larger scatterers (large euphausiids and small fish) which dominate the near surface (0-200 m) acoustic measurements at night, but migrate to depths greater than 250 m during the day. Scattering in the near surface region during the day would then be due to smaller, although perhaps relatively more abundant scatterers such as small euphausiids and large copepods.

The occurrence of a large scatterer in a small-scatterer dominated field will cause a large relative intensity change, and the sporadic occurrence of such a scatterer will cause a high degree of intensity variability. The occurrence of the same large scatterer in other regions, where large scatterers already form the dominant acoustic source, will cause only a small fractional change in back-scattered intensity, and sporadic occurrence will not result in significantly increased intensity variability. Thus, the high values of relative intensity variability observed in the region of the daytime intensity trough may be due to the occasional occurrence of larger scatterers in a background field composed of



small scatterers. Since a similar pattern of near surface variability is seen in the Doppler velocity, it is suggested that the occasionally occurring, larger scatterers are also more mobile.

The general pattern of vertical migration is symmetric about local noon, but careful analysis reveals differences in the upward and downward migration rates. For the upper and intermediate layers, the time between minimum and maximum observed depths is shorter for the upward portion of the cycle (Fig. 3.3). Velocity estimates based on the slopes of the intensity ridges show that the upward migration has an average rate from 10 to 20% faster than the downward migration. The tendency for upward migration rates to be faster than downward was also seen by Greenblatt (1982). He found that the transition from low to high scattering levels at a depth of 87 m at dusk (upward migration) was approximately 60% faster than the transition from high to low scattering strength at dawn (downward migration). Comparison of upward and downward migration rates for the lower layer in the present study shows the opposite tendency; the upward migration is some 10% slower than the downward migration.

The migration speeds based on the slope of the ridges in the intensity anomaly field effectively measure the average speed of scatterers within the layer. Since the layers change in thickness as they move upward and downward, it is clear that the velocities within the layer are not uniform. Portions of the scatterer population may move significantly faster or slower than the mean speed. The vertical velocities from the Doppler sonar come from an intensity-weighted sum of the scatterer velocities within the insonified volume: Scatterers of high intensity are more heavily weighted in the volume-average velocity than those of low intensity. The intensity ridges which define the scattering layers are superimposed on a background intensity field composed of non-migrating scatterers. The scatterers in this background field are assumed to be passively drifting, moving in response to the dynamic velocities within the surrounding fluid volume. The largest contribution to vertical velocity due to dynamical sources comes from high frequency internal waves. Maximum values of vertical velocity for these waves can be expected to be of order  $0.5 \text{ cm s}^{-1}$  when averaged in the manner used to form the vertical velocity anomaly (Fig. 3.5). Contributions to vertical velocity from lower frequency dynamical sources will be considerably less than  $0.1 \text{ cm s}^{-1}$ . Thus, the background intensity field tends to weight the Doppler velocities towards small values compared to the scatterer migration rates.

The increase in vertical velocity magnitude at the core of the lower layer is consistent with the increasing magnitude of the intensity anomaly: As the intensity ridge defining the migrating scattering layer becomes more dominant over the background, non-migratory scattering field, the Doppler velocities approach the speeds computed from the slope of the intensity ridge. The velocity anomalies in the region of the upper layer, however, do not match the values computed from the slope of the intensity ridges in the same region. In fact, the velocity anomalies are the most pronounced where the migration rate of the upper layer appears to be near zero (Fig. 3.6). This can be explained by considering the intermediate layer which migrates from about 600 m up to at

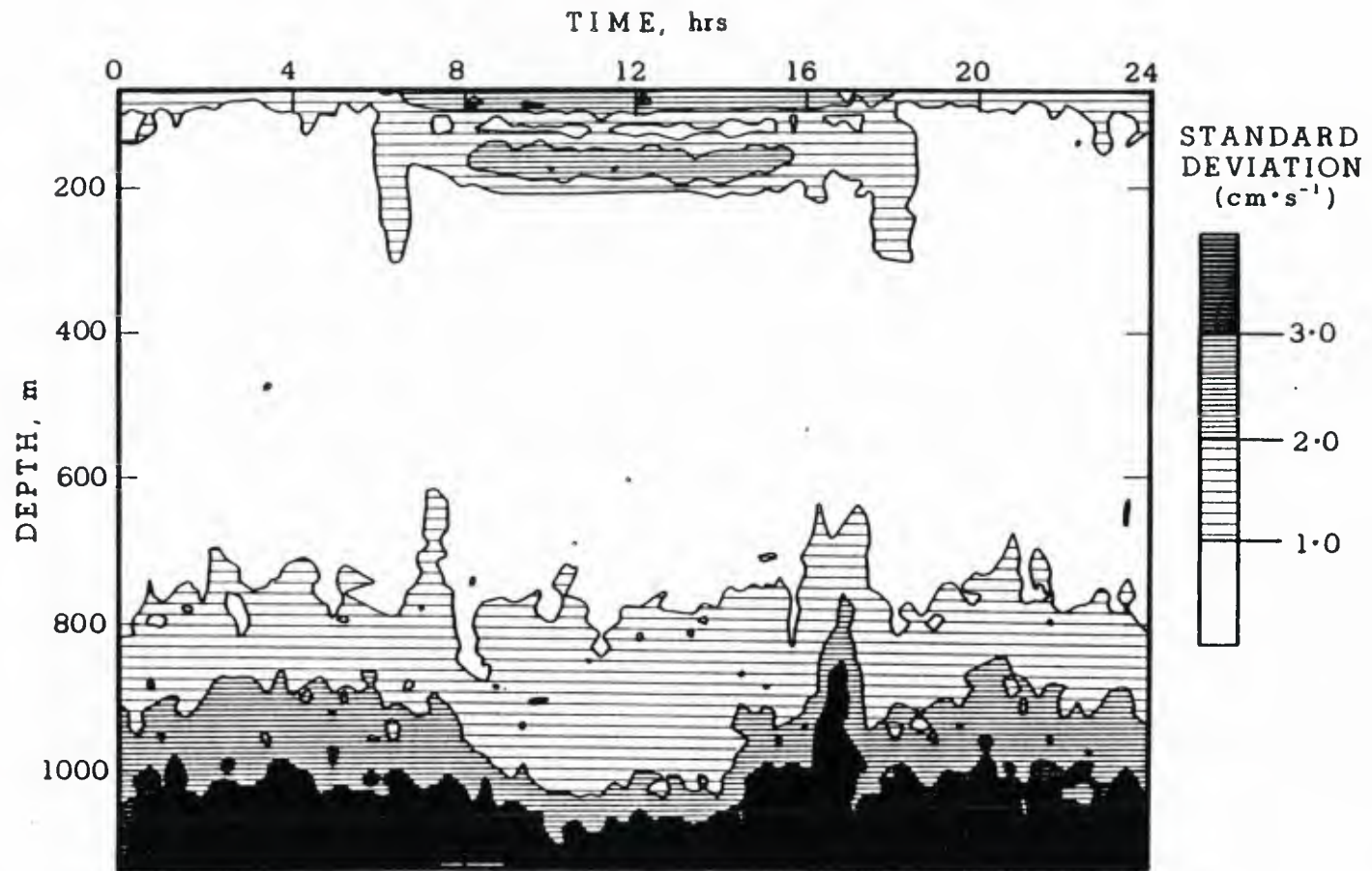


**Figure 3.8.** *Vertical velocity standard deviation contours.* Standard deviation of the 13 vertical velocity arrays is shown. Interpretation is the same as that for Fig. 3.7. The contour interval is  $1.0 \text{ cm s}^{-1}$ , and the contour levels are given in the key above.

least the depth of the upper layer (Fig. 3.3). As the ridge defining the intermediate layer merges with that of the upper layer, its subsequent movement becomes unclear. Careful observation of the intensity data reveals the existence of a steeply sloped, downward perturbation of the upper layer intensity ridge as it merges with the intermediate layer (e.g. features between 200 and 250 m depth at 0630 hrs. in Fig. 3.4). This suggests that the intermediate layer may continue to migrate upward, "through" the upper layer. This is supported by the Doppler velocity data which show large vertical velocity magnitudes in the region where the intermediate and upper layers intersect (Fig. 3.6). In this case, the scatterers of the upper layer form the nearly stationary background field, and the faster moving scatterers from the intermediate layer produce the vertical velocity anomaly. The magnitudes of the Doppler velocities in this region reach a maximum of  $3.6 \text{ cm s}^{-1}$ , in good agreement with the average migration rate of  $3.7 \text{ cm s}^{-1}$  computed from the slopes of the intensity ridges defining the intermediate layer.

### 3.5 Chapter summary

The principal result of this study is the observation of three distinct acoustical scattering layers whose patterns of vertical migration show a high degree of persistence over a time period of 13 days, and horizontal scales of order 50 km. The three layers are observed over a depth interval of 60 to 1200 m using a high frequency (67 kHz) Doppler sonar. The patterns of diurnal migration are evident in both the backscattered intensity and Doppler velocity. Analysis of the variations of intensity and velocity from a long-term temporal mean state provide complementary methods of characterizing the migration patterns. The daytime depths of the three scattering layers are about 300, 560, and 1000 m. Typical layer thickness is of order 100 m. Analysis of both intensity and Doppler velocity data indicates average migration rates of about 1, 3, and  $4 \text{ cm s}^{-1}$ , respectively, for the successively deeper layers. Upward migration for the two shallowest layers appears to be 10 to 20 percent faster than downward migration, while the opposite is true for the deepest layer. Differences between day and night profiles of backscattered intensity at the depths of the scattering layers are found to be significant compared to differences between successive days or successive nights. In general, day-to-day variability in the intensity field is small compared to the magnitude of the intensity anomalies which define the scattering layers. The only exception is an isolated region from 100-250 m depth during the day. The high variability in this region may be explained by changes in the size class of the dominant scatterers from day to night.

## CHAPTER IV

### BIASING OF THE COVARIANCE-BASED SPECTRAL MEAN ESTIMATOR IN THE PRESENCE OF BAND-LIMITED NOISE

#### 4.1 Introduction

The covariance processing (CP) technique, introduced by Rummler (1968) is now well established in the analysis of data from pulse-to-pulse coherent meteorological Doppler radars (Doviak and Zrnic, 1984). The technique has also been applied to the measurement of atmospheric winds using pulse-to-pulse incoherent Doppler sonars (Underwood, 1981). Oceanographic applications include Doppler sonars using both incoherent (Pinkel, 1979; 1983a; Christensen, 1983) and coherent (Lhermitte, 1983; Lhermitte and Poor, 1983) systems. All of these Doppler systems measure the mean Doppler shift in the spectrum of backscattered energy from a pulsed transmission to gain knowledge of the velocity field in the medium.

The estimation of spectral mean frequency (spectral first moment) by the CP technique for a Gaussian shaped signal spectrum contaminated by additive noise has been considered by many investigators including Miller and Rochwarger (1972), Sirmans and Bumgarner (1975b), and Underwood (1981). These authors have concluded that covariance-based processing (also known as "pulse-pair" processing) provides an unbiased estimate of the spectral mean frequency for all signal-to-noise ratios (SNR) if the additive noise is "white". The hypothetical case of truly uncorrelated or "white" noise in the received signal would require that the noise spectrum have constant energy density and an infinite bandwidth. For an operational instrument with finite overall bandwidth, the noise can be considered "white" only if the noise spectrum has nearly constant energy density over a range of frequencies which is large compared to the bandwidth of the signal of interest.

In a pulsed Doppler system, the overall receiver bandwidth must be at least as large as the inverse pulse length to maintain acceptable fidelity of the received echo (Doviak and Zrnic, 1984). For incoherent Doppler systems which do not employ pulse-to-pulse Doppler shift "tracking" (Rowe and Young, 1979), it is necessary for the receiver bandwidth to be larger than the inverse pulse length in order to accommodate a range of Doppler shifts. Increasing receiver bandwidth beyond that required by the above constraints is undesirable since it results in a decrease in the signal-to-noise ratio. The result is a band-limited noise spectrum at the receiver output with a bandwidth which may not be significantly larger than the signal bandwidth. This band-limited noise has non-zero autocovariance at small time lags and must be considered in evaluating the performance of the CP technique of mean frequency estimation.



This study shows that the CP mean frequency estimator exhibits a significant bias at low SNR if the noise bandwidth is not large compared to the signal bandwidth. The nature of the bias is to force the CP estimated Doppler shift towards the center of the frequency band passed by the receiver. Biases as large as 7 to 50 percent are predicted for signal-to-noise ratios from 10 dB to 0 dB, respectively. Incoherent Doppler systems are often operated under the conditions of low SNR and large signal-to-noise bandwidth ratio where this biasing effect is important.

This chapter first reviews the CP technique and develops a theoretical framework for estimating the biasing effect of band-limited noise on covariance-based mean frequency estimates. It is found that the magnitude of the bias for a given Doppler shift can be expressed in terms of the signal-to-noise power ratio and the ratio of the normalized covariance amplitude for the signal to that for the noise. Methods of correcting for noise-biasing are discussed next with emphasis on situations where the noise covariance is not known explicitly. It is shown that bias correction in the absence of noise covariance measurements can be accomplished using estimates of the signal and noise bandwidths and models of the signal and noise covariance functions. Finally, the covariance modelling technique of bias correction is applied to oceanic velocity measurements made with a pulse-to-pulse incoherent Doppler sonar using the CP mean frequency estimator.

## 4.2 Covariance Processing (CP)

The covariance-based estimator for spectral moments has been extensively described by many authors (Miller and Rochwarger, 1972; Serafin, 1975; Sirmans and Bumgarner, 1975b; Passarelli and Siggia, 1981; Lhermitte and Serafin, 1984) with emphasis on application to coherent radar and sonar processing. A brief description of the CP technique as used for the estimation of mean Doppler shift is given in this section.

A simple Doppler system interrogates a sample volume in the medium with a pulsed transmission of the form

$$X_o(t) = a \cos(2\pi f_c t) G(t) \quad (4.1)$$

where

$$G(t) = \begin{cases} 1 & t_o \leq t \leq t_o + T_p \\ 0 & \text{otherwise,} \end{cases}$$

$f_c$  is the carrier frequency, and  $T_p$  is the pulse length. The received signal is the sum over the sample volume of contributions to amplitude and phase from many individual scatterers. It is convenient to refer to the region of space interrogated by the transmitted pulse using the along-beam dimension of the sample

volume, commonly called a range gate. The signal received at time  $t$  after the start of transmission comes from a range gate of extent  $\Delta r = cT_p/2$  centered at  $r = ct/2 - cT_p/4$  and can be expressed as (Serafin, 1975)

$$X(t) = \text{Re} \left\{ \exp[ i2\pi f_c t ] S(t) \exp[ i\phi(t) ] \right\} \quad (4.2)$$

where  $S(t)$  and  $\phi(t)$  are the resultant amplitude and phase, respectively.

Since only the complex envelope,  $S(t) \exp[ i\phi(t) ]$  of (4.2) is of interest, a homodyning or heterodyning system is often used to remove the carrier frequency and separate the received signal into in-phase (I) and quadrature (Q) components. The I and Q components, properly normalized, can be combined to form the complex envelope

$$Z(t) \equiv S(t) \exp[ i\phi(t) ] = I(t) + iQ(t) \quad (4.3)$$

The squared magnitude of  $Z$  gives the received signal power,  $S^2$ , and the phase of  $Z$  is related to the Doppler shift.

The mean Doppler shift introduced by an aggregate of moving scatterers is related to the average velocity within the sampling volume. The scatterers within the volume may have varying acoustic cross sections and be moving at slightly different speeds. As a result, the received signal does not contain a single Doppler shift, but rather a distribution of received power with frequency forming a Doppler spectrum  $P(f)$  with a power-weighted mean Doppler shift

$$\bar{f} = \int_{-\infty}^{\infty} f P(f) df / \int_{-\infty}^{\infty} P(f) df \quad (4.4)$$

The component of velocity along the transmitter beam axis is given by

$$v = \underline{v} \cdot \underline{d} = c\bar{f} / 2f_c \quad (4.5)$$

where  $\underline{v}$  is the average velocity in the sample volume,  $\underline{d}$  is the unit vector in the direction of the beam, and  $c$  is the speed of wave propagation in the medium. The volume-averaged radial velocity (4.5) is a fundamental measurement for all Doppler systems. Knowledge of  $\bar{f}$  is sufficient to determine  $v$  since  $c$  and  $f_c$  are known constants for a particular system operating in a given medium.

Classical methods for determining the mean Doppler shift involve computing the power spectrum of the complex receive signal (4.3) and estimating the power weighted mean frequency from (4.4). With the CP technique, the Doppler spectrum is not computed; instead the spectral moment is determined from the complex covariance function

$$C(\tau) = \langle Z(t)Z^*(t+\tau) \rangle \quad (4.6)$$

where the brackets imply ensemble averaging and  $*$  denotes conjugation.

Exploiting the fact that the Doppler spectrum is the Fourier transform of the covariance function

$$P(f) = \int_{-\infty}^{\infty} C(\tau) \exp[-i2\pi f\tau] d\tau \quad (4.7)$$

it can be shown (Appendix B) that the first spectral moment is well approximated by

$$\hat{\bar{f}} = (2\pi\tau)^{-1} \text{Arg} [ C(\tau) ] \quad (4.8)$$

For a noise-free, symmetric Doppler spectrum  $\hat{\bar{f}}$  is an unbiased estimator for  $\bar{f}$  as  $\tau$  approaches zero. In practice, the estimator performs well for covariance lags  $\tau \ll \sigma_s^{-1}$ , where  $\sigma_s$  is the bandwidth of the Doppler spectrum. The CP mean frequency estimator (4.8) can be applied to both coherent and incoherent Doppler systems, but differences in the computation of covariance must be recognized. Further discussion of the CP technique, and its application to coherent and incoherent Doppler systems, can be found in Appendix B.

### 4.3 CP in the presence of band-limited noise

**a. Description of noise biasing.** The presence of background noise is unavoidable in a realizable Doppler system. Contributions to noise power can be separated into two additive components: 1) system noise, observed at the receiver input, and 2) noise generated by the receiver. Multiplicative noise, due to distortion or non-linearity in the system electronics, will not be considered here. Contributions to system noise are primarily from the ambient noise of the medium, transmit-receive switches, and transmission lines. Receiver noise comes from amplifiers, multipliers and filters in the receive circuitry. The system noise spectrum contains energy over a wide range of frequencies and typically has a bandwidth which is large compared to that of the received signal. If, in addition, the system noise spectrum has nearly constant energy density in the frequency range of interest, then the system noise may be considered "white".

The noise at the receiver output is the sum of system noise and receiver noise. This noise is band-limited by the receiver filter(s) and has a covariance function characterized by a finite decay time or correlation time of order  $\sigma_n^{-1}$ , where  $\sigma_n$  is the noise bandwidth, taken at the -3 dB points of the receiver frequency response function. Since the noise covariance at the receiver output has a finite decay time, the concept of true "white" noise (noise covariance = 0 for lags  $> 0$ ) in the received signal is invalid, even if the system noise is approximately "white". It is possible for the noise in the received signal to be considered effectively "white" if the noise covariance has a decay time much shorter than the sampling interval of the signal. If the signal portion of the Doppler spectrum has a -3 dB bandwidth of  $\sigma_s$ , then the signal covariance must

be computed at lags less than  $\sigma_s^{-1}$  to recover useful phase information. Taking the noise covariance decay time to be  $\sigma_n^{-1}$  and the sampling interval to be  $\leq \sigma_s^{-1}$ , the condition for validity of the "white" noise approximation is  $\sigma_n^{-1} \ll \sigma_s^{-1}$  or

$$\sigma_s / \sigma_n \ll 1 \quad (4.9)$$

It is the interest of this paper to consider situations where condition (4.9) does not hold, so that estimation of spectral moments using (4.8) requires the consideration of additive, band-limited noise in the received signal.

The effect of band-limited noise on the CP estimator has not been explored extensively by previous authors. This is because most applications of the CP technique have been to pulse-to-pulse coherent Doppler radars, where the "white" noise approximation is valid. In fact, the nature of the coherent processing scheme (Appendix B) whether it is applied to meteorological radars or oceanic sonars, makes the condition (4.9) strongly satisfied. This can be confirmed by computing signal-to-noise bandwidth ratios for the coherent Doppler systems described by Sirmans and Bumgarner (1975a):  $\sigma_s \sim 10$  Hz,  $\sigma_n \sim 1$  MHz,  $\sigma_s / \sigma_n \sim 10^{-5}$  and by Lhermitte (1983):  $\sigma_s \sim 1$  Hz,  $\sigma_n \sim 17$  kHz,  $\sigma_s / \sigma_n \sim 6 \times 10^{-5}$ . In contrast, if we compute bandwidth ratios for the incoherent systems of Underwood (1981):  $\sigma_s \sim 10$  Hz,  $\sigma_n \sim 100$  Hz,  $\sigma_s / \sigma_n \sim 10^{-1}$  and Pinkel (Table 1.1):  $\sigma_s \sim 30$  Hz,  $\sigma_n \sim 200$  Hz,  $\sigma_s / \sigma_n \sim 10^{-1}$ , it is seen that the "white" noise approximation is marginally valid at best. For any Doppler system where the noise bandwidth is not much greater than the signal bandwidth, and for pulse-to-pulse incoherent systems in particular, biasing of the CP estimator due to band-limited noise must be considered.

The effect of band-limiting on the signal and noise covariance functions is shown graphically in Fig. 4.1. The figure is representative of the incoherent Doppler sonar of Pinkel (1983a), which operates with a signal-to-noise bandwidth ratio of order  $10^{-1}$ . In order to minimize the variance of the CP mean frequency estimator, it is desirable to operate such a system in the region  $0 < \tau \sigma_s \leq 0.2$ , where  $\tau \sigma_s$  is the normalized covariance lag (Miller and Rochwarger, 1972). Inspection of Fig. 4.1 shows that the noise covariance amplitude is not negligible compared to that of the signal for small values of normalized lag when SNR is near 1.0. A detailed discussion of the effect of band-limited noise on the CP mean frequency estimator, including the effects of SNR and the noise-to-signal covariance amplitude ratio, is given below.

Given that the receiver output, composed of in-phase and quadrature signals, is corrupted by additive band-limited noise with covariance  $C_n(\tau)$ , the complex signal-plus-noise can be written

$$Z_{sn}(t) = [I(t) + N_I(t)] + i[Q(t) + N_Q(t)] \quad (4.10)$$

with  $I$  and  $Q$  as in (4.3) and where the total noise power is  $N^2 = \langle N_I^2 \rangle + \langle N_Q^2 \rangle = C_n(0)$ . The noise is considered to have zero mean and to be uncorrelated with the signal. If the noise spectrum is symmetric



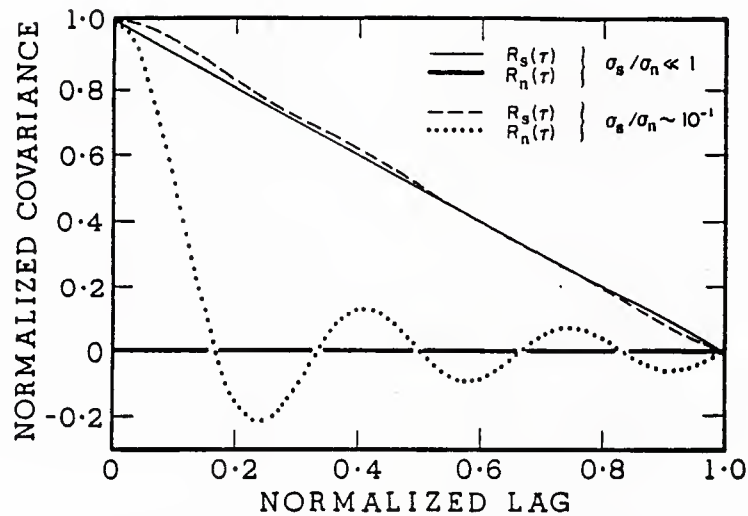


**Figure 4.1.** *Effect of band-limiting.* Normalized amplitude of signal and noise covariance vs. normalized lag  $\tau\sigma_s$  for different signal-to-noise bandwidth ratios. For  $\sigma_s/\sigma_n \ll 1$  the noise covariance (dark line) is taken to be zero for lags greater than zero, and the signal covariance (light line) is a "triangle" function. For  $\sigma_s/\sigma_n \sim 10^{-1}$  the noise covariance (dotted) decays as  $\text{sinc}(\tau\sigma_n)$ , and the signal covariance (dashed) shows some distortion due to band-limiting. In the band-limited case, the amplitude of the normalized noise covariance is not negligible compared to that of the signal for small values of normalized lag.

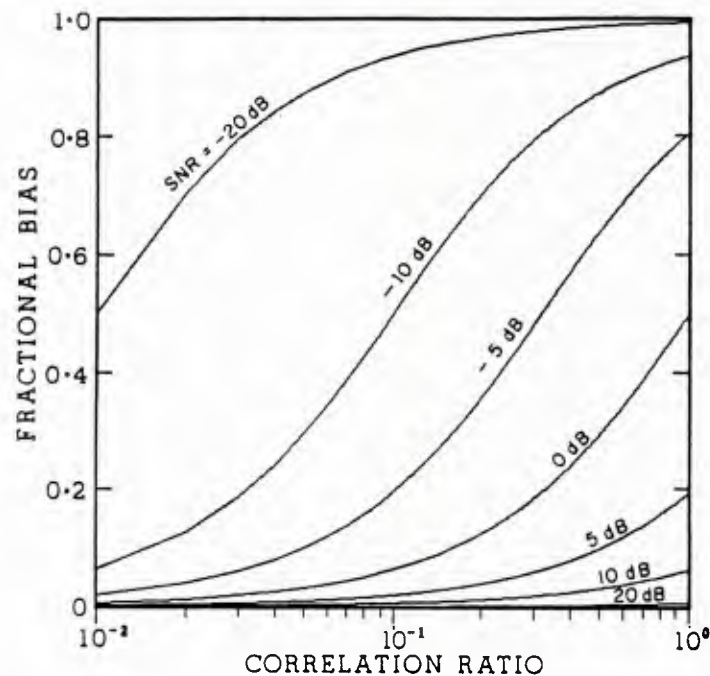


**Figure 4.2.** *Fractional bias vs. covariance amplitude ratio.* Fractional bias  $(\hat{T} - T) / T$  vs. normalized covariance amplitude ratio  $\alpha = R_n / R_s$ , and  $\text{SNR} = S^2/N^2$ . Normalized Doppler shift is fixed at  $\bar{\gamma} = 0.5$ . Values are computed from (4.14).

about zero frequency, then  $N_I$  and  $N_Q$  are statistically independent (Helstrom, 1968) and the signal-plus-noise covariance is

$$\begin{aligned}
 C_{sn}(\tau) &= \langle Z_{sn}(t) Z_{sn}^*(t + \tau) \rangle \\
 &= \langle S(t)S(t + \tau) \rangle \exp[i2\pi\bar{f}\tau] + \langle N_I(t)N_I(t + \tau) \rangle \\
 &\quad + \langle N_Q(t)N_Q(t + \tau) \rangle \\
 &= C_s(\tau) \exp[i2\pi\bar{f}\tau] + C_n(\tau)
 \end{aligned} \tag{4.11}$$

where  $C_s$  and  $C_n$  are the signal and noise covariance amplitudes, respectively. Note that with these assumptions the noise covariance appears only in the real part of  $C_{sn}$ .

Dividing (4.11) by the signal-plus-noise power,  $C_{sn}(0) = S^2 + N^2$ , produces the normalized covariance function

$$\begin{aligned}
 R_{sn}(\tau) &\equiv \frac{C_{sn}(\tau)}{C_{sn}(0)} = \frac{\text{SNR}}{\text{SNR} + 1} R_s(\tau) \exp[i2\pi\bar{f}\tau] \\
 &\quad + \frac{1}{\text{SNR} + 1} R_n(\tau)
 \end{aligned} \tag{4.12}$$

which can be used in place of  $C(\tau)$  in (4.8) to give the CP mean frequency estimator for signal plus band-limited noise

$$\hat{\bar{f}} = (2\pi\tau)^{-1} \arctan \left[ \frac{\sin(2\pi\bar{f}\tau)}{\cos(2\pi\bar{f}\tau) + \alpha(\tau) / \text{SNR}} \right] \tag{4.13}$$

where  $\alpha(\tau) = R_n(\tau) / R_s(\tau)$  is the normalized, noise-to-signal covariance amplitude ratio and  $\text{SNR} = S^2 / N^2$  is the signal-to-noise power ratio. The term  $(\alpha / \text{SNR})$  is identified as the biasing factor due to band-limited noise. Using the definitions of  $R_s$ ,  $R_n$ , and  $\text{SNR}$ , the biasing factor can be alternately expressed as the noise-to-signal covariance ratio  $C_n(t) / C_s(t)$ . The expression as used in (4.13) separates the part of the bias which is due to the relative magnitude of the noise covariance at non-zero lag from the part due to the noise power (covariance at zero lag). This separation facilitates much of the discussion which follows.

The expression (4.13) can be generalized by recognizing that the covariance for an operational Doppler system will be obtained at discrete lags related to the sampling interval for the complex envelope (see B.14). The parameters in (4.13) are non-dimensionalized using the nyquist frequency  $f_{nyq} = (2\tau_o)^{-1}$ , where  $\tau_o$  is the sampling interval. Taking  $\bar{\gamma} = \bar{f} / f_{nyq}$  as the non-dimensional Doppler shift, and  $\tau' = \tau f_{nyq}$  as the non-dimensional covariance

lag gives the normalized CP mean frequency estimator

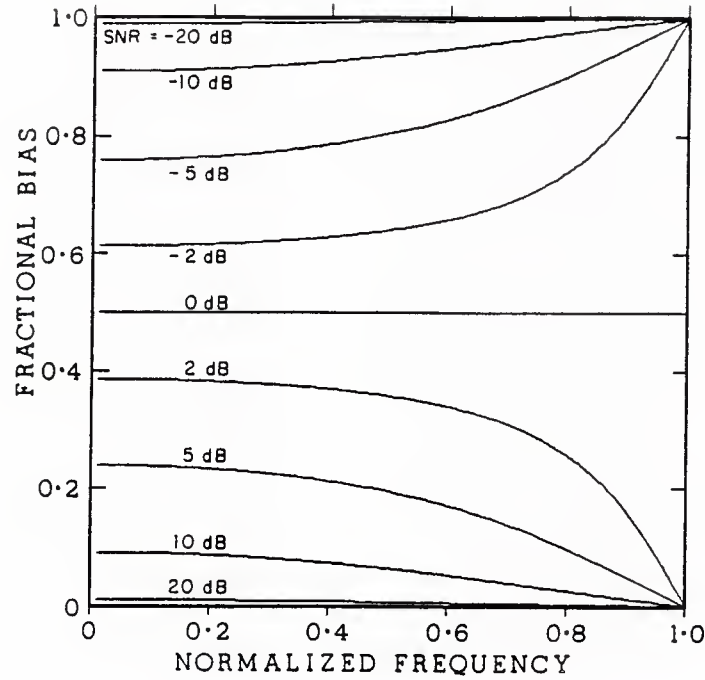
$$\hat{\bar{\gamma}} = \hat{\bar{f}} / f_{\text{nyq}} = \frac{1}{\pi} \arctan \left[ \frac{\sin \pi \bar{\gamma}}{\cos \pi \bar{\gamma} + \alpha(\tau') / \text{SNR}} \right] \quad (4.14)$$

If  $\text{SNR} \gg 1$  or  $R_s(\tau) \gg R_n(\tau)$  (equivalent to condition (4.9) being satisfied) then an unbiased mean frequency estimate is recovered from (4.14). Otherwise there is a bias which depends on SNR and the value of  $\alpha$  at lag  $\tau$ . The covariances  $R_s$  and  $R_n$  will both be positive for small lags and the effect of the biasing term will be to increase the magnitude of the denominator in (4.14), thereby decreasing  $\bar{\gamma}$  towards zero, regardless of whether the true mean frequency is positive or negative. The nature of the bias is to force the CP estimated Doppler shift towards the center of the frequency band passed by the receiver. In situations where pulse-to-pulse tracking of Doppler shift (Rowe and Young, 1979) is not used, the expressions (4.13) and (4.14) imply a bias towards zero velocity. For the more general case where tracking is employed, the bias is towards the velocity corresponding to the frequency at the center of the tracking band.

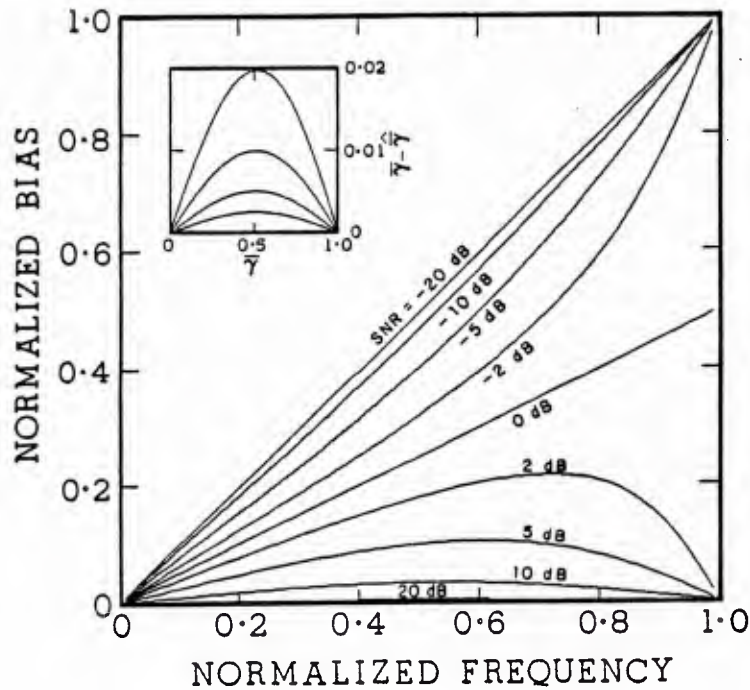
The behavior of the fractional bias  $(\bar{f} - \hat{\bar{f}}) / \bar{f}$  vs.  $\alpha$  for various values of SNR is shown in Fig. 4.2. The curves are computed from (4.14) assuming that  $\tau$  is the first available covariance lag for a given sampling interval ( $\tau = \tau_0$ ). The value of the true Doppler shift is fixed by taking  $\bar{\gamma} = 1/2$ , or  $\bar{f} = (4\tau_0)^{-1}$ . Choosing  $\bar{\gamma} = 1/2$  makes the bias magnitudes in Fig. 4.2 representative of the maximum expected values of both the fractional bias (Fig. 4.3) and the "absolute" bias (Fig. 4.4) for  $\text{SNR} > 0\text{dB}$ .

Figure 4.2 shows that fractional bias ranging from 7 to 50 percent may be expected as SNR falls from 10 dB to 0 dB with  $\alpha = 1.0$ . For  $\alpha = 0.1$ , the expected bias ranges from 1 to 7 percent for the same values of SNR. It was shown above that incoherent Doppler systems often have signal-to-noise bandwidth ratios of order 0.1. For systems incorporating Doppler frequency "tracking" (Rowe and Young, 1979), this ratio may approach 1.0. Depending on the nature of the signal and noise covariance functions, and the covariance lag used for a given system (e.g. Table 4.1), the resulting values of  $\alpha$  can easily be 0.10 or larger. Hence, for a "typical" incoherent Doppler sonar ( $0.10 \leq \alpha \leq 1.0$ ) operating in a low SNR environment ( $0 \text{ dB} \leq \text{SNR} \leq 10 \text{ dB}$ ) biasing due to band-limited noise may cause errors of 1 to 50 percent in the CP mean frequency estimate.

Hansen (1985b) presents an expression for a noise biased CP mean frequency estimator similar to (4.13). Hansen's expression does not include the parameter  $\alpha(\tau)$ , and hence is valid only in the limit as  $\tau \rightarrow 0$  where the normalized covariance amplitude ratio  $\alpha(\tau) = R_n(\tau) / R_s(\tau)$  is expected to approach 1.0. Considering only this limiting case obscures the role of the changes in  $\alpha(\tau)$  for different signal and noise covariance functions at finite lags. The importance of this effect can be seen from Fig. 4.2: Hansen's expression may significantly over-estimate the biasing effect if the true value of  $\alpha$  is less than one. As an extreme example, it has been shown by previous authors (Miller and



**Figure 4.3.** *Fractional bias vs. Doppler shift.* Fractional bias  $(\bar{\gamma} - \hat{\gamma}) / \bar{\gamma}$  vs. normalized Doppler shift  $\bar{\gamma} = \bar{\gamma} / f_{\text{nyq}}$ , and  $\text{SNR} = S^2 / N^2$ . Normalized covariance amplitude ratio is fixed at  $\alpha = 1.0$ . Values are computed from (4.14). Note that  $\bar{\gamma} = \bar{\gamma} / 2$  for all  $\bar{\gamma}$  at  $\text{SNR} = 1.0$  as a consequence of the half angle formula:  $\tan^{-1} [\sin \theta / (\cos \theta + 1)] = \theta / 2$ .



**Figure 4.4.** *Normalized bias vs. Doppler shift.* Normalized bias  $(\bar{\gamma} - \hat{\gamma}) / \bar{\gamma}$  vs. normalized Doppler shift and SNR. Parameters are as in Fig. 4.3. Inset shows normalized bias vs. normalized Doppler shift for SNR of 16 (upper line), 32, 64, and 128.



**Table 4.1.** *Covariance amplitude ratios for the MPL Doppler sonar.* Predicted values of normalized covariance amplitude ratio  $\alpha = R_n(k\tau_0) / R_s(k\tau_0)$  for the MPL Doppler sonar are given in the table. Values for lag 1 ( $k = 1$ ) and lag 2 ( $k = 2$ ) are shown for both Gaussian and boxcar spectral models. The sampling frequencies of 400 Hz and 500 Hz represent the two different values used during the MILDEX experiment.

CORRELATION RATIO				
	$f_0 = 500 \text{ Hz}$		$f_0 = 400 \text{ Hz}$	
<b>k</b>	<b>Gauss.</b>	<b>Boxcar</b>	<b>Gauss.</b>	<b>Boxcar</b>
<b>1</b>	<b>0.59</b>	<b>0.82</b>	<b>0.44</b>	<b>0.71</b>
<b>2</b>	<b>0.12</b>	<b>0.30</b>	<b>0.04</b>	<b>0.03</b>

Rochwarger, 1972; Sirmans and Bumgarner, 1975b) that the CP mean frequency estimator is unbiased for all SNR if the noise covariance is zero for lags greater than zero. This result is recovered from (4.13), but not from Hansen's expression, which predicts a bias dependent only on SNR.

The magnitude of the bias predicted by (4.13) depends on both  $(\alpha / \text{SNR})$  and  $\bar{\gamma}$ , the value of the true Doppler shift. The dependence of the fractional bias on the normalized Doppler shift  $\bar{\gamma}$  is illustrated in Fig. 4.3 for various values of SNR. The value of  $\alpha(\tau)$  is fixed at 1.0, so these curves represent the maximum expected biases. The fractional bias decreases with increasing values of  $\bar{\gamma}$  for  $\text{SNR} > 1$ , and increases with increasing  $\bar{\gamma}$  for  $\text{SNR} < 1$ . Significant values of fractional bias ( $\geq 10\%$ ) occur for all but the highest Doppler frequencies when SNR is between 10 dB and 0 dB. The magnitude of the normalized bias  $\bar{\gamma} - \bar{\gamma}$  as a function of  $\bar{\gamma}$  and SNR is shown in Fig. 4.4. For  $\text{SNR} > 1$  the bias has a maximum near  $\bar{\gamma} = 1/2$ . Note that the noise biasing term has the same effect as a DC offset in the in-phase channel, as described by Sirmans and Bumgarner (1975b), if SNR is considered as the signal-to-DC power ratio (compare their Fig. 9 to Fig. 4.4, inset).

**b. Correction of noise biasing: Noise covariance known.** The bias predicted by (4.13) can be corrected if the magnitude of the noise covariance can be determined for the lag at which the signal-plus-noise covariance is measured. Most Doppler systems measure the echo intensity (covariance at  $\tau = 0$ ) as well as the complex covariance at one or more non-zero lags. The available covariance lags

are determined by the sampling interval of the system. If the complex envelope is sampled at intervals  $\tau_o$ , then the covariance has the form  $C(k\tau_o)$ , where  $k = 0, 1, 2, \dots$  is the lag index (see B.14). The discretely sampled signal-plus-noise covariance for the first three lags ( $k = 0, 1, 2$ ) can be written

$$C_{sn}(0) = S^2 + N^2 \quad (4.15a)$$

$$C_{sn}(\tau_o) = S^2 R_s(\tau_o) \exp [i2\pi\bar{f}\tau_o] + N^2 R_n(\tau_o) \quad (4.15b)$$

$$C_{sn}(2\tau_o) = S^2 R_s(2\tau_o) \exp [i2\pi\bar{f}2\tau_o] + N^2 R_n(2\tau_o) \quad (4.15c)$$

If the noise covariance function (equivalently the noise spectrum) for the system is known and considered invariant from pulse to pulse, then  $C_n(\tau) = N^2 R_n(\tau)$  can be subtracted from  $C_{sn}(\tau)$  to produce an unbiased estimate of  $\bar{f}$  from any non-zero lag covariance (Miller and Rochwarger, 1970; 1972). In practice  $C_n(\tau)$  is rarely known a priori, but must be estimated from a time interval where there is no transmission, or from a small fraction of the return at far range where the echo intensity has decayed significantly.

The most straightforward way to correct for biasing due to correlated noise without making the assumption of time-invariant noise covariance is to choose the PRT to be longer than the decay time of the return echo. In this case a fraction of the return at far range will have virtually no contribution from the signal, and the noise covariance for a given lag can be estimated directly from  $C_{sn}$  (i.e. for  $\text{SNR} \ll 1$ ,  $C_{sn}(\tau) \approx C_n(\tau)$ ). A time-varying bias correction can then be made by subtracting estimates of  $C_n(\tau)$ , averaged over the "noise-only" region of a pulse or group of pulses, from the corresponding signal-plus-noise covariance. Unfortunately, extending the PRT by a sufficient amount to obtain accurate noise covariance estimates results in fewer pulses, and hence larger velocity variance, in a given averaging interval.

Underwood (1981) describes a bias-correction technique which uses estimates of noise power from a segment of the return where  $\text{SNR} \ll 1$  to eliminate the noise contribution to the signal-plus-noise envelope. Underwood's method is equivalent to subtracting estimates of  $\langle N_I \rangle$  and  $\langle N_Q \rangle$  from  $Z_{sn}(t)$  in (4.10) prior to computing the covariance. If  $N_I$  and  $N_Q$  do not have zero mean this processing step is necessary to prevent biasing from DC offsets in the I and Q channels (Sirmans and Bumgarner, 1975b). It is important to realize that correction for DC offsets in the received signal will not eliminate biasing due to non-zero noise covariance, and that knowledge of the noise power is insufficient to make a bias correction to the measured signal-plus-noise covariance unless  $R_n(\tau)$  is known.

The sensitivity of bias to SNR (Figs. 4.2 - 4.4) means that small fluctuations in the noise power from an assumed constant value, or uncertainties in the noise covariance estimate from a small sample can lead to significant bias errors even if correction is attempted. In a situation where noise power varies considerably over time and the noise covariance cannot be measured in isolation

( $\text{SNR} \geq 1$  over the PRT), bias correction by the methods described above is not possible. It is desirable to have a method of estimating a time-varying noise covariance directly from the measured values of the signal-plus-noise covariance without requiring  $\text{SNR} \ll 1$  over some portion of the measurement. Such a method is introduced in the next section.

c. *Correction of noise biasing: Noise covariance unknown.* Without prior knowledge or real-time measurement of the noise covariance, bias correction cannot be done by the methods described in section (4.3b). Instead, a correction method which accounts for the biasing effect of band-limited noise without requiring direct measurement of noise covariance is needed. This can be accomplished by introducing models of the signal and noise covariance functions. The covariance modeling approach allows correction for noise biasing using measurements of signal-plus-noise covariance at more than one lag. In addition to providing a bias correction technique, covariance models can be used to predict potential biasing problems for the general class of Doppler systems to which they apply. The modeling approach, of course, is only effective to the extent that the covariance functions of the model are representative of those encountered during operation of the instrument.

It is sufficient to model the covariance function amplitude as a function of lag. The environmentally dependent parameters, Doppler shift and SNR, are determined from the data. A composite covariance  $R_{\text{sn}}(\tau) = R_s(\tau) + R_n(\tau)$  is considered where  $R_s$  and  $R_n$  are the covariance function amplitudes normalized by the signal and noise power, respectively. This approach yields the normalized spectra directly from the model covariances through the Fourier transform relationship (4.7). Doppler radar data have been successfully modeled using a Gaussian shaped signal covariance plus additive noise (Sirmans and Bumgarner, 1975a). If the noise covariance is also taken as Gaussian shaped, the signal and noise model covariances can be written

$$R_s(\tau) = \exp \left[ -2\pi^2 \tau^2 b_s^2 \right] \quad (4.16a)$$

$$R_n(\tau) = \exp \left[ -2\pi^2 \tau^2 b_n^2 \right] \quad (4.16b)$$

where the bandwidth parameters  $b_s$  and  $b_n$  are determined by the -3 dB widths  $\sigma_s$  and  $\sigma_n$  of the signal and noise spectra, respectively ( $b_s = .425 \sigma_s$ , and  $b_n = .425 \sigma_n$  for the Gaussian case). The corresponding normalized spectra for signal and noise are

$$P_s(f) = (2\pi)^{-1/2} b_s^{-1} \exp \left[ -f^2 / 2b_s^2 \right] \quad (4.17a)$$

$$P_n(f) = (2\pi)^{-1/2} b_n^{-1} \exp \left[ -f^2 / 2b_n^2 \right] \quad (4.17b)$$

The expressions (4.16) and (4.17) will be called the Gaussian model.

Detailed studies of Doppler sonar data by Hansen (1984; 1986) and by the authors show that for incoherent systems, using gated pulses of the form

(4.1) and "boxcar" receive filters, the Gaussian model may not be appropriate. For systems where the bandwidth-pulse length product  $\sigma_n T_p$  is greater than one, the signal covariance can be successfully modelled as a "triangle" function, corresponding to a  $\text{sinc}^2$  signal spectrum. The noise covariance has the form of a sinc function due to the band-limiting effect of the "boxcar" receive filter (Fig. 4.1). Specifically, the signal and noise covariance functions are

$$R_s(\tau) = \begin{cases} (1 - b_s \tau) & |\tau| < b_s^{-1} \\ 0 & \text{otherwise} \end{cases} \quad (4.18a)$$

$$R_n(\tau) = \text{sinc} [ b_n \tau ] \quad (4.18b)$$

where here  $b_s = 1.13\sigma_s$ ,  $b_n = \sigma_n$ , and  $\text{sinc}(x) = \sin(\pi x) / \pi x$ . The corresponding normalized spectra are

$$P_s(f) = b_s^{-1} \text{sinc}^2 [ f / b_s ] \quad (4.19a)$$

$$P_n(f) = b_n^{-1} \Pi [ f / b_n ] \quad (4.19b)$$

where  $\Pi(x)$  is the "boxcar" function

$$\Pi(x) = \begin{cases} 1 & -\frac{1}{2} \leq x \leq \frac{1}{2} \\ 0 & \text{otherwise} \end{cases}$$

Since this model results from taking the transmitted pulse to be "boxcar" in time (see (4.1)) and the noise spectrum to be "boxcar" in frequency, (4.18) and (4.19) will be called the boxcar model. A comparison of the spectra predicted by the boxcar model to observed Doppler spectra for the system of Pinkel (1983a) is shown in Fig. 4.5.

The effect of band-limiting on the signal covariance, amounting to a convolution of (4.16a) and (4.18a) with  $\text{sinc}[b_n \tau]$ , is to cause a slight distortion of the covariance function shape (Fig. 4.1). This effect could easily be incorporated into the models. The error in computing  $\alpha(\tau)$  without considering the effect of band-limiting on the signal covariance is less than 5% for the application considered in this paper (Sec. 3.4). Thus, including this effect was considered unnecessary.

The Gaussian and boxcar models both yield solutions for  $R_s(\tau)$  and  $R_n(\tau)$  for any lag if the signal and noise bandwidths are known, and in principle allow a solution for the unknowns  $\bar{T}$ ,  $S^2$  and  $N^2$  from the three equations (4.15). This general solution is nonlinear and is quite sensitive to small deviations of the data from the model predictions. Bias corrections based on this solution performed poorly in tests using actual sonar data (Sec. 3.4). A much simpler and more robust solution, which requires only two autocovariance lags, is possible if the phase change of the signal is small over the sample interval. This condition



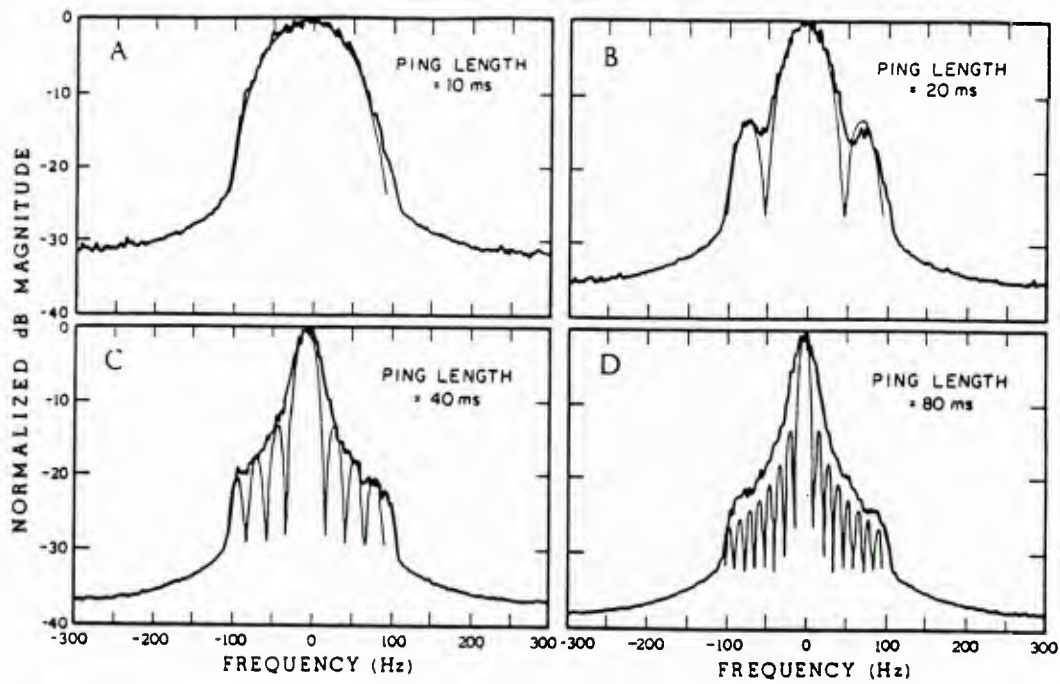


**Figure 4.5.** Normalized spectra for the MPL Doppler sonar. Observed spectra (dark lines) for pulse lengths of a) 10 ms, b) 20 ms, c) 40 ms, and d) 80 ms are compared with spectra predicted by the boxcar model (light lines). Periodogram spectral estimates are made from a 256 point FFT of the return from a single pulse and averaged over 100 pulses to produce the observed spectra. The data have been passed through a 100 Hz low-pass filter in the receiver prior to processing. The model spectra, initially computed from (4.19) with  $-97.5 \text{ Hz} \leq f \leq 97.5 \text{ Hz}$ ,  $b_s = T_p^{-1}$ ,  $b_n = 195 \text{ Hz}$ , and  $\bar{f} = 0$ , are slid to the left to simulate the approximate -12 Hz Doppler shift in the observed data. Adapted from Hansen (1984), used with permission.

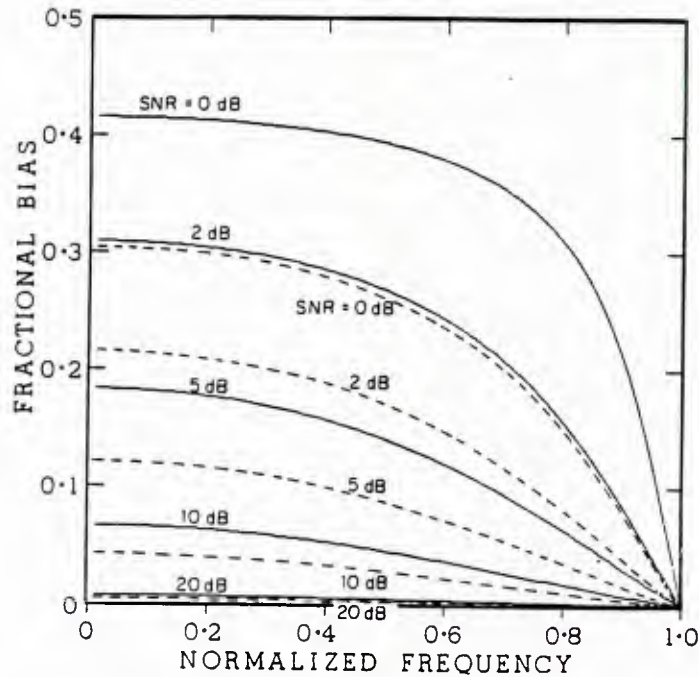


**Figure 4.8.** Fractional bias vs. Doppler shift for the MPL Doppler sonar. Fractional bias  $(\hat{f} - \bar{f}) / \bar{f}$  vs. normalized Doppler shift  $\bar{\gamma} = \bar{f} / f_{nyq}$ , and  $\text{SNR} = S^2 / N^2$  for the MPL Doppler sonar using the Gaussian spectral model (dashed line) and the boxcar spectral model (solid line). Values are computed from (4.14) with  $f_o = 400 \text{ Hz}$ ,  $f_{nyq} = f_o / 2 = 200 \text{ Hz}$ ,  $\tau' = \tau_o f_{nyq} = 1/2$  and  $\alpha(\tau') = 0.44$  (Gaussian model) or  $\alpha(\tau') = 0.71$  (boxcar model).

can be expressed in terms of the magnitude of the mean Doppler shift compared to the Nyquist frequency. Assume that  $\bar{T}$  is being estimated from the first non-zero lag covariance (4.15b). If  $|\bar{T}| \ll (4\tau_o)^{-1} = f_{\text{nyq}} / 2$  then  $|2\pi \bar{T} \tau_o| \ll \pi / 2$  and  $\cos(2\pi \bar{T} \tau_o) \approx 1$ . This implies that the magnitude of  $C_{\text{sn}}(\tau_o)$  can be well approximated by

$$|C_{\text{sn}}(\tau_o)| \approx C_s(\tau_o) + C_n(\tau_o) = S^2 R_s(\tau_o) + N^2 R_n(\tau_o) \quad (4.20)$$

so that  $S^2$  and  $N^2$  (equivalently SNR) can be estimated from (4.15a) and (4.20). The values of  $R_s$  and  $R_n$  are obtained from the model covariances (4.16) or (4.18) using values of signal and noise bandwidth appropriate for the system of interest. Bias correction can be accomplished by subtracting the value of  $N^2 R_n(\tau_o)$  estimated using (4.15a) and (4.20) from (4.15b), and computing  $\bar{T}$  according to (4.8). The conditions for validity of this approximation can be generalized for any covariance lag by requiring

$$|\bar{T}| \ll (2k)^{-1} f_{\text{nyq}} \quad (4.21)$$

where  $k$  is the lag index. Bias correction can be made using any two lags which satisfy (4.21).

#### 4.4 Bias correction trials for the MPL Doppler sonar

A narrow-beam, high-power, pulse-to-pulse incoherent Doppler sonar system has been developed at the Marine Physical Laboratory (MPL) of the Scripps Institution of Oceanography to measure the velocity field of the upper ocean. In a typical deployment the MPL Doppler system uses multiple downward-slanting beams to provide profiles of velocity from  $\sim 100$  m to  $\sim 1200$  m in depth with  $\sim 20$  m depth resolution and precision of order  $.01 \text{ m s}^{-1}$  (Pinkel, 1983a). Under some conditions the far ranges of such profiles are contaminated by additive noise and show a biasing towards zero Doppler shift (zero velocity) as described in Section 3.3a. Bias correction trials for velocity data collected during October and November of 1983 as part of the Mixed Layer Dynamics Experiment (MILDEX) are described in this section. Details of the sonar configuration during the experiment can be found in Section 1.3.3 and Table 1.1.

For a system where accurate models of signal and noise covariance are available, knowledge of the signal and noise bandwidths at the receiver output is sufficient to predict potential biasing problems, as well as correct for biasing if it exists. The -3 dB signal bandwidth for the MPL Doppler sonar is well approximated by  $\sigma_s = 0.885 T_p^{-1}$ . The noise bandwidth, taken at the -3 dB points of the final receive filter, is  $\sigma_n = 195 \text{ Hz}$ . A pulse length of  $T_p = 30 \text{ ms}$  was used during the MILDEX experiment, giving  $\sigma_s / \sigma_n = 29.5 / 195 = 0.15$ . The relatively large value of the bandwidth ratio implies that the noise cannot be

considered "white" (see (4.9)) and that biasing at low SNR is potentially important.

By using the appropriate covariance model, and estimates of  $\sigma_s$  and  $\sigma_n$  for the system, the covariance amplitude ratio  $\alpha(\tau)$  can be computed. Values of  $\alpha$  computed from both the Gaussian and boxcar covariance models using the estimates of  $\sigma_s$  and  $\sigma_n$  given above for the MPL Doppler sonar are shown in Table 4.1. Once  $\alpha$  is known, the bias for a given  $\tau$  can be predicted for various SNR using (4.13). For the values of  $\alpha$  given in Table 4.1, Fig. 4.2 shows that significant bias is expected in velocities computed from lag 1 covariances for  $\text{SNR} \leq 10$  dB, with lag 2 biases being somewhat less. Although the biasing effect can be reduced by using larger lags, the uncertainty in the mean frequency estimator increases sharply for increasing lags (Miller and Rochwarger, 1972) making this approach undesirable. The magnitude of the predicted lag 1 bias vs. normalized Doppler shift for the MPL sonar using both Gaussian and boxcar models is shown in Fig. 4.6.

The difficulty in bias correction for the MILDEX sonar data is twofold: first, the noise power level ( $N^2$ ) varies considerably over time and may vary from one sonar beam to another, making the use of a constant noise threshold inadequate. Second, the PRT is short enough that the echo has not completely died away before the next pulse is transmitted. Thus, no measurements of noise covariance are available during data collection. This situation discourages use of the simplest correction methods, which assume that the noise covariance is time-invariant and measurable, and makes solutions to (4.15) using spectral models to predict  $R_s$  and  $R_n$  the most appealing method. Since the RMS Doppler shift for the MILDEX data set (computed from non-biased data) was  $O(10 \text{ Hz}) \ll f_{\text{nyq}} / 2 = 100 \text{ Hz}$ , it was decided to use the "small  $\bar{f}$ " assumption (4.21) to obtain approximate solutions to (4.15) using covariance measured at lag pairs  $k = (0,1)$ ,  $(1,2)$ , or  $(0,2)$ .

Previous results (e.g. Fig. 4.5) indicated that the boxcar model would best represent the data from the MPL sonar during the MILDEX experiment. A more sensitive test was performed by comparing observed covariance slopes to the slopes predicted by the models in regions of high SNR (maximum slope) and low SNR (minimum slope). Results are shown in Fig. 4.7. Correction trials using the  $k = (0,1)$  and  $(0,2)$  covariance pairs showed poor results due to the deviation of observed slopes from values predicted by the spectral models. The Gaussian model significantly underestimates the minimum slope and overestimates the maximum slope for the  $k = (0,1)$  lag pair (Fig. 4.7a). The boxcar model overestimates the minimum slope and underestimates the maximum slope (Fig. 4.7b) which is due in part to the smoothing of the covariance peak at  $\tau = 0$  from the convolution neglected in the derivation of (4.18a). Both models do a better job of predicting the observed slopes for the  $k = (1,2)$  lag pair. The Gaussian model now overestimates the minimum slope, but does a fair job of predicting the maximum slope (Fig. 4.7c). The good agreement of the  $k = (1,2)$  covariance pair with the predictions of the boxcar model (Fig. 4.7d) prompted its use in the final correction scheme.

The bias correction was implemented by the following four steps: 1) the signal-plus-noise covariance  $C_{sn}(k\tau_o)$ , computed according to (B.14b) for each



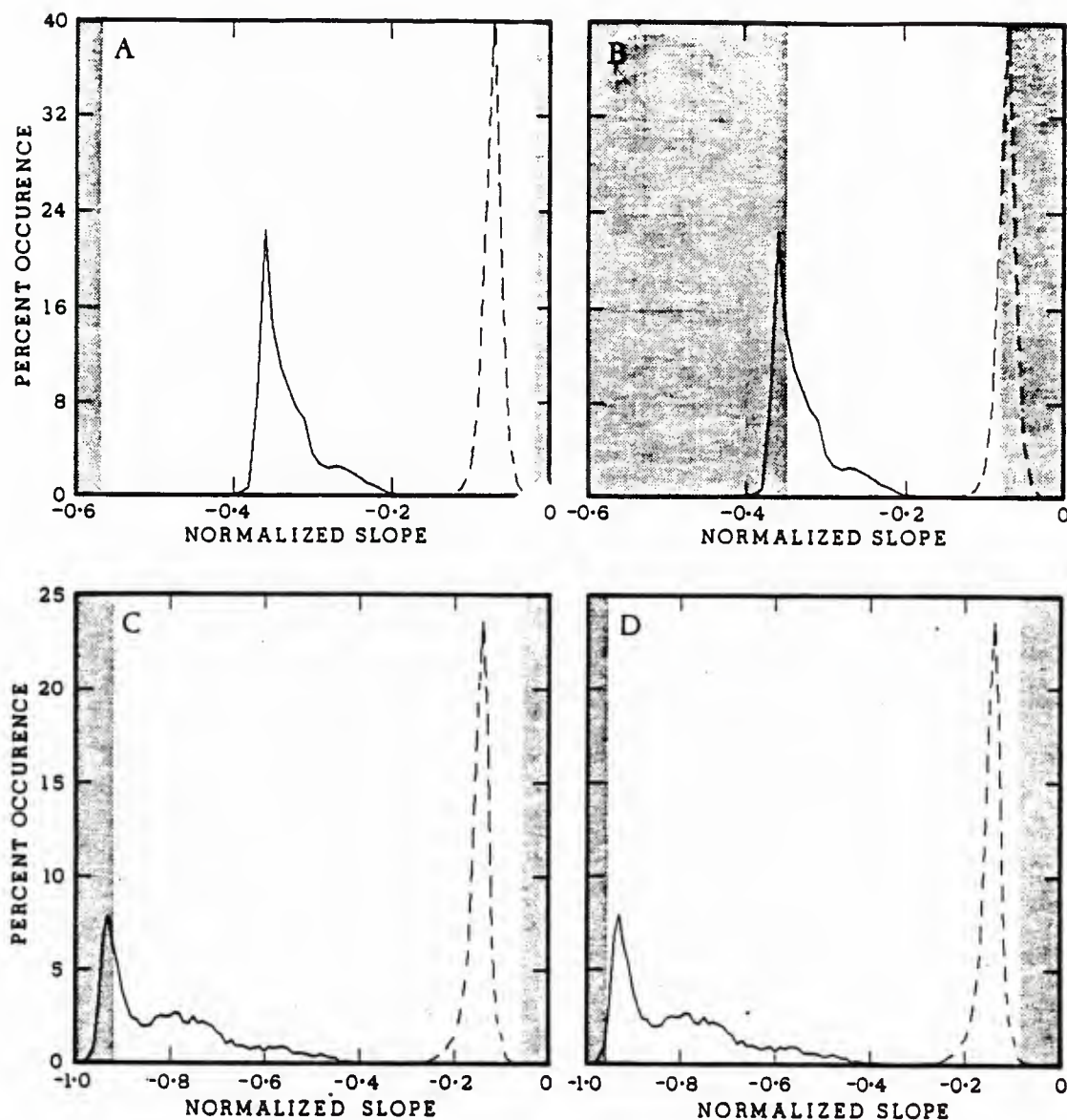


**Figure 4.7.** *Covariance slopes: Model vs. data comparison.* Histograms of normalized covariance slopes for the MPL Doppler sonar computed from 6400 3-minute average covariance profiles. Upper two panels show histograms of  $\langle (C_{nn}(\tau_0) - C_{nn}(0)) / C_{nn}(0) \rangle$  where the brackets represent an average of the 5 range bins of each profile with the smallest SNR (minimum slope, solid lines) or an average of the 5 range bins with the largest SNR (maximum slope, dashed lines). Boundaries of the shaded areas indicate minimum and maximum autocovariance slopes predicted by the Gaussian (a) and boxcar (b) spectral models. Lower two panels show histograms of  $\langle (C_{nn}(2\tau_0) - C_{nn}(\tau_0)) / C_{nn}(\tau_0) \rangle$  computed in the same manner as above and compared with the predictions of the Gaussian (c) and boxcar (d) models. The models are successful to the extent that the observed slopes from the small and large SNR regions have values which are near the predicted minimum and maximum slopes, respectively, yet remain within the unshaded area.



pulse, was averaged over 90 transmit sequences to produce a 3-minute average covariance profile; 2) noise covariance profiles were estimated from the signal-plus-noise covariance using the  $k = (1,2)$  lag pair under the assumption (4.21), and covariance amplitudes  $R_s$  and  $R_n$  predicted from the boxcar model with the values of  $\sigma_s$  and  $\sigma_n$  given earlier in this section; 3) the average noise covariance  $\bar{C}_n(\tau_o)$ , was computed over the low SNR region of each profile with the restriction  $0 \leq \bar{C}_n(\tau_o) \leq \text{Re} \{C_{sn}(\tau_o)\}$ ; 4) the noise covariance estimate was subtracted from the real part of the measured signal-plus-noise covariance for each range gate to produce an unbiased estimate of velocity from

$$\hat{v} = \frac{c}{4\pi f_c \tau_o} \arctan \left[ \frac{\text{Im} \{C_{sn}(\tau_o)\}}{\text{Re} \{C_{sn}(\tau_o)\} - \bar{C}_n(\tau_o)} \right] \quad (4.22)$$

It was found that corrections based on the method outlined above tended to over-compensate for the bias error, making velocities at far range too large. It was anticipated that the noise covariance would be overestimated by approximately 10% when using the  $k = (1,2)$  pair since (4.21) is not strongly satisfied for lag 2. However, direct comparison of measured and estimated values of noise covariance from a short section of data where independent noise measurements were available showed that  $\bar{C}_n$  overestimated the true value by  $\sim 30\%$ . To correct for this overestimation the value of  $\bar{C}_n$  was reduced by 30% prior to step 4.

It was also found that velocity "spiking" sometimes occurred at far range due to very small values of the denominator in (4.22) when  $\bar{C}_n \approx \text{Re} \{C_{sn}\}$ . This problem was diminished by using a power series expansion of the denominator in terms of  $\epsilon = \bar{C}_n / \text{Re} \{C_{sn}\}$ :

$$\frac{\text{Im} \{C_{sn}\}}{\text{Re} \{C_{sn}\} - \bar{C}_n} = \frac{\text{Im} \{C_{sn}\}}{\text{Re} \{C_{sn}\} (1 - \epsilon)} = \frac{\text{Im} \{C_{sn}\}}{\text{Re} \{C_{sn}\}} (1 + \epsilon + \dots \epsilon^P) \quad (4.23)$$

truncated at  $P = 5$ .

Results of the bias correction for data sections with varying degrees of noise contamination are shown in Fig. 4.8. Comparison of corrected and uncorrected velocity profiles shows that biasing can be important over a depth range of as much as 1/3 of the total depth of the profile.

#### 4.5 Chapter summary

The mean frequency estimator based on the covariance processing (CP) or "pulse-pair" technique is unbiased in the presence of true "white" noise ( $R_n(\tau) = 0$  for  $\tau > 0$ ). Although the case of true "white" noise does not arise in practice, the "white" noise approximation can be made if  $\sigma_n \gg \sigma_s$ , where  $\sigma_n$  is the -3 dB bandwidth of the receive filter and  $\sigma_s$  is the -3 dB signal bandwidth.

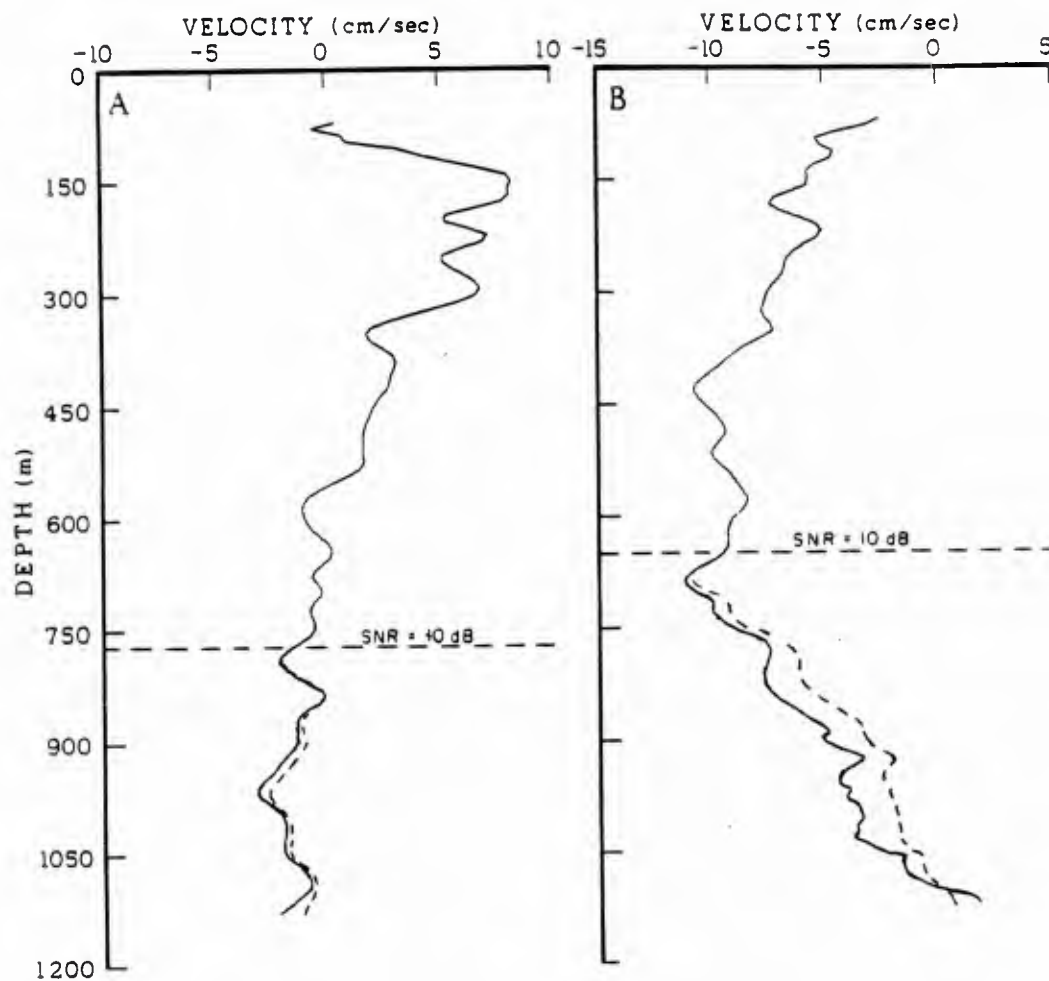


**Figure 4.8.** *Bias corrected velocity profiles.* Mean velocity profiles from the MPL Doppler sonar for two different sections of the MILDEX experiment. Data represent the mean after averaging 50 3-minute profiles (2.5 hr). Results are shown for uncorrected profile (dashed line) and profile after final bias correction (solid line). Horizontal dashed lines show range where  $\text{SNR} = 10 \text{ dB}$ . SNR is computed using the same method as for the final bias correction.

If this approximation is not valid, then the signal must be considered corrupted by additive, band-limited noise, and the CP estimator will show a bias at low SNR. The magnitude of bias for the CP mean frequency estimator in the presence of band-limited noise can be expressed in terms of the true mean,  $\bar{f}$ , the signal-to-noise power ratio, SNR, and the normalized, noise-to-signal covariance amplitude ratio,  $\alpha(\tau)$ . The nature of the bias is to force the CP estimated Doppler shift towards the center of the frequency band passed by the receiver. Pulse-to-pulse incoherent Doppler systems are often operated under conditions of low SNR and large signal-to-noise bandwidth ratio (large  $\alpha$ ) where biasing effects are important. For a typical operating range of an incoherent Doppler system ( $0 \text{ dB} \leq \text{SNR} \leq 10 \text{ dB}$  and  $0.1 \leq \alpha \leq 1$ ) bias errors as large as 7 to 50 percent may be expected for the CP mean frequency estimate.

Several methods of bias correction are available. The simplest correction methods assume that the noise covariance is known or measurable, and may also assume that noise power is time-invariant. The presence of time-varying noise power combined with inadequate or unavailable noise covariance measurements may make the use of these techniques impossible. For systems where multiple lags of covariance are measured, a method of estimating time-varying noise covariance and SNR has been presented. The method can be used even when no direct measurements of noise covariance are available, but does require knowledge of  $\sigma_s$  and  $\sigma_n$  as well as models for signal and noise covariance functions. In addition to providing a generalized bias correction method, covariance models allow prediction of potential bias effects for the class of Doppler systems to which they apply.

The data from a pulse-to-pulse incoherent Doppler sonar were found to be in good agreement with a simple covariance model, and the covariance modelling technique of bias correction was applied to oceanic velocity measurements made using the CP mean frequency estimator. Biasing was found to be important in regions of low SNR which may be as much as 1/3 of the total depth of the profile.

## APPENDIX A

### Correction for platform motion

#### A.1 Platform motion

Correction for platform motion requires consideration of azimuthal rotation (heading) and tilts in two axes (equivalent to pitch and roll) relative to a fixed reference frame. The reference frame used for the analysis of platform motion is a right-handed coordinate system with origin along the centerline of FLIP's hull at the depth of the sonar mounting deck. This coordinate system is shown in plan view in Fig. A.1. Positive x and y directions are to the East and North, respectively, and z is positive upwards along the axis of the local gravitational vector. The reference frame is equivalent to a standard geographic tangent plane coordinate system (Neumann and Pierson, 1966).

Ship's heading was maintained by a servo controlled bi-directional thruster mounted beneath the waterline on FLIP's hull. The thruster was linked to the ship's gyrocompass through an adjustable azimuth control device which could be programmed to maintain a desired heading with very high accuracy in winds up to  $15 \text{ m s}^{-1}$ . Heading values, measured in degrees clockwise from North, were recorded directly from the gyrocompass controller at a sampling rate of 4 Hz.

The tilt of the platform with respect to the reference frame was sensed by two accelerometers mounted to FLIP's hull on the same deck which provided the sonar mounts (Fig. 1.7). Tilt is defined in terms of "pitch" and "roll" angles measured by the accelerometers. It is shown in Section A.3 that for the three minute averaging intervals used in the analysis of velocity data, the accelerometers can unambiguously measure tilts of  $0.4^\circ$  or greater. Note that the pitch and roll axes defined for the accelerometer measurements do not correspond to the fore-aft and port-starboard directions on the ship (Fig. A.1).

#### A.2 Heading correction

There are four values of heading ( $45^\circ$ ,  $135^\circ$ ,  $225^\circ$ , and  $315^\circ$ ) which result in one of the downward-slanting sonars pointing in the direction of each of the four compass points. These are called the four primary heading directions, each separated by  $90^\circ$  in azimuth. The thruster and azimuth controller were used to maintain the ship's heading to within a few degrees of one of the four primary heading directions during the majority of the experiment (Fig. 1.5). When the ship is oriented in one of the primary heading directions, the slant velocities from the sonars can be interpreted directly in terms of East (u) and North (v) components without the necessity of azimuthal coordinate rotation. Due to the high degree of heading stability provided by the thruster, no correction was made for the azimuthal motion of the platform other than to properly account for the  $90^\circ$  incremental heading changes as described below.



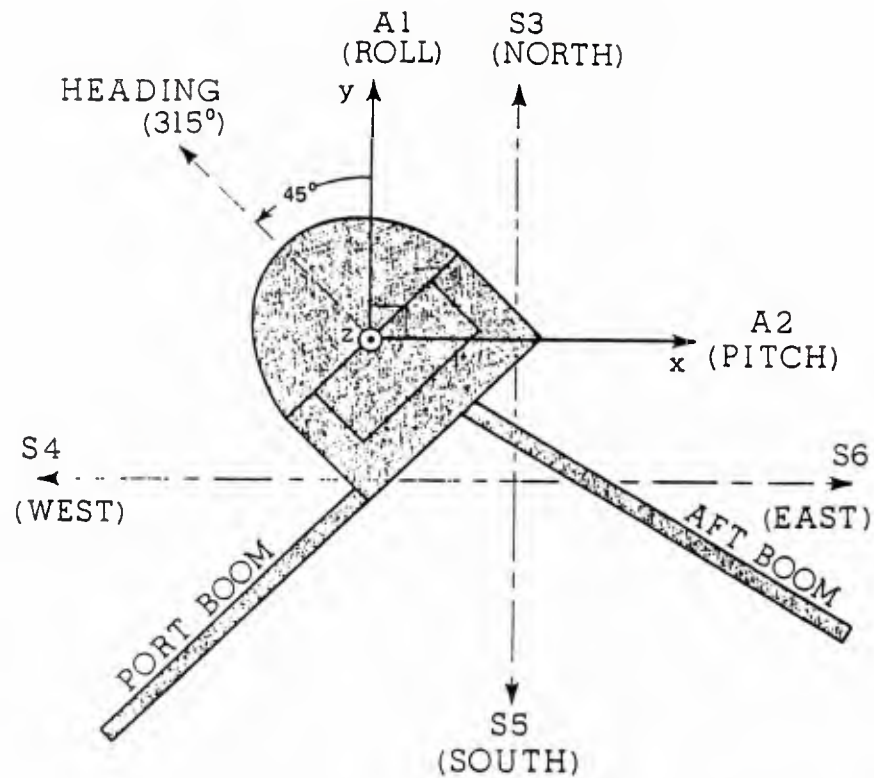


**Figure A.1.** Plan view of FLIP coordinate system. The reference (geographic) coordinate system is defined relative to the centerline of FLIP's hull. Solid arrows indicate positive directions for  $x$  (East) and  $y$  (North) axes. The  $z$ -axis is positive upwards. The relationship between sonar and accelerometer identification codes and geographic coordinates is shown for a heading of  $315^\circ$ . This relationship changes as the ship's heading changes (Table A.1). The offset of the origins of the sonar beams from  $(x, y, z) = (0, 0, 0)$  is ignored in the analysis.

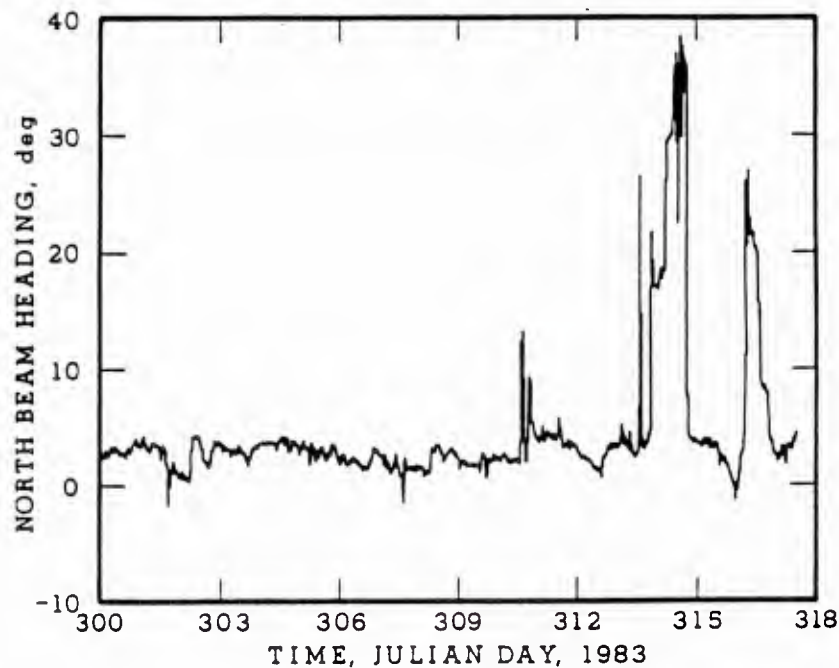


**Figure A.2.** Heading of the North beam. One of the four downward-slanting sonar beams is always in the "North quadrant" ( $\pm 45^\circ$  from  $0^\circ$ ) and is designated the "North beam". Heading for the North beam is shown in degrees, clockwise from North, after correction according to Table A.1. Heading for the East, South, and West beams is found by adding 90, 180, and 270 degrees, respectively, to the heading of the North beam.

The relationship of the sonars and accelerometers to the geographic coordinate system for the four primary heading directions is given in Table A.1.

**Table A.1. Heading correction table** The relationship of sonar and accelerometer identification codes to the geographic coordinate system for the four primary headings is shown. For the actual heading correction, values within the bounds shown in column two were considered to be at the primary heading.

HEADING CORRECTION TABLE							
Nominal Heading (deg)	Values Accepted (deg)	Beam Direction				Tilt Angle	
		E	S	W	N	Pitch	Roll
45	$0 < \theta \leq 90$	S3	S6	S5	S4	A1	-A2
135	$90 < \theta \leq 180$	S4	S3	S6	S5	-A2	-A1
225	$180 < \theta \leq 270$	S5	S4	S3	S6	-A1	A2
315	$270 < \theta \leq 360$	S6	S5	S4	S3	A2	A1

To facilitate data processing, each sonar of the six sonar array, and the two accelerometers, were given identification codes. The identification codes for the four downward-slanting sonars are S3 through S6, and the accelerometers are identified by A1 and A2. For a heading of  $315^\circ$ , sonars S3, S4, S5, and S6 point in the direction of North, West, South, and East, respectively, accelerometer A1 senses tilts in the y-z plane, and A2 senses tilts in the x-z plane (Fig. A.1). During processing, buffers are set up to accept sonar data for North, South, East and West pointing beams, and accelerometer data corresponding to positive pitch and roll angles. By changing the identification code (and sign if necessary) of the data which goes into each of the buffers according to Table A.1 after  $90^\circ$  incremental heading changes, data from the sonar array can be treated as though it were measured from four beams fixed in the direction of the four compass points, with pitch and roll angles measured in the x-z and y-z planes. The heading of the North beam after correction according to Table A.1 is shown in Fig. A.2. During the calm period from day 300 to 313 the heading was maintained at an average value of  $2.8^\circ$  East of North with a standard deviation of about  $1^\circ$ . From day 313 to 315 high winds and large swell caused deviations of as much as  $30^\circ$  from the desired heading. The heading of the East, South, and West beams are given by adding  $90^\circ$ ,  $180^\circ$ , and  $270^\circ$ , respectively, to the heading of the North beam.

### A.3 The accelerometer measurements

In order for the accelerometers to be used effectively as "inclinometers" to measure platform tilt, the distinction must be made between apparent accelerations, due to the inclination of the platform in the earth's gravitational field, and true accelerations, due primarily to surface waves. It is useful to define a threshold value of tilt where the apparent accelerations dominate over true accelerations. Beyond this threshold value, accelerometer measurements can be unambiguously interpreted as platform tilt and converted to degrees using

$$\theta = (180/\pi) \sin^{-1}(a/g) \quad (\text{A.1})$$

where  $a$  is the apparent acceleration measured by the instrument and  $g$  is the gravitational constant ( $g = 980 \text{ cm s}^{-2}$ ). For low frequency motion (less than 0.01 Hz), the true accelerations are a very small fraction of  $g$  and the measurements can be directly interpreted in terms of tilt. For higher frequency motions, the true accelerations may be as much as a few hundredths of  $g$ , and more care is needed in interpreting the measurements.

Wind waves and swell can cause significant horizontal and vertical accelerations of the platform in the frequency band between 0.03 and 0.2 Hz. The observed response of FLIP to ocean waves has been summarized by Spiess (1968). He shows that for frequencies greater than 0.05 Hz the vertical motion of the platform is less than 10% of the surface wave amplitude, and the horizontal motion of the laboratory deck level is approximately equal to the surface wave amplitude. Rudnick (1964) gives some of the data on which these conclusions were based. Values of rms true acceleration reported by Rudnick for the frequency band between 0.01 and 0.25 Hz are  $18 \text{ cm s}^{-2}$  for horizontal acceleration and  $2 \text{ cm s}^{-2}$  for vertical acceleration. Following the suggestion of Rudnick, I have taken four-fifths of the horizontal acceleration to be due to true acceleration, with the remainder being due to tilt.

The wave conditions during MILDEX (rms wave height  $\sim 1 \text{ m}$ ) were similar to those during the experiment reported by Rudnick (maximum wave height 2-3 m) so that the latter can be used as a guide to determine the threshold for unambiguous tilt measurement. The accelerometer data used in the MILDEX analysis were recorded every 0.25 s and averaged over 3 min. The dominant contribution to the true acceleration comes from wave periods of order 10 s, so that estimates of rms true acceleration for the 3 min average data should be reduced by about a factor of 3 from the values given by Rudnick. This gives an estimated rms horizontal acceleration of about  $6 \text{ cm s}^{-2}$  and a rms vertical acceleration of about  $0.6 \text{ cm s}^{-2}$  for the MILDEX data. The effect of the small vertical acceleration (about  $7 \times 10^{-3}g$ ) will be ignored in the analysis. Using (A.1), the estimated horizontal acceleration gives a tilt measurement threshold of  $\sim 0.4^\circ$ . It can be shown that significant errors in the estimates of vertical velocity and stress result from tilts of order  $0.5^\circ$  or greater, hence the tilt angle threshold of  $0.4^\circ$  is adequate for the purpose of correction for tilt errors in the 3 min average velocity data.

#### A.4 The rotation matrices

In order to formalize the tilt correction, it is necessary to introduce rotation angles relating the tilted frame to the reference frame. Coordinate rotation is typically described in terms of the Euler angles (Teichmann, 1969). The axis and angle conventions adopted for the FILP analysis are shown in Fig. A.3. The  $\tilde{i}$ ,  $\tilde{j}$ , and  $\tilde{k}$  unit vectors are in the East, North, and "up" directions, respectively, and the Euler angles are

$$\begin{aligned}\phi &= \text{pitch angle, positive for } +\tilde{i} \text{ vector (East beam) depressed} \\ \rho &= \text{roll angle, positive for } +\tilde{j} \text{ vector (North beam) depressed} \\ &\quad \text{(measured relative to pitched axes)}\end{aligned}$$

The angles measured by the accelerometers are not exactly the Euler angles, but for simplicity in the analysis it is convenient to assume that they are equivalent. This assumption introduces an error proportional to  $\sin \theta$ , where  $\theta$  is the tilt angle. By defining the first rotation angle (pitch) to be the smaller of the two observed tilt angles the resulting error is reduced to order  $4 \times 10^{-3}$  which can be safely neglected in the following analysis.

A vector in the rotated frame can be expressed in the reference frame using the rotation matrices

$$M_\phi = \begin{bmatrix} \cos\phi & 0 & \sin\phi \\ 0 & 1 & 0 \\ -\sin\phi & 0 & \cos\phi \end{bmatrix} \quad (\text{A.2})$$

$$M_\rho = \begin{bmatrix} 1 & 0 & 0 \\ 0 & \cos\rho & \sin\rho \\ 0 & -\sin\rho & \cos\rho \end{bmatrix} \quad (\text{A.3})$$

Given a vector  $\tilde{r}' = (r'_x, r'_y, r'_z)$  in the rotated frame, the corresponding vector in the reference frame is

$$\begin{aligned}\tilde{r} &= M_\phi M_\rho \tilde{r}' \\ &= \begin{bmatrix} \cos\phi r'_x - \sin\phi \sin\rho r'_y + \sin\phi \cos\rho r'_z \\ \cos\rho r'_y + \sin\rho r'_z \\ -\sin\phi r'_x - \cos\phi \sin\rho r'_y + \cos\phi \cos\rho r'_z \end{bmatrix} \quad (\text{A.4})\end{aligned}$$

For a slant velocity vector measured at some range  $r$  along the beam axis in the rotated frame, the correction for platform motion can be considered in two stages. First, the correction for *translation* of the velocity vector to a new position in space, and second, the correction for the *rotation* of the vector from its nominal angle. The implementation of these two stages of correction will be discussed below.



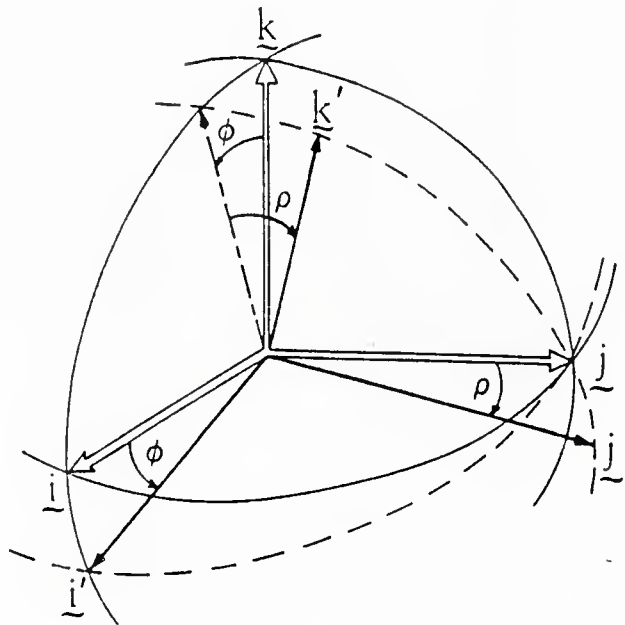


**Figure A.3.** *Rotation of coordinates.* Starting from the reference frame with the unit vectors  $\underline{i}$ ,  $\underline{j}$ , and  $\underline{k}$ , in the direction of North, East, and "up", respectively, the system is first rotated about the  $\underline{j}$  axis through the pitch angle  $\phi$ . Next, the system is rotated about the  $\underline{i}'$  axis through the roll angle  $\rho$ , giving the unit vectors  $\underline{i}'$ ,  $\underline{j}'$ , and  $\underline{k}'$ . Any vector in the rotated frame can be expressed in the reference frame using the rotation matrices (see text).

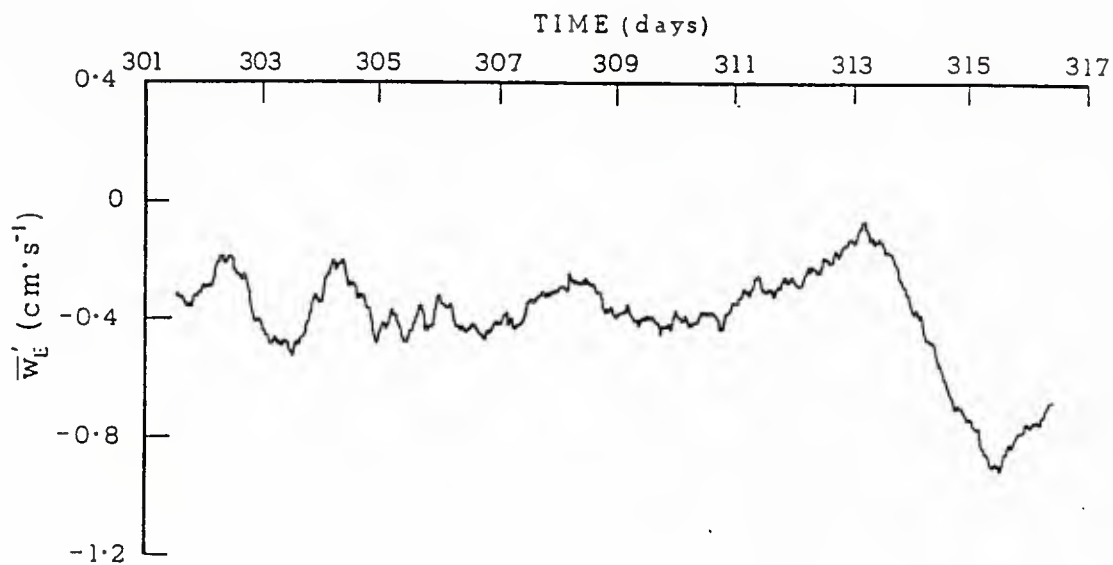


**Figure A.4.** *Uncorrected vertical velocity: East axis.* Vertical velocity is estimated from the uncorrected slant velocities of the East and West beams using (A.25). Significant offsets from zero and excursions of order  $0.4 \text{ cm s}^{-1}$  can be seen. The slant velocities are averaged over 312 m in depth and 30 min in time prior to vertical velocity computation, and the resulting vertical velocity time series is averaged with a 24.5 hr running mean filter before plotting.

### A.5 Translation correction

The slant velocity measured in the reference frame at range  $r$  along the beam axis is considered to be at position  $(x_0, y_0, z_0)$ , and at angle  $\theta_0$  from the horizontal, where  $\theta_0$  is the depression angle of the beam. If the velocity measured in the tilted frame is written as  $\underline{V}'(x', y', z')$  then the velocity corrected for the translation to the nominal position  $(x_0, y_0, z_0)$  (but not corrected for rotation) is given by

$$\underline{V}'(x_0, y_0, z_0) = \underline{V}'(x', y', z') + d\underline{V}' \quad (\text{A.5})$$

where

$$d\underline{V}' = \frac{\partial \underline{V}'}{\partial x} dx + \frac{\partial \underline{V}'}{\partial y} dy + \frac{\partial \underline{V}'}{\partial z} dz$$

From (A.5) it is clear that the translation correction requires knowledge of the distance between the measurement points in the tilted frame and the reference frame, and the derivative of velocity along the path connecting the two points. In practice, only the derivative of velocity along the beam axis is known, and some approximation to (A.5) must be made. It will be assumed that vertical derivatives are much larger than horizontal derivatives in the geographic coordinate system ( $\partial/\partial z \gg \partial/\partial x, \partial/\partial y$ ) so that

$$d\underline{V}' \approx \frac{\partial \underline{V}'}{\partial z} dz \quad (\text{A.6})$$

The translation correction will be illustrated below using the East beam; correction for the other beams is analogous.

In order to implement the translation correction according to (A.5) with the approximation (A.6) it is necessary to estimate the vertical derivative of  $\underline{V}'$  and the differential depth  $dz$ . The slant velocity profiles provide an estimate of the range derivative of  $\underline{V}'$ , which must be properly scaled to give an estimate of the vertical derivative. The range derivative of slant velocity for the East beam in the tilted frame is given by

$$\frac{d\underline{V}'}{dr'} = (\underline{E}' \cdot \nabla') \underline{V}' = \left[ \cos\theta_0 \frac{\partial}{\partial x'} - \sin\theta_0 \frac{\partial}{\partial z'} \right] \underline{V}' \quad (\text{A.7})$$

where

$$\underline{E}' = \cos\theta_0 \underline{i}' - \sin\theta_0 \underline{k}'$$

is the unit vector in the direction of the East beam in the tilted coordinate system. Using the chain rule and (A.4) to write derivatives in the tilted frame in terms of the geophysical coordinates, and neglecting horizontal derivatives in the geophysical frame gives

$$\frac{d\underline{V}'}{dr'} = -(\sin\phi \cos\theta_0 + \cos\phi \cos\rho \sin\theta_0) \frac{\partial \underline{V}'}{\partial z} \quad (\text{A.8})$$

The expression (A.8) allows the range derivative in the tilted frame to be related to the vertical derivative by a scale factor computed from the tilt angles.

The differential depth is determined from the difference between the vertical coordinates at range  $r$  in the tilted frame and the reference frame. The vertical coordinate at range  $r$  in the reference frame can be written as

$$z_0 = r [ \underline{E} \cdot \underline{k} ] = -r \sin \theta_0 \quad (\text{A.9})$$

where

$$\underline{E} = \cos \theta_0 \underline{i} - \sin \theta_0 \underline{k}$$

is the unit vector in the direction of the East beam in the reference frame. The vertical coordinate corresponding to range  $r$  in the tilted frame is expressed in the reference frame as

$$z = r [ ( M_\phi M_\rho \underline{E}' ) \cdot \underline{k} ] = -r ( \sin \phi \cos \theta_0 + \cos \phi \cos \rho \sin \theta_0 ) \quad (\text{A.10})$$

giving

$$dz = z - z_0 = r [ (1 - \cos \phi \cos \rho) \sin \theta_0 - \sin \phi \cos \theta_0 ] \quad (\text{A.11})$$

For each range  $r$  where a velocity measurement is made in the tilted frame, the vertical derivative of velocity is estimated from (A.8), the differential depth  $dz$  is computed from (A.11), and the translation correction implemented according to (A.5) and (A.6). The corrections for the West, North, and South beams differ only in that the values of the appropriate unit vectors are substituted for  $\underline{E}'$  and  $\underline{E}$  in (A.7) through (A.9).

#### A.6 Rotation correction

Once the translation correction has been made, the rotation correction amounts to an adjustment of the magnitude of  $\underline{V}'(x_0, y_0, z_0)$  using the rotation matrices (A.2) and (A.3). This final step the the correction for platform motion gives the slant velocity in the geophysical coordinate system as

$$\begin{aligned} \underline{V}(x_0, y_0, z_0) &= M_\phi M_\rho \underline{V}'(x_0, y_0, z_0) \\ &= \begin{bmatrix} \cos \phi u' - \sin \phi \sin \rho v' + \sin \phi \cos \rho w' \\ \cos \rho v' + \sin \rho w' \\ -\sin \phi u' - \cos \phi \sin \rho v' + \cos \phi \cos \rho w' \end{bmatrix} \end{aligned} \quad (\text{A.12})$$

The correction is conceptually straightforward, but is complicated by the fact that the individual components of  $\underline{V}'$  are not known; only the *projection* of the velocity onto the beam axis is measured (Sec. 1.4). An effective and relatively simple correction can still be made by substituting the Janus velocities for the unknown velocity components in the correction terms. The rotation

correction developed in this section uses the Janus horizontal velocity to correct for errors in the vertical velocity measured by each beam. A scale analysis shows that errors in the measured horizontal velocities are small and do not require correction.

Errors in the velocity components measured in the tilted frame can be estimated by using the rotation matrices (A.2) and (A.3) to express  $\underline{V}'$  in terms of the true velocities  $u$ ,  $v$ , and  $w$ . The resulting expression for the components of  $\underline{V}'$  is

$$\begin{bmatrix} u' \\ v' \\ w' \end{bmatrix} = \begin{bmatrix} \cos\phi u & - & \sin\phi w \\ -\sin\phi \sin\rho u + \cos\rho v & - & \cos\phi \sin\rho w \\ \sin\phi \cos\rho u + \sin\rho v & + & \cos\phi \cos\rho w \end{bmatrix} \quad (\text{A.13})$$

Before performing the rotation correction for each component, scaling parameters are introduced to simplify the error terms and allow estimation of error magnitudes. The horizontal velocity components are expected to be of the same scale, but different from the scale of the vertical velocity. The pitch and roll angles are of the same scale and have magnitudes of  $\leq 2^\circ$  (Fig. 1.5). With these considerations the velocities and tilt angles are scaled as follows

$$\begin{aligned} u, v &\sim U_0, & w &\sim W_0 \\ \sin\phi, \sin\rho &\sim \sin\Phi_0 \\ \cos\phi, \cos\rho &\sim 1 \end{aligned} \quad (\text{A.14})$$

Using (A.13) and (A.14) the rotation errors in the velocity components can be expressed as

$$\begin{aligned} \epsilon_1 &= u' - u = \sin\Phi_0 W_0 \\ \epsilon_2 &= v' - v = \sin\Phi_0 W_0 + (\sin\Phi_0)^2 U_0 \\ \epsilon_3 &= w' - w = 2 \sin\Phi_0 U_0 \end{aligned} \quad (\text{A.15})$$

For a typical "large" tilt angle magnitude of  $\Phi_0 = 1.5^\circ$  and  $W_0 / U_0 < 1$ , rotation errors in horizontal velocity are less than 3%. The ratio of vertical to horizontal velocity for oceanic motions with vertical scale  $D$  and horizontal scale  $L$  goes like the aspect ratio  $\delta = D/L$ . The largest contribution to horizontal kinetic energy comes from low (sub-inertial) frequencies where  $\delta \ll 1$ . Clearly rotation errors in horizontal velocity are not important for these low frequencies.

The aspect ratio remains less than one except for motions such as high frequency internal waves and turbulence. Turbulent velocity fluctuations cannot be measured by the Doppler sonar used in the MILDEX experiment due to the large averaging volume ( $> 1000 \text{ m}^3$ ) and long averaging time (3 min) of the velocity estimates compared to the space and time scales of the turbulence. In the internal wave band, the aspect ratio can be estimated from the ratio of horizontal to vertical wavenumber. For linear internal waves in an incompressible, Boussinesq fluid, this ratio is (Gill, 1982)

$$\delta = \frac{\kappa_h}{\kappa_z} = \left[ \frac{N^2 - \omega^2}{\omega^2 - f^2} \right]^{-1/2}$$



where  $\omega$  is the wave frequency,  $f$  is the inertial frequency, and  $N^2 = -g\rho^{-1} d\rho/dz$  is the buoyancy frequency. The aspect ratio exceeds one in the internal wave band for  $\omega > N/\sqrt{2}$ . For  $\omega = 0.99 N$ , the aspect ratio is  $\sim 7$  and the rotation errors in horizontal velocity may be as large as 20% of  $U_0$ . However, it must be realized that the expected measurement uncertainty in the velocity estimate also becomes larger at high frequency. For  $N = 2$  cph, the averaging interval of the measurement at  $\omega = 0.99 N$  is  $(.99 N)^{-1} \sim 30$  min, and the expected measurement uncertainty for horizontal velocity is about  $0.2 \text{ cm s}^{-1}$  (Sec 1.4) or 20% of  $U_0$  for  $U_0 = 1 \text{ cm s}^{-1}$ . Hence even at the highest frequencies of the internal wave band the rotation errors are not a dominant source of error in the horizontal velocity estimates.

In contrast to the horizontal velocity errors, the rotation errors for vertical velocity are largest for low frequency, and decrease as the aspect ratio increases. Errors in vertical velocity are less than 5% for  $W_0 / U_0 > 1$  with a tilt angle of  $1.5^\circ$ . This implies that rotation errors for vertical velocity in the high frequency portion of the internal wave band will not be significant. For lower frequencies, however, horizontal velocities can easily be twenty times vertical velocities giving  $W_0 / U_0 = 0.05$  and a corresponding rotation error of  $> 100\%$ . Errors of this magnitude are unacceptable and must be corrected. Details of the rotation correction for vertical velocity are given below.

The correction for rotation errors in vertical velocity is accomplished by estimating the horizontal components required by (A.12) from the Janus velocities and applying the appropriate correction factor to the slant velocities of each beam. Consider the slant velocity for the East and West beams, after correction for translation error, but before the correction for rotation error

$$V_E' = -u_E' \cos\theta_0 + w_E' \sin\theta_0 \quad (\text{A.16a})$$

$$V_W' = +u_W' \cos\theta_0 + w_W' \sin\theta_0 \quad (\text{A.16b})$$

It has been shown that  $u' = u$  for the purposes of this analysis, but that  $w'$  will have a significant error. The correction terms for vertical velocity in terms of the velocity components measured in the tilted frame are found from (A.12). For the East and West beam vertical velocities, these terms are

$$\alpha_E = u_E' \sin\phi + v_E' \cos\phi \sin\rho \quad (\text{A.17a})$$

$$\alpha_W = u_W' \sin\phi + v_W' \cos\phi \sin\rho \quad (\text{A.17b})$$

where the term  $w'(1 - \cos\phi \cos\rho)$  has been neglected (this term is less than  $1 \times 10^{-3} w'$  for the observed values of tilt). The difficulty is that  $u'$  and  $v'$  cannot be determined at the same point where  $V_E'$  and  $V_W'$  are measured, but must be estimated from the Janus velocities

$$\bar{u}' = \frac{V_W' - V_E'}{2 \cos\theta_0} = \frac{1}{2}(u_W' + u_E') + \frac{1}{2}(w_W' - w_E') \tan\theta_0 \quad (\text{A.18a})$$

$$\bar{v}' = \frac{V_S' - V_N'}{2 \cos\theta_0} = \frac{1}{2}(u_S' + u_N') + \frac{1}{2}(w_S' - w_N') \tan\theta_0 \quad (\text{A.18b})$$

It will be of use later to note that the Janus velocities can be re-written as

$$\bar{u}' = u_E' + \frac{1}{2}(u_W' - u_E') + \frac{1}{2}(w_W' - w_E') \tan \theta_0 \quad (\text{A.19a})$$

$$\bar{v}' = v_E' + \left(\frac{v_S'}{2} + \frac{v_N'}{2} - v_E'\right) + \frac{1}{2}(w_S' - w_N') \tan \theta_0 \quad (\text{A.19b})$$

or

$$\bar{u}' = u_W' + \frac{1}{2}(u_E' - u_W') + \frac{1}{2}(w_W' - w_E') \tan \theta_0 \quad (\text{A.19c})$$

$$\bar{v}' = v_W' + \left(\frac{v_S'}{2} + \frac{v_N'}{2} - v_W'\right) + \frac{1}{2}(w_S' - w_N') \tan \theta_0 \quad (\text{A.19d})$$

The corrected slant velocities for the East and West beams defined in terms of the Janus velocities are

$$V_E = V_E' - \alpha \sin \theta_0, \quad V_W = V_W' - \alpha \sin \theta_0 \quad (\text{A.20})$$

where the correction term is

$$\alpha = \bar{u}' \sin \phi + \bar{v}' \cos \phi \sin \rho \quad (\text{A.21})$$

and is the same for the two beams. In fact, all four slant velocities will now be corrected by the same factor  $\alpha$  given in (A.21), except for slight differences due to mechanical alignment errors (see Sec A.7). This correction factor properly accounts for rotation errors in  $w$  which come from the  $u'$  and  $v'$  terms in (A.12), but introduces new errors due to the difference between the desired corrections (A.17), and the value of (A.21).

Returning to the scale analysis introduced previously shows that the correction is successful in the sense that the original errors in slant velocity, of order  $2 U_0 \sin \Phi_0$ , are reduced to errors of order  $\Delta U_0 \sin \Phi_0$ , where  $\Delta U_0$  is the magnitude of the horizontal velocity difference between beams. Specifying the scales for the velocity differences as

$$u_E - u_W, \quad v_S - v_N, \quad \text{etc} \sim \Delta U_0 \quad (\text{A.22})$$

$$w_E - w_W, \quad w_S - w_N, \quad \text{etc} \sim \Delta W_0$$

in addition to the scaling of (A.14), and taking  $\sin \theta_0, \cos \theta_0 \sim 1$  for simplicity, allows estimation of rotation errors before and after correction. Using the uncorrected slant velocities from (A.16), and the error terms (A.17) with  $u' = u$ , and  $v' = v$  it can be shown that the errors in the slant velocities and Janus vertical velocities before correction are

$$\epsilon_{v'} \sim 2 U_0 \sin \Phi_0$$

(A.23)

$$\epsilon_{\bar{w}} \sim 2 U_0 \sin \Phi_0 + \frac{1}{2} \Delta U_0$$

Using the corrected slant velocities from (A.20), and substituting the forms (A.19) for the Janus velocities in the correction factor (A.21), the errors after correction are

$$\epsilon_V \sim \Delta U_0 \sin \Phi_0 + \Delta W_0 \sin \Phi_0$$

(A.24)

$$\epsilon_{\bar{w}} \sim \frac{1}{2} \Delta U_0 + \Delta U_0 \sin \Phi_0 + \Delta W_0 \sin \Phi_0$$

It has been shown that the most significant rotation errors for vertical velocity occur at low frequency where  $U_0$  is large compared to  $W_0$ ,  $\Delta U_0$ , and  $\Delta W_0$ . For the uncorrected velocities this can result in large errors in  $V'$  and  $\bar{w}'$ , but for the corrected velocities, there are no errors larger than order  $\Delta U_0$  and  $\Delta W_0$ . The term  $\frac{1}{2}\Delta W_0$  in  $\epsilon_{\bar{w}}$  is a consequence of the Janus estimation technique and is independent of tilt.

#### A.7 Mechanical alignment errors

In the previous discussion, it was assumed that the accelerometer measurements could be directly related to the tilt angles of the sonar beams. This is a good approximation, but is associated with some error due to the fact that the accelerometers and sonars are attached to FLIP's hull in different ways (Fig. 1.7). The design tolerances of the mechanical components separating the accelerometer package from the sonar transducer panels can easily result in alignment errors of a few degrees between the measurement planes of the accelerometers and the sonars. In addition, a vertical line drawn through the vertex of the v-shaped sonar mounts in the un-tilted reference frame may not form the bisector of the angle between the sonar panels. This will cause a small bias in the velocities measured by the two beams, even after correction for platform motion. The magnitude of both of these mechanical alignment errors can be determined quite accurately by the analysis described below.

The analysis of mechanical alignment errors is based on the assumption that the depth-time average of the true vertical velocity is small compared to the magnitude of the errors. The data set for the analysis consisted of slant velocity and tilt angle measurements averaged over 30 min in time for a 16 day interval from day 301 to 317. The slant velocities were further averaged over a 312 m depth interval between 328 and 640 m. The first step is to compute the uncorrected vertical velocity from

$$\bar{w}_E' = \frac{V_W' + V_E'}{2 \sin \theta_0}, \quad \bar{w}_N' = \frac{V_S' + V_N'}{2 \sin \theta_0} \quad (\text{A.25})$$

The resulting vertical velocity estimates for the East and North beam pairs, low-passed with a 24.5 hr running mean filter, are shown in Figs. (A.4) and (A.5), respectively. These plots show excursions of as large as  $0.8 \text{ cm s}^{-1}$ , as well as offsets of about  $0.35 \text{ cm s}^{-1}$  from zero. Expected values of measurement uncertainty for vertical velocity averaged over 24 hrs and 300 m in depth are of order  $0.01 \text{ cm s}^{-1}$ . Typical values of true vertical velocity for these averaging scales are less than or equal to the measurement precision. Clearly the fluctuations in the uncorrected vertical velocities are not from true velocities or measurement uncertainty, and are presumably due to platform motion. A high degree of correlation is observed between the fluctuations in  $\bar{w}'$  and the error term computed from the same data using (A.21), confirming that the uncorrected data is contaminated by tilt errors.

The optimal correction for platform motion is considered to be one which minimizes the depth-time averaged vertical velocity estimate. Since mechanical alignment errors are expected to be important in the tilt correction, the parameters  $\epsilon_\phi$ ,  $\epsilon_\rho$ , are included in the correction to represent the effects of alignment errors on pitch and roll angles. A bias factor  $b$  is included in the slant velocities to account for the effect of alignment errors on the beam pairs. It is important to realize that although the beams from each pair of sonars (E-W or N-S beams) may be assumed to be in the same plane, the planes formed by the two beam pairs may not be orthogonal. This is incorporated in the analysis by allowing different alignment error parameters for each beam pair. The resulting correction is applied to the slant velocities in the same sense as in (A.20) so that the vertical velocities corrected for rotation error (translation error is not important for the depth averaged velocities) are given by

$$\bar{w}_E = (2 \sin \theta_0)^{-1} \left[ (V'_W - \alpha_E \sin \theta_0) + (V'_E - \alpha_E \sin \theta_0 + b_E) \right] \quad (\text{A.26a})$$

$$\bar{w}_N = (2 \sin \theta_0)^{-1} \left[ (V'_S - \alpha_N \sin \theta_0) + (V'_N - \alpha_N \sin \theta_0 + b_N) \right] \quad (\text{A.26b})$$

where

$$\alpha_E = \bar{u}' \sin(\phi + \epsilon_{\phi E}) + \bar{v}' \cos(\phi + \epsilon_{\phi E}) \sin(\rho + \epsilon_{\rho E}) \quad (\text{A.27a})$$

$$\alpha_N = \bar{u}' \sin(\phi + \epsilon_{\phi N}) + \bar{v}' \cos(\phi + \epsilon_{\phi N}) \sin(\rho + \epsilon_{\rho N}) \quad (\text{A.27b})$$

For each beam pair the three alignment errors (e.g.  $\epsilon_{\phi E}$ ,  $\epsilon_{\rho E}$ , and  $b_E$ ) are allowed to vary over a representative range, and the mean-square error is computed for each combination of values. The desired values are those which minimize the mean-square error. The parameters determined from this minimization procedure are given in Table A.2. The depth-time averaged vertical velocities after correction according to (A.26), using (A.27) and the alignment error parameters from in Table A.2, are shown in Fig. A.6. Comparing the initial (before correction) and final (after correction) statistics from Table A.2 shows that the rotation correction has reduced the mean velocity to less than  $0.05 \text{ cm s}^{-1}$  and reduced the velocity variance by nearly an order of magnitude. The remaining vertical velocity variance is slightly larger than that expected from measurement uncertainty alone, and presumably comes from differences in horizontal velocity over the distance separating the beams.



**Table A.2.** *Tilt correction results.* Minimization of the mean square error of the corrected vertical velocity estimated from (A.26) and (A.27) yields the value of the alignment error angles  $\epsilon_\phi$ ,  $\epsilon_\rho$  and the bias  $b$  as reported in the table. Initial mean and variance are for uncorrected vertical velocity estimates. Final mean and variance are after rotation correction using the values of alignment error parameters given in the table. All statistics are for estimates averaged over 312 m in depth and 24.5 hrs in time.

TILT CORRECTION RESULTS		
Beam pair ID codes	( 4, 6 )	( 3, 5 )
Nominal direction	East	North
Initial mean (cm s <sup>-1</sup> )	- 0.40	- 0.33
Final mean (cm s <sup>-1</sup> )	0.045	0.048
Initial var. (cm <sup>2</sup> s <sup>-2</sup> )	$0.29 \times 10^{-1}$	$0.11 \times 10^{-1}$
Final var. (cm <sup>2</sup> s <sup>-2</sup> )	$0.37 \times 10^{-2}$	$0.17 \times 10^{-2}$
$\epsilon_\phi$ (deg)	- 0.5	0.0
$\epsilon_\rho$ (deg)	+ 2.3	- 0.1
$b$ (cm s <sup>-1</sup> )	0.64	0.51

The discussion of mechanical alignment errors in terms of the rotation correction has served to produce estimates of the alignment error parameters as well as introduce the correction terms for slant velocity. The angle errors included in (A.27) are important not only in the rotation correction, but also in the translation correction given in Section A.5. For example, the expressions for the range derivative (A.8) and the differential depth (A.11) of the East beam including mechanical alignment errors become

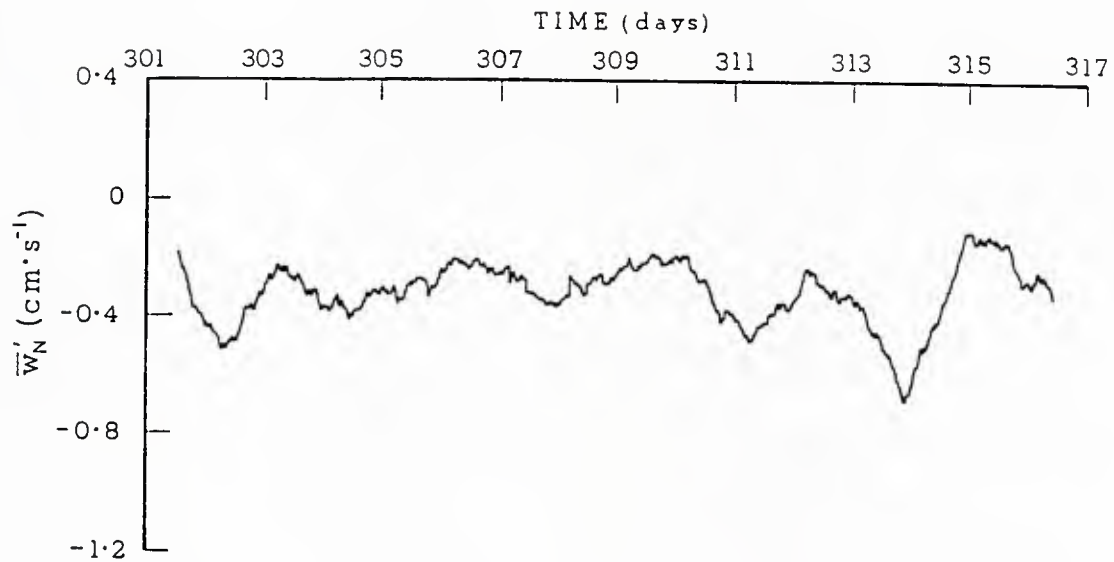


Figure A.5. *Uncorrected vertical velocity: North axis.* As in Fig. A.3, but for North and South beams.

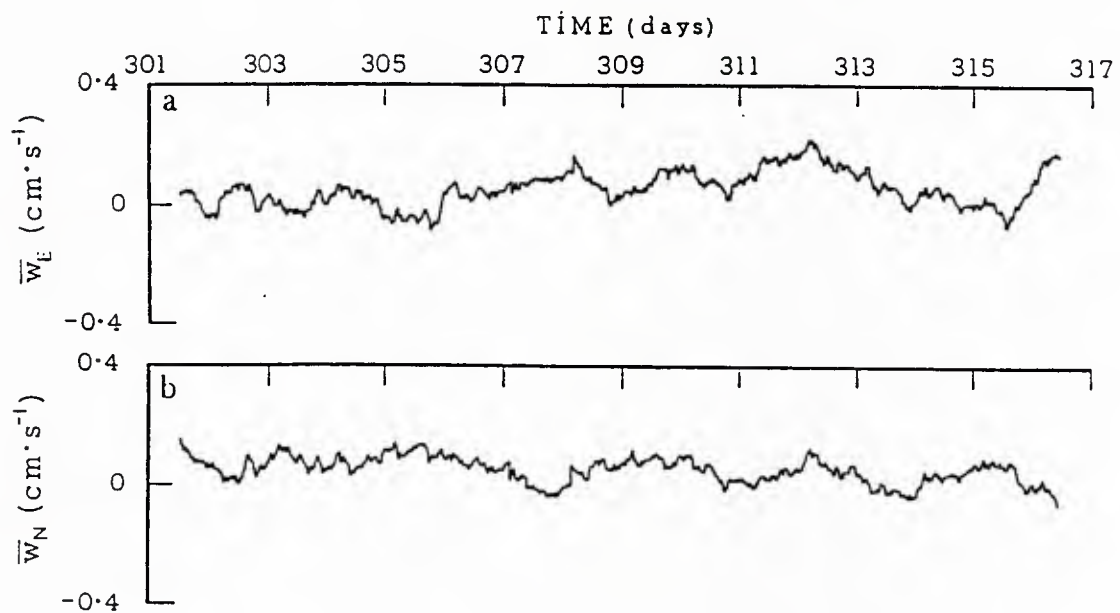


Figure A.8. *Corrected vertical velocity.* Vertical velocities are estimated from (a) East-West and (b) North-South beam pairs with correction for platform motion using (A.26), the correction factors (A.27), and the values of alignment error parameters given in Table A.2. Averaging is the same as in Fig. A.3.

Note that if the Janus horizontal velocities are computed from corrected slant velocities in the same manner as the Janus vertical velocities in (A.26), the terms involving the tilt angles drop out, but the bias terms are effective in the correction.

## APPENDIX B

### The Covariance Processing Technique and its Application to Coherent and Incoherent Doppler Systems

Assume that the complex envelope of the received signal measured by a Doppler system can be written as

$$Z(t) = S(t) \cos\phi(t) + iS(t) \sin\phi(t) = S(t) \exp[i\phi(t)] \quad (B.1)$$

where  $S(t)$  and  $\phi(t)$  are the resultant amplitude and phase, respectively. It is desired to measure the mean Doppler frequency of the received signal. The mean frequency is typically defined as the first moment of the normalized Doppler spectrum

$$\bar{f} = \int_{-\infty}^{\infty} f P(f) df / \int_{-\infty}^{\infty} P(f) df \quad (B.2)$$

The covariance processing (CP) technique provides an estimate of  $\bar{f}$  directly from the covariance function of the complex envelope. The complex covariance is

$$C(\tau) = \langle Z(t)Z^*(t+\tau) \rangle \quad (B.3)$$

where the brackets imply ensemble averaging and  $*$  denotes conjugation.

The CP technique exploits the fact that the covariance function and the Doppler spectrum are Fourier transform pairs

$$P(f) = \int_{-\infty}^{\infty} C(\tau) \exp[-i2\pi f\tau] d\tau \quad (B.4)$$

$$C(\tau) = \int_{-\infty}^{\infty} P(f) \exp[i2\pi f\tau] df \quad (B.5)$$

Since the spectrum is real, the covariance function must be Hermitian, implying that its amplitude will be even and its phase will be odd. The covariance function can thus be expressed in polar form as

$$C(\tau) = h(\tau) \exp[i2\pi g(\tau)] \quad (B.6)$$

where  $h(\tau)$  is a real, even function of  $\tau$  and  $g(\tau)$  is real, odd.

It is well known that the moments of a random variable are related to the derivatives of its characteristic function evaluated at zero (Papoulis, 1965). If the probability density function of a random variable  $s$  is  $p(s)$  then the characteristic function is

$$Q(x) = \int_{-\infty}^{\infty} p(s) \exp[isx] ds \quad (B.7)$$



and the  $n$ th moments of  $s$  are

$$\mu_n(s) = (i)^{-n} \frac{dQ(x)}{dx^n} \Big|_{x=0} \quad (B.8)$$

The normalized Doppler spectrum can be interpreted as the probability density function for the distribution of Doppler shifts in the received signal (Serafin, 1975; Doviak and Zrnic, 1984). It follows that the normalized covariance function  $C(\tau) / h(0)$  is identified as the characteristic function for the angular Doppler frequency  $\omega_d = 2\pi f_d$ . The mean Doppler frequency (first spectral moment) is then given by

$$\bar{f} = (2\pi)^{-1} \mu_1(\omega_d) = [i2\pi h(0)]^{-1} \frac{dC(\tau)}{d\tau} \Big|_{\tau=0} \quad (B.9)$$

Using (B.6) the derivative in (B.9) can be expressed as

$$\begin{aligned} \frac{dC}{d\tau} \Big|_{\tau=0} &= [i2\pi h(\tau) \exp[i2\pi g(\tau)] dg/d\tau + \exp[i2\pi g(\tau)] dh/d\tau] \Big|_{\tau=0} \\ &= i2\pi h(0) \frac{dg}{d\tau} \Big|_{\tau=0} \end{aligned} \quad (B.10)$$

so that (B.9) becomes

$$\bar{f} = \frac{dg}{d\tau} \Big|_{\tau=0} \quad (B.11)$$

Approximating  $dg/d\tau$  at  $\tau = 0$  using the first two terms of the Taylor series expansion of  $g(\tau)$  about zero gives

$$\frac{dg}{d\tau} \Big|_{\tau=0} \sim [g(\tau) - g(0)] / \tau = g(\tau) / \tau \quad (B.12)$$

Since  $\text{Arg}[C(\tau)] = 2\pi g(\tau)$  the relations (B.11) and (B.12) can be used to relate the estimate of  $\bar{f}$  directly to the covariance function giving the CP mean frequency estimator

$$\hat{\bar{f}} \equiv (2\pi\tau)^{-1} \text{Arg}[C(\tau)] \sim \bar{f} \quad (B.13)$$

For a noise-free, symmetric Doppler spectrum  $\hat{\bar{f}}$  is an unbiased estimator for  $\bar{f}$  as  $\tau$  approaches zero.

The covariance processing technique can be applied to both pulse-to-pulse coherent and incoherent Doppler systems. The principle differences involve the relationship between the pulse repetition time and the correlation time of the scattering field. These differences, and their effect on the computation of covariance, are discussed below.

A schematic representation of the transmission sequence for a generalized Doppler system is shown in Fig. B.1a. Following the development of

Doviak and Zrnic (1984) a conceptual separation is made between *range time* and *pulse time* (Fig. B.1b). The range-time increment  $\tau_r$ , is the time interval between samples of the echo from a particular transmission. The pulse-time increment  $\tau_p$ , is the time delay between successive transmissions. It can be seen that successive samples at fixed range are separated by  $\tau_p$ , generally called the pulse repetition time (PRT). The separation of time scales will facilitate the description of covariance estimation and serve to emphasize the differences between coherent and incoherent processing.

In a coherent system, discrete samples of the complex envelope  $Z(t)$  are conveniently expressed in pulse time for fixed range and can be written as  $Z_j(m \tau_p)$  where  $m=1, 2, 3, \dots$  is the pulse index and the subscript  $j$  is the range index. The covariance function for a range time  $j \tau_r$  is estimated from a sequence of  $M$  pulses by

$$\hat{C}(k\tau_o) = \frac{1}{M} \sum_{m=1}^M Z_j(m\tau_p) Z_j^*((m+k)\tau_p) \quad (B.14a)$$

where  $k=0, 1, 2, \dots, K$  is the lag index and  $\tau_o = \tau_p$ . The designation  $\tau_o$  for the covariance lag interval is introduced to give a general form for the covariance estimate, whether from a coherent ( $\tau_o = \tau_p$ ) or incoherent ( $\tau_o = \tau_r$ ) system. For  $k=1$  (lag 1),  $Z(m\tau_p)$  and  $Z((m+1)\tau_p)$  are samples from two successive pulses, and substituting  $\hat{C}(\tau_o)$  from (B.14a) into (B.13) yields the "pulse-pair" mean frequency estimate. To obtain meaningful covariance measurements with a coherent system it is necessary to maintain the phase of the transmitted waveform precisely from one pulse to the next so that the only contribution to phase differences is from the motion of the scatterers. The covariance estimate will approach zero for lags greater than  $K = T_c/\tau_o$  where  $T_c$  is the scattering correlation time (Pinkel, 1980).

The scattering correlation time plays a key role in the distinction between coherent and incoherent processing. The time  $T_c$  can be considered as the maximum separation between samples of  $Z$  which can be allowed while still maintaining phase coherence. Samples at intervals greater than  $T_c$  will contain no useful Doppler information. Considering the definition of  $K$  above, it is clear that the condition  $\tau_o \leq T_c$  must be satisfied in order to have at least one useful covariance lag. Recalling that  $\tau_o$  is equivalent to the PRT for a coherent system, this restriction means that the received signal for a given range gate will be phase-coherent between one pulse and the next and gives the pulse-to-pulse coherent sonar its name.

An incoherent Doppler system derives its name from the fact that the PRT is much greater than  $T_c$ , making samples at the same range gate from two successive pulses phase-incoherent. A Doppler shift estimate can still be obtained, however, by sampling the received signal at intervals shorter than the PRT. This is accomplished by sub-sampling the return from a single pulse at an interval  $\tau_r$  which is less than the pulse length  $T_p$ . The returns from times  $j\tau_r$  and  $(j+1)\tau_r$  will come from a region of space which is highly overlapped for  $\tau_r \ll T_p$ , and the two successive samples will have the effect of being time-delayed versions of the return from a common-volume range gate centered at

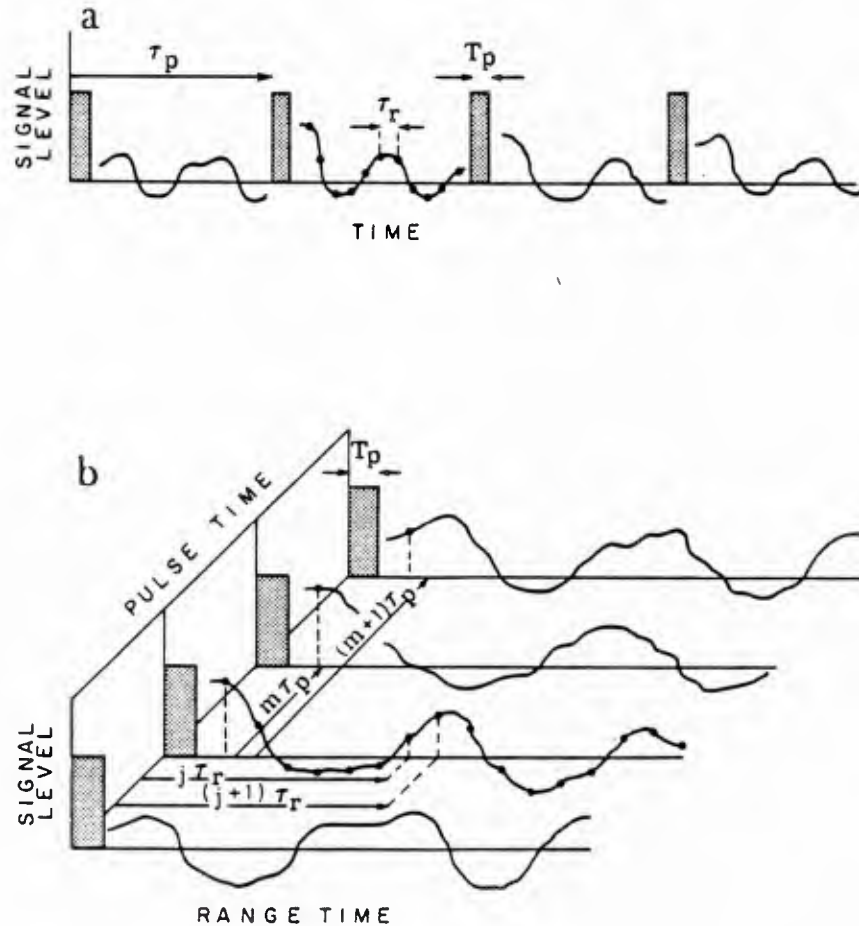


**Figure B.1.** *Schematic representation of Doppler sonar transmission.* Schematic representation of several transmission sequences for a generalized Doppler system in actual time (a), and separated into range time and pulse time (b). Shaded areas represent pulse transmissions and "wiggly" lines represent returns from the in-phase channel. Note the difference between the pulse length  $T_p$  and the pulse repetition time  $\tau_p$ . The range delay  $\tau_r$  can be interpreted as the digitization interval of the system. The relative sizes of  $T_p$ ,  $\tau_p$ , and  $\tau_r$  will be different for coherent and incoherent systems.

$$r_j = c [ j \tau_r / 2 - (T_p - \tau_r) / 4 ].$$

Samples of the complex envelope for an incoherent system are best expressed in terms of range time for a particular pulse and written  $Z_m(j \tau_r)$ . The covariance function for a given common-volume range gate is estimated from each pulse and averaged incoherently over  $M$  pulses giving

$$\hat{C}(k \tau_o) = \frac{1}{M} \sum_{m=1}^M Z_m(j \tau_r) Z_m^*((j+k) \tau_r) \quad (\text{B.14b})$$

where  $k$  is as in (B.14a) but here  $\tau_o = \tau_r$ . The essential difference from the coherent processing scheme, highlighted by the exchange of subscripts and sample indices, is that range time is substituted for pulse time to generate the desired covariance lags. An important consequence is that it is not necessary to maintain the phase of the transmitted waveform between pulses. Since covariance samples for an incoherent sonar come from the same pulse rather than a pair of pulses, the general term covariance processing is preferred to "pulse-pair" processing.

The covariance estimate for the incoherent system will approach zero for lags greater than  $K = T_p / \tau_o$ , implying that  $\tau_o \leq T_p$  is the condition on the sampling interval in order to have at least one useful covariance lag. The maximum useful covariance lag is defined in terms of  $T_p$  rather than  $T_c$  due to the fact that successive samples must be from overlapping volumes in space in order to retain phase coherence, even if the time between samples is short compared to the correlation time. An efficiently designed incoherent Doppler system will have a pulse length no greater than the correlation time (Pinkel, 1980), so that the condition  $\tau_o \leq T_p$  on the sampling interval also insures that the fundamental constraint  $\tau_o \leq T_c$  is satisfied. In practice both coherent and incoherent systems operate under conditions where  $\tau_o \ll T_c$ .



## References

- Andersen, N. R. and B. J. Zahuranec (Ed.), 1977: *Oceanic Sound Scattering Prediction*, Plenum Press, New York, 859 pp.
- Anderson, V. C., 1950: Sound scattering from a fluid sphere. *J. Acoust. Soc. Am.*, **22**, 426-431.
- Appell, G. F., T. N. Mero, J. J. Sprenke, and D. R. Schmidt, 1985: An intercomparison of two acoustic Doppler current profilers. *Proc. Oceans '85*, 723-730.
- Barham, E. G., 1963: Siphonophores and the deep scattering layer. *Science*, **140**, 826-828.
- Barham, E. G., 1966: Deep scattering layer migration and composition: Observations from a diving saucer. *Science*, **151**, 1399-1403.
- Bary, B. M. and R. E. Pieper, 1971: Sonic scattering studies in Soanich Inlet, British Columbia: A preliminary report. In: *Proceedings of an International Symposium on Biological Sound Scattering in the Ocean*, Maury Center for Ocean Science, Report No. MC-005, G. B. Farquhar, Ed., 601-611.
- Bell, T. H., 1975: Topographically generated internal waves in the open ocean. *J. Geophys. Res.*, **80**, No. 3, 320-327.
- Bitterman, D. and D. Wilson, 1983: Ocean current profiling with a shipboard Doppler acoustic backscatter system. *Proc. Oceans '83*, 27-31.
- Booker, J. R. and F. P. Bretherton, 1967: The critical layer for internal gravity waves in a shear flow. *J. Fluid Mech.*, **27**, No. 3, 513-539.
- Bradbury, M. G., D. P. Abbott, R. V. Bovbjerg, R. N. Mariscal, W. C. Fielding, R. T. Barber, V. B. Pearse, S. J. Proctor, J. C. Ogden, J. P. Wourms, L. R. Taylor, Jr., J. G. Christofferson, J. P. Christofferson, R. M. McPhearson, M. J. Wynne, and P. M. Stromberg, Jr., 1964: Studies on the fauna associated with the deep scattering layers in the equatorial Indian Ocean, conducted on R/V *TE VEGA* during October and November. In: *Proceedings of an International Symposium on Biological Sound Scattering in the Ocean*, Maury Center for Ocean Science, Report No. MC-005, G. B. Farquhar, Ed., 409-452.
- Bretherton, F. P., 1969: Momentum transport by gravity waves. *Quart. J. Roy. Met. Soc.*, **95**, No. 404, 213-243.

- Briscoe, M. G., 1975: Preliminary results from the trimoored Internal Wave Experiment (IWEX). *J. Geophys. Res.*, **80**, No. 27, 3872-3884.
- Broutman, D., 1982: The interaction of short-wavelength internal waves with a background current. *Ph.D. Thesis*, Univ. of California, San Diego.
- Castile, B. D., 1975: Reverberation from plankton at 330 kHz in the Western Pacific. *J. Acoust. Soc. Am.*, **58**, No. 5, 972-976.
- Chapman, R. P., O.Z. Bluy, and R.H. Adlington, 1971: Geographic variations in the acoustic characteristics of deep scattering layers. In: *Proceedings of an International Symposium on Biological Sound Scattering in the Ocean*, Maury Center for Ocean Science, Report No. MC-005, G. B. Farquhar, Ed., 306-317.
- Christensen, J. L., 1983: A new acoustic Doppler current profiler. *Sea Technol.*, **24**, No. 2, 10-13.
- Clarke, G. L., 1971: Light conditions in the sea in relation to the diurnal migrations of animals. In: *Proceedings of an International Symposium on Biological Sound Scattering in the Ocean*, Maury Center for Ocean Science, Report No. MC-005, G. B. Farquhar, Ed., 41-50.
- Davis, R. E., R. de Szoeki, D. Halpern, and P. Niiler, 1981: Variability in the upper ocean during MILE. Part I: The heat and momentum balances. *Deep-Sea Res.*, **28A**, 1427-1451.
- Doviak, R. J. and D. S. Zrnic, 1984: *Doppler Radar and Weather Observations*, Academic Press, Orlando, 458 pp.
- Dunlap, C. R., 1971: A reconnaissance of the deep scattering layers in the eastern tropical Pacific and the Gulf of California. In: *Proceedings of an International Symposium on Biological Sound Scattering in the Ocean*, Maury Center for Ocean Science, Report No. MC-005, G. B. Farquhar, Ed., 395-408.
- Farquhar, G. B. (Ed.), 1971: *Proceeding of an International Symposium on Biological Sound Scattering in the Ocean*, March 31-April 2, 1970, Arlie House Conference Center, Warrenton, VA, Maury Center for Ocean Science, Report No. MC-005, 629 pp.
- Frankignoul, C. J. and T. Joyce, 1979: Internal wave variability during IWEX. *J. Geophys. Res.*, **84**, No. C2, 769-776.
- Friedl, W. A., G. V. Pickwell, and R. J. Vent, 1977: The MINOX program: An example of a multidisciplinary oceanic investigation. In: *Oceanic Sound Scattering Prediction*, B. J. Zahuranec, Ed., Plenum Press, New York, 591-618.

- Garrett, C. and W. H. Munk, 1972: Space-time scales of internal waves. *Geophys. Fluid Dyn.*, **2**, 225-264.
- Garrett, C. and W. H. Munk, 1975: Space-time scales of internal waves: A progress report. *J. Geophys. Res.*, **80**, No. 3, 291-297.
- Garrett, C., 1979: Mixing in the ocean interior. *Dyn. Atmos. Oceans*, **3**, 239-265.
- Garrett, C., 1984: Parameterizing the effects of internal waves: Simple ideas and things we need to know. In: *Internal Gravity Waves and Small Scale Processes*, Proceedings, Hawaiian Winter Workshop, Univ. of Hawaii at Manoa, Jan. 17-20, 1984, P. Müller and R. Pujalet, Ed., 171-181.
- Gill, A. E., 1982: *Atmosphere - Ocean Dynamics*, Academic Press, New York, 662 pp.
- Gill, T. P., 1965: *The Doppler Effect: An introduction to the theory of the effect*, Academic Press, New York, 149 pp.
- Greenblatt, P., 1981: Sources of acoustic backscattering at 87.5 kHz. *J. Acoust. Soc. Am.*, **70**, No. 1, 134-142.
- Greenblatt, P., 1982: Distributions of volume scattering observed with an 87.5 kHz sonar. *J. Acoust. Soc. Am.*, **71**, No. 4, 879-885.
- Greenlaw, C. F., 1977: Backscattering spectra of preserved zooplankton. *J. Acoust. Soc. Am.*, **62**, No. 1, 44-52.
- Greenlaw, C. F., 1979: Acoustical estimation of zooplankton populations. *Limnol. Oceanogr.*, **24**, No. 2, 226-242.
- Greenlaw, C. F. and W. G. Percy, 1985: Acoustical patchiness of mesopelagic micronekton. *J. Mar. Res.*, **43**, 163-178.
- Halliday, D. and R. Resnick, 1970: *Fundamentals of Physics*, Wiley and Sons, New York, 827 pp.
- Hansen, D. S., 1984: Considerations in upper ocean Doppler velocimetry. *Ph.D. Thesis*, Univ. of California, San Diego.
- Hansen, D. S., 1985a: Asymptotic performance of a pulse-to-pulse incoherent Doppler sonar in an oceanic environment. *IEEE J. Ocean. Eng.*, **OE-10**, No. 2, 144-158.
- Hansen, D. S., 1985b: Receiver and analog homodyning effects on incoherent Doppler velocity estimates. *J. Atmos. Ocean. Technol.*, **2**, 644-655.

- Hansen, W. J. and M. J. Dunbar, 1971: Biological causes of scattering layers in the Arctic Ocean. In: *Proceedings of an International Symposium on Biological Sound Scattering in the Ocean*, Maury Center for Ocean Science, Report No. MC-005, G. B. Farquhar, Ed., 508-526.
- Helstrom, C. W., 1968: *Statistical Theory of Signal Detection*, Pergamon Press, Long Island City, 470 pp.
- Hersey, J. B. and R. H. Backus, 1962: Sound scattering by marine organisms. *The Sea*, Vol. 1, M. N. Hill, Ed., Wiley Interscience, New York, 498-539.
- Holliday, D. V. and R. E. Pieper, 1980: Volume scattering strengths and zooplankton distributions at acoustic frequencies between 0.5 and 3 mHz. *J. Acoust. Soc. Am.*, **67**, No. 1, 135-146.
- Jacobs, D. C. and C. S. Cox, 1987: Internal wave stress-shear correlations: A choice of reference frames. *Geophys. Res. Lett.*, in press.
- Jenkins, G. M. and D. G. Watts, 1968: *Spectral Analysis and its Applications*, Holden-Day, San Francisco, 525 pp.
- Johnson, R. K., 1977: Sound scattering from a fluid sphere revisited. *J. Acoust. Soc. Am.*, **61**, No. 2, 375-377.
- Joyce, T. M., D. S. Bitterman, and K. E. Prada, 1982: Shipboard acoustic profiling of upper ocean currents. *Deep-Sea Res.*, **29**, 903-913.
- Kampa, E. M., 1971: Photoenvironment and sonic scattering. In: *Proceedings of an International Symposium on Biological Sound Scattering in the Ocean*, Maury Center for Ocean Science, Report No. MC-005, G. B. Farquhar, Ed., 51-59.
- Kinzer, J., 1971: On the contribution of Euphausiids and other planktonic organisms to scattering layers in the eastern North Pacific. In: *Proceedings of an International Symposium on Biological Sound Scattering in the Ocean*, Maury Center for Ocean Science, Report No. MC-005, G. B. Farquhar, Ed., 476-489.
- Kosro, P. M., 1985: Shipboard acoustic current profiling during the Coastal Ocean Dynamics Experiment. *Ph.D. Thesis*, University of California, San Diego.
- Lhermitte, R., 1973: Meteorological Doppler radar. *Science*, **182**, 258-262.
- Lhermitte, R., 1983: Doppler sonar observations of tidal flow. *J. Geophys. Res.*, **88**, No. C1, 725-742.



- Lhermitte, R. and H. Poor, 1983: Multi-beam Doppler sonar observations of tidal flow turbulence. *Geophys. Res. Lett.*, **10**, No. 8, 717-720.
- Lhermitte, R. and R. Serafin, 1984: Pulse-to-pulse coherent Doppler sonar signal processing techniques. *J. Atmos. Ocean. Technol.*, **1**, No. 4, 293-308.
- Mack, C., 1966: *Essentials of Statistics for Scientists and Technologists*, Plenum/Rosetta, New York, 174 pp.
- McComas, C. H. and F. P. Bretherton, 1977: Resonant interaction of oceanic internal waves. *J. Geophys. Res.*, **82**, No. 9, 1397-1412.
- McIntyre, M. E., 1980: An introduction to the generalized Lagrangian-mean description of wave, mean-flow interaction. *Pure Appl. Geophys.*, **118**, 152-176.
- Mero, T. N., G. F. Appell, and D. L. Porter, 1983: Sea-truth experiments on acoustic Doppler current profiling systems. *Proc. Oceans '83*, 21-26.
- Miller, K. S. and M. M. Rochwarger, 1970: On estimating spectral moments in the presence of colored noise. *IEEE Trans. Inf. Theory*, **IT-16**, No. 3, 303-309.
- Miller, K. S. and M. M. Rochwarger, 1972: A covariance approach to spectral moment estimation. *IEEE Trans. Inf. Theory*, **IT-18**, No. 5, 588-596.
- Munk, W. H., 1981: Internal waves and small scale processes. In: *Evolution of Physical Oceanography*, B. Warren and C. Wunsch, Ed., 264-291.
- Müller, P., 1976: On the diffusion of momentum and mass by internal gravity waves. *J. Fluid Mech.*, **77**, No. 4, 789-823.
- Müller, P., G. Holloway, F. Henyey, and N. Pomphrey, 1986: Nonlinear interactions among internal gravity waves. *Rev. Geophys. Space Phys.*, **24**, No. 3, 493-536.
- Müller, P., D. J. Olbers, and J. Willebrand, 1978: The IWEX spectrum. *J. Geophys. Res.*, **83**, No. C1, 479-500.
- Neumann, G. and W. J. Pierson, 1966: *Principles of Physical Oceanography*, Printice-Hall, Englewood Cliffs, 545 pp.
- Occhiello, L. and R. Pinkel, 1979: A Doppler sonar controller. *Proc. Oceans' 79*, 148-152.

- Olbers, D. J., 1983: Models of the oceanic internal wave field. *Rev. Geophys. Space Phys.*, **21**, No. 9, 1224-1233.
- Papoulis, A., 1965: *Probability, Random Variables, and Stochastic Processes*, McGraw-Hill, New York, 583 pp.
- Passarelli, R. E. and A. D. Siggia, 1981: The autocorrelation function and Doppler spectral moments: Geometric and asymptotic interpretations. *Proc. 20th Conf. Radar Meteorology*, Amer. Meteor. Soc., Boston, Mass., 301-307.
- Pearcy, W. G. and R. S. Mesecar, 1971: Scattering layers and vertical distribution of oceanic animals off Oregon. In: *Proceedings of an International Symposium on Biological Sound Scattering in the Ocean*, Maury Center for Ocean Science, Report No. MC-005, G. B. Farquhar, Ed., 381-394.
- Pettigrew, N. R. and J. D. Irish, 1983: An evaluation of a bottom-mounted Doppler acoustic profiling current meter. *Proc. Oceans '83*, 182-186.
- Pinkel, R., 1979: Observations of a strongly nonlinear motion in the open sea using a range-gated Doppler sonar. *J. Phys. Oceanogr.*, **9**, No. 4, 675-686.
- Pinkel, R., 1980: Acoustic Doppler techniques. In: *Air-Sea Interaction*, F. Dobson, L. Hasse and R. Davis, Ed., Plenum Press, New York, 171-199.
- Pinkel, R., 1981: On the use of Doppler sonar for internal wave measurements. *Deep-Sea Res.*, **28A**, No. 3, 269-289.
- Pinkel, R., 1982: On estimating the quality of Doppler sonar data. *Proc. IEEE 2nd Working Conference on Current Measurement*, Hilton Head, S.C., 113-116.
- Pinkel, R., 1983a: Doppler sonar observations of internal waves: Wavefield structure. *J. Phys. Oceanogr.*, **13**, No. 5, 804-815.
- Pinkel, R., 1983b: MILDEX 1983, a Mixed Layer Dynamics Experiment. *Tech. Memo MPL TM-354*, Marine Physical Laboratory, Scripps Institution of Oceanography, San Diego, CA.
- Pinkel, R., 1984: Doppler sonar observations of internal waves: the wavenumber frequency spectrum. *J. Phys. Oceanogr.*, **14**, No. 8, 1249-1270.
- Pinkel, R., 1985: A wavenumber-frequency spectrum of upper ocean shear. *J. Phys. Oceanogr.*, **15**, 1453-1469.

- Pinkel, R., A. Plueddemann, and R. Williams, 1987: Internal wave observations from FLIP in MILDEX. *J. Phys. Oceanogr.* in press.
- Regier, L., 1979: Near-surface currents in the LDE. *Polymode Scientific Reports*, 1, Massachusetts Institute of Technology, Cambridge, Mass., 81-83.
- Regier, L., 1982: Mesoscale current fields observed with a shipboard profiling acoustic current meter. *J. Phys. Oceanogr.*, **12**, 880-886.
- Rowe, F. D. and J. W. Young, 1979: An ocean current profiler using Doppler sonar. *Proc. Oceans '79*, 292-297.
- Rowe, F. D., K. L. Deines, and R. L. Gordon, 1986: High resolution current profiler. *Proc. IEEE 3rd Working Conference on Current Measurement*, Airlie, VA.. in press.
- Ruddick, B. R., 1977: Observations of interaction between the internal wavefield and low frequency flows in the North Atlantic. *Ph.D. Thesis*, Woods Hole Oceanographic Institution.
- Ruddick, B. R., 1980: Critical layers and the Garrett-Munk spectrum. *J. Marine Res.*, **38**, No. 1, 135-145.
- Ruddick, B. R. and T. M. Joyce, 1979: Observations of interaction between the internal wavefield and low frequency flows in the North Atlantic. *J. Phys. Oceanogr.*, **9**, 498-517.
- Rudnick, P., 1964: FLIP: An oceanographic buoy. *Science*, **146**, 1268-1273.
- Rummler, W. D., 1968: Introduction of a new estimator for velocity spectral parameters. *Tech. Memo MM-68-4121-5*, Bell Telephone Laboratories, Whippany, N.J..
- Sanford, T. B., 1982: Velocity profiling: Some expectations and assurances. *Proc. IEEE 2nd Working conf. on Current measurement*, Hilton Head, S.C., 101-112.
- Sanford, T. B., R. G. Drever, and J. H. Dunlap, 1985: An acoustic Doppler and electro-magnetic velocity profiler. *J. Atmos. Ocean. Technol.*, **2**, 110-124.
- Serafin, R. J., 1975: Information extraction from meteorological radars. *Atmos. Technol.*, **6**, 46-54.

- Sirmans, D. and B. Bumgarner, 1975a: Numerical comparison of five mean frequency estimators. *J. Appl. Meteor.*, **14**, 991-1003.
- Sirmans, D. and B. Bumgarner, 1975b: Estimation of spectral density mean and variance by covariance argument techniques. *Proc. 16th Radar Meteorology Conf.*, Amer. Meteor. Soc., Boston, Mass., 6-13.
- Slater, E. and R. Pinkel, 1979: A 32 KW Doppler sonar. *Proc. Oceans '79*, 137-141.
- Spiess, F. N., 1968: Oceanographic and experimental platforms. *Ocean Engineering*, J. F. Brahtz, Ed., Wiley and Sons, New York, N.Y., 553-587.
- Squier, E. D., 1968: A Doppler shift flowmeter. *ISA Marine Sciences Instrumentation Symposium*, 16-19 January 1968, Florida.
- Teichmann, H., 1969: *Physical Applications of Vectors and Tensors*, G. G. Harrap and Co., London, 235 pp.
- Theriault, K. B., 1981: Bounds on pulsed-Doppler current profiler performance. *Tech. memo. No. 634*, Bolt, Beranek, and Newman, Inc., Cambridge, MA.
- Theriault, K. B., 1986: Incoherent multibeam Doppler current profiler performance: Part I - Estimate variance. *IEEE J. Ocean. Eng.*, **OE-11**, No. 11, 7-15.
- Thorpe, S. A., 1981: An experimental study of critical layers. *J. Fluid Mech.*, **103**, 321-344.
- Toman, K., 1984: Christian Doppler and the Doppler effect. *Eos, Trans. Am. Geophys. Union*, **65**, 1193-1194.
- Trump, C. L., B. S. Okawa, and R. H. Hill, 1985: The characterization of a midocean front with a Doppler shear profiler and a thermister chain. *J. Atmos. Ocean. Technol.*, **2**, 508-516.
- Underwood, K. H., 1981: Sodar signal processing methods and the Riso 78 experiment. *Ph.D. Thesis*, Penn. State University.
- Urick, R. J., 1983: *Principles of Underwater Sound*, McGraw-Hill, New York, 423 pp.



Van Trees, H., 1968: *Detection, Estimation, and Modulation Theory: Part I*, Wiley, New York, 697 pp.

Vlasak, W., 1968: Further development in the Doppler method of water-velocity measurement. *IEEE, Trans. Geosci. Electronics*, **GE-6**, 197-204.

Wiseman, W. J., R. M. Crosby, and D. W. Pritchard, 1972: A three dimensional current meter for estuarine applications. *J. Mar. Res.*, **30**, 153-158.

# ONR/MPL GENERAL DISTRIBUTION LIST

Chief of Naval Research  
Department of the Navy  
Arlington, Virginia 22217-5000  
Code 12, 122(2), 102C  
111, 112, 113,  
1122PO, 425-AC, 480

ONRDET  
NSTL Station  
Bay St. Louis, Mississippi 39529-5004  
Code 112, 1121, 1122CS, 422CB,  
1122PO, 1125GG

Director  
Office of Naval Research  
Branch Office  
1030 East Green Street  
Pasadena, California 91106-2485

Commander  
Naval Sea Systems Command  
Washington, D. C. 20362  
Code 63, 63R, 63R-23

Commanding Officer  
Naval Ocean Research and  
Development Activity  
NSTL Station  
Bay, St. Louis, Mississippi 39529-5004  
Code 100, 110, 300, 330,  
340, 350, 360, 500

Commander  
U.S. Naval Oceanographic Office  
NSTL Station  
Bay St. Louis, Mississippi 39522-5004  
Atten: Bill Jobst

Assistant Secretary of the Navy  
(Research Engineering & Systems)  
Department of the Navy  
Washington, D. C. 20360

Defense Advanced Res. Proj. Agency  
TTO - Tactical Technology Office  
1400 Wilson Boulevard  
Arlington, Virginia 22209-2308  
Atten: Capt. Kirk Evans

National Oceanic & Atmospheric  
Administration  
Ocean Engineering Office  
6001 Executive Boulevard  
Rockville, Maryland 20852

Commander  
Space and Naval Warfare  
Systems Command  
Washington, D. C. 20360  
Code PDW-124, 32QA

Commander  
Naval Ship Res. & Dev. Center  
Bethesda, Maryland 20084

Executive Secretary  
Naval Studies Board  
National Academy of Sciences  
2101 Constitution Avenue, N.W.  
Washington, D.C. 20418

Director  
Strategic Systems Proj. Ofc. (PM-1)  
Department of the Navy  
Washington, D. C. 20361  
Code NSP-2023

Commander  
Naval Ocean Systems Center  
San Diego, California 92152  
Code 00, 01, 16, 94, 531  
5301, 71, 72

Commander  
Submarine Development Group ONE  
Fleet Post Office  
San Diego, California 92152

Commanding Officer  
Civil Engineering Laboratory  
Naval Construction Battalion Center  
Port Hueneme, California 93043  
Code L40, L42

Commanding Officer  
Naval Underwater Systems Center  
Newport, Rhode Island 02844  
Atten: Dr. K. A. Kemp, Code 8213

Officer in Charge  
Naval Underwater Systems Center  
New London Laboratory  
New London, Connecticut 06320  
Code 900, 905, 910, 930, 980

Director of Research  
U.S. Naval Research Laboratory  
Washington, D. C. 20375  
Code 2620, 2627, 5000, 5100, 5800

Commander  
Naval Surface Combat Systems Center  
White Oak  
Silver Spring, Maryland 20910

Commanding Officer  
Naval Coastal Systems Laboratory  
Panama City, Florida 32401

STOIA  
Battelle Columbus Laboratories  
505 King Avenue  
Columbus, Ohio 43201

Commander  
Naval Air Systems Command  
Washington, D. C. 20361  
Code 370

Commanding Officer  
U.S. Naval Air Development Center  
Attention: Jim Howard  
Warminster, Pennsylvania 18974

Director  
Defense Documentation Center  
(TIMA), Cameron Station  
5010 Duke Street  
Alexandria, Virginia 22314

Institute for Defense Analyses  
1801 North Beaugard Street  
Arlington, Virginia 22311

Superintendent  
U.S. Naval Postgraduate School  
Monterey, California 93940

Chief Scientist  
Navy Underwater Sound Reference Div.  
U.S. Naval Research Laboratory  
P.O. Box 8337  
Orlando, Florida 32806

Supreme Allied Commander  
U.S. Atlantic Fleet  
ASW Research Center, APO  
New York, New York 09019  
Via: ONR 100 M. CNO OP092D1,  
Secretariat of Military,  
Information Control, Committee

Director  
Institute of Marine Science  
University of Alaska  
Fairbanks, Alaska 99701

Director  
Applied Physics Laboratory  
Johns Hopkins University  
Johns Hopkins Road  
Laurel, Maryland 20810  
Atten: J. R. Austin

Director  
College of Engineering  
Department of Ocean Engineering  
Florida Atlantic University  
Boca Raton, Florida 33431

Director  
Marine Research Laboratories  
c/o Marine Studies Center  
University of Wisconsin  
Madison, Wisconsin 53706

Director  
Applied Research Laboratory  
Pennsylvania State University  
P.O. Box 30  
State College, Pennsylvania 16802

Director  
Applied Physics Laboratory  
University of Washington  
1013 East 40th Street  
Seattle, Washington 98105

Director  
The Univ. of Texas at Austin  
Applied Research Laboratory  
P.O. Box 8029  
Austin, Texas 78712

Director  
Lamont-Doherty Geological Observatory  
Torrey Cliff  
Palisades, New York 10964

Director  
Woods Hole Oceanographic Institution  
Woods Hole, Massachusetts 02543

Director  
Inst. of Ocean Science Engineering  
Catholic University of America  
Washington, D.C. 20017

National Science Foundation  
Washington, D. C. 20550

Office of Naval Research  
Resident Representative  
c/o Univ. of California, San Diego  
Mail Code Q023  
La Jolla, California 92093

University of California, San Diego  
Marine Physical Laboratory  
Branch Office  
La Jolla, California 92093

U230442